Deep Carbon Dioxide and Volatile Degassing in the Lesser Antilles Arc: Origin, Source and Budget

TiVonne A. Howe

Lancaster Environment Centre

Lancaster University

This thesis is submitted for the degree of

Doctor of Philosophy

February 2025

Abstract

This thesis provides novel constraints on volatile systematics and magmatic plumbing systems at Soufrière Hills Volcano (SHV), Montserrat and La Soufrière volcano, St Vincent, which are two of three volcanoes in the Lesser Antilles arc that have erupted in the last 100 years.

In this thesis, SHV melt inclusions in magma erupted across 15 years of activity from 1995-2010 are characterised in order to improve our understanding of the plumbing system, better interpret current unrest, and thus aid risk management. Through the use of total CO_2 and H_2O, solubility models reveal a vertically extensive transcrustal magma mush system beneath SHV. The inferred depth range of 5.7–17 km, spanning the upper to mid crust, far exceeds previously published estimates of 5-6 km, which omitted the 90 % of CO_2 hosted within vapour bubbles. The measurements of total CO_2 enabled the pre-eruptive CO_2 budget to be calculated across the studied Phases and, together with published remote sensing-derived fluxes, reveal that the maximum amount of CO_2 that can be fluxed through magma at this volcano is ~1500-1750 tonnes/day, indicating that measured CO_2 fluxes above this threshold is due to CO_2 flushing. To further quantify the release of total CO_2 from Soufrière Hills Volcano, a preliminary soil CO_2 survey shows that diffuse degassing of CO_2 at this volcano amounts to ~340 g m^{-2} day^{-1} in 2021/2022, a reduction of more than 90% from diffuse CO_2 degassing in 2008.

Melt inclusions at La Soufrière are also characterised, providing the first full melt inclusion dataset (H_2O, total CO_2, S, Cl, and F) for the explosive phase of the 2020/2021 eruption, and indeed for any eruption at this volcano, enabling the reconstruction of magma storage characteristics, pre-eruptive volatile budgets, and volatile emissions to the atmosphere. Depths inferred from the H_2O and CO_2 contents of melt inclusions are 2.4–8.9 km, and correspond well with independent depth estimates from clinopyroxene-only barometry of 1.1–8.0 km. In contrast to SHV, La Soufrière melt inclusion bubbles are largely empty. However, the presence of carbonates suggests that CO_2 was lost from these bubbles. Additionally, we provide evidence of polybaric crystallisation based on mineral-liquid equilibria, mineral barometry and melt inclusion thermobarometry. Using the improved petrological method, we estimate that a minimum of 2.99 Mt H_2O, 0.14 CO_2, 0.39 Mt SO_2, and 0.18 Mt HCl was emitted during the explosive phase of the 2020/2021 eruption. Preliminary soil CO_2 surveys show that the contribution of diffuse CO_2 degassing to the total CO_2 output is negligible (76 kg day^{-1}) compared to CO_2 fluxes from passive degassing. Altogether, this thesis provides critical information on CO_2 systematics at Soufrière Hills Volcano and La Soufrière St Vincent in the Lesser Antilles, refines our understanding of the magmatic system at Soufrière Hills Volcano, and provides independent pressure and depth estimates at La Soufrière volcano.

Table of Contents

List of Figures

List of Tables

Acknowledgements

Hearty thanks are extended to my supervisors for guiding me through the last four years. Thank you for all of your help in putting this project together, and for agreeing to be a part of my team. Firstly, to Hugh, for your immense motivation and support. For always being confident in me and the progress of this thesis, despite the many, many setbacks faced over the years! To TC, for believing in me and having taught me so much from my days at the MVO as well as during this PhD. And to Séverine, for introducing me to the world of melt inclusions and for your guidance and support. Thank you all for sharing your knowledge and for helping me to achieve the goals set by my 18-year-old self. I have indeed learned a lot and I am greatly appreciative.

Many thanks to my co-authors, Federica and Paul for your contributions that made the papers and by extension this thesis possible. Federica, thank you for your kindness and your warm welcoming spirit during my time at LMV.

To my parents, Yvonne and Trevor, my friends and my family – thank you, thank you, thank you for your support and encouragement, and for your belief in me.

I would also like to thank everyone who played a part in helping me to submit this thesis in one way or the other. Nicolas at LMV for teaching me sample prep, Jean-Luc and Iris for showing me the way around the microprobe, Cees-Jan and Laurette for their help with the ionprobe, and Dave at LEC for his help with carbon isotopic analysis. Many thanks are also extended to Margaret Hartley and David Neave for their discussions particulary on melt inclusion reconstruction. To everyone who braved the Caribbean sun and accompanied me in the field… Thank you!

Sincere thanks are also extended to the Government of Montserrat for funding, making this project possible.

Author's Declaration

I, TiVonne A Howe, declare that, other than where the contribution of others is specified, this thesis is entirely my own work, and has not been submitted for the award of a degree at this or any other university.

This thesis is 57,374 words in length, excluding the title page, abstract, table of contents, list of figures, list of tables and references, and is therefore within the word limit as specified by Lancaster Environment Centre.

TiVonne A. Howe

Multi-author Declaration

Please see below the list of publications included in this thesis with information regarding my contributions to each.

Chapter 2

Melt inclusion bubbles provide new insights into crystallisation depths and CO_2 systematics at Soufrière Hills Volcano, Montserrat

Published in Frontiers in Earth Science, 2025, Volume 12
https://doi.org/10.3389/feart.2024.1509409

TiVonne A Howe, Thomas E Christopher, Séverine Moune, Hugh Tuffen, Federica Schiavi

TAH, TEC, SM and HT co-developed the concept. TAH prepared and analysed samples and processed and interpreted the data. SM guided data interpretation and TEC and HT contributed to data interpretation. FS contributed to Raman analysis and data processing. HT led PhD supervision and TEC and SM co-supervised the PhD. TAH drafted the manuscript and figures, and all authors contributed to the article and reviewed and approved the submitted version.

Chapter 3

Volatile emissions and magma storage conditions for the 2021 explosive eruption at La Soufrière volcano, St Vincent from melt inclusions

Manuscript submitted to Volcanica

TiVonne A. Howe, Thomas E. Christopher, Séverine Moune, Hugh Tuffen, Paul D. Cole, Federica Schiavi

TAH, TEC, SM and HT co-developed the concept. PDC collected and provided samples. TAH prepared and analysed samples and processed and interpreted the data. SM guided data interpretation and TEC, HT and PDC contributed to data interpretation. FS contributed to Raman analysis and data processing. HT led PhD supervision and TC and SM co-supervised the PhD. TH drafted the manuscript and figures, and all authors contributed to the article, reviewed and approved the submitted version.

Chapter 4

Investigating diffuse CO_2 degassing at Soufrière Hills Volcano, Montserrat and La Soufrière volcano, St Vincent

In preparation for submission to Bulletin of Volcanology

TiVonne A. Howe, Thomas E. Christopher, Séverine Moune, Hugh Tuffen

TAH, TEC, SM and HT co-developed the concept. TAH and TEC conducted fieldwork. TAH analysed samples and processed and interpreted the data. TEC, SM and HT contributed to data interpretation. HT led PhD supervision and TC and SM co-supervised the PhD. TH drafted the manuscript and figures, and all authors contributed to the article, reviewed and approved the submitted version.

All co-authors have signed below to confirm this.

Sincere Regards,

TiVonne A Howe, Thomas E Christopher, Séverine Moune, Hugh Tuffen, Federica Schiavi, Paul Cole

1 Introduction

Magmas stored within the crust contain varying proportions of volatile species, which are mainly sourced from the mantle during the generation of the crust, but also derived from other sources such as hydrothermal circulation, seawater percolation through faults or carbon-or water-rich sediments (Figure 1.1; Zellmer et al., 2014). During subduction, these volatiles are returned to the mantle, with 20-80% of carbon in the subducting crust being recycled to the outer Earth, reprecipitated in the mantle, or remains in the accretionary wedge (Johnston et al., 2011; Keleman & Manning, 2015; Mason et al., 2017). Subduction zones therefore are a significant feature in the cycle of major volatiles including carbon, and regulate atmospheric CO_2 concentrations over geological time scales (Johnston et al., 2011; Clift, 2016). As magmas migrate upwards from the mantle into the crust, their concentrations can increase via processes such as crystallisation-driven fractionation (Mason et al., 2017). Meanwhile, their solubility decreases as the confining pressure reduces, and this leads to saturation and subsequent exsolution (e.g. Wallace et al., 2015a; Edmonds and Woods, 2018).

Carbon is cycled through the atmosphere, biosphere and hydrosphere and is linked to the inner Earth by plate tectonics, with the inner Earth accounting for 90% of all terrestrial carbon (van der Meer et al., 2014; Mason et al., 2017; Plank and Manning, 2019; Wong et al., 2019). Carbon sinks at the Earth's surface include (i) carbon stored with the ocean, dissolved as bicarbonate (Plank and Manning, 2019), (ii) carbonate minerals (e.g. calcite and argonite) precipitated from seawater or fluids derived from seawater in the upper oceanic crust during low temperature alteration (Bickle, 1996; Gillis and Coogan, 2011; Mason et al., 2017) and (iii) organic carbon in soils and vegetation, and those making up ocean- and land-dwelling organisms (Bickle, 1996; Mason et al., 2017; Plank and Manning, 2019). The pathway for carbon release from the inner to the outer Earth includes the decarbonation of metamorphic rocks containing carbon, and mantle fluids that enter the lithosphere and are released through faults and fractures, both at tectonic regimes, in particular zones of continental collision, and more importantly volcanic regimes (subduction zones, rift valleys and hotspots), which account for 40–70% of carbon return to the outer Earth (Bickle, 1996; van der Meer et al., 2014).

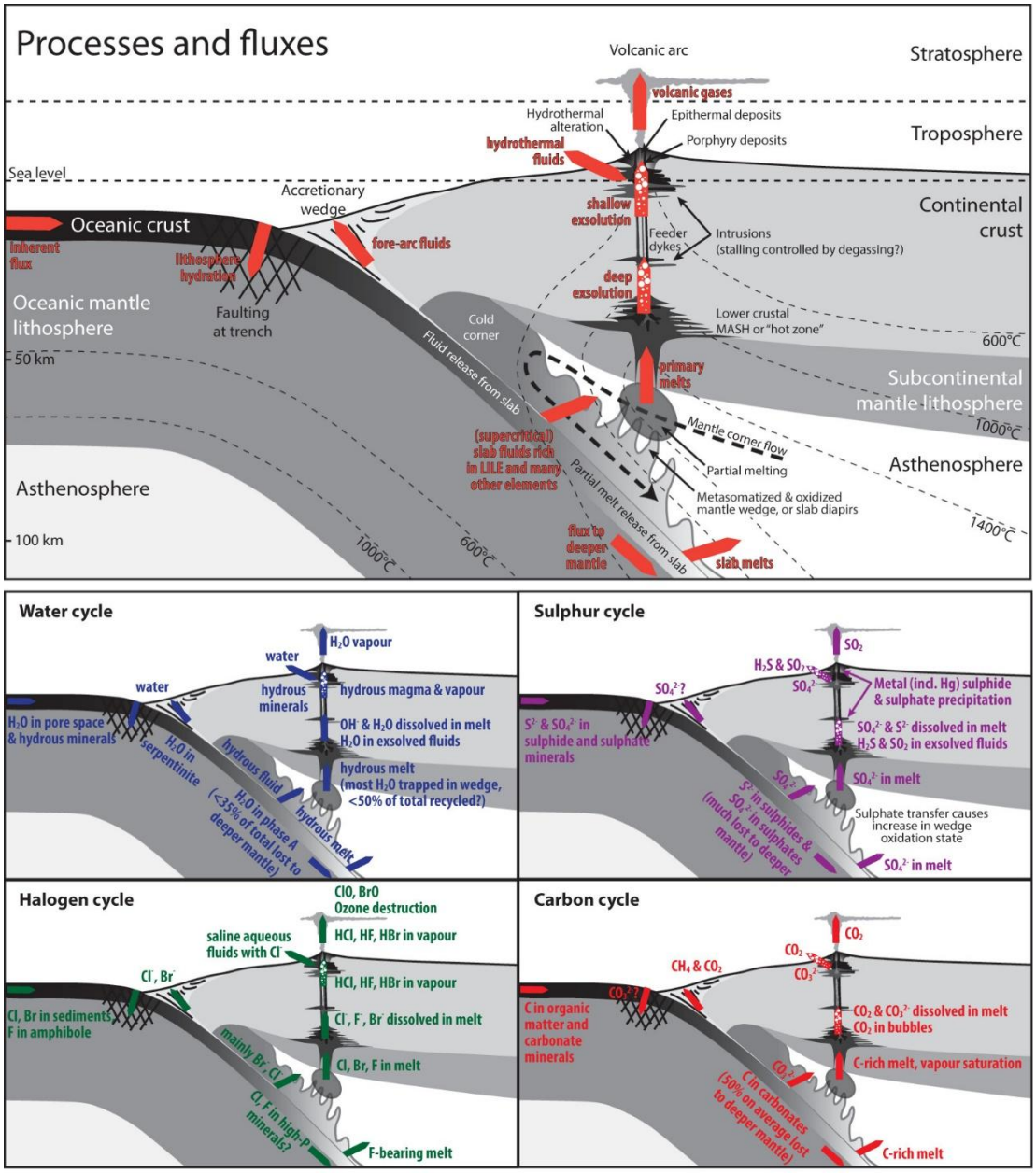

Figure 1.1 - Subduction zone processes showing the introduction and release pathways for volatiles including H_2O, S, Cl, F and CO_2. From Zellmer et al., (2014). - Subduction zone processes showing the introduction and release pathways for volatiles including H_2O, S, Cl, F and CO_2. From Zellmer et al., (2014).

Volatiles in magma are predominantly made up of H, C, O, S, Cl and F, and are either dissolved within the magma or exist as gas or vapour within the magmatic system. H_2O is generally the most abundant, followed by CO_2, but the other volatiles also play significant roles (Gerlach, 1980; Symonds et al., 1994; Best, 2003). Gases exsolved from basaltic magma typically contain greater CO_2 than H_2O concentrations, likely due to a greater abundance in some mantle source regions (Lowenstern, 2001) as well as deeper and more complete exsolution to the vapour phase. In global arc settings, magmatic H_2O concentrations vary greatly, from <0.5 to >8 wt.%, dependent on the subducted H_2O input (Wallace, 2005). Magmatic CO_2 concentrations in arc settings are also highly variable, and when quantified in melt inclusions using techniques such as IR spectroscopy or ion microprobe analysis their concentrations may range from 0 to ~2500 ppm (Wallace, 2005; Wallace et al., 2015a). The actual magmatic concentrations may, however, be higher than these recorded values if some degassing had occurred prior to inclusion entrapment (Wallace, 2005). Sulphur and chlorine are similarly variable among global arcs, with magmas containing 900-2500 ppm and 500-2000 ppm in the melt respectively (Wallace, 2005; Wallace et al., 2015a).

Volatiles such as carbon dioxide in volcanic settings fundamentally control the storage, ascent and eruptibility of magma. Volatile fluxes also play a pivotal role in the carbon cycle, and have thus influenced global climate change over billions of years (Dasgupta and Hirschmann, 2010). Carbon dioxide in magma has the ability to dictate eruptive styles, and drive explosive eruptions through its exsolution and degassing (e.g. Burton et al., 2007; Allard, 2010; Allison et al., 2021). Carbon can also flush from the mantle or deeper crust up into magmatic storage regions in the mid- to upper crust (e.g. Yoshimura and Nakamura, 2011; Caricchi et al., 2018), leading to pressure build-up and the fracture-driven opening of pathways for rapid magma ascent. Estimates of carbon release associated with volcanic activity are uncertain, due to lack of direct measurements (Burton et al., 2013). While estimates of released quantities of other volatiles, such as sulphur dioxide, can be supplemented by Earth-observing satellites (e.g. Theys et al., 2019; Queißer et al., 2019; Cofano et al., 2021), applying this technology to carbon dioxide is particularly challenging, due to its rapid dilution in the atmosphere once released (Burton et al., 2013). However, a combination of gas measurements and petrological approaches can yield approximate constraints on volcanic CO_2 emissions. Estimates of carbon release from volcanoes vary widely, from 67– 600 Mt carbon yr^{-1}, with volcanoes in arc settings contributing 10–30% of this quantity (Plank and Manning, 2019; Wong et al., 2019).

There are a number of parameters that influence the exsolution of volatiles such as CO_2, including the structure and pressure regime of the plumbing system. Understanding of these parameters is particularly important at island arcs such as the Lesser Antilles as they provide valuable insights into volcanic activity, and therefore contribute to hazard and risk mitigation. In the Lesser Antilles many

people reside on the flanks of active volcanoes, and volcanism has recently had a destructive impact on the region (e.g. the eruption of Soufrière Hills Volcano, Montserrat, 1995-2010).

Due to its exsolution from magmas at deep crustal depths (Edmonds and Wallace, 2017), surface emissions of CO_2 and CO_2-volatile ratios such as CO_2/SO_2 or CO_2/S_T can serve as a precursory signal for processes occurring in the deeper system (e.g. Burton et al., 2007; Pérez et al., 2012; Aiuppa et al., 2017; Aiuppa et al., 2021), such as migration of magma to shallower storage regions, which may in lead to an eruption due to magma decompression and subsequent volatile exsolution. The migration of hot magma from depth into upper or mid crustal regions of magma storage within a transcrustal magmatic system (Cashman et al., 2017) can cause the eruption of substantial amounts of previously stored magma. Diffuse degassing of CO_2 is well-characterised in many volcanic settings, and is prevalent in arc settings (e.g. Hernandez et al., 2001a; Hernandez et al., 2001b; Notsu et al., 2005; Klein et al., 2024). However, diffuse CO_2 degassing is poorly studied in the Lesser Antilles arc, and thus, the deep carbon budget remains poorly understood and baseline (inter-eruption) carbon fluxes remain poorly defined.

This thesis presents new data related to magmatic glasses trapped in an assemblage of minerals, in the form of melt inclusions, to provide new insights into the nature of the magmatic storage regions beneath Soufrière Hills Volcano, Montserrat and La Soufrière volcano, St Vincent (Figure 1.14). The compositions of melt inclusion glasses together with their host minerals place constraints on the temperature, pressure and therefore depth of residence of magma within the plumbing system, using solubility-pressure relationships for magmatic volatiles and independent thermobarometric constraints from the composition of mineral phases and glasses. The composition and flux of CO_2 diffused through the soil in hydrothermally active areas of both islands are also quantified, and compared to fluxes released through plumes in an effort to estimate the total CO_2 flux released from each volcanic system.

1.1 Structure and Organisation of the Thesis

This thesis focuses primarily on two volcanic systems in the Lesser Antilles arc – Soufrière Hills Volcano, Montserrat and La Soufrière volcano, St Vincent, and uses volatiles in melt inclusion glasses and bubbles, and CO_2 diffused through the soil to uncover CO_2 and other volatile systematics at these volcanoes.

Chapter 1 - In the first section, there is a brief introduction of the science underlying the study of magmatic CO_2, explanation of the importance of volatiles within magmatic systems, and an overview of diffuse CO_2 degassing.

In the second section, there is an explanation of melt inclusions and their use to reconstruct magmatic systems. This includes detailed discussion of magmatic carbon and the important role of vapour bubbles, in which the vast majority of the melt inclusion's carbon may reside. I discuss the use of volatile concentrations to reconstruct entrapment pressures, and also the bigger picture of how petrologically reconstructed CO_2 fluxes can be integrated and compared with surface measurements of emissions.

In the third section, there is an introduction to the Lesser Antilles volcanic arc and its volcanic systems, to provide geological context for the two case studies.

Chapter 2 presents a modified version of the research article '*Melt inclusion bubbles provide new insights into crystallisation depths and* CO_2 *systematics at* Soufrière *Hills Volcano, Montserrat*', published in 2025 in the journal Frontiers in Earth Science (Howe et al., 2025). Here, plagioclase and orthopyroxene-hosted melt inclusions are used to estimate saturation pressures of H_2O and CO_2 in melt inclusion glasses and bubbles for four phases of eruptive activity at Soufrière Hills Volcano, Montserrat. Using the solubility relationships with pressure of H_2O and CO_2 revealed that the magmatic system consists of a vertically extensive magma storage region from ~5.7 to 17 km through the upper and mid crust, comparable to other systems in the Lesser Antilles arc.

Chapter 3 outlines the work presented in the research article '*Volatile emissions and magma storage conditions for the 2021 explosive eruption at La Soufrière volcano, St Vincent from melt inclusions*' submitted to the journal Volcanica in 2025. This study uses olivine, plagioclase, orthopyroxene and clinopyroxene hosted melt inclusions to provide an independent estimation of magma storage parameters for the 2020-2021 eruption of La Soufrière volcano, St Vincent. I use H_2O-CO_2 solubility models, liquid-crystal equilibria, mineral barometry and modelling of CO_2/S_T ratios in melt inclusions together with CO_2/S_T ratios in the plume to demonstrate the presence of two main crystallising bodies

within the crust, where migration of the deeper body into the shallow body at approximately 6.4 km depth led to decrepitation and loss of CO_2 prior to eruption. Using an improved approach to the petrological method where the gas phase is accounted for in addition to the melt, the release of H_2O, CO_2, SO_2 and HCl to the atmosphere during the explosive phase of the eruption was estimated at 2.99, 0.14, 0.39 and 0.18 Mt respectively.

Chapter 4 presents the research article '*Investigating diffuse* CO_2 *degassing at Soufrière Hills Volcano, Montserrat and La Soufrière volcano, St Vincent*' in preparation for submission to the journal Bulletin of Volcanology. This chapter investigates the role of CO_2 degassing through surface manifestations of the hydrothermal system at La Soufrière volcano and Soufrière Hills Volcano, and its contribution to the total CO_2 output of both volcanoes. Diffuse CO_2 flux has decreased at Soufrière Hills Volcano over the last 15 years by >90%. Unlike other arc volcanoes such as La Soufrière de Guadeloupe, the process of diffuse CO_2 degassing is currently not a significant contributor to the total CO_2 output at Soufrière Hills Volcano, and La Soufrière, St Vincent.

Chapter 5 provides a discussion of elements of the thesis.

Chapter 6 is a conclusion of the thesis.

1.2 Motivation for this work

Volcanic arc settings represent one of the most dynamic, and destructive geological zones on Earth. One of the key components of volcanism in these settings are volatiles, which have the ability to influence and drive eruptions. Therefore, understanding the behaviour, distribution and role volatiles in arc settings is essential, as well as their implications on the Earth and its climate through their release into the atmosphere.

Overall, the study of volatiles allows improved understanding of interactions within the entire volcanic system, encompassing the mantle, crust and the surface, and through their investigation, we can advance our knowledge of fundamental processes which have the potential to affect millions of people who live in arc settings such as the Lesser Antilles.

While volatiles have been well studied among the Lesser Antilles arc (e.g. Edmonds et al., 2001; Bouvier et al., 2010; Edmonds et al., 2014; Cassidy et al., 2015; Balcone-Boissard et al., 2018; Camejo-Harry et al., 2018; Camejo-Harry et al., 2019; Cooper et al., 2020; Balcone-Boissard et al., 2023; Metcalfe et al., 2022), there are still some gaps in our knowledge of melt inclusions in the arc, in particular CO_2 content. This thesis therefore aims to:

1) Characterise the total volatile content of melt inclusions at Soufrière Hills Volcano, Montserrat where the contribution from vapour bubbles have not been analysed for eruptions over a 15-year period from 1995-2010. This new analysis allows for magma storage parameters such as pressure and temperature across the majority of the eruptive period to be calculated and for temporal trends to be ascertained, and the loading of important greenhouse gases such as CO_2 into the atmosphere to be quantified. Additionally, the contribution of diffuse CO_2 degassing to the total CO_2 output of the magmatic will be quantified.

2) Characterise the total volatile content of melt inclusions at La Soufrière volcano, St Vincent, by (i) taking into account the contribution of volatiles from vapour bubbles, (ii) providing an updated dataset of CO_2 in melt inclusions from various host phenocrysts previously unaccounted for and therefore provide the first estimates of pressure using H_2O-CO_2 solubility relationships, and (iii) estimate the full volatile budget of the system. The first full volatile panel (H_2O, CO_2, S, Cl and F) for any eruption at this volcano, as well as the most recent 2020-2021 eruption will be provided. This allows for the first calculations of magma storage characteristics (pressure, temperature) using volatile data for any eruption at La Soufrière. The volatile budget of the magmatic system will also be calculated, along with volatile release

of the main volatile elements. The contribution of diffuse CO_2 degassing to the total CO_2 output will also be quantified.

1.3 Magmatic Systems

A *magmatic system* consists of the production of magmas in the mantle, their storage within the crust, and their transportation to the surface in explosive or effusive eruptions (Cashman et al., 2017). The term magma refers to that portion of the system that is eruptible, which may contain up to 55-65% crystals, along with an exsolved volatile phase (Sparks and Cashman, 2017), where the abundance of these phases (melt, crystals and exsolved volatile phase) are determined by parameters such as pressure, temperature, oxygen fugacity and the chemical composition of the magmatic components (Best, 2003). Magmatic system models have shifted from the view of a singular pool of collected magma towards a model which describes a transcrustal complex network of crystal-rich mushes (Figure 1.2; Marsh, 2004; Cashman et al., 2017). Magmatic systems may span a wide range of temperatures and pressures, where magma can be undersaturated with volatiles at high pressures and temperatures, or volatile-saturated as pressure and temperature decrease. Therefore, over the magmatic system, growing crystals have the ability to trap volatiles - undersaturated or saturated melts, which can be used to reconstruct the conditions of their formation (Cashman and Edmonds, 2019).

The depth at which magma resides in the crust prior to eruption is based on a number of factors. The first control on magma storage depth is the concept of neutral buoyancy, where magmas rise through the crust based on the buoyancy of the melt in comparison to that of the host crustal rock. The magma residence depth is therefore determined when the densities of the melt and crust is equal – the *zone of neutral buoyancy* (Walker et al., 1988). Secondly, rheological conditions determine magma storage depths where heterogeneities within the crust (e.g. layers of particularly strong rock) have the ability to stop magma ascent and instead force magma to flow laterally (Mazzarini et al., 2010; Gudmundsson, 2011). More recently, it has been determined that the H_2O content of magma may play a significant role in the storage depths of mafic-intermediate composition systems (Rasmussen et al., 2022), as during magma ascent through the crust, H_2O saturation is achieved resulting in degassing, followed by an increase in magma viscosity and crystal growth which in turn hinders further ascent.

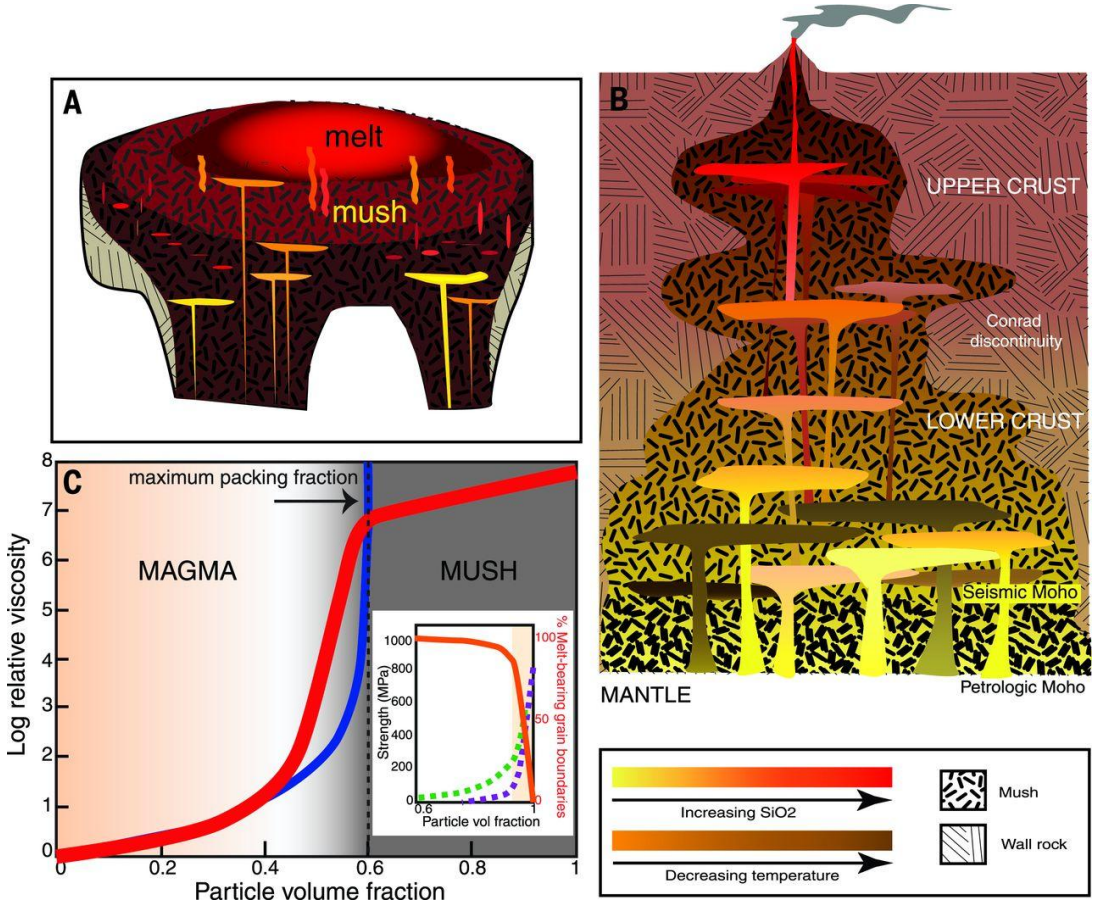

Figure 1.2 – Schematic of a magmatic system. In [A], mafic magma is recharged from deeper levels, followed by migration of more silica rich melts. [B] Schematic of a vertically extensive magma storage region. Connections between ponding zones can be temporary, and can therefore lead to destabilisation of the ponds. [C] The transition from magma to mush depends occurs at ~60% of crystals by volume. The blue line is calculated assuming 60% volume, and the Roscoe-Einstein formula while the red line is calculated based on Costa et al., (2009). From Cashman et al., (2017).

1.3.1 Volatiles in Magmatic Systems

In magmatic systems, the solubility of a volatile species refers to the maximum concentration of a volatile that can be dissolved in silicate melt at a given combination of conditions to include pressure, temperature, composition of the magma, partial pressure or fugacity of oxygen and the presence of other volatiles (Blank and Brooker, 1994; Wallace and Anderson, 2000; Best, 2003; Cashman, 2004; De Vivo et al., 2005; Parfitt and Wilson, 2008; Wallace et al., 2015a; Edmonds and Wallace, 2017). As magmas rise through the crust, an exsolved volatile phase can form when the concentrations of the volatile species in the melt exceeds their solubilities, thereby becoming saturated (De Vivo et al., 2005; Edmonds and Wallace, 2017). Exsolution can occur as a result of decompression, or during isobaric cooling and crystallisation (Figure 1.3; Edmonds and Woods, 2018). As a response to vapour saturation, bubbles may nucleate and grow in the melt (Sparks, 1978; Edmonds and Wallace, 2017; Edmonds and Woods, 2018).

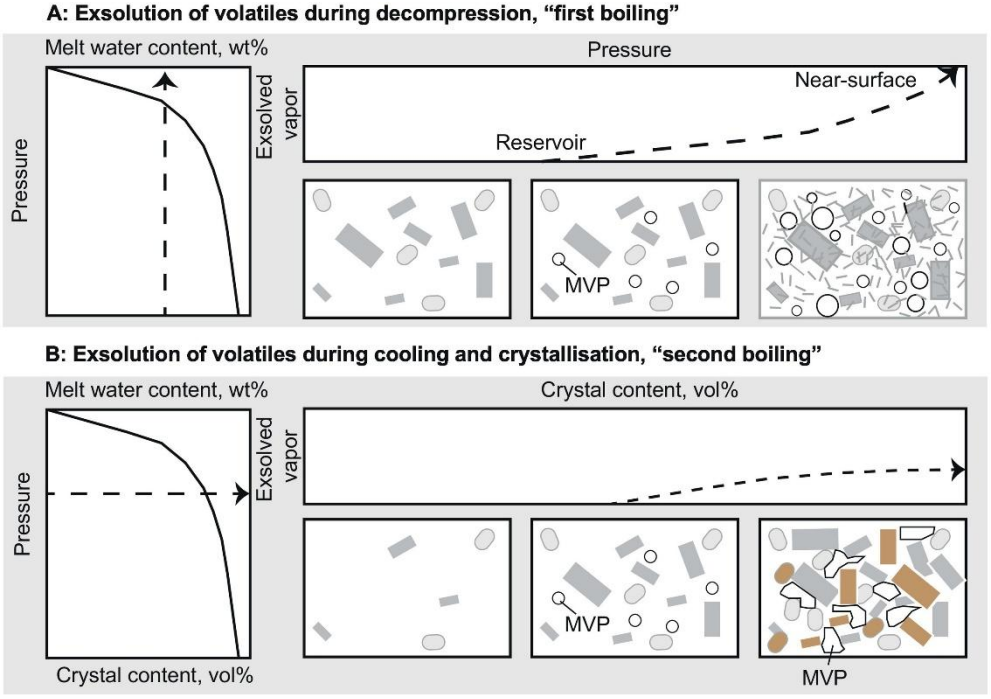

Figure 1.3 – Depiction of volatile saturation in magmas. [A] Volatile saturation can be achieved by decompression, which leads to crystallisation as a result of degassing. [B] Volatile saturation can be achived due to cooling and crystallisation, and an exsolved volatile phase. MVP refers to the exsolved magmatic volatile phase. From Edmonds and Woods, (2018).

Bubble nucleation occurs when a sufficient oversaturation overcomes the energy barrier for a stable bubble nucleus to form (Gardner et al., 1999; Parfitt and Wilson, 2002; Shea, 2017; Gardner et al., 2023). Homogenous bubble nucleation occurs in a fluid medium (higher surface energy), where volatile molecules randomly come together to form a bubble, or heterogenous nucleation, where molecules form on an irregular, pre-existing surface such as crystals (Figure 1.4; Parfitt and Wilson, 2002; Gardner et al., 2023). These heterogeneities control the level of supersaturation required to allow the nucleation process to begin (Gardner et al., 1999, Shea, 2017; Gardner et al., 2023). The number or density of bubbles generated in a nucleation step depends on the rate of decompression (e.g. Hamada et al., 2010) and the availability of nuclei to promote heterogeneous nucleation (Shea, 2017).

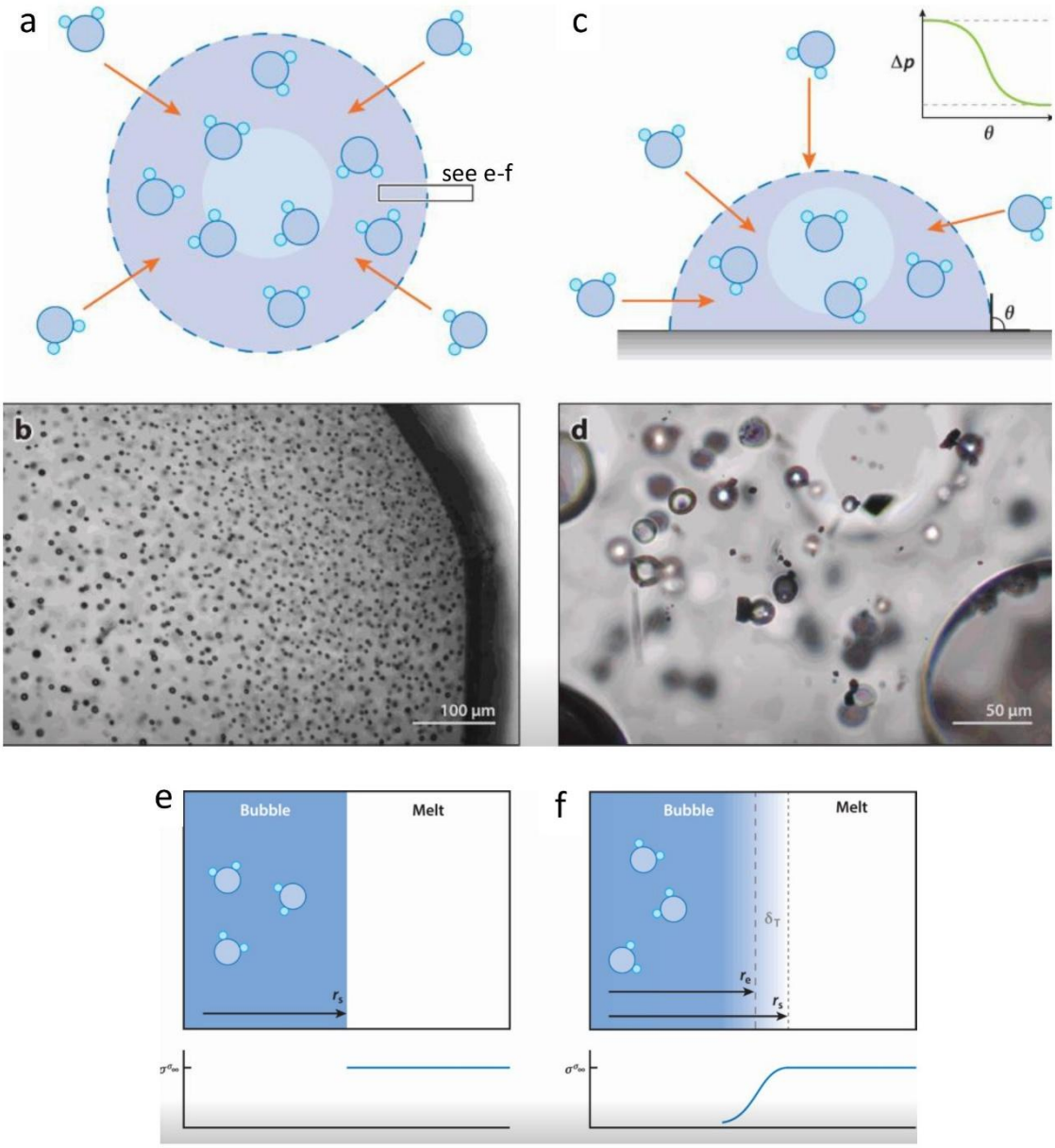

Figure 1.4 – Diagram showing two processes by which bubble nucleate in silicate melts. [A] Homogeneous nucleation – here, volatiles come together in the melt to form a new phase. [B] Example of homogenous nucleation of H_2O bubbles in a rhyolitic melt. [C] Heterogeneous nucleation – in this process, volatiles come together on a pre-existing surface. Supersaturation in this case depends on the contact angle (θ) between the bubble and the pre-existing surface. [D] Example of heterogeneous nucleation on a magnetite crystal (which are the opaque squares) in a rhyolitic melt. Modified from Gardner et al., (2023).

After a stable bubble nucleates, the next step involves growth. Bubbles that form within a non-stressed volume of magma take on a spherical shape due to surface tension that minimizes the surface area. If shear stresses are imposed, the bubble shape is determined by the interplay between viscous stresses and surface tension, and defined by the capillary number (e.g. Rust et al., 2003). Bubble sizes are generally on the scale of microns to centimetres, however, in some low viscosity basaltic magmas, they can reach as much as 10 metres (Best, 2003). Bubble growth is dependent on several factors including the viscosity of the melt which controls how much the bubble wall can expand, diffusion of volatiles into a bubble across a concentration gradient, coalescence of bubbles to form a larger bubble, Ostwald ripening where volatiles migrate from small bubbles into larger ones through bubble walls, magma ascent, associated with decompression and heat loss, volatile concentration, and the solubility of the volatile (Figure 1.5; Cashman and Mangam, 1994; Gardner et al., 2000; Best 2003). However, bubbles mainly grow by (i) volatile diffusion into the bubble, (ii) decompression, and (iii) coalescence (e.g. Sparks, 1978; Gardner et al., 1999; Gardner et al., 2000; Parfitt and Wilson, 2002). Numerical studies show that diffusion and viscosity-controlled bubble growth are determined by the decompression rate, viscosity and initial saturation pressure (Toramaru, 1995). Bubble growth controlled by diffusion is also determined by the availability of the volatile species being degassed, composition of the melt, temperature and solubility. Decompression-triggered growth is governed by the upward velocity of the magma and its rise distance (goverened by Stoke's Law), and the overall bubble growth may in turn be controlled by the viscosity of the melt, as this may be the factor limiting the rate of expansion of gas bubbles (Sparks, 1978; Toramaru, 1995; Parfitt and Wilson, 2008). As the magma rises, the volume of gas in the nucleated bubbles increase due to decreasing pressure according to the ideal gas law (Equation 1.1) These bubble growth regimes all depend on the availability of volatiles to be degassed and the bubble size (Sparks, 1978; Toramaru, 1995). The diffusion regime generally produces small bubbles, whilst growth by decompression produces bigger bubbles (Sparks, 1978).

$$PV = nRT \tag{1.1}$$

The ideal gas law of Equation 1.1 shows the relationship between pressure (P), volume (V), n (number of moles), R (the gas constant) and temperature (T). Here it is demonstrated that for a fixed amount of gas, pressure and volume are inversely related at constant temperature, which can be expressed as Boyle's Law in Equation 1.2:

$$P_1V_1 = P_2V_2 \tag{1.2}$$

Where P_1 is the initial pressure felt by the gas, V_1 is the volume occupied by the gas, P_2 is the pressure felt by the gas after decompression, and V_2 is the volume occupied by the gas after decompression.

During magma ascent, the pressure exerted on the bubble decreases, which allows for expansion of the walls with no addition of volatiles into the bubble. Decompression also promotes exsolution of volatiles from the melt into bubbles but in this process, it is paired with diffusion.

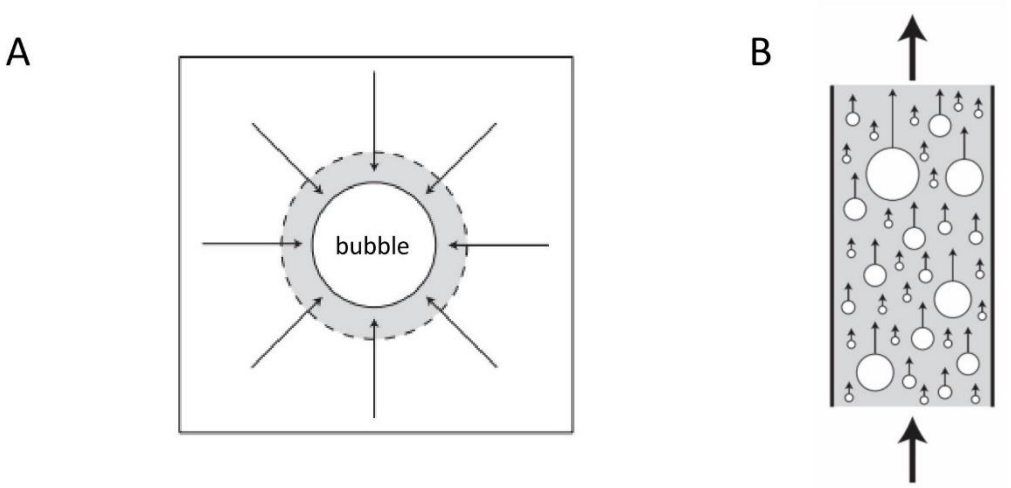

Figure 1.5 – Main controls on bubble growth. Adapted from Parfitt and Wilson, (2009). [A] Molecules of the exsolving volatiles move from an area of high concentration around the outside of the bubble into the bubble, where a concentration gradient exists. As the concentration of volatiles around the bubble diminishes, another concentration gradient is created between the area surrounding the bubble and the wider magma chamber. [B] Bubble growth by coalescence. Bubble growth by coalescence is only significant under certain circumstances. The volatiles within bubbles are low density; therefore, bubbles are always more buoyant than the magma in which they are contained. As bubbles rise throughout the magma column, it is acted upon by two forces – the buoyancy force and the drag force. Once the ascent rate of the bubble is not too fast, the bubble should maintain a spherical shape. If the diameter of the bubble remains small enough, the drag component is controlled only by the melt viscosity.

1.3.1.1 CO_2 in Magmatic Systems

CO_2 within silicate glasses can occur as two different species: the molecular form (CO_2), or as carbonate (CO_3^{2-}) anions (Blank and Brooker, 1994; Wallace and Anderson, 2000; Wallace et al., 2015a). In mafic silicate glasses, the only carbon species present is the carbonate anion, whilst molecular CO_2 is more important in the most silica-rich glasses, reflecting the degree of melt polymerization (Wallace and Anderson, 2000). Melts in the range between tholeiitic basalt and rhyolite are likely to contain both CO_2 molecules and carbonate ions (Holloway and Blank, 1994; Wallace and Anderson, 2000). As CO_2 dissolves to form carbonate ions, it has the potential to react with the melt and therefore, certain cations such as Ca^{2+}, K^+, and Na^+ have a high influence (and to a lesser extent Mg^{2+} and Fe^{2+}) on its solubility. As a result, carbonate is more soluble in alkaline basalts than it is in alkali-poor tholeiites. On the other hand, molecular CO_2 does not react with the melt, therefore, there should be less variation of CO_2 solubility with the alkalinity of more evolved magmas (Dixon, 1997; Lowenstern, 2001).

The solubility of CO_2 in basalts and rhyolites is similar (Figure 1.6) and one to two orders of magnitude less than H_2O (Ni and Keppler, 2013; Scholz et al., 2023) at comparable pressure and temperature.

Due to its low solubility (e.g. VolatileCalc, Newman and Lowenstern 2002; MagmaSat, Ghiorso and Gualda, 2015), CO_2 exsolves from the melt at greater depths and lesser degrees of crystallisation than H_2O. The exsolution of CO_2 can impact the greater magmatic system by reducing the concentration of other volatiles present in the magma such as water, as small amounts of H_2O and other volatiles will diffuse into CO_2 bubbles during exsolution (Parfitt and Wilson, 2008). These mixed volatile bubbles can either migrate towards the top of the magma chamber or can be lost from the entire system, leaving the magma H_2O-depleted. The timing of magmatic CO_2 exsolution will dictate which volatile will have the most important role in driving eruptions. In deep-ocean settings, H_2O exsolution is suppressed by the high confining pressure, and so exsolution of magmatic CO_2 can drive explosive eruptive activity (Helo et al., 2011). In shallower, lower-pressure settings, CO_2 is lost from the magma before an eruption, and thus another volatile (typically H_2O on Earth) will be the dominating volatile during an eruption. Finally, the pressurisation associated with CO_2 exsolution can drive failure of the walls of magmatic reservoirs and thus open pathways for magma ascent (Best, 2003; Parfitt and Wilson, 2008; Edmonds and Wallace, 2017).

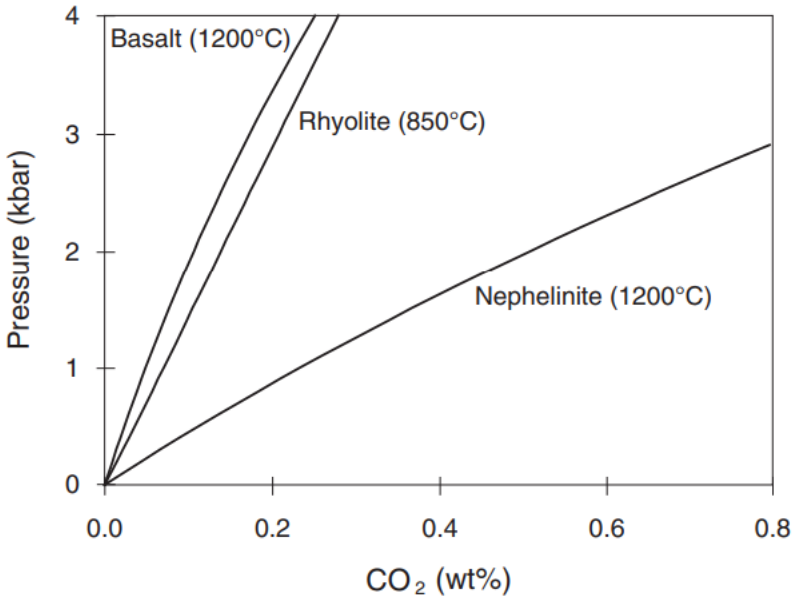

Figure 1.6 – CO_2 solubility is generally comparable in basalt (calculated using Iacono-Marziano et al., 2012) and rhyolite (calculated using Newman and Lowenstern, 2002) melts. In contrast, there is a strong increase in solubility for a nephelenitic melt (alkali-rich, silica-poor). From Wallace et al., (2015a).

1.3.1.2 H_2O, Sulphur and Halogens (Chlorine and Fluorine) in Magmatic Systems

In silicate melts, H_2O is dissolved as two species – hydroxyl (OH^-) groups and as H_2O molecules, with varying proportions based on total water content, temperature and pressure (Stopler, 1982; Stopler, 1989; Sparks et al., 1994). Similarly, to CO_2, H_2O solubility in the melt is pressure and temperature dependent, with solubility decreasing with increasing temperature (Figure 1.7), but unlike CO_2, the solubility of H_2O is greater in rhyolite than in basalts, although this is mainly due to differences in rhyolite and basaltic temperatures, instead of their differences in composition (Wallace et al., 2015a). The controls on solubility therefore has implications for the depths at which H_2O exsolves from the magma, where it exsolves at much shallow depths than CO_2, and H_2O in basaltic magmas exsolving at shallower depths than rhyolitic magmas. H_2O content in magmas vary with tectonic setting, where mid-ocean ridge basalts contain little H_2O, at 0.3-0.5 wt.%, followed by hotspot generated basalts at 0.5-1.5 wt.% H_2O (Edmonds and Wallace, 2017). In global arc settings, mafic magmas are generally made up to 2-6 wt.% H_2O, where the average differs by arc. However, the global H_2O average as measured in melt inclusions is 3.9±0.4 wt.%, and can infer saturation at the final magma storage depth prior to eruption (Plank et al., 2013).

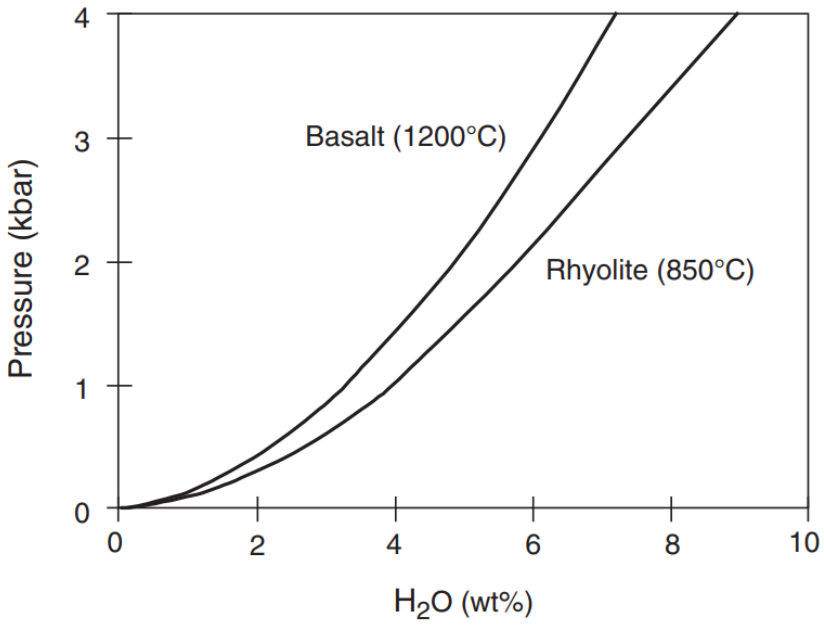

Figure 1.7 – Solubility of H_2O in a basalt vs rhyolite melt. Solubility is stronger in rhyolite due to the lower temperature. From Wallace et al., (2017a).

Unlike H_2O, the solubility of sulphur decrease with increasing temperature, but also heavily depends on the oxidation state of the magma, as similarly to CO_2 and H_2O, it can dissolve as two species. In reduced states below FMQ+1 (the sulphate-sulphide transition at the fayalite-magnetite-quartz buffer; Figure 1.8A), sulphur dissolves as sulphide (S^{2-}) and exsolves more favourably, while in oxidised states, it dissolves as sulphate (SO_4^{2-}) and less favourably partitions (when partitioning occurs, it is governed by Equation 1.3, and refers to the ratio of a volatile element between two phases, for example between melt and vapour), into the vapour phase (Edmonds and Wallace, 2017). The solubility of these two species can differ greatly due to differences in the size and bonding behaviour (Carroll and Webster, 1994).

$$\frac{S_{gas}}{S_{melt}} = K_s\,, \tag{1.3}$$

Sulphur concentrations in arc magmas are highly variable and may range between 0-6 wt.% of its composition, existing the melt phase, as well as a vapour phase (Wallace and Gerlach, 1994; Wallace, 2001), with the vapour phase accounting for up to 90 wt.% of the total sulphur budget (Scaillet et al., 2003). Modelling of sulphur in magmas erupted from Mt Etna (Italy) has shown that it begins to exsolve at pressures of ~140 MPa (Spillaert et al., 2006b), however, fluid-melt partitioning of sulphur can be modelled individually using melt inclusion compositions using models such as Sulfur_X (Ding et al., 2023).

Volcanic SO_2 injected into the stratosphere during explosive eruptions may form sulfate aerosol, which affect the radiative budget of the atmosphere by reflecting solar radiation back into space and cooling the atmosphere, but also by absorbing radiation which then heats the stratosphere (Robock, 2000).

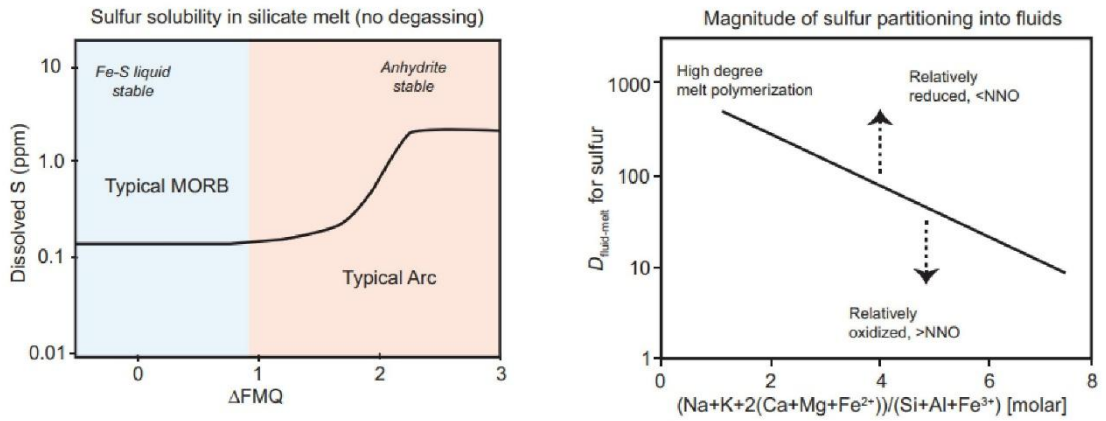

Figure 1.8 – Solubility of sulphur in silicate melts. [A] Solubility of S vs oxygen fugacity for mid-ocean ridge vs arc settings. This shows the lower solubility of S under different conditions as sulphide vs

sulphate. [B] Controls on S portioning between the vapour and melt phases. NNO is the nickle-nickle oxide buffer. From Edmonds and Wallace, (2017).

Chlorine solubility in magmas, like that of CO_2, H_2O and S is also influenced by pressure and temperature, and the concentration of total alkalis and Al_2O_3 (Carroll and Webster, 1994). Like sulphur, chlorine does not favour the melt, and instead partitions into an aqueous fluid where it can exist at >70 wt.%, in comparison to as low as hundreds of ppm in the melt, or in cases of magmas that are H_2O-CO_2 vapour saturated, partitions into the vapour at 1-8 times greater than that of the melt (Carroll and Webster, 1994; Wallace et al., 2015a). Therefore, chlorine degassing from the melt occurs at incredibly shallow pressures, modelled at Mt Etna to be ~100 MPa (Spillaert et al., 2006b).

Fluorine solubility is most affected by melt compositions, and in basaltic-intermediate magmas, only a few hundred ppm is typically dissolved (Wallace et al., 2015a). Owing to its high solubility, fluorine partitions more favourably into the liquid phase, and therefore, similarly to chlorine, degasses at very shallow pressures, modelled at 10 MPa at Mt Etna (Spillaert et al., 2006b; Wallace et al., 2015a).

1.4 Melt inclusions

Technological advances allow for better estimates of volcanic gas flux from active volcanoes through ground based (e.g. Edmonds et al., 2002; Edmonds et al., 2003; Christopher et al., 2010; Christopher et al., 2014b), airborne based (e.g. Rose et al., 1988; Tu et al., 2004) and satellite-based (e.g. Theys et al., 2019; Queißer et al., 2019; Burton et al., 2021; Cofano et al., 2021) media using direct sampling, in-situ and remote sensing measurement techniques. However, there are often limitations associated with these methods. For example, (i) these techniques cannot be applied to inactive volcanoes since their magmatic systems have shut down and there is no input of volatiles to be exsolved, thus have no passive or active plumes, and (ii) volatiles degassed through plumes and fumaroles interact with the atmosphere, and can dilute the original concentration (Burton et al., 2013; Coca et al., 2014). Petrological methods can also be used to constrain the concentration and flux of magmatic volatiles including CO_2 (Devine et al., 1984; Scaillet et al., 2003), and these hinge on two pieces of evidence. Firstly, melt inclusions trapped in crystals within the magmatic system (see section 1.2) record volatile concentrations and melt composition. Secondly, groundmass glasses of tephra or lava provide a sample of the erupted magma, and the proportion of its volatiles that remained in solution in the melt, as opposed to being exsolved en route to the surface (e.g Moore and Bodnar, 2019). The difference between the volatile concentration of melt inclusions and groundmass glasses can therefore indicate the amount of volatile species released from the magma into the surround environment during its eruption and ascent.

Melt inclusions (MI) are small parcels of melt (~1-300 µm; Lowenstern, 1995; Bodnar and Student, 2006; Audetat and Lowenstern, 2014) trapped in minerals and may contain crystals, glass and vapour bubbles, of which the latter two contain volatiles. Melt inclusions (e.g. Figure 1.9) exist in both volcanic and plutonic rocks and are formed during crystal growth as melt is trapped within the crystal. They occur individually or together in what is known as melt inclusion assemblages. Assemblages can occur as randomly-spaced inclusions, in growth zones, or in zones of resorption in crystals (Figure 1.10; Moore et al., 2015).

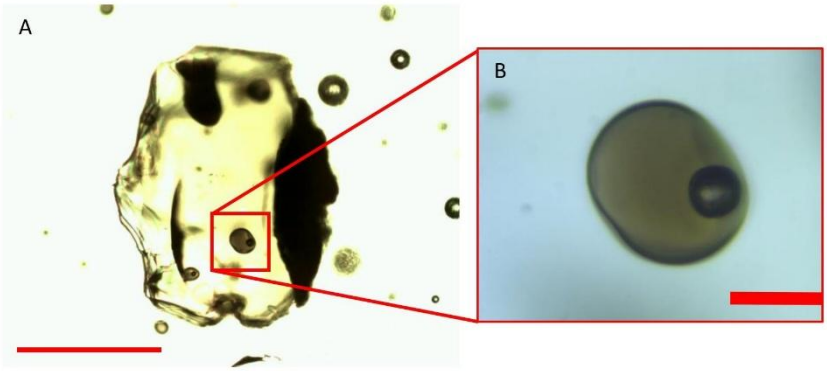

Figure 1.9 – Example of a melt inclusion hosted in an olivine crystal from La Soufrière volcano, St Vincent. Scale bar on [A] represents 200 µm. Scale bar on [B] represents 50 µm.

Generally, there are two types of melt inclusions: (i) vitreous melt inclusions that are formed by rapid quenching of high temperature magma to form glass, and can also contain bubble(s), and (ii) crystalline melt inclusions, commonly associated with plutonic rocks, but can also be found in volcanic rocks such as lava domes, where the melt inclusion crystallises during slow cooling and decompression. These melt inclusions often comprise of a mixture of mineral phases and vapour-filled bubbles (Audetat and Lowestern, 2014).

Formation of Melt Inclusions

Overall, there are three types of melt inclusions (Figure 1.10; Lowenstern, 1995; Audetat and Lowenstern, 2014). **Primary melt inclusions** are formed during crystal growth or regrowth, thus, trapping any phase present in the magma during crystal growth. **Pseudo-secondary melt inclusions** form where fracturing of the host crystal occurs during crystallisation, allowing fluid to fill the fracture which becomes trapped after healing. Since pseudo-secondary inclusions and their host crystals were formed at the same stage, the inclusions reflect the chemistry of the magma at the time of entrapment. **Secondary melt inclusions** are formed by fracturing of the crystal after crystallisation has ended, trapping fluid after healing.

In the case of silicate melt inclusions, primary inclusions are the predominant focus of study, and are determined to be any inclusion trapped during crystal growth or during regrowth after dissolution (Lowenstern, 1995; Wallace et al., 2021). After complete seclusion of the melt inclusion from the melt by its host, their shapes are typically irregular. Melt inclusions then achieve a more consistent shape by a process of post-entrapment evolution of their morphology, where dissolution and re-

precipitation changes the shape to that with the lowest surface area per volume – a sphere – or that with the lowest surface energy – a negative crystal shape (Manley, 1996; Steele-Macinnis et al., 2011).

Melt inclusions therefore capture a snapshot of the magma at the time of entrapment, and a range of characteristics of the magma can be discerned, including magma storage conditions such as chemistry, pressure, temperature, and oxygen fugacity, as well as the volatile budget of the volcanic system and degassing processes, volatile contents of primary melts or the mantle, magma ascent, and its magmatic evolution (Spillaert et al., 2006; Moune et al., 2007; Hartley et al., 2014; Neave et al., 2017; Hartley et al., 2018; Zurek et al., 2019; Feignon et al., 2022; Wieser et al., 2023).

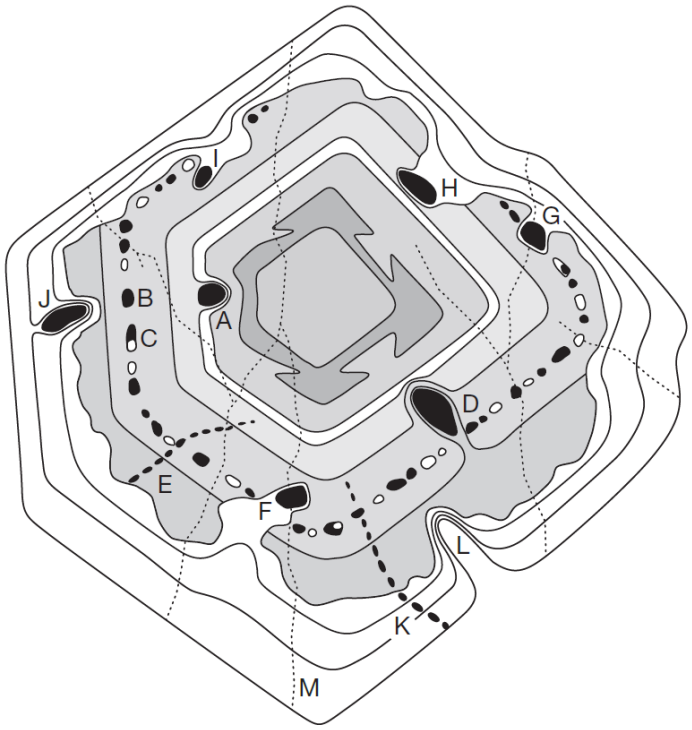

Figure 1.10 – Illustration of different types of melt inclusions trapped in a host crystal. Inclusion A-D represent primary melt inclusions trapped along a surface irregularity (A), growth zones, and structure caused by resorption or dissolution (D). The melt inclusions of E are an example of psuedosecondary inclusions formed sometime between the outer grey crystal zone and a dissolution event. Melt inclusions F, G, H and I are also primary, having formed within resorption or dissolution craters within the early forming crystal. Melt inclusion J formed in the same manner as D, but is younger. The melt inclusions in K, while similar to E are secondary, forming after final crystal growth. Structure L occurred from resorption or dissolution and had the potential to trap a melt inclusion if the crystal continued to grow. The structures of M are cracks or trails of fluid inclusions cutting across the crystal. Cracks through melt inclusions (e.g. F, G) enable modification of their compositions. From Audetat and Lowenstern, (2014).

1.4.1 *Post-entrapment Modification of Melt Inclusions*

After entrapment, melt inclusions can evolve from their parental magma. Post-entrapment modification, including diffusion of water between inclusions and host or melt (Gaetani et al., 2012), post-entrapment crystallisation (PEC), or growth of crystals or the formation of vapour bubble/s (Steele-Macinnis et al., 2011; Créon et al., 2018) can alter the original composition (both major and volatile element) of the inclusion, rendering it unrepresentative of the starting magma composition, and complicating understanding of the magmatic record. Thus, prior to the use of melt inclusions to unlock magmatic processes, the original contents must be reconstructed where possible (e.g. Rasmussen et al., 2020). However, the modification processes themselves can shed light on steps in the pre-quench evolution of the magma, including re-equilibration, magma ascent and eruption, and cooling (Wallace et al., 2021).

1.4.1.1 H^+ diffusion

During ascent from the deeper crust, volatiles in magma can exsolve according to their individual solubility-pressure dependencies. As crystals within the magma seek equilibrium, volatile species such as H_2O can diffuse from the crystal into the surrounding (melt-rich) environment. While melt inclusions can act as zones of retention of H_2O and other volatiles, H_2O can be either lost or gained through the diffusion process, as H^+ protons diffuse through their host crystal (Barth and Plank 2021).

Due to rapid H^+ diffusion through host crystals such as olivine, H_2O concentrations in melt inclusions can change on very short timescales. For example, Gaetani et al., (2012) found H_2O diffusing through crystals over timescales of <24 hours, where a constant ^{18}O value remained throughout the experiment, except at the olivine rim, indicating that (i) there was no addition of external oxygen in the hydration process and (ii) that the increase in H_2O in the melt inclusion was the product of diffusion of protons through its olivine host. This is relevant as processes such as ascent/eruption and especially cooling of volcanic deposits after eruption occur on these short timescales. Studies of eruptive products at Fuego volcano, Guatemala (Berlo et al., 2011; Lloyd et al., 2011) have shown how cooling rates determine the influence of H^+ diffusion in on measured water concentration. More rapidly-cooled, smaller particles (Fauria and Manga, 2018) have higher melt inclusion H_2O concentrations than samples of slower-cooled bombs and lava flows, which can retain magmatic temperatures over days-years after eruption (e.g. Tuffen et al., 2013) and thus diffusively lose H^+ from their melt inclusions.

Diffusive loss in quenched samples can be fingerprinted by examining D/H ratios, as H diffuses quicker than D, but only up to the point of total re-equilibration (Hauri, 2002; Halis et al., 2015). Factors influencing the extent of H^+ diffusion in olivine-hosted melt inclusions are explored in detail by Barth and Plank (2021), with the sizes of the host crystal and melt inclusions and the water content evolution of the external magma especially important, as explored below.

Factors contributing to the re-equilibration of H_2O include:

1) The partition coefficient (K_D) of H^+, where K_D refers to the ratio of water in the host crystal vs the silicate melt (Equation 1.4; Newcombe et al., 2020). K_D of nominally anhydrous minerals ranges from ~0.0007–0.026 (Aubaud et al., 2004; Newcombe et al., 2020). Olivine has the lowest K_D value, such that the H_2O content of olivines within mafic arc magmas with on average 3.9±0.4 wt.% H_2O is only ~0.004 wt.%, or 40 ppm (Plank et al., 2013; Newcombe et al., 2020). Plagioclase K_D varies with melt water content. In H_2O-poor conditions (melt H_2O ≤1 wt.%), K_D is ≈0.01, while in H_2O-rich conditions with melt H_2O ≥4 wt.%, K_D is only ≈0.005. K_D has an intermediate value of 0.01-0.005 for melt H_2O ranging between 1-4 wt.% (Hamada et al., 2013).

$$K_D = \frac{H_2O_{crystal}}{H_2O_{melt}} \quad 1.4$$

2) Diffusivity/diffusion coefficients of water-bearing species H^+, -OH, and H_2O_m. H^+ diffusivity is the rate of diffusive mobility imposed by a concentration gradient (Barth and Plank, 2021). This rate has the impact of controlling diffusion timescales *t* according to Equation 1.5:

$$t \approx \frac{x^2}{2D} \quad 1.5$$

where x is distance and D is diffusivity. Diffusion rates depend on diffusion mechanisms and the type of host crystal, and strongly on temperature (Qin et al., 1992; Johnson and Rossman, 2013). H^+ diffusivity in plagioclase tends to be lower than those in other nominally anhydrous minerals such as olivine, garnet and pyroxene (Johnson and Rossman, 2013). In quartz, the diffusivity is often in the range of 10^{-10} to 10^{-7} m^2 sec^{-1} but can be as low as 10^{-13} m^2 sec^{-1} (Qin et al., 1992).

3) Distance between inclusion and host rim - The differences in H_2O concentration between the melt inclusion and magma create a concentration gradient where diffusion occurs from the area of higher concentration to that of lower concentration. The overall length of the concentration gradient increases with time, according to the relationship defined by Equation 1.6 (Barth and Plank, 2021):

$$x \propto \sqrt{Dt} \qquad 1.6$$

where D is again H^+ diffusivity and t time. As a result, central melt inclusions will be less affected by H^+ diffusion than those closer to host rims.

4) Melt inclusion size influences the amount of H^+ diffusion and water loss occurring during re-equilibration. This is because (i) smaller melt inclusions contain a smaller volume of volatiles than larger inclusions, and therefore have less H_2O to be transferred during the re-equilibration process, and (ii) a small surface area allows less H_2O into the host (Chen et al., 2012; Barth and Plank, 2021).

Therefore, H^+ diffusion is an important post-entrapment modification as it can lead to H_2O loss or increase in melt inclusions, but also has additional effects on melt inclusions. Firstly, water loss leads to pressure decrease, which in turn causes CO_2 exsolution into vapour bubbles in response to this decompression which in turn would need to be accounted for. Secondly, dehydration (H^+ diffusion into the melt inclusion) causes a reduction in $Fe^{3+}/\Sigma Fe$, whereas $Fe^{3+}/\Sigma Fe$ increases during hydration (H^+ diffusion out of the melt inclusion; Gaetani et al., 2012).

1.4.1.2 Post-Entrapment Crystallisation (PEC)

Post-entrapment crystallisation (PEC) of melt inclusions can modify their major and volatile compositions. There is some disagreement as to whether PEC occurs in all melt inclusions (Kent, 2008) or only those that have cooled at relatively slow rates (Steele-Macinnis et al., 2011; Bucholz et al., 2013), however, PEC occurs in all volcanic related environments, from magma storage to eruption, and occurs when melt from the inclusion crystallizes on the inclusion wall during cooling (Steele-Macinnis et al., 2011) due to the availability of nucleation sites. PEC can also be triggered by degassing and decompression. While PEC may not be easily identifiable using optical microscopy, it can be identified by a crystalline texture on the inclusion rim using backscattered electron microscopy (Kent, 2008). PEC can alter host as well as melt inclusion chemistry. In olivine, alteration tends to involve Fe depletion and MgO enrichment in the melt inclusion (Danyushevsky et al., 2000), while more albitic rich crystal rims develop in plagioclase (Nielson et al., 1995), together with changes in the Ca/Al ratio, Mg#, MgO, FeO, CaO and Al_2O_3 contents of the inclusion (Zhang et al., 2016).

1.4.1.3 Vapour Bubble Formation

Bubble formation in silicate melt inclusions can result from a number of pathways, based on the pressure-volume-concentration characteristics of the melt inclusion-host crystal system (Steele-Macinnis et al., 2011; Moore et al., 2015). These include: (i) post-entrapment crystallisation; as melt crystallises on the inclusion wall, the transition of phases leads to a volume and pressure decrease in the inclusion. This in turn triggers volatile supersaturation, and thus causes a vapour bubble to nucleate and is usually the first step in vapour bubble formation (Aster et al., 2016). CO_2 can then migrate into the vapour bubble as a result of decreases in the solubility of CO_2 (Hartley et al., 2014), related not only to pressure changes, but to changes in major oxide element composition (Weiser et al., 2021), especially in basalts, where CO_2 solubility is also a function of major oxide element composition (Maclennan, 2017); (ii) differential thermal contraction of the melt inclusion and its host – this process has a large influence on vapour bubble formation and growth and occurs during cooling. The host crystal and the melt inclusion have differing thermal expansivities, resulting in the melt contracting more than the host (Aster et al., 2016). The volume of melt decreases while the density increases during cooling from high magmatic temperatures at eruption to the glass transition temperature at 900-1000 °K (Ryan and Sammis, 1981; Gottsmann et al., 2004) and leads to bubble growth (Hanyu et al., 2020; Weiser et al, 2021). It is estimated that during cooling, a temperature

difference of 100°C leads to formation of a bubble that is ~0.9-1.6 vol% of the inclusion (Wallace et al., 2015b); (iii) H_2O loss as previously discussed in section 1.3.1.1, and (iv) a combination of those outlined above.

Bubbles are sometimes described as a vacuum, containing no volatiles (e.g. Steele-Macinnis et al., 2011; Moretti et al., 2018), however, it is argued that it is impossible for bubbles to be empty, as, for this to occur, the bubble must maintain a vacuum from its inception, while the melt remains at higher pressure, throughout its cooling history (Moore et al., 2015). Since there is the potential for volatile sequestration into the bubble, measuring volatiles in the glass portion alone has the potential to underestimate the total volatile concentration, making it difficult to calculate accurate magma chamber characteristics, crystallisation pressure, solubility pressures and other properties.

Volatiles such as CO_2, H_2O and S have been shown to be contained in the bubble in varying amounts, with more than 90% of CO_2 as vapour, up to 50% of CO_2 as carbonates, up to 60% of sulphur as sulphates/sulphides, and up to 16% of H_2O stored in bubbles (Hartley et al., 2014; Moore et al., 2015; Esposito et al., 2016 Hanyu et al., 2020; Schiavi et al., 2020; Venugopal et al., 2020). Since carbonates, sulphates, sulphides, halides and other minerals are made of other elements (major and minor), there is also the potential for these elements (e.g. Na, Ca, Mg, Fe or Cu) to be sequestered to the bubble (Schiavi et al., 2020; Venugopal et al., 2020). The implications of not taking the bubble into account can be significant, since calculating parameters such as pressure requires quantified amounts of volatiles, particularly H_2O and CO_2. Underestimation of volatile content can then have additional effects on the calculation of other parameters such as oxygen fugacity, of which pressure is a factor, as well as modelling of CO_2/S_T, and calculating pre-eruptive volatile budgets and volatile release into the atmosphere.

Cooling rate influences volatile sequestration to the bubble, as for H^+ diffusion (section 1.3.1.1). It has been found that melt inclusions in rapidly quenched tephra at Laki volcano, Iceland contained less CO_2 in bubbles than melt inclusions in lava flows, due to the rapid cooling of tephra, which reduced the amount of CO_2 able to diffuse into bubbles before quenching. Lava flows cooled quickly enough to prohibit crystal growth in the glass, but slowly enough to allow CO_2 diffusion across the bubble interface before quenching (Hartley et al., 2014).

1.4.2 *Assessment and Reconstruction of Original Melt Compositions*

Since post-entrapment modifications can alter original melt inclusion compositions, it is of great importance that each inclusion be assessed for a series of post-entrapment modifications in order to identify erroneous results, and where possible, correct these modifications. Melt inclusions that have crystallised or nucleated bubbles can be rehomogenised by heating, until a single homogenous melt is formed. However, heating can trigger volatile loss such as H_2O diffusion out of the inclusion, or even decrepitation (Audetat and Lowenstern, 2014) and so is not appropriate for quantification of volatile concentrations.

Assessment and Reconstruction of PEC in Melt Inclusion Glasses

The assessment for PEC is based on the degree of host crystal-melt inclusion equilibrium. If equilibrium is achieved, PEC is likely negligible, and the melt inclusion composition is representative of the starting composition. If equilibrium is not achieved, PEC has likely altered the melt inclusion (and potentially also host) composition. In all melt-mineral pairs, equilibrium is assessed on the basis of the partition coefficient K_D, and the extent of PEC can be quantified. Alternatively, equilibrium can be assessed by comparing the melt inclusion compositions to an established liquid line of descent (LLD) for related whole rock and groundmass glass compositions (e.g. section 2.5.2.1 and section 3.5.3.1). A departure of melt inclusion composition from the LLD indicates that compositions are out of equilibrium, although the degree of PEC cannot be calculated. In olivine- and pyroxene-hosted melt inclusions, melt inclusions affected by PEC should show lower FeO than the LLD on a plot of FeO vs SiO_2 for instance. In plagioclase, melt inclusions can be tested against various LLDs. For example, disequilibrium due to PEC should show lower Al_2O_3 in the Al_2O_3 vs K_2O LLD, or higher MgO increasing the MgO vs K_2O LLD. The compositions of affected melt inclusions can then be corrected by adding the composition of the host back into the inclusion until compositions reflect the LLD or until equilibrium is achieved.

In olivine-hosted melt inclusions, K_D is assessed based on the Fe-Mg exchange coefficient shown in Equation 1.7:

$$K_D(Fe-Mg)^{ol-liq} = \left[\frac{X_{Fe}^{ol}\, X_{Mg}^{liq}}{X_{Mg}^{ol}\, X_{Fe}^{liq}}\right] \quad 1.7$$

where X_b^a is the cation fraction of b in a (Putirka, 2008), and 'ol' and 'liq' refer to olivine and liquid respectively.

The partitioning of Fe and Mg between the melt inclusion (liq) and the host olivine (ol) does not vary greatly with temperature, and so K_D is achieved at 0.30±0.03 (Roedder, 1979; Toplis, 2005; Putirka, 2008). Fe-Mg exchange in olivine occurs on relatively fast timescales ($10^{-15.0\pm0.6}$ m^2 sec^{-1} at 1200°C), and diffusive equilibration of Fe and Mg has the potential to be significant where cooling rates are slow in comparison to crystallisation (Kent, 2008).

Equilibrium in plagioclase-melt pairs are determined using anorthite (An; $CaAl_2Si_2O_8$) - albite (Ab; $NaAlSi_3O_8$) exchange shown in Equation 1.8:

$$K_D(An-Ab)^{plag-liq} = \frac{X_{Ab}^{plag} X_{AlO_{1.5}}^{liq} X_{CaO}^{liq}}{X_{An}^{plag} X_{NaO_{0.5}}^{liq} X_{SiO_2}^{liq}} \quad 1.8$$

Equilibrium in plagioclase-melt pairs are temperature dependent, where plagioclase-melt pairs in systems <1050 °C are in equilibrium at 0.10±0.05, and those trapped at >1050 °C are in equilibrium at 0.27±0.11 (Putirka, 2008). X_b^a is the cation fraction of b in a (Putirka, 2008).

Assessment of equilibrium in pyroxene-melt pairs is based on host-melt Fe-Mg ratios (Equation 1.9; Putirka, 2008). Fe-Mg exchange is also possible in pyroxene-hosted melt inclusions, however, this process is slower in pyroxene than in olivine at $10^{-19.7\pm1.7}$ m^2 sec^{-1} for clinopyroxene (Müller et al., 2013) and $10^{-19.3\pm0.7}$ m^2 sec^{-1} for orthopyroxene (Dohmen et al., 2016) In this equation, 'px' refers to pyroxene and 'liq' to liquid.

$$K_D(Fe-Mg)^{px-liq} = \frac{\left[\frac{Fe}{Mg}\right]_{px}}{\left[\frac{Fe}{Mg}\right]_{liq}} \quad 1.9$$

Reconstruction of Volatiles

Volatiles in PEC-affected melt inclusions can be reconstructed on the basis that H_2O, CO_2, S, Cl and F behave incompatibly during crystallisation, leading to increased concentrations (Rosenthal et al., 2015; Neave et al., 2017). The Rayleigh fractionation equation (Equation 1.10) is therefore used to correct volatiles to their original concentration:

$$C_1/C_0 = F^{(D-1)}, \quad 1.10$$

where: C_1 = is the concentration of volatiles measured in the MI, C_0 = concentration of volatiles in the original melt before PEC, F = is the amount of host added back into the MI, and D = is the bulk partition coefficient (Cann, 1982).

1.4.3 *Reconstructing Vapour Bubble Contents*

In melt inclusions, it is possible for more than 90% of CO_2 to be sequestered to the bubble (section 1.3.1.3), and it is therefore of utmost importance to add CO_2 from the bubble back into the total inclusion before using melt inclusion CO_2 to estimate pressure, as the outcomes can be greatly affected. The use of Raman spectroscopy as a technique for measuring CO_2 in vapour bubbles has been well documented (e.g. Esposito et al., 2011; Hartley et al., 2014; Hanyu et al., 2020), since the wavenumber separation (Δ) between the two main Raman bands due to Fermi resonance can be a good tool for measuring CO_2 density (Kawakami et al., 2003). The Raman spectra of CO_2 consists of four vibrational modes (Fall et al., 2011; Kawakami et al., 2003; Lamadrid et al., 2017): a symmetric stretching mode, two degenerate bending modes, and an antisymmetric stretching mode.

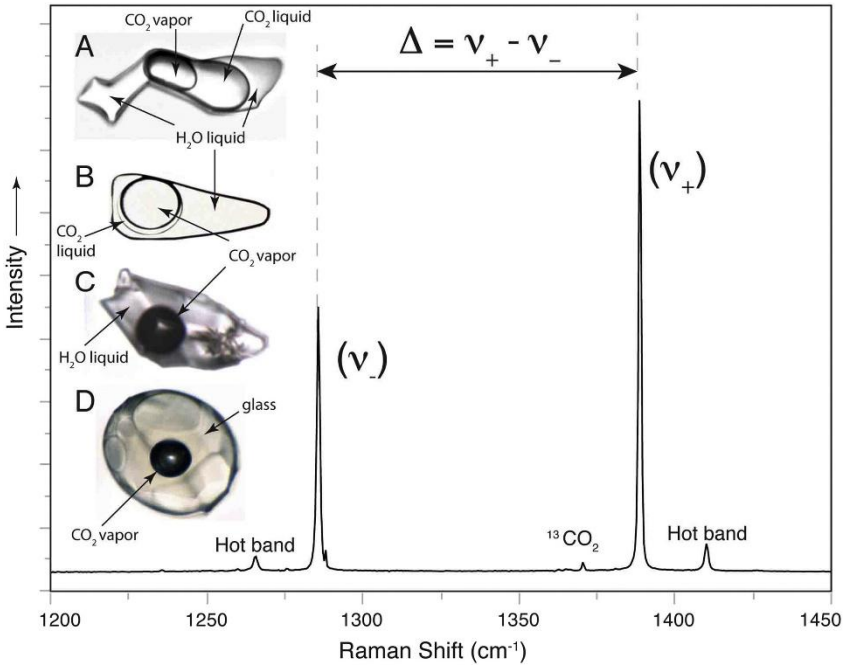

Figure 1.11 - Raman spectra of a bubble hosted in a melt inclusion. Here the Fermi diad (Δ) at 1388.3 cm^{-1} (v_+) and 1285.4 cm^{-1} (v_-) are shown and is density dependent. Hot bands are caused by the thermal energy of the vibrating molecules. [A] Fluid inclusion containing liquid H_2O and CO_2 in its liquid and vapour phases. [B] Fluid inclusion containing liquid H_2O and a vapour bubble containing CO_2. A thin film of liquid CO_2 can also be seen on the rim of the bubble. [C] Melt inclusion with glass and vapour bubble components. The vapour bubble contains CO_2. From Lamadrid et al., (2017).

As v_2 and v_1 have almost the same properties, they perturb each other by Fermi resonance, causing the two modes to split into two distinct CO_2 frequencies at 1388.3 cm^{-1} (v_+) and 1285.4 cm^{-1} (v_-), known as the Fermi diad bands (Figure 1.11; Kawakami et al., 2003), and the wavenumber separation (Δ) at the Fermi diad is density dependent (Fall et al., 2011). The use of Fermi diad as a measurement tool for the density of CO_2 vapour in melt inclusion bubbles has been well studied (e.g. Kawakami et al., 2003; Fall et al., 2011; Lamadrid et al., 2017), producing 3rd order polynomial equations linking Fermi diad and CO_2 vapour density. The use of the Fermi diad as a densimeter has several advantages, including the large range over which CO_2 density can be measured (≤1.168 gm^{-3}; Kawakami et al., 2003), the fact that CO_2 vapour is not susceptible to temperature increases caused by the laser used in Raman spectrometry, and the small size of bubbles that can be analysed (1 µm; Kawakami et al., 2003). However, these equations are instrument-specific, and use of an inappropriately calibrated densimeter yields large errors in CO_2 densities. In the absence of a calibration curve specific to the Raman spectrometer used in this thesis, the densimeter of Lamadrid et al., (2017) is adopted, based

on similarities between their instrument setup and the one used in this thesis. The Fermi diad (Δ) is linked to CO_2 density (ρ) by Equation 1.11:

$$\rho = -36.42055 + (0.354812 \times \Delta) \quad 1.11$$

After density of CO_2 in bubbles is calculated, mass balance equations are used to correct the total CO_2 held in the melt inclusions, based on the amount sequestered to the bubble, by taking the mass of CO_2 in the bubble and adding it back into the mass of melt inclusion glass, using Equation 1.12:

$$[CO_2]_{bubble} = \frac{\rho_{CO_2} V_{bubble}}{\rho_{glass} V_{glass}} x\ 10^6\ , \quad 1.12$$

where $[CO_2]_{bubble}$ indicates the amount that the concentration of CO_2 in the entire melt inclusion will be increased when the bubble is taken into account. The volume of the bubble is calculated based on a spherical shape, and volume of the melt inclusion glass is based on the 3D shape of the inclusion. Melt inclusion glass density is calculated using DensityX (Iacovino and Till, 2019), which relates the densities of hydrous silicate melts to their pressure, temperature, and major oxide compositions.

1.4.4 Magmatic Parameters That May Be Derived From Melt Inclusions

1.4.4.1 Major and Volatile Elements of Silicate Melts

Melt inclusion compositions can shed light on a number of magmatic processes and storage conditions for example including the estimates of pressure and depth, but can also be used to classify magmatic products (e.g. based on total alkali vs silica or potassium vs silica), track magmatic evolution as the melt undergoes differentiation, identify different magma sources within the system as mentioned earlier (section 1.3; Spillaert et al., 2006a; Hartley et al., 2014; Feignon et al., 2023).

The primary focus of this thesis is the volatile species stored in the glass and bubble components of melt inclusions which can be used to estimate minimum pressures of melt entrapment and therefore infer the depths of the magmatic storage region, and together with their host crystals calculate temperature (e.g. Lowenstern, 1995; Wallace et al., 1999; Wieser et al., 2021; Feignon et al., 2022), reconstruct pre-eruptive volatile budgets of the system (e.g. Wallace, 2005; Moune et al., 2007), estimate degassing into the atmosphere together with measured gas emissions (e.g. Devine et al., 1984; Scaillet et al., 2003; Wallace, 2005), model compositional evolution of the vapour phase during magma ascent (e.g. Ding et al., 2023), and infer degassing paths from magma storage regions to the surface (e.g. Spilliaert et al., 2006; Blundy and Cashman, 2008; Métrich and Wallace, 2008; Ding et al., 2023).

1.4.4.2 Temperature

Magmatic system temperatures at the time of melt inclusion formation can be discerned from various methods, including use of major oxide element melt inclusion compositions following corrections for PEC. In this thesis, five different thermometers are utilised to calculate temperatures in olivine-, plagioclase-, orthopyroxene- and clinopyroxene-hosted MI.

Thermometry based on olivine-melt equilibria is long-established, since the first study using olivine-liquid Ni partitioning (Hakli and Wright, 1967). Updated models (e.g. Arndt 1997) also based on Ni partitioning yielded errors of ≥100 °C. Subsequently, Mg partitioning was used as the basis for olivine-liquid thermometry (Beattie 1993), however, this thermometer can overestimate temperature in hydrous experiments. Putirka (2008) presented an updated model (their Equation 22), also based on Mg partitioning, with a lower uncertainty of ±29 °C. Temperatures calculated using Equation 22 from

Putirka, (2008) were on average 60 °C less than previously published studies. A thermometer independent from olivine-equilibria is presented, which shows a linear relationship between temperature and melt MgO content (Sugawara, 2000) in Equation 1.13:

.

$$T(K) = 1316 + 12.95X_{MgO}^{liq}(mol\%)\,, \qquad 1.13$$

where $X_{MgO}^{liq}(mol\%)$ is calculated based on Equation 1.14:

$$X_{MgO}^{liq}(wt\%) = 0.012 + 0.591X_{MgO}^{liq}(mol\%) + 0.0035X_{MgO}^{liq}(mol\%)\,. \qquad 1.14$$

A linear relationship exists at MgO content >25 mol%, using Equation 1.15:

$$X_{MgO}^{liq}(wt\%) = 0.68X_{MgO}^{liq}(mol\%)\,. \qquad 1.15$$

Equation 1.13 is therefore applied to olivine-hosted melt inclusions in this thesis, as values are comparable to those in the literature, and due to its low error on temperature of ±12 °C.

Orthopyroxene-hosted melt inclusion temperatures are assessed using Equations 28a of Putirka, (2008) - an updated thermometer to Beattie (1993), which overestimated temperature in hydrous melts, and underestimated it in anhydrous melts. Equation 28a is based on orthopyroxene-melt equilibria in the following Equation 1.16 where:

$$\frac{10^4}{T(K)} = 4.07 - 0.329[P(GPa)] + 0.12\left[H_2O^{liq}\right] \qquad 1.16$$

$$+0.567ln\left[\frac{X_{Fm_2Si_2O_6}^{opx}}{\left(X_{SiO_2}^{liq}\right)^2\left(X_{FeO}^{liq} + X_{MnO}^{liq} + X_{MgO}^{liq}\right)^2}\right]$$

$$-3.06\left[X_{MgO}^{liq}\right] - 6.17\left[X_{KO_{0.5}}^{liq}\right] + 1.89\left[Mg\#^{liq}\right] + 2.57[X_{Fe}^{opx}],$$

where $X^{opx}_{Fm_2Si_2O_6}$ refers to enstatite + ferrosilite (EnFs), and Fm = Fe + Mn + Mg (Putirka, 2008). The standard error is estimate is ±28 °C, and this thermometer is applicable to a wide range of pressures, temperatures, SiO_2 and H_2O contents to which the studied magmatic systems in this thesis belong.

Temperatures for clinopyroxene-hosted melt inclusions are calculated based on clinopyroxene-liquid equilibria, where the liquid components are cation fractions calculated on an anhydrous basis without renormalisation of wt%. values (Putirka, 2008). The thermometer outlined in Equation 1.17 is an update to those of Putirka et al., (1996) and Putirka et al., (2003), which produced temperature errors of up to ±60 °C. Errors associated with Equation 1.17 are ±42 °C:

$$\frac{10^4}{T(K)} = 7.53 - 0.14ln\left(\frac{X^{cpx}_{Jd}\, X^{liq}_{CaO}\, X^{liq}_{Fm}}{X^{cpx}_{DiHd}\, X^{liq}_{Na}\, X^{liq}_{Al}}\right) + 0.07\left(H_2O^{liq}\right) - 14.9\left(X^{liq}_{CaO}\, X^{liq}_{SiO_2}\right) \qquad 1.17$$

$$-0.08ln\left(X^{liq}_{TiO_2}\right) - 3.62\left(X^{liq}_{NaO_{0.5}} + X^{liq}_{KO_{0.5}}\right) - 1.1\left(Mg\#^{liq}\right)$$

$$-0.18ln\left(X^{cpx}_{EnFs}\right) - 0.027P(kbar)$$

Here, Jd is jadeite ($NaAlSi_2O_6$), DiHd is diopside-hedenbergite ($Ca(Mg,Fe)Si_2O_6$), EnFs is ($FmSi_2O_6$) where Fm = Fe + Mn + Mg. The term $Mg\#^{liq}$ refers to $\left[\frac{\frac{MgO^{liq}}{40.3}}{\frac{MgO^{liq}}{40.3}+\frac{FeO^{liq}}{71.85}}\right]$.

Plagioclase-hosted melt inclusion temperatures are calculated using two thermometers:

firstly, Equation 24a of Putirka, (2008):

$$\frac{10^4}{T(K)} = 6.4706 + 0.3128\ln\left(\frac{X^{plag}_{An}}{X^{liq}_{CaO}\left(X^{liq}_{AlO_{1.5}}\right)^2\left(X^{liq}_{SiO_2}\right)^2}\right) - 8.103\left(X^{liq}_{SiO_2}\right) \qquad 1.18$$

$$+4.872\left(X^{liq}_{KO_{0.5}}\right) + 1.5346\left(X^{plag}_{Ab}\right)^2 + 8.661\left(X^{liq}_{SiO_2}\right)^2$$

$$-3.341\times10^{-2}\left(P(kbar)\right) + 0.18047\left(H_2O^{liq}\right)$$

where components (X) are calculated as cation fractions in Equation 1.18. All liquid components (except H_2O^{liq}) are cation fractions, calculated on an anhydrous basis without normalisation of wt.%.

H_2O^{liq} refers to H_2O wt.% in the melt. This thermometer has a standard error of estimate of ±36 °C (Putirka, 2008). Secondly, the hygrometer of Waters and Lange, (2015) is used, which is based on the plagioclase-melt exchange of the anorthite and albite components between the plagioclase and the melt (Equation 1.19). Since plagioclase composition is highly H_2O- and temperature-dependent (Kudo and Weill, 1970; Putirka, 2008), H_2O and major oxide element compositions of the plagioclase-hosted melt inclusions can be used to infer temperature to ±12 °C (Waters and Lange, 2015).

$$An_{plag} + Ab_{liq} = An_{liq} + Ab_{plag} \, . \qquad 1.19$$

1.4.4.3 Pressure and depth

The major and volatile element compositions of individual phenocryst-hosted melt inclusions can be used to estimate their entrapment pressures, based on the solubility-pressure relationship of H_2O and CO_2. There are several mixed volatile (H_2O-CO_2) solubility models available, for example VolatileCalc (Newman and and Lowenstern, 2002), Liu (Liu et al., 2005), Iacono-Marziano (Iacono-Marziano et al., 2012), and MagmaSat (Ghiorso and Gualda, 2015). However, some models are only applicable to melts within their specific calibrated range (e.g. VolatileCalc for alkali basalts between 40-49 wt.% SiO_2).

In this thesis, the mixed-volatile solubility model MagmaSat (Ghiorso and Gualda, 2015) is applied, and is operated in the thermodynamic model engine VESIcal (Iacovino et al., 2021). MagmaSat is a thermodynamic model built on rhyolite-MELTS (Gualda et al., 2012) and is calibrated based on experimental data from Duan (2014), Papale et al. (2006), and Moore (2008) in order to calculate H_2O-CO_2 solubility in silicate melts. MagmaSat is used to estimate saturation pressures for melt in the range 0-10 kbars and 800-1400 °C, over a wide compositional range, and is therefore suitable for use in this thesis.

Pressures calculated in MagmaSat are then converted to depths using Equation 1.20:

$$MI_{depth} = \frac{p}{\rho g}\ , \qquad 1.20$$

where p is the pressure calculated in MagmaSat based on H_2O-CO_2 solubility, ρ is the density of the crust beneath the Lesser Antilles at 2660 kg m^{-3} (Christeson et al., 2008), and g is the acceleration due to gravity (9.81 m s^{-2}).

A range of saturation pressures can then be estimated from melt inclusion compositions, although pressures and inferred depths are taken as minimum values, due to the low solubility of CO_2, and the potential that the melt inclusion trapped a degassing magma.

As with melt inclusion barometry, there are several clinopyroxene barometers utilising clinopyroxene-only compositions or clinopyroxene-liquid compositions (e.g. Nimis, 1995, Nimis 1999, Putirka et al., 1996, Putirka et al., 2003; Putirka, 2008; Neave and Putirka, 2017; Petrelli et al., 2020; Wang et al., 2021; Jorgenson et al., 2022). Since clinopyroxene is a common mineral with a wide stability field over various magma parameters including pressure, and melt composition (Wieser et al., 2023), its application can be extended to many volcanic regimes including arc settings. However, there are limitations including quantification of the liquid composition may prove difficult or even impossible in natural samples, as well as instances of magma mixing which cause the melt composition in equilibrium with the clinopyroxene difficult to pinpoint (Putirka, 2008; Wang et al., 2021). Therefore, clinopyroxene-only barometers remove these limitations.

For the purposes of the thesis, two clinopyroxene-only barometers are considered which are calibrated based on a six oxygen basis.

Equation 1.21 presents a clinopyroxene-only barometer which has been applied to the Lesser Antilles arc (Equation 30 of Putirka, 2008) by Weber et al., (2023):

$$P(kbar) = -48.7 + 271\frac{10^4}{T(K)} + 32\frac{10^4}{T(K)} ln\left[\frac{X^{cpx}_{NaAlSi_2O_6}}{X^{liq}_{NaO_{0.5}} X^{liq}_{AlO_{1.5}} \left(X^{liq}_{SiO_2}\right)^2}\right] \quad 1.21$$

$$-8.2ln\left(X^{liq}_{FeO}\right) + 4.6ln\left(X^{liq}_{MgO}\right) - 0.96ln\left(X^{liq}_{KO_{0.5}}\right) - 2.2ln\left(X^{cpx}_{DiHd}\right)$$

$$-31\left(Mg\#^{liq}\right) + 56\left(X^{liq}_{NaO_{0.5}} + X^{liq}_{KO_{0.5}}\right) \pm 0.76\left(H_2O^{liq}\right)$$

where the term DiHd is diopside-hedenbergite ($Ca(Mg,Fe)Si_2O_6$),term $Mg\#^{liq}$ refers to $\left[\frac{\frac{MgO^{liq}}{40.3}}{\frac{MgO^{liq}}{40.3}+\frac{FeO^{liq}}{71.85}}\right]$, and H_2O^{liq} refers to H_2O wt.% in the melt.

Equation 1.22 gives the second clinopyroxene-only barometer used, which is Equation 1 of Wang et al., (2021):

$$P(kbar) = a \times NLT \times lnAl^{VI} + bSi + cFe^{tot} + dMg + eCa + fNa + g, \quad 1.22$$

where Al^{VI} refers to the octahedral alumina contents, Fe^{tot} refers to total Fe and NLT is a nonlinear term that is dependent on the composition of clinopyroxene only and given by Equation 1.23:

$$NLT = \frac{\omega Al^{VI}}{\omega_0 Al^{VI} + \omega_1 Ti + \omega_2 Cr + \omega_3 Fe^{tot} + \omega_4 Mn + \omega_5 Mg} \quad 1.23$$

a to g and ω_i in Equation 1.23 represent parameters used to calibrate the equation.

Both clinopyroxene-only barometers are associated with high errors, as the Wang et al., (2021) barometer has a root mean square error of 180 MPa, while the error associated with Putirka, (2008)'s barometer is significantly greater at 450 MPa. The error associated with the clinopyroxene-only barometer of Putrika, (2008) is particularly egregious, as it spans the entirety of the upper and mid-crustal regions, and comparisons of calculated pressures vs expected pressures estimated with this method reveals low gradients and high y-intercepts, leading to overestimation of calculated pressures

of clinopyroxene crystallised at low pressures and underestimating pressures for clinopyroxene crystallised at high pressure (Wieser et al., 2023). The clinopyroxene-only barometer of Wang et al., (2021) is therefore more appropriate for use, although it is necessary to also apply the barometer by Putirka, (2008) for comparison with published data.

1.5 Diffuse Degassing of CO_2

CO_2 is steadily fed to geothermal systems, and as a result, large amounts of CO_2 are released from active volcanoes during eruptions as well as during repose periods (Aiuppa et al., 2019; Fischer and Aiuppa, 2020). This release of CO_2 can occur from different areas comprising the volcano, including passive degassing from plumes and fumaroles, and through diffuse degassing through soil on the flanks. CO_2 released through diffuse degassing can be substantial in comparison to CO_2 released from fumaroles and can even be released on the same scale as that degassed through crater plumes (Chiodini et al., 1998; Carapezza and Granieri, 2004; Chiodini et al., 2008).

Passive degassing through plumes and fumaroles as well as their compositions are well characterised for Soufrière Hills Volcano, Montserrat over a vast time period of 1995-2025 (e.g. Edmonds et al., 2001; Edmonds et al., 2002; Christopher et al., 2014a), and for the 2020-2021 eruption of La Soufrière volcano, St Vincent (Joseph et al., 2022), and are therefore not the focus of this thesis. However, these data will be integrated with the melt inclusion dataset gained here.

It is important however to note that diffuse degassing may not occur over the entire volcanic system, but rather in discrete areas of Diffuse Degassing Structures or DDS (Chiodini et al., 2001), which are controlled by factors such as geological and structural features as well as morphological features (Chiodini et al., 1998; Chiodini et al., 2008). Studying the concentration or flux of CO_2 being passively released through the soil has implications for areas such as geothermal exploration and identifying active structural features as faults and fractures act as highways for the release of gases but can also be used as a monitoring tool for active volcanoes and may help identify future eruption sites (e.g. Chiodini et al., 1998; Hernandez et al., 2001b; Viveiros et al., 2010).

At depth, high temperature hydrothermal fluids containing CO_2 and other gases convect upwards towards the soil. During ascent, the fluid mixture cools and the steam portion changes phase to become a liquid, however, as CO_2 is non-condensable, it remains a gas and is released at the soil-air interface, forming the basis of diffuse CO_2 degassing (Hernandez et al., 2001a; Hernandez et al., 2001b; Chiodini et al., 2008; Viveiros et al., 2010). At diffuse degassing sites, CO_2 is released into the atmosphere by diffusion or by advection (Chiodini et al., 1998). In diffusion, CO_2 is released to the atmosphere when there is a concentration gradient ($dC/d\lambda$) between the soil and the air and is proportionally related as is explained by Fick's Law in Equation 1.24:

$$\varphi_d = -vD\left(\frac{dC}{d\lambda}\right) \qquad 1.24$$

Where φ_d is the steady state diffusive flux, v is the soil porosity and D is the diffusive coefficient.

In advection, CO_2 is released to the atmosphere under the force of a pressure gradient (dP/dλ). The flow of CO_2 by advection (φ_a) can be explained by Darcy's Law in Equation 1.25:

$$\varphi_a = \left(\frac{k}{\mu}\right)\left(\frac{dP}{d\lambda}\right), \qquad 1.25$$

where k is the specific permeability of the soil and μ is CO_2 viscosity.

The sum of the diffusive flux and the advection flux amounts to the total flux. In general, low values of CO_2 total flux are thought to be governed by diffusion, while advection is the main driver of passive CO_2 degassing, generating higher CO_2 fluxes (Chiodini et al., 1998).

1.5.1 *Methods Used to Measure Soil CO_2 Flux*

Soil CO_2 flux can be measured by both direct and indirect methods. Indirect methods focus on soil CO_2 concentration, and can only be applied to steady state diffuse fluxes (e.g. Dueñas et al., 1995). However, it is a requirement to estimate the porosity of the soil the CO_2 is flowing through, and the diffusive coefficient. Direct methods can be carried out through dynamic or static techniques. Techniques used include soda lime or alkali traps which absorb CO_2 released from the soil into an inverted closed container (static), soil CO_2 concentration profiles (dynamic), open dynamic chamber methods (dynamic), closed chamber/accumulation chamber method (static) and gas chromatography (Chiodini et al., 1996b; Chiodini et al., 1998; Chiodini et al., 2001; Welles et al., 2001; Carapezza and Granieri, 2004). These techniques have been compared and it was found that there is a difference between measured fluxes of CO_2 across different techniques. Static chamber techniques, for example, measure between 10-30% less soil CO_2 than dynamic chamber techniques and dynamic chamber techniques measure lower soil CO_2 than soil CO_2 concentration profiles. This difference in values using different techniques may relate to the differing effect of environmental factors on certain techniques, the protocols attached to each technique, and the amount of CO_2 being released from the soil. The accumulation chamber technique is thought to be the best technique to apply in volcanological or geothermal settings since it is not affected by changes in soil characteristics (Chiodini et al., 1996b; Chiodini et al., 1998; Knoepp and Vode, 2002).

Meterological and environmental factors have been shown to influence soil CO_2 flux, and may affect the interpretation of this data. Soil CO_2 flux are dependent on a number of factors, including rainfall, soil temperature, air temperature, relative humidity, barometric pressure, soil water content, soil type (linked to porosity), wind speed, diurnal changes and seasonal changes (Hinkle, 1994; Chiodini et al., 1998; Viveiros et al., 2008; Boudoire et al., 2017). Studies of how environmental factors influence CO_2 flux have been conducted at different volcanoes in different environments and climates around the globe such as Mount Etna, Piton de la Fournaise and Kilauea Volcano (Hinkle et al., 1994; Boudoire et al., 2017; Luizzo et al., 2013). These studies show that soil temperature, air temperature and barometric pressure were the biggest influences on CO_2 flux, except in areas where there was snowfall or rainfall. However, rainfall and snowfall had only short term effects on the CO_2 concentrations (e.g. Boudoire et al., 2017; Viveiros et al., 2008; Viveiros et al., 2009; Hinkle, 1994). Parameters such as barometric pressure and rainfall had a particularly strong influence in areas where CO_2 concentrations are low (Viveiros et al., 2009). While it is therefore important to analyse the data in order to remove these influences, this is applicable only where long time series are available.

In order to identify skewed results and correct for the effects of meteorological and environmental factors, different approaches can be taken. For example, where soil CO_2 measurements are continuous, daily averages can be calculated in order to remove the effect of daily cycles of pressure and temperature (e.g. Boudoire et al., 2017). Additionally, time series of soil CO_2 flux can be compared against time series of meteorological parameters in order to identify correlations between CO_2 flux and its influencing factors, where filtering methods can then be applied (Viveiros et al., 2008; Viveiros et al., 2009; Boudoire et al., 2017).

1.5.2 *Sources of CO_2 in Diffuse Degassing Structures*

In areas of diffuse degassing, the soil CO_2 flux often has two sources - organic/biogenic sources via microbial decomposition of soil organic matter and root respiration or volcanic-hydrothermal sources, as well as a mixture of these two (Camarda et al., 2007; Chiodini et al., 2008; Bloomberg et al., 2014). When presenting the data on logarithmic probability plots (e.g. Figure 1.12), the sources can be differentiated into populations by the change in gradient along the curve. This method of separating data into individual populations was first used in relation to studying soil CO_2 flux by Chiodini et al., (1998). The process however was coined by Sinclair (1974) for graphical representation and analysis of geochemical data. This method of graphical representation and analysis, however, fails to differentiate the sources of CO_2 if (i) the soil CO_2 flux is fed by both biogenic and volcanic sources and (ii) if the soil CO_2 flux originating from a biogenic source is on the same order of magnitude as that of a volcanic source. Soil CO_2 fluxes of up to ~tens of g $m^{-2}day^{-1}$ are thought to be biogenic in origin, with fluxes of >100 g $m^{-2}day^{-1}$ likely volcanic-hydrothermal in origin (Chiodini et al., 2008).

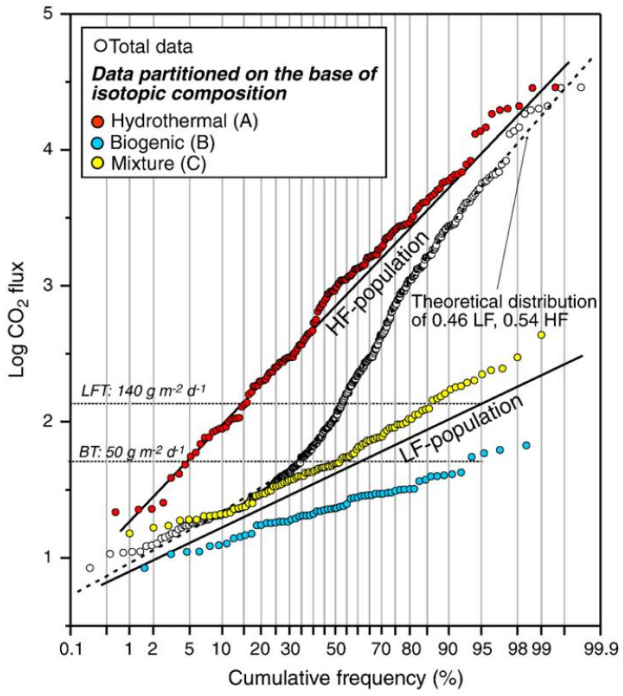

Figure 1.12 – Example of a logarithmic probability plot used to discern populations in a dataset of soil CO_2 flux. Black lines show the trend of the data for high fluxes (HF) and low fluxes (LF) using a geostatistical approach. From Chiodini et al., (2008).

Carbon exists as three different isotopes with differing abundances, all consisting of the element 'C', six protons, but with differing number of neutrons, and therefore differing masses. ^{12}C makes up ~99% of all carbon on Earth, with ~1% being ^{13}C and <0.0001% existing as ^{14}C (NOAA, 2023). Carbon is introduced into subduction zones by different sources and processes, such as subducted carbon through limestone and other rock types, organic carbon, magmagenesis, crustal contamination of the melts and interaction with hydrothermal fluids (Sano and Marty, 1995; Sano and Williams, 1996). Therefore, carbon isotopic composition can help to determine the source of carbon at each volcanic system. CO_2 released at subduction zone volcanoes can be classified into three components based on carbon isotopic signatures (Sano and Marty, 1995; Mason et al., 2017):

(i) Organic carbon: -20 to -40‰

(ii) Mantle: -6 ± 2‰

(iii) Inorganic carbon: ~0‰.

Isotope fractionation can lead to a change in the carbon isotope during exsolution (Pedroni et al., 1999) as the lighter ^{13}C is degassed while the heavier ^{12}C remains in the magma, however, most magmas degas CO_2 completely due to its low solubility in silicate melts, which means that no isotopic fractionation is typically observed in either melts or gases. (Mason et al., 2017).

The isotopic composition of volcanic CO_2 ranges from -1.29 to -9.54 ‰ in low to high temperature fumaroles in arc settings (e.g. Cerro Negro, Unzen and Rabul-Tavurvur volcanoes, Sano and Williams, 1996). However, while these values generally fall within mantle sources as discussed above, it is possible to have mixing of the three components, with ~65% of carbon in high temperature volcanic gases being derived from subducted marine carbonates (Sano and Williams, 1996).

1.6 Geological Context of the Lesser Antilles Arc

1.6.1 Plate Tectonic Setting

The Lesser Antilles, Greater Antilles and the Leeward Antilles form a larger network of arcs that are situated on the Caribbean Plate. It is proposed that the Caribbean Plate is a product of the Galapogos Hotspot on the former Farallon Plate, being thickened by hotspot eruptions from 94-88 Ma. After this, during the Early Campian, the Caribbean Plate then migrated eastward from the Pacific, between North and South America to its current position in the Altantic (Figure 1.13; Pindell et al., 1988; Christeson et al., 2008; Neill et al., 2011; Nerlich et al., 2014).

During the eastward migartion of the Caribbean Plate, a subduction zone formed on the leading edge, creating a north-south trending ~200 km long underwater volcanic island arc - the Aves Ridge, which began volcanism in the Late Cretaceous (Christeson et al., 2008 Neill et al., 2011; Pindell and Kennan, 2009), likely the Upper Turonian (Macdonald et al., 2000). The cesation of Aves Ridge volcanism has been determined as Early Cenozoic, although the exact timing is debated (Tomblin, 1975; Macdonald et al, 2000; Christeson et al., 2008; Pindell and Kennan, 2009; Neill et al., 2011).

The location of the Lesser Antilles, separated from the Aves Ridge by the ~150 km wide, 600 km long north south trending Grenada Basin (Bouysse et al., 1990; Christeson et al., 2011), is likely the location of the remnant accretionary prism of the Aves Ridge.

The Lesser Antilles Arc is the surface manifestation of subduction of the western central Atlantic Plate (North and South American Plates) beneath the eastern boundary of the Caribbean Plate, forming an island arc subduction zone (Macdonald et al., 2000; Evain et al., 2011; Melekhova et al., 2019).

The arc is approximately 850 km long and is aligned sub-meridionally from Saba in the north to Grenada in the south (Christeson et al., 2008; Evain et al., 2011; Kopp et al., 2011). The northern boundary of the Lesser Antilles is separated from the Greater Antilles at the point of maximum curvature in the subduction zone, by the Anegada Passage which is a NE-SW trending graben complex of Neogene age (Bouysse et al., 1990; Laurencin et al., 2017). At the southern termination, geophysical data indicates that the oldest rocks of the Lesser Antilles extend southwards beyond Grenada and is now located beneath Venezuela on the South American plate (Bouysse 1988). Physical manifestation of the southern boundary between the Lesser Antilles and South American plate takes the form of a >1000 km long right oblique transform fault which forms the El Pilar-San Sebastian-Oca strike-slip system along the coast of Venezuela (Speed 1985; Clark et al., 2008).

Geophysical data suggests a convergence rate between the two plates of ~2cm/year in a 67° ENE trend (DeMets, et al., 2000). This convergence rate is slow in comparison to other island arcs such as the Java arc which has a convergence rate of 8.1 cm/year, the Phillipine subduction zone which has a convergence rate of 8.0 cm/year and the Chilean segment of the South American subduction zone which has an average convergence rate of 8.5 cm/year (Jarrard et al., 1986).

Low magma production rates in the Lesser Antilles arc is a consequence of the slow convergence rate (Macdonald et al., 2000). For instance, the magma production rate for a 300-year period (1680-1980) and a 100,000 period has been calculated for the Lesser Antilles arc (Wadge, 1984) with an average convergence rate of 2 cm/year (DeMets, 2000) and the Central American arc which has a convergence rate of 6-9 cm/year (DeMets, 2001). In the 300-year period, only three Lesser Antilles volcanoes erupted (La Soufrière - St Vincent, Mt Pelee – Martinique and Kick 'em Jenny) compared with 23 Central American volcanoes. Field measurements of erupted material (tephra, lava domes, lava flows) produced magma production rates of 5 $km^3Ma^{-1}km^{-1}$ for the Lesser Antilles over a 300-year period vs 62 $km^3Ma^{-1}km^{-1}$ and 4 $km^3Ma^{-1}km^{-1}$ for the Lesser Antilles vs 31 $km^3Ma^{-1}km^{-1}$ for Central America over a 100,000-year period (Wadge, 1984). The magma production rate for the Lesser Antilles arc may be an order of magnitude less than that of the Central American subduction zone, whose convergence rate is 4 times faster than the Lesser Antilles subduction zone (DeMets, 2001). However, while the results are significant, there is some uncertainty in the volume estimates due to erosion, with lava flows, domes and younger tephra deposits being calculated to roughly <20% precision, whereas estimates on volume of older tephra deposits having been subjected to more erosion are less precise (Wadge, 1984).

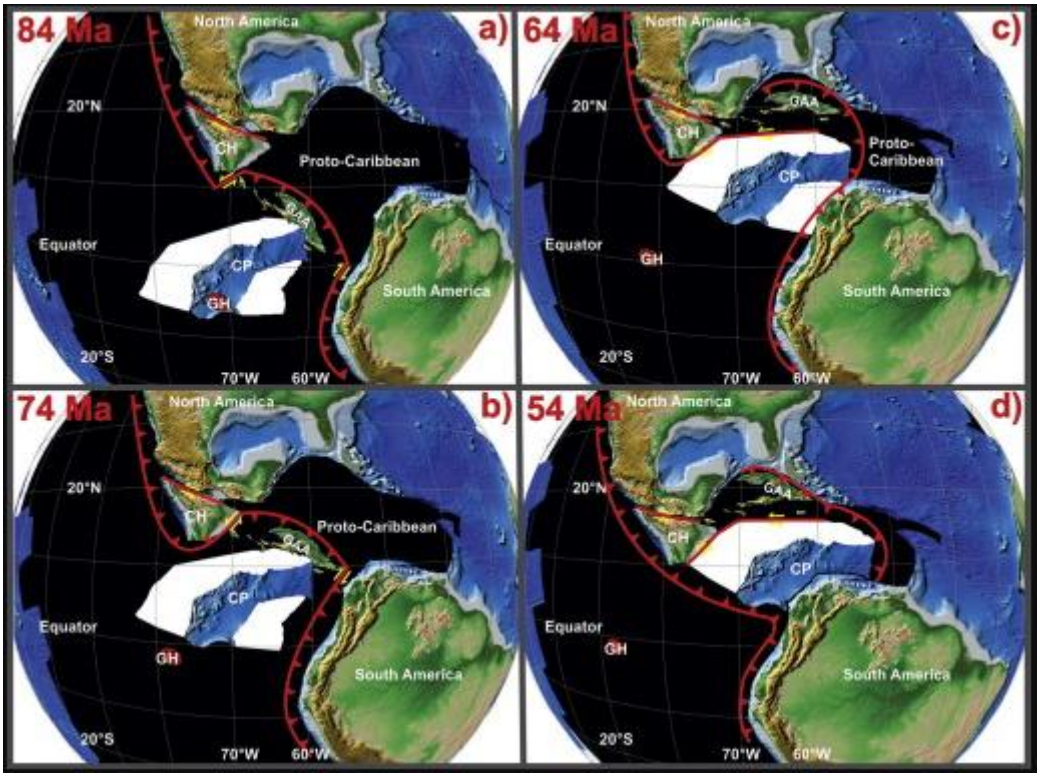

Figure 1.13 – Reconstruction of the Caribbean Plate (CP) through time. The Caribbean Plateau and parts of the Farallon Plate (in white) that have either been subdcuted or obducted. From Nerlich et al., 2014.

1.6.2 Age and Migration of the Arc

There are two phases of volcanic activity associated with the Lesser Antilles island arc, separated by a pause of 9-10 million years. The first phase occurred from the start of the Early Eocene and ended during the mid-Oligocene at around 30-28 Ma. Following this phase, a pause in volcanism occurred as the volcanic front migrated westward. The second phase began at the start of the Burdigalian in the Miocene approximately 22-19Ma and is continued today (Bouysse et al. 1990; Bouysse and Westercamp, 1990; Evain et al., 2011).

The process of arc migration is common in oceanic-oceanic (island arc) subduction settings – for example, the Lesser Antilles island arc, the Bashi Segment double arc (Yang et al., 1996), but also occurs in other subduction settings (e.g. oceanic-continental Central Aleutian Arc, Jicha and Mahlburg Kay, 2018; Andean Southern Volcanic Zone, Mahlburg Kay et al., 2005). Arc migration in island arc settings is usually the result of large buoyant features, causing the cessation of volcanism as the active magmatic front migrates towards the original subduction zone, and a new active arc forms. Arc migration away from the subduction front is highly unusual (Allen et al., 2019). The collision of a bathymetric high (e.g. large igneous provinces, seamounts, oceanic aseismic ridges) has been numerically modelled and may result in uplift of the overriding plate, decrease in dip of the subducted slab, change in seismicity, topographical changes, and spatial and temporal gaps in volcanism (Bouysse and Westercamp, 1990; Gerya et al., 2009; Mason et al., 2010). During subduction at the Caribbean-Atlantic plate boundary, collision of a bathymetric high such as a buoyant ridge is suggested to be the cause of the gap in volcanism and migration of the arc during the Late Oligocene to Lower Miocene at it moved into the northern segment of the subduction zone resulting in a stall in the subduction process and subsequently a stall in magma generation and therefore volcanism. The subducted section ahead of the ridge falls off, melts, and the northern segment of the arc (north of Martinique) is uplifted by a combination of isostaic rebound and mechanical effects after which a new slab is formed (Bouysse and Westercamp, 1990). After the 9-to-10-million-year pause, the front of the new slab reaches magma generation depth. The new volcanic line north of Martinique was offset by up to 60 km (Smith et al., 1980).

Since the 1970s, the mechanisms behind the pause in volcanism and the migration of the Lesser Antilles island arc has been debated, with theories suggesting migration of the active arc due to strike-slip movement of a transform fault (Fink, 1972), interruption of ocean floor spreading and a change in the relative spreading rate leading to migration of the northern segment of the arc (Briden et al., 1979), increase in subduction rate and migration of the northern segment of the arc due to an ill-

defined transform fault at the southern boundary of the arc (Smith et al., 1980), and subduction or attempted subduction of a piece of the Bahamas Platform leading to a change in dip of the subducting slab leading to migration (McCann and Skyes, 1984).

While reactivation of volcanism began in the Early Miocene based on nanofossil biostratigraphy (Natland, 1984; Shipboard Scientific Party, 1984), eruptive events can only be identified south of the present bifurcation where older volcanoes are still present, while in the northern segment where the arc is bifurcated, submarine volcanoes took several million years to breach the ocean surface (Bouysse and Westercamp, 1990).

The islands of the older, eastern arc are known as the Limestone Caribees, and comprise the islands of Sombrero, Dog, Anguilla, St Martin, St Maarten, St Barthelemy, Barbuda, Antigua, Grande Terre, Marie Galante and La Desirade. These islands saw active volcanism during the Upper Jurassic to the Lower Oligocene, save for Sombrero, Barbuda, Grande Terre and Marie Galante which lack volcanic basements. The Limestone Caribbees have been quiescent since the late Oligocene and are covered by sedimentary rocks.

The Volcanic Caribbees (Figure 1.14) refer to islands of the western, younger arc, where volcanism occurred ~2.58 million years ago to the present. These islands can be classified into three linear zones (Wadge and Shepard, 1984), which differ in geochemistry and structure (Sigurdsson and Carey, 1981) and are as follow:

1) Northern Group, comprising Saba, St Eustatius, St Kitts, Nevis, Redonda, Montserrat
2) Central Group comprising Guadeloupe, Dominica, Martinique,
3) Southern Group comprising St Lucia, St Vincent, Grenada

Since the Lower Pleistocene, volcanoes across eleven islands and one submarine volcano have erupted (Sigurdsson and Carey, 1981), and at present, there are twenty-one active or potentially active volcanoes distributed between these islands (Lindsay et al., 2005).

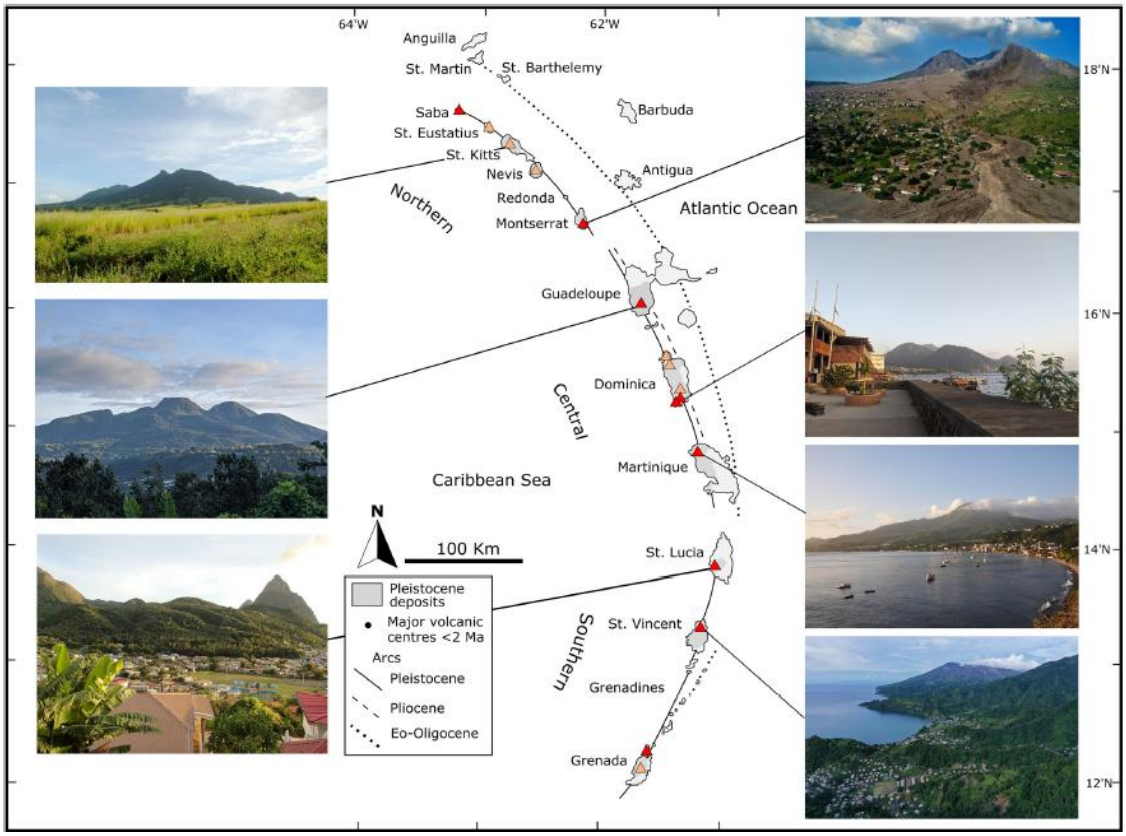

Figure 1.14 – Overview of the Lesser Antilles arc showing the older western arc (Limestone Caribbees) and the younger eastern arc (Volcanic Caribbees). The twenty-one potentially active volcanoes are marked as red (eruptions since 1270 CE) or orange (eruptions in the Holocene) triangles (some volcanoes on Dominica are not marked). From Metcalfe et al., (2023a).

1.6.3 Geochemistry of the Lesser Antilles Arc

The geochemistry of the Lesser Antilles is similar to that of global island arcs (e.g. based on MgO vs CaO) and erupted products are Low-K and Medium-K types (Macdonald et al., 2000). However, within the arc there is variability: the Northern Group of volcanic islands produces magmas belonging to the tholeiite suite, and Central Group islands are typically calc-alkaline (Baker et al., 1977; Rea and Baker, 1980; Macdonald et al., 2000). In the south, erupted products are alkaline classification (Baker et al., 1977; Rea and Baker, 1980), although classification can become more complex, producing what are termed 'C-series' – high CaO, SiO_2 undersaturated or 'M-series' – high MgO, SiO_2 saturated compositions (Macdonald et al., 2000). The Northern and Central islands mainly produce andesite with small volumes of basalt (<10%), even lower amounts of dacite and even rarer rhyolite, and the Southern islands produce rocks mainly basalt and basaltic andesite (Rea and Baker, 1980; Figure 1.15).

The major element composition of the Lesser Antilles melt inclusions hosted in a range of phenocrysts including olivine, plagioclase, orthopyroxene, clinopyroxene, hornblende, iron oxides and quartz covers the entire subalkaline field within the total alkali vs silica plot from basalt to rhyolite from 42-81 wt.% SiO_2 (Figure 1.16; Arculus and Wills, 1980; Devine and Sigurdsson, 1983; Bardintzeff, 1984; Coulon et al., 1984; Mosbah et al., 1991; Bardintzeff, 1992; Devine and Sigurdsson, 1995; Barclay et al., 1998; Devine et al., 1998; Heath et al., 1998; Martel et al., 1998; Edmonds et al., 2001; Edmonds et al., 2002; Pichavant et al., 2002; Harford et al., 2003; Gurenko et al., 2005; Buckley et al., 2006; Hamala et al., 2006; Toothhill et al., 2007; Boudon et al., 2008; Bouvier et al., 2008; Humphreys et al., 2009; Bouvier et al., 2010a; Bouvier et al., 2010b; Humphreys et al., 2010; Mann et al., 2013; Williamson et al., 2010; Edmonds et al., 2014; Cassidy et al., 2015; Edmonds et al., 2016; Melekhova et al., 2017; Balcone-Boissard et al., 2018; Camejo-Harry et al., 2019; Cooper et al., 2019; d'Augustin et al., 2020; Cooper et al., 2020; Solaro et al., 2020; Balcone-Boissard et al., 2023; Metcalfe et al., 2022).

The northern arc produces magmas that are generally evolved (Figure 1.16) with St Eustatius (68-74 wt.% SiO_2; Cooper et al., 2019; Cooper et al., 2020), St Kitts (59-76 wt.% SiO_2; Toothill et al., 2007; Melekhova et al., 2017; Cooper et al., 2020) and Montserrat (69-81 wt.%; Barclay et al., 1998; Edmonds et al., 2001; Harford et al., 2003; Humphreys et al., 2010; Mann et al., 2013; Williamson et al., 2010) having dacite to rhyolite melt inclusion compositions. Saba (46-56 wt.%; Roobol and Smith, 2004) and Redonda (51 wt.%; Cooper et al., 2020) are less evolved at basalt to basaltic andesite compositions. While the northern arc's melt inclusion SiO_2 contents are highly variable, their total alkalis ($Na_2O + K_2O$) are comparable (1.70-6.60 wt.%) across Saba, St Eustatius, St Kitts and Redonda.

Total alkalis in Montserrat melt inclusions however extend to higher values, across a range of 3.60-9.82 wt.%.

The islands of the central arc are generally evolved (Figure 1.16) and are comparable in melt inclusion SiO_2 contents, with erupted products of volcanoes on Dominica and Martinique having 62-79 wt.% (Gurenko et al., 2005; Hamala et al., 2006; Balcone-Boissard et al., 2018; d'Augustin et al., 2020; Cooper et al., 2020; Solaro et al., 2020) and 65-78 wt.% SiO_2 (Coulon et al., 1984; Martel et al., 1998; Pichavant et al., 2002; Cooper et al., 2020) respectively. However, melt inclusion SiO_2 contents of the erupted products of volcanoes on Guadeloupe are very differentiated, from 49-79 wt.% (Mosbah et al., 1991; Boudon et al., 2008; Cooper et al., 2020; Metcalfe et al., 2022). Total alkalis are highly variable and comparable across Guadeloupe (0.91-7.01 wt.%) and Dominica (1.23-7.98 wt.%), but restricted to 5.90-7.88 wt.% in Martinique.

Across the southern arc, melt inclusion SiO_2 contents are most variable in St Vincent (40-77 wt.%; Devine and Sigurdsson, 1983; Bardintzeff, 1984; Bardintzeff, 1992; Heath et al., 1998; Bouvier et al., 2008; Bouvier et al., 2010a; Cooper et al., 2020), followed by Grenada (42-74 wt.%; Arculus and Wills, 1980; Bouvier et al., 2010a; Bouvier et al., 2010b Cooper et al., 2020) and Kick 'em Jenny (47-57 wt.%; Devine and Sigurdsson, 1995; Camejo-Harry et al., 2019). St Lucia and Petit Mustique in the Grenadines have evolved melt inclusion SiO_2 contents restricted to 76-78 wt.% and 67-69 wt.% respectively (Cooper et al., 2020). Similarly to SiO_2 contents, total alkalis are most variable in St Vincent, Grenada and Kick 'em Jenny (1.00-9.59 wt.%) and occupy narrow ranges at 4.90-6.07 wt.% for Petit Mustique and 6.97-7.49 wt.% for St Lucia (Figure 1.16).

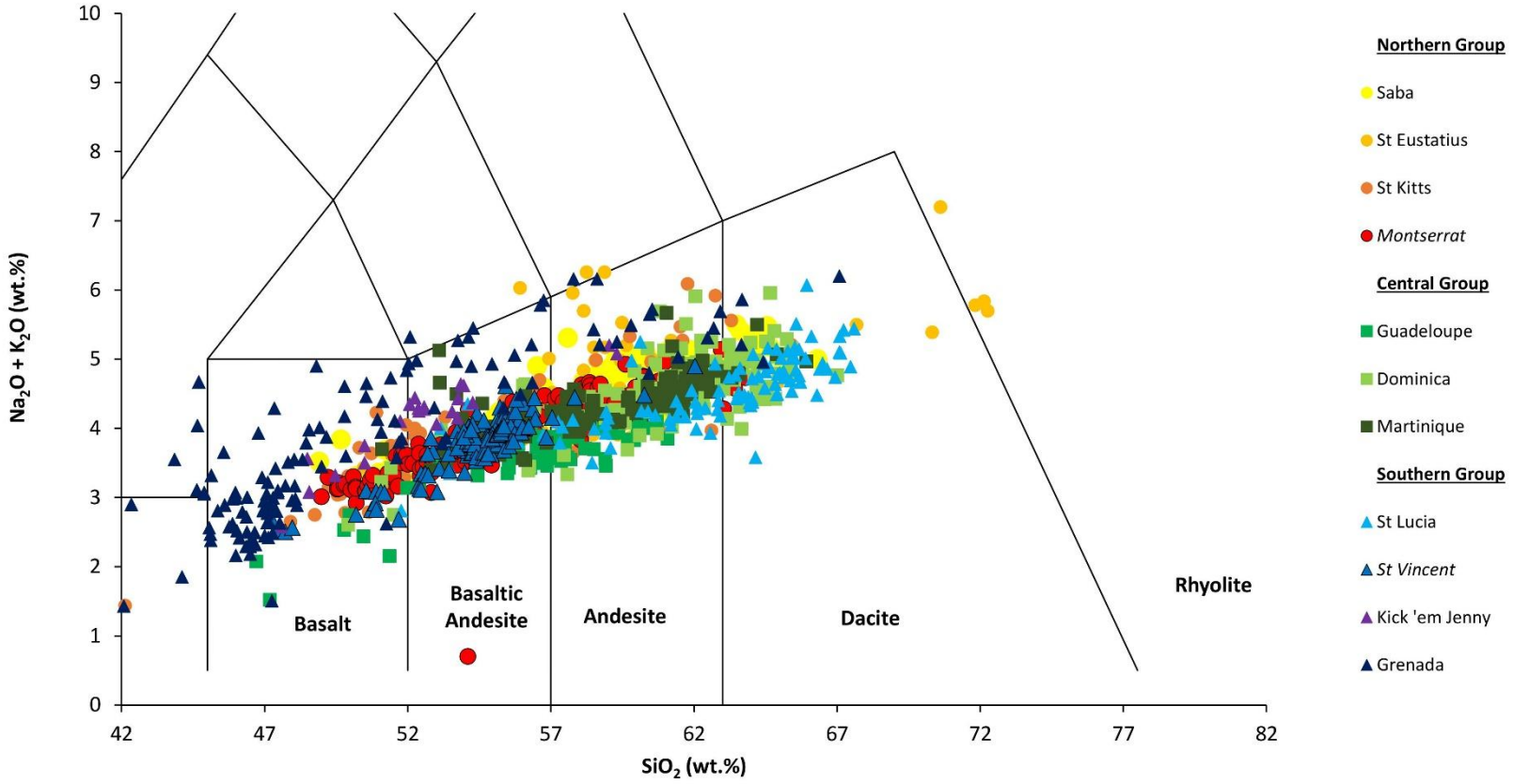

Figure 1.15 - Total alkali vs silica plot for whole rock compositions across the Lesser Antilles Arc. Whole rock compositions are generally basaltic andesite and andesite, but can vary from basalt to dacite.

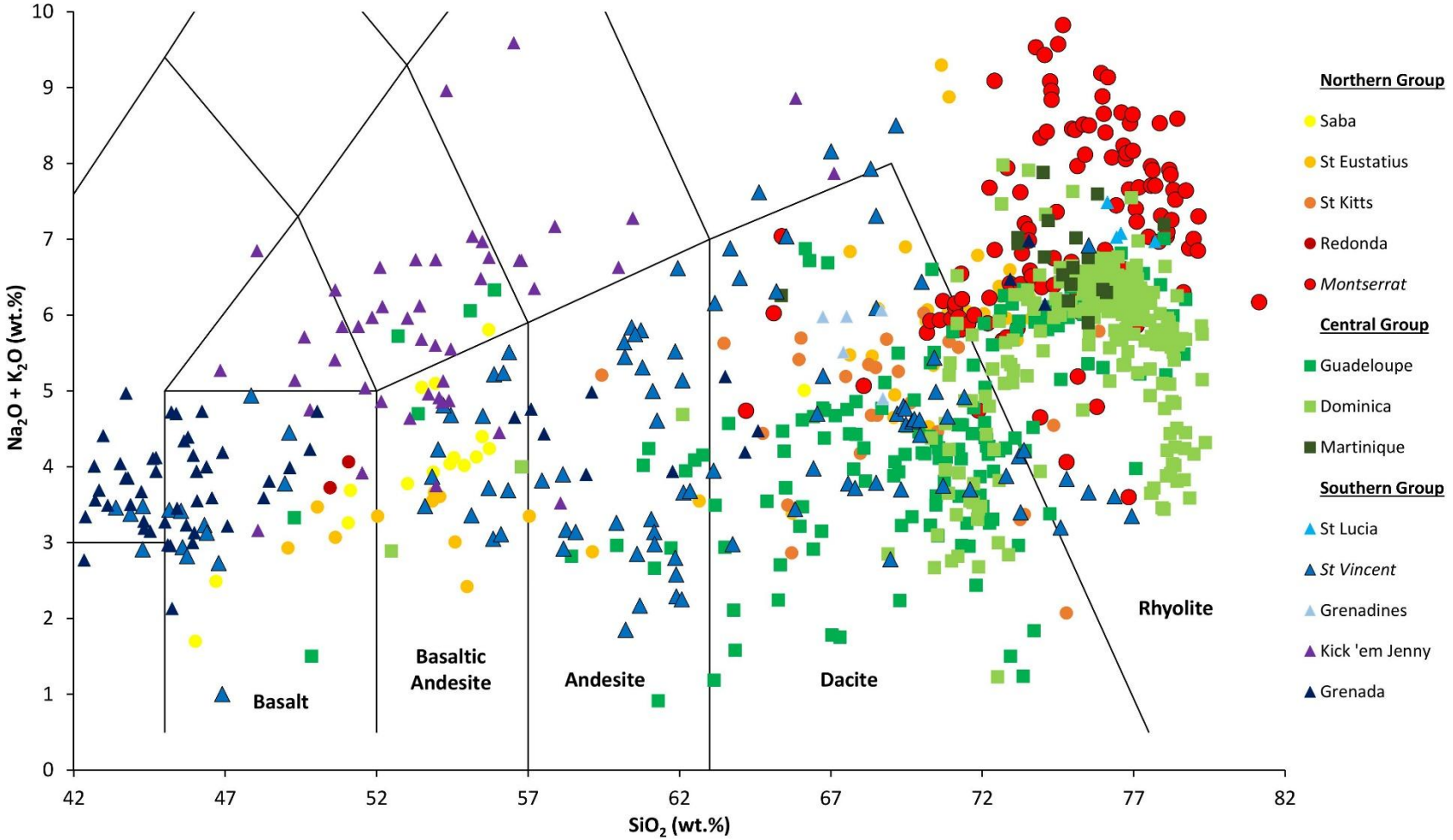

Figure 1.16 - Total alkali vs silica plot for melt inclusions across the Lesser Antilles Arc showing great variability. The Northern and Central islands are typically more evolved than those in the Southern arc. The systems at the focus of this study are located in the Northern Group (Soufrière Hills Volcano, Montserrat – generally rhyolitic melt) and Southern Group (La Soufrière, St Vincent – basaltic to rhyolitic melt).

Along the arc, volatile contents in melt inclusions are highly variable, and show no systematic relationship between volatile content and location within the arc with melt inclusion host or major oxide element composition; however, Cl/F ratios indicate common magma sources (Balcone-Boissard et al., 2023). The islands within the Central Group produce the highest volatile contents, possibly linked to the high magma production rates in the area (Cooper et al., 2020; Balcone-Boissard et al., 2023).

Overall, H_2O, CO_2, S, Cl and F in the arc ranges from 0 to 9 wt%., below detection limit to 4000 ppm, below detection limit to 780 ppm, 40 to 6100 ppm and 75 to 1600 ppm respectively (Devine and Sigurdsson, 1983; Mosbah et al., 1991; Barclay et al., 1998; Devine et al., 1998; Heath et al., 1998; Martel et al., 1998; Martel et al., 2000; Edmonds et al., 2001; Pichavant et al., 2002; Harford et al., 2003; Gurenko et al., 2005; Hamala et al., 2006; Toothhill et al., 2007; Boudon et al., 2008; Bouvier et al., 2008; Humphreys et al., 2009; Bouvier et al., 2010a; Mann et al., 2013; Williamson et al., 2010; Edmonds et al., 2014; Cassidy et al., 2015; Melekhova et al., 2017; Balcone-Boissard et al., 2018; Camejo-Harry et al., 2018; Camejo-Harry et al., 2019; Cooper et al., 2019; d'Augustin et al., 2020; Cooper et al., 2020; Balcone-Boissard et al., 2023; Metcalfe et al., 2022).

Melt inclusions trapped in a variety of host types allow for magma storage conditions to be revealed throughout its evolution. Volatiles (H_2O-CO_2) in erupted products from across the region therefore identify a wide range of vertically extensive magma storage depths, mostly confined to the upper and mid crustal regions, but some extend deep into the lower crust (St Kitts, Guadeloupe, St Lucia) at depths greater than 18 km (Figure 1.17; Balcone-Boissard et al., 2023; Metcalfe et al., 2023a). Pressures derived from melt inclusion barometry are provided in Table 1.1. No pressure estimates derived from melt inclusion H_2O-CO_2 are available for Martinique, St Lucia and St Vincent. Pressures presented in Table 1.1 for these volcanoes are therefore calculated using other methods such as experimental petrology, geodetic modelling or mineral or xenolith barometry. Where only pressure is published, depth is calculated assuming a crustal density of 2660 kg m^3 (Christeson et al., 2008).

More detail on the systems of interest are provided in section 1.6.2 (Soufrière Hills Volcano) and section 1.7.2 (La Soufrière volcano).

Island	H_2O (wt.%)	CO_2 (ppm)	Pressure (MPa)	Depth (km)
St Eustatius[a]	0.1-9.1	0-1350	0-426	0-15
St Kitts[b]	0.41-8.17	15-1292	50-640	2-25
Montserrat[c,d]	0.00-7.29	0-1032	0-300	0-12
Guadeloupe[e,f]	0.29-5.50	9-1507	190–220	6-9
Dominica[g,h]	0.71-7.63	28-4012	80-750	3-27
Martinique[e,l,j]	0.20-6.80	2-381	150-250	7-12
St Lucia[e,k]	2.03- 3.58	7-602	110-720	4-26
St Vincent[e,l,m,n]	0.83-5.31	76-103	200-400	6-18
Kick 'em Jenny[n]	0.20-5.02	37-3157	170-325	7-12
Grenada[e]	0.16-8.44	16-239	-	-

Table 1.1 – H_2O and CO_2 data, along with pressures and inferred depths for magma storage regions along the Lesser Antilles Arc. Data is compiled from:
a – Cooper et al., (2019)
b – Melekhova et al., (2017)
c – Barclay et al., 1998
d – Edmonds et al., 2014
e – Cooper et al., 2020
f – Metcalfe et al., 2022
g – Balcone-Boissard et al., 2018
h – d'Augustin et al., 2020
i – Martel et al., (1998, 2000)
j – Pichavant et al., 2002
k – Bezard et al., 2017
l – Fedele et al., 2021
m – Camejo-Harry et al., 2023
n – Weber et al., 2023

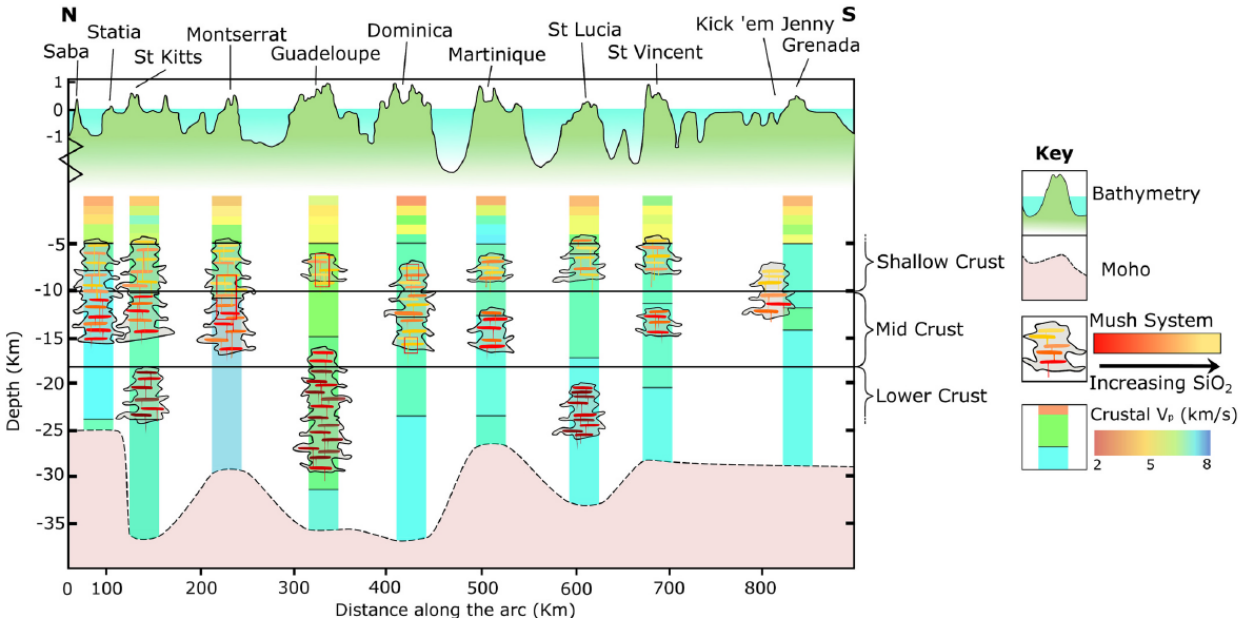

Figure 1.17 – Diagram showing the diverse magma storage regions across the Lesser Antilles arc which consist of both laterally and vertically extensive crystal mushes. These storage regions range from the upper to lower crust. In general, storage regions in the upper crust are more evolved, coming less evolved with depth. From Metcalfe et al., 2023a.

1.7 Soufrière Hills Volcano, Montserrat

1.7.1 Volcanic Evolution of Soufrière Hills Volcano

Montserrat (Figure 1.18) is located within the Northern Group of islands in the Volcanic Caribbees. The island of Montserrat is built of four volcanic centres (Silver Hills, Centre Hills, Soufrière Hills, South Soufrière Hills), of which the oldest and most northerly volcano dates to 2.6 Ma (Harford et al., 2002). The volcanic centres comprising Montserrat are predominantly andesitic (Silver Hills, Centre Hills, Soufrière Hills), with lesser amounts of basalt-basaltic andesite produced by South Soufrière Hills (Rea and Baker, 1980).

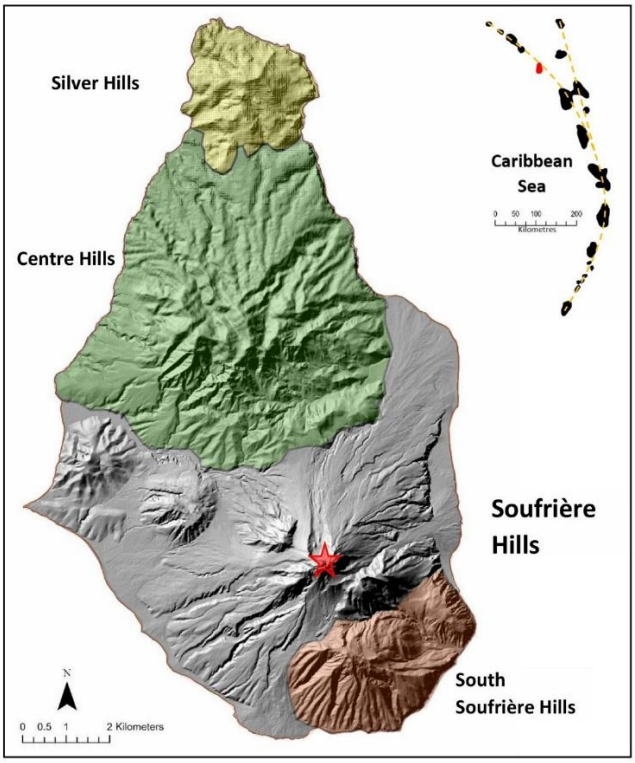

Figure 1.18 – Map of Montserrat outlining the major volcanic centres. Soufrière Hills Volcano is marked by the red star.

From 2.6 Ma to present, volcanism migrated south, with the Soufrière Hills Volcano (170 ka) being active at the same time as South Soufrière Hills at around 130 ka (Harford et al., 2002). At present, the only active centre is the Soufrière Hills Volcano which is a lava dome complex consisting of five domes which produced both lava flow and pyroclastic deposits (Sparks and Young, 2002). Between 31 and 16 ka, Soufrière Hills have been active, producing mainly block and ash flows and surges. Prior to this present stage of activity (1995-present; Chapter 2), Soufrière Hills was active ~700-200 years ago (Roobol and Smith, 1998). Like other Lesser Antillean volcanoes (e.g. La Soufrière de Guadeloupe, Plat Pays Volcanic Complex Dominica, Montagne Pelée Martinique, La Soufrière St Vincent; Boudon et al., 1987 Le Friant et al., 2002; Le Friant et al., 2003; Le Friant et al., 2006; Boudon et al., 2007; Le Friant et al., 2009), Soufrière Hills Volcano has been subjected to flank collapses of voluminous amount of material both in pre-historic (e.g. ~4 ka) and historical times (e.g. 1997, 2010) at the site of the youngest and currently active dome (Roobol and Smith, 1998; Voight et al., 2002; Le Friant et al., 2004; Stinton et al., 2014).

During historical times, there have been three instances of volcano-seismic crises, showing signs of unrest. These crises have occurred roughly every thirty years from 1897-1899, 1933-1935 and 1966-1967 and are associated with volcano-tectonic earthquakes, deformation, and enhanced fumarolic activity resulting from failed eruptions consisting of magma ascent which failed to breach the surface (Powell, 1938; Shepherd et al., 1971; Aspinall et al., 1998; Sparks and Young, 2002; Wadge et al., 2014).

The current stage of activity began with phreatic eruptions on July 18 1995, marking the first instance of surface activity at Soufrière Hills Volcano in ~400 years (Kokelaar, 2002; Sparks and Young, 2002). Fresh magma came to the surface on November 15 1995, and the extrusion lasted for 846 days; this period is known as Phase 1. During this and subsequent Phases, growth and collapse of multiple lava domes led to generation of pyroclastic density currents (PDCs); the activity also included Vulcanian and sub-Plinian explosions (Wadge et al., 2014). The culmination of Phase 1 occurred on March 10 1998, marked by the termination of lava extrusion, producing 331 x 10^6 m^3 of lava over 28 months at a rate of 4.5 m^3s^{-1} (Sparks and Young, 2002; Wadge et al., 2014).

Phase 2 began on November 27 1999 with lava extrusion, creating a new dome and replacing that which collapsed during the pause following Phase 1 (Wadge et al., 2014). The cycle of dome growth and subsequent collapses during Phase 2 led to 303 x 10^6 m^3 of dome material being removed during three major collapses, the largest of these ending in a Vulcanian explosion on July 12-13 2003 (Edmonds et al., 2006; Wadge et al., 2014). During the collapse of July 12 – 13 PDCs reaching the sea generated tsunamis (as far south as Guadeloupe), recorded on borehole dilatometer signals (Mattioli et al., 2007), along with

explosions created by PDC-seawater interaction which triggered a surge inland with enough heat to create charcoal from vegetation (Edmonds and Herd, 2005; Edmonds et al., 2006). With a duration of 1339 days, Phase 2 was the longest of the five phases, producing 336 x 10^6 m^3 of lava at an average rate of 2.9 m^3s^{-1}. Phase 2 ended on July 28 2003 following cessation of extrusion (Wadge et al., 2014).

Phase 3 began on August 1 2005 and lasted for 627 days. A total volume of 282 x 10^6 m^3 of lava was extruded at an average rate of 5.6 m^3s^{-1} with minimum and maximum rates of <0.5 to ~20 m^3s^{-1}. The extrusion rates began to wane around four months prior to the end of the phase on April 20 2007, the activity ended leaving a dome in the crater (Ryan et al., 2010; Wadge et al., 2014).

The first measurements of CO_2 and H_2S in the plume were carried out during July 8 – 15 using Multisensor Gas Analyser System (MultiGAS), two weeks before the Vulcanian explosion which started Phase 4. CO_2 fluxes over the eight-day period ranged from 640 – 2750 tonnes/day, with an average of 1468 tonnes/day. Atmospheric H_2O hindered the measurement of H_2O in the plume (Edmonds et al., 2010). Phase 4 is divided into two sub-phases, defined by two periods of dome growth (Komorowski et al.,). Phase 4a from July 29 – October 1 2008, and Phase 4b from December 3 – January 3 2008. Overall, Phase 4 was the shortest phase, lasting only 158 days, producing 39 x 10^6 m^3 of lava at an average rate of 2.9 m^3s^{-1}, the lowest volume throughout the eruption (Wadge et al., 2014).

Phase 5 of the eruption began on October 9 2009 with lava extrusion and ended on February 11 2012. Like previous phases Phase 5 was defined by dome collapses, Vulcanian explosions and subsequent PDCs (Cole et al., (2014). Over the 125-day period, 70 x 10^6 m^3 of lava was extruded (Stinton et al., 2014) at an average rate of 6.8 m^3s^{-1} (Wadge et al., 2014). This marks the most recent occurrence of lava extrusion as of March 2024.

1.7.2 Geochemistry and Architecture of Soufrière Hills Volcano

The eruptive products (lava and pumice) of Soufrière Hills Volcano are andesitic in nature, over a narrow range of 56.78-63.79 wt.% SiO_2 (Murphey et al., 2000; Zellmer et al., 2003; Plail et al., 2018). There is evidence of magma mixing and mingling at Soufrière Hills Volcano where the eruptive products can be banded, however, there is no chemical variation between bands (Murphy et al., 2000). Mafic inclusions are also a feature, increasing in both volume fraction and size throughout this eruptive period (Plail et al., 2018).

The major element compositions of melt inclusions hosted in plagioclase, orthopyroxene, hornblende and quartz at Soufrière Hills Volcano indicate a rhyolitic melt, but extending into the dacitic field based on total alkali vs silica over a range of 69.43-81.15 wt.% SiO_2 (Le Bas et al., 1986; Barclay et al., 1998; Devine et al., 1998; Edmonds et al., 2001; Harford et al., 2003; Buckley et al., 2006; Humphreys et al., 2010; Mann et al., 2013). Melt inclusions from Soufrière Hills Volcano are some of the most evolved in the arc, most similar to Dominica in the Central Group, but have the highest total alkalis of the entire arc (Figure 1.16).

H_2O in melt inclusions at Soufrière Hills Volcano are similar to the overall arc in their variability and extent, ranging from 0.03-6.86 wt.% (Barclay et al., 1998; Humphreys et al., 2009; Mann et al., 2013; Edmonds et al., 2014; Edmonds et al., 2016). CO_2 is reported at a general range of below detection limit to 387 ppm (Barclay et al., 1998; Edmonds et al., 2014), with a few inclusions ranging 546-1032 ppm (Edmonds et al., 2014). However, it is important to note that these inclusions are based on the concentration in the glass only, and the presences of bubbles in these inclusions are reported (Edmonds et al., 2014). Melt inclusion S contents range from below detection limit to 780 ppm Edmonds et al., 2001; (Edmonds et al., 2014), some of the highest in the arc. Cl and F range 298-5335 ppm (Devine et al., 1998; Edmonds et al., 2001; Harford et al., 2003; Humphreys et al., 2009; Mann et al., 2013; Edmonds et al., 2014) and below detection limit to 833 ppm respectively (Edmonds et al., 2001; Edmonds et al., 2014)

H_2O-CO_2 solubility relationships (based on VolatileCalc; Newman and Lowenstern, 2002) place the storage region of Soufrière Hills predominantly at 5-6 km depth (Barclay et al., 1998; Edmonds et al., 2014), with a few (n=3) inclusions plotting deeper at 11.5 km (Edmonds et al., 2014) based on 2660 kg m^{-3} crystal density (Christeson et al., 2008). Petrology, geophysics, seismology and deformation data (e.g. Aspinall et al., 1998; Barclay et al., 1998; Mattioli et al., 1998; Devine et al., 2003; Rutherford and Devine, 2003; Elsworth et al., 2008; Mattioli et al., 2008; Foroozan et al., 2010; Miller et al., 2010; Christopher et al.,

2014; Edmonds et al., 2014) are consistent with these depth estimates as is shown in Figure 1.19, and constraints on the plumbing system is further discussed in Chapter 2.

The Soufrière Hills Volcano has been extensively studied across both geochemical and geophysical techniques. However, the constraints on volatiles, particularly H_2O and CO_2 has been limited to the early Phases of eruption (Phases 1-3) and no volatile data exists for Phases 4-5. Additionally, studies on volatiles have been limited to the glass phase of the melt inclusion, leaving the contents of the bubble unknown.

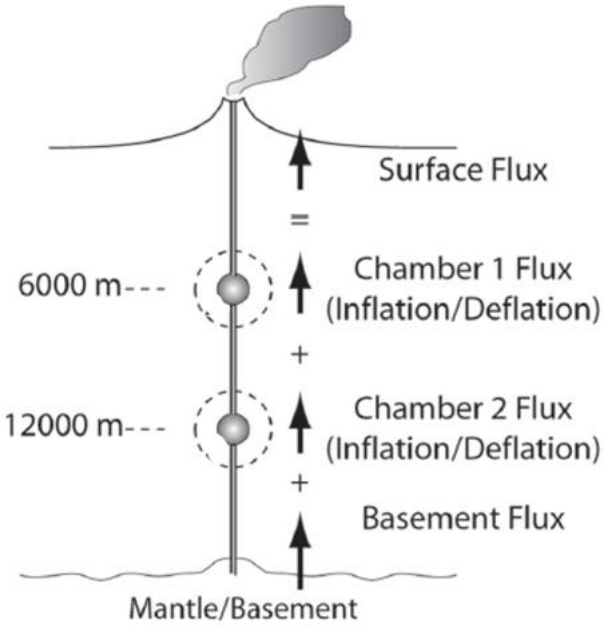

Figure 1.19 – The two magma chamber model of Soufrière Hills Volcano as proposed by Elsworth et al., (2008). The deep storage region is located at ~12 km depth while the shallow region is situated at ~6 km depth.

1.8 La Soufrière Volcano, St Vincent

St Vincent is located in the Southern Group of islands of the Lesser Antilles arc and is constructed of Pliocene to Recent basalts and basaltic andesites (Aspinall et al., 1973), which are the products of four stratovolcanoes aligned from north to south (Le Friant et al., 2009, Cole et al., 2019). K-Ar dating shows a progression of volcanism in St Vincent over time from south to north with the formation of four volcanic centres (South East Volcanics, Grand Bonhomme, Morne Garu and La Soufrière), with the youngest and most northerly volcano – La Soufrière – being constructed from 700 ka Ma to the present day. (Figure 1.20; Briden et al., 1979). Prior to the construction of La Soufrière, volcanism in St Vincent has been dated to ~2.7 Ma to 11 ka (Briden et al., 1979), revealing volcanism between centres overlapped. Monogenetic spatter cone activity has occurred predominantly in the south, unrelated to the migration of volcanism northward (Rowley, 1978; Lindsay et al., 2005). It is however noted that ages provided by Briden et al., (1979) are overestimated, likely due to K loss caused by alteration processes which affected K-Ar derived ages, noted by more recent K-Ar studies at Guadeloupe, and supported by comparison with geomagnetic polarity data (Carlut et al., 2000).

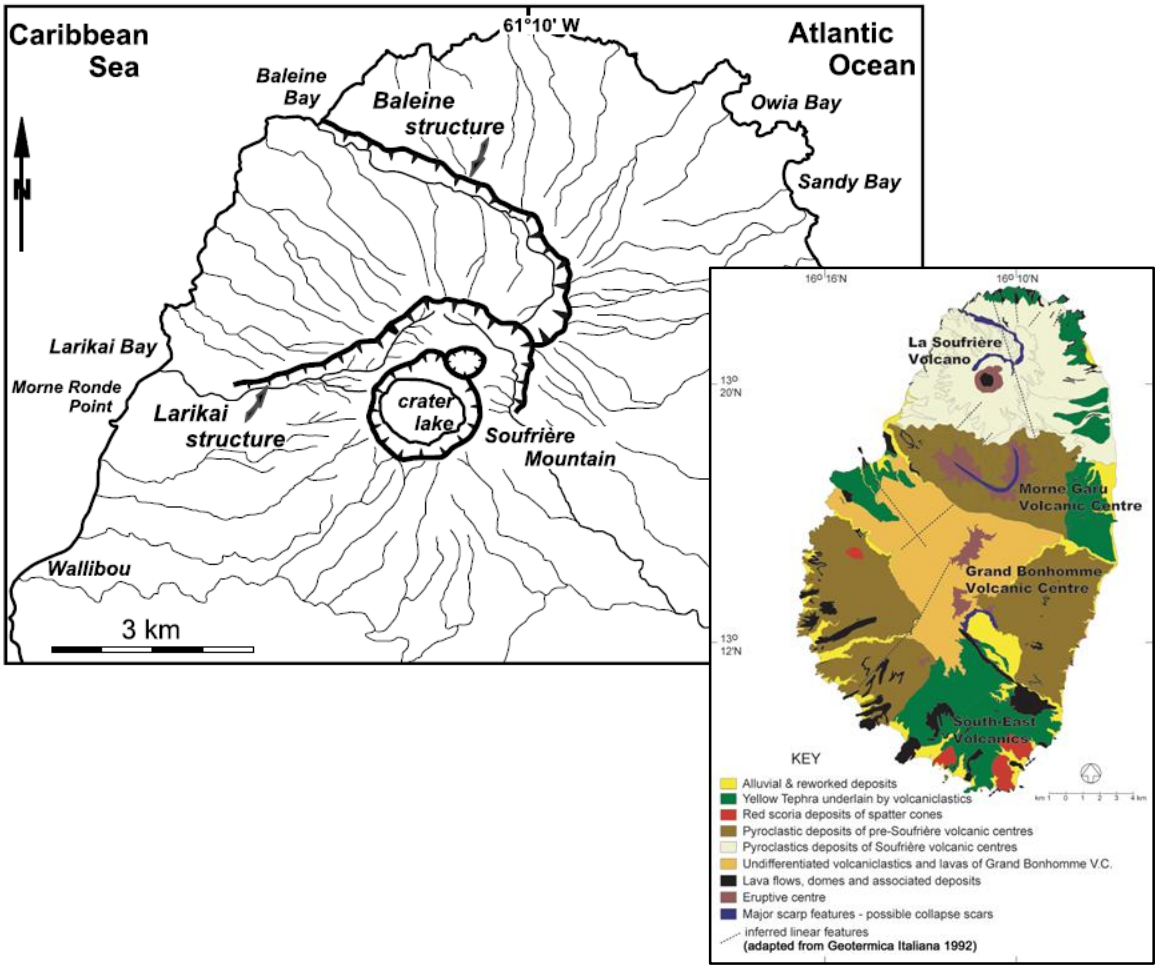

Figure 1.20 – Map of the La Soufrière edifice and the horse-shoe shapes structures representing flank collapses. From Boudon et al., (2008). Inset Map shows the island if St Vincent with La Soufrière in the North. From Lindsay et al., (2005).

1.8.1 Volcanic Evolution of La Soufrière volcano

During the construction of La Soufrière, there have been two major collapses of the edifice as portrayed by two horseshoe shaped scars (Robertson, 2005; Boudon et al., 2007; Le Friant et al., 2009). The oldest scar, known the Baleine structure, was formed by the excavation of greater than 10 km^3 from the cone (Boudon et al., 2007). Although the exact timing of the event is not defined, based on the extent of lava flows, the collapse likely occurred several hundred thousand years from present (Boudon et al., 2007; Le Friant et al., 2009). After the collapse of the first cone, a new cone – the Somma – was built on the southern edge of the Baleine structure. The subsequent collapse of the Somma saw 3-5 km^3 of material. Based on the age of the present cone at La Soufrière, it is inferred that the collapse of the Somma took place several thousand years ago (Boudon et al., 2007).

At present day, La Soufrière stands 1220 m above sea level (Aspinall et al., 1973, Shepard et al., 1979), with a base extending outward to 11 km (Aspinall et al., 1973). At the summit, the main features are three craters: (i) the large (1.6 km wide; Lindsay et al., 2005), pre-existing main summit crater which hosts (ii) a smaller crater formed during the April 2021 explosive eruption, and (iii) a small crater approximately 450 m wide and 60 m deep, which formed during the 1812 eruption (Aspinall et al., 1973, Lindsay et al., 2005).

At La Soufrière, there have been two recorded styles of documented eruption– an explosive “St Vincent” or “traditional Soufrière” style eruption associated with high explosivity, strong seismicity, high magma production rate, and large volumes of ejecta, and an effusive style eruption associated with no pre- or syn-eruptive seismicity, low magma effusion rate and a lower volume of ejected material, producing lava domes. Historical (from 1700s to present) eruptions have either been standalone eruptions of either explosive activity or effusive activity, but has also been transition eruptions where effusion transitions into explosions, or vice versa, as described below and summarised in Table 1.2. The first eruption of the historical period occurred in May 1718 and consisted of an explosive eruption emanating from the summit crater. Following this, the successive eruption of La Soufrière was also explosive in nature, lasting from 27th April to 9th June, 1812 (Lindsay et al., 2005). However, this explosion occurred from a newly formed crater on the rim of the summit. To date, this has been the only eruption from that crater. During the 1900s, three eruptions of La Soufrière occurred. Following a yearlong seismic crisis, La Soufrière once more erupted explosively from 6th May, 1902 to 30th March, 1903, ejecting ~0.42 km^3 of material (Shepherd et al., 1979). Approximately 68 years later, a change in eruptive style occurred, as a dome of 80 $\times 10^6$ m^3 of lava was erupted into the summit crater over a six-month period from October 1971 to

March 1972 (Shepherd et al., 1979). In 1979, the behaviour of the volcano changed again, this time producing the first transition eruption in historical times. The eruptions began on 13th April 1979 with a series of explosions lasting until the 26th April 1979 (Graham and Thirlwall, 1981), producing 15.5×10^6 m^3 (Shepherd and Sigurdsson, 1982). After the 26th April, the eruptions transitioned to effusive activity for the next six months (Graham and Thirlwall, 1981; Shepherd and Sigurdsson, 1982; Devine and Sigurdsson, 1983), with 47×10^6 m^3 of lava dome being built (Shepherd and Sigurdsson, 1982).

Date	Eruptive Style	Repose Period	VEI
1718	Explosive	138	
1784	Effusive		
1812	Explosive	96	4
1902/1903	Explosive	90	4+
1971	Effusive		
1979	Transition (ex to eff)	77	3
2020/2021	Transition (eff to ex)	41	4

Table 1.2 – Compilation of volcanic eruptions at La Soufrière over the last 600 years. Repose period refers to the repose period between explosive events which has been decreasing. VEI refers to the Volcanic Explosivity Index. 'ex' refers to explosive activity, 'eff' refers to effusive activity. Data from Aspinall et al., (1973); Shepard et al., (1979); Cole et al. (2019); Robertson et al., (2023).

1.8.2 Geochemistry and Architecture of La Soufrière volcano

Overall, the eruptive products of La Soufrière are generally basaltic to andesitic at 47.21-62.03 wt.% SiO_2 (Graham and Thirlwall, 1981; Heath et al., 1998; Cole et al., 2019; Fedele et al., 2019; Joseph et al., 2022). Total alkali vs silica (TAS; Le Bas et al., 1986) plots show that while the older pre-historic products span the entire range, whole rock products of the 1440, 1540 and historic eruptions are all basaltic andesite (Graham and Thirwall, 1981; Heath et al., 1998; Cole et al., 2019; Fedele et al., 2019). Samples from 1902-1903 are found to have basaltic (Cole et al., 2019) and andesite-dacite components (Carey and Sigurdsson, 1978). Additionally, the relationship K_2O vs SiO_2 of both pre-historic and historic samples demonstrate the tholeiitic affinity of La Soufrière rocks (Le Maitre, 2002).

Melt inclusions capture a large compositional variation at La Soufrière, with SiO_2 contents ranging from 40-77 wt.% (Devine and Sigurdsson, 1983; Bardintzeff, 1984; Heath et al., 1998; Bouvier et al., 2008; Bouvier et al., 2010; Cooper et al., 2020), and are one of the most varied within the arc (Figure 1.16). Volatiles measured in erupted products during pre-historic times to the 1979 eruption are highly variable across H_2O, Cl and F, but are less varied in CO_2 and S. H_2O ranges from 0.83-5.31 wt.% (Bouvier et al., 2008; Bouvier et al., 2010; Cooper et al., 2020). Cl contents are most comparable to that of the Central arc, at a general range of 0.07-032 wt.%, with three inclusions yielding 0.42-0.61 wt.% Cl (Heath et al., 1998; Bouvier et al., 2010). La Soufrière melt inclusions contain some of the highest F concentrations along the arc, with a total range of 0-1600 ppm (Heath et al., 1998). CO_2 is poorly studied at La Soufrière, with two melt inclusions measuring 76 and 103 ppm (Cooper et al., 2020). S has only been measured in olivine hosted melt inclusions from the 1979 eruption, where it ranged from below detection limit (50 ppm) to 558 ppm (Devine and Sigurdsson, 1983).

Geophysical, geochemical and petrological indicators suggest a dual magma storage zone beneath La Soufrière (Figure 1.21). The deeper storage region is located at ~13 km depth based on xenolith petrology. The deeper magma storage region is thought to connect to the shallower storage region (~6 km) during magma recharge events, triggering eruptions such as the 1902-1903 eruption (Fedele et al., 2021). Further evidence for the interaction between two magma storage regions is in the form of banded scoria (which are products of the 1902-1903 and 1979 eruptions), indictaing that the two magma storage regions are of differing chemistries (Carey and Sigurdsson, 1978; Shepherd et al., 1979).

The La Soufrière volcano is less well studied than some Lesser Antilles volcanoes such as Soufrière Hills Volcano, Montserrat or La Soufrière de Guadeloupe. There exists a very sparse dataset of melt inclusion volatiles, and the full complement of the main volatiles (H_2O, CO_2, S, Cl, F) have not been studied for a single eruption. Owing to the poor constraints of volatile data at this volcano, estimates on pressure are based on petrological, seismic and deformation modelling techniques only.

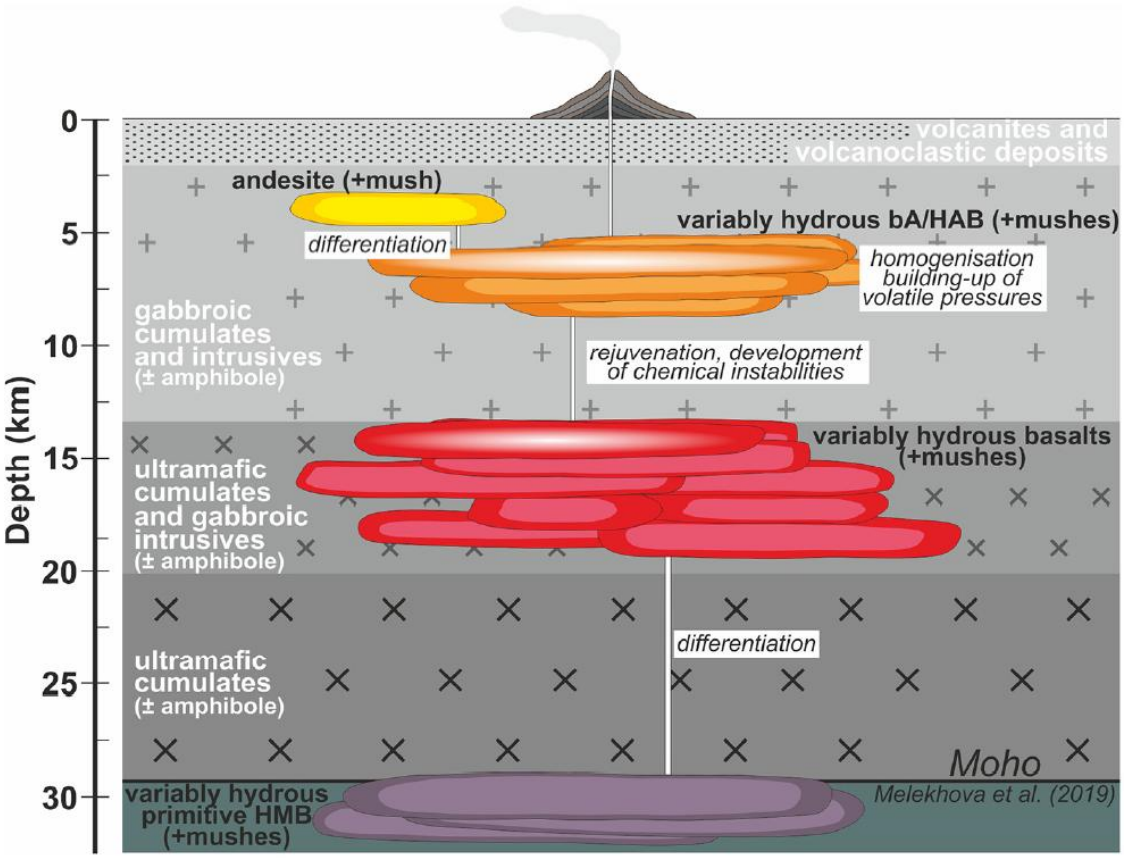

Figure 1.21 – Schematic of the La Soufrière plumbing system showing two magma storage regions within the crust. From Fedele et al., 2021.

2 Melt inclusion bubbles provide new insights into crystallisation depths and CO_2 systematics at Soufrière Hills Volcano, Montserrat

2.1 Abstract

Improved understanding of the magmatic system of Soufrière Hills Volcano, Montserrat (SHV) is needed to inform future hazard management strategy, and remaining uncertainties include the depth of magma storage and the source of ongoing gas emissions. Eruptive activity between 1995 and 2010 has been proposed to be sourced from either a dual chamber or transcrustal mush-based magmatic system, with volatile solubility models using H_2O and CO_2 from melt inclusion (MI) glass estimating depths of 5-6 km. To date, published SHV MI volatile data have neglected the vapour bubbles now known to sequester the bulk of MI magmatic carbon. Total CO_2 concentrations in SHV magma are therefore underestimated, together with volatile-derived entrapment pressures and inferred magma storage depths. Here, we present a new dataset of volatile (H_2O and total CO_2) and major element concentrations in plagioclase- and orthopyroxene- hosted SHV MI, that span almost all of the eruptive activity (Phases 1, 2, 4 and 5), and include the first measurement of bubble-hosted CO_2 for SHV and indeed the Lesser Antilles Arc. Analyses were conducted using Raman spectroscopy, ion microprobe, and electron probe analysis. Dacitic–rhyolitic MI occur within andesitic whole rock compositions. Volatiles in MI glass are similar to published studies (H_2O 2.47-7.26 wt.%; CO_2 13-1243 ppm). However, bubble-hosted CO_2 contributes 9-3145 ppm, to total inclusion CO_2 with 5-99% (median 90%) of CO_2 sequestered within bubbles, and total CO_2 concentrations (131-3230 ppm) are significantly higher than previously published values. Inferred entrapment depths from our dataset range from 5.7-17 km – far greater than previous estimates – and support a vertically elongated magmatic system where crystallisation spanned both upper- and mid-crustal depths. Our CO_2 measurements enable new estimation of CO_2 sources and fluxes. As a total of 4.5 Mt of CO_2 was held in SHV magma during the aforementioned phases, the maximum amount of CO_2 that can be emitted from a batch of SHV magma is ~1500-1750 tonnes/day. Measured CO_2 fluxes are significantly higher, indicating additional input of CO_2 into the system from greater depths. Our study shows that including bubble-hosted CO_2 redefines understanding of the SHV plumbing system.

2.2 Introduction

Mitigation of risk at active island arc volcanoes is a significant challenge (Joseph et al., 2022) that requires detailed understanding of the nature of the magmatic plumbing system and the origin and significance of its gas emissions. Soufrière Hills Volcano is arguably one of the most monitored and studied arc volcanoes, with detailed datasets and models constraining the geochemical, petrological, seismological and geodetic components of the volcanic system (e.g. Aspinall et al., 1998; Barclay et al., 1998; Devine et al., 2003; Ryan et al., 2010; Edmonds et al., 2014; Plail et al., 2018). The current eruption began in 1995, and has produced both intermittent explosions and dome growth between 1995–2010 (Wadge et al., 2014). While magma extrusion has not been observed since 2010, ongoing unrest includes (i) deformation of the volcano caused by melt injection into a crustal reservoir, proposed to be dual sourced at ~5–6 km and ~17 km depth (Neuberg et al., 2022) or mush based and vertically extensive, spanning the upper- and mid-crustal regions with a base at ~17 km (Alshembari et al., 2024), (ii) seismicity mainly in the form of volcano-tectonic earthquakes that are attributed to pressurisation and fracturing related to magma injection and migration (Smith, 2013), and (iii) emission of SO_2 at an average rate of 374±140 tonnes/day (from February 2010 to December 2014) with occasional higher fluxes (~10x) accompanying volcano tectonic earthquake swarms and associated with migration of magma (Christopher et al., 2015).

During the ongoing hiatus of surface activity, some significant advances in technologies and methods are yet to be applied to the Soufrière Hills system. In particular, the application of Raman spectroscopy as a tool for measuring volatiles in vapour bubbles (e.g. Hartley et al., 2014; Moore et al., 2015; Moore and Bodnar, 2019) now permits more accurate measurement of total CO_2 in magmatic melt inclusions. Melt inclusions are small parcels of melt trapped during crystal growth and can represent the pre-eruptive magma, giving insight into the evolving geochemical and physical environment of subsurface magma within the plumbing system (e.g. Kent, 2008; Moore et al., 2015). The post-entrapment generation of bubble(s) allows sequestration of a proportion of the magmatic volatile species in the vapour phase – in particular, CO_2. Methodological development now allows the vapour bubble CO_2 to be quantified via Raman spectroscopy, revealing that in some cases more than 90% of the total CO_2 content of the inclusion resides in the bubble. This implies that previous measurements of melt inclusion CO_2, made solely on dissolved CO_2 within melt inclusion glass, could have severely underestimated magmatic CO_2 contents (Moore et al., 2015; Wieser et al., 2021). As a consequence, constraints on magma storage depths from CO_2-dependent volatile solubility models have been underestimated (e.g. Hartley et al., 2014; Moore et

al., 2015; Hanyu et al., 2020). In this study, we use ion microprobe (SIMS) and Raman spectroscopy measurements to provide the first full CO_2 contents of melt inclusions from Soufrière Hills Volcano, using melt inclusions from four of the five phases of the 1995-2010 eruptive activity. This leads to refined and more realistic constraints on the storage depths and volatile systematics of this important eruption.

2.3 Geological Setting

The Lesser Antilles Arc trends roughly N-S, and extends ~850 km (Figure 2.1 inset). The arc is the product of subduction of the Atlantic Plate at a 67° (ENE) vector beneath the Caribbean Plate, at an overall rate of ~2cm/year (DeMets et al., 2000), erupting 5 $km^3Ma^{-1}km^{-1}$ of magma over a 300-year period from 1680–1980 (Wadge et al., 1984). The arc consists of two lines of volcanism, separated by age, marked by a central boundary at Martinique (Figure 2.1 inset). To the west exists the volcanic islands, where volcanism occurred during the Neogene to present (Macdonald et al., 2000), and to the east, islands where volcanism prevailed during the Upper Jurassic to the Lower Oligocene, with their volcanic basements now covered by sedimentary rocks (Bouysse et al., 1990). The arc can also be divided based on characteristics such as magma chemistry, seismicity, and overall structure (Balcone-Boissard et al., 2023; a et al., 2023a). The islands in the north, from Saba to Montserrat, can be tholeiitic (St Kitts, Redonda) and calc-alkaline (Saba, Montserrat), producing andesite (Rea, 1974, Brown et al., 1977; Rea and Baker, 1980; Baker, 1984; Macdonald et al., 2000). In the central and southern islands, andesites, basaltic andesites and basalts are most prevalent (Brown et al., 1977; Macdonald et al., 2000). Beneath the arc, the crust can be divided into four layers based on crustal structure, with the Mohorovičić discontinuity (Moho) varying between 25-37 km depth (Melekhova et al., 2019).

2.3.1 Soufrière Hills Volcano, Montserrat

Montserrat is the sixth island from the north of the active volcanic chain and forms part of the northerly group of islands (Figure 2.1; Macdonald et al., 2000). It consists of four stratovolcanoes, three of which are dormant (Silver Hills, Centre Hills and South Soufrière Hills), last erupting 0.96±0.25 million years ago (Rea, 1974). The active Soufrière Hills Volcano (SHV) is a volcanic complex located in the southern part of

Montserrat, and its most recent eruption commenced on 18th July 1995, with the extrusion of crystal-rich andesitic magma (Robertson et al., 2000; Sparks and Young, 2002). This involved predominantly effusive activity, leading to the growth of lava dome complexes punctuated by dome-collapse events. Other activity involved explosive Vulcanian events of up to VEI 2-3 (Robertson et al., 2000; Cassidy et al., 2018), and less intense ash venting (Cole et al., 2014).

A total of 988 x 10^6 km^3 (Wadge et al., 2014) of material was produced over five phases of dome building activity that are interspersed with 'pauses', marked by a cessation in lava extrusion (Table 2.1). SHV has produced cycles of activity on both the sub-daily and sub-annual scale. Sub-daily cycles in Phase 1 consisted of explosions coinciding with ground deformation and seismicity (Voight et al., 1998), while in Phase 2, seismicity coincided with peaks in SO_2 flux (Young et al., 2003). This cyclic behavior ceased during Phase 3, and occurred again in Phases 4 and 5 in the form of seismic cycles where swarms of hybrid earthquakes merged to form continuous tremor (Cole et al., 2014; Odbert et al., 2014).

The 15-year eruptive activity is extensively detailed in a number of studies including Robertson et al., (2000); Kokelaar (2002); Sparks and Young (2002); Harford et al., (2003) for Phases 1-2 and Wadge et al., (2014) for Phases 1-5, and is summarised in Table 2.1 below.

Phase/Pause	Date	Duration	Erupted volume (x 10^6 m^3)	Mean effusive rate (m^3s^{-1})	Eruptive characteristics
Phase 1	(18/07/1995 - 10/03/1998)	846 days	331	4.5	V, s-P, PDC, LDG, LDC
Pause 1	(11/03/1998 - 26/11/1999)	627 days	-	-	
Phase 2	(27/11/1999 - 28/07/2003)	1339 days	336	2.9	V, PDC, LDG, LDC
Pause 2	(29/07/2003 - 31/07/2005)	735 days	-	-	
Phase 3	(01/08/2005 - 20/04/2007)	627 days	282	5.6	LDG
Pause 3	(21/04/2007 - 28/07/2008)	466 days	-	-	
Phase 4	(29/07/2008 - 03/01/2009)	158 days	39	2.9	V, LDG,
Pause 4	(04/01/2009 - 08/10/2009)	279 days	-	-	
Phase 5	(09/10/2009 - 11/02/2010)	125 days	70	6.8	LDG, LDC, V
Pause 5	(12/02/2010 - present)	~5,300 days as of October 2024	-	-	

Table 2.1 - Characteristics of eruptive phases. V = Vulcanian, s-P = sub-Plinian, PDC = pyroclastic density current, LDG - lava dome growth, LDC = lava dome collapse. Compiled from Kokelaar, (2002), Edmonds et al., (2006), Ryan et al., (2010), Sparks and Young, (2002), Cole et al., (2014), Wadge et al., (2014).

2.3.1.1 Constraints on petrology and the plumbing system

SHV products are phenocryst-rich (30-45 vol%), with an assemblage of plagioclase, amphibole, orthopyroxene, titanomagnetite and quartz (<0.5%), and minor amounts of clinopyroxene occurring as microphenocrysts or as overgrowth rims on orthopyroxene, plus apatite and ilmenite (Humphreys et al., 2009; Edmonds et al., 2014). Petrological features such as mineral phases and enclave textures are similar throughout the eruptive phases, as described in Christopher et al. (2014). Whole rock compositions from all phases are largely andesitic and range from 57-64 wt.% SiO_2 (Murphy et al., 2000; Zellmer et al., 2003; Plail et al., 2018), while groundmass glass compositions, published for Phases 1-3, are 70-80 wt.% SiO_2 (Edmonds et al., 2001; Edmonds et al., 2002; Harford et al., 2003; Buckley et al., 2006; Humphreys et al., 2010).

Geochemical and geophysical studies point to both a two-tiered magma storage region (e.g. Aspinall et al., 1998; Barclay et al., 1998; Devine et al., 2003; Rutherford and Devine, 2003; Foroozan et al., 2010; Miller et al., 2010; Christopher et al., 2014; Edmonds et al., 2014) or a transcrustal mush system at Soufrière Hills (e.g. Edmonds et al., 2016; Gottsmann et al., 2020; Alshembari et al., 2024). Published measurements of dissolved H_2O and CO_2 contents within plagioclase and quartz-hosted melt inclusion glasses are 4.07-5.05 wt% H_2O and <60 ppm CO_2 for Phase 1 inclusions (Barclay et al., 1998), and ≤6.40 wt% H_2O and ≤546 ppm CO_2 for Phase 3 inclusions (Edmonds et al., 2014). These translate, via the solubility-pressure model VolatileCalc (Newman and Lowenstern, 2002), to pressure and thus depth estimates of ~130 MPa, and 5-6 km for Phase 1 (Barclay et al., 1998) and ≤300 MPa for Phase 3 (Edmonds et al., 2014) which is equivalent to ~7-11 km. Edmonds et al., (2014) attributes the higher CO_2 content of a few plagioclase- and orthopyroxene-hosted inclusions of 836 and 1032 ppm to CO_2 flushing, which occurs when CO_2- rich fluids are released from deeper in the magmatic system, in shallow conduit systems, or from carbonate sources, and interact with magmas stored in the upper or mid-crust (e.g. Rust et al., 2004; Marianelli et al., 2005; Spilliaert et al., 2006; Blundy et al., 2010; Caricchi et al., 2018).

However, these CO_2 measurements neglect melt inclusion bubble-hosted CO_2 and are thus likely severely underestimated (e.g. Hartley et al., 2014; Moore et al., 2015; Wieser et al., 2021). The estimated magma storage depths of 5-6 km are similar to earthquake hypocentral depths and seismic tomographic data

(Aspinall et al., 1998; Miller et al., 2010). Mineral geochemistry also yields shallow storage depths (around 5-6 km), via Al-in-hornblende geobarometry (Rutherford and Devine, 2003) and clinopyroxene-melt equilibria (Christopher et al., 2014). However, iron oxide compositions (Devine et al., 2003) point to deeper storage regions >10 km, along with H_2O contents of enstatites (Edmonds et al., 2016), which indicate a magma storage region that is vertically elongated through the crust.

A two-tiered model is suggested from geodesy, where best-model fits to GPS data from Phase 1 identify a source at ~6 km depth (Mattioli et al., 1998), seemingly switching to a deeper-fed region at 10.4 ± 2.1 km during the later phases (Mattioli et al., 2010). Foroozan et al., (2010) suggests 5 km and 17 km deep storage regions, also based on GPS data. More recently, geodetic modelling using 3D crustal mechanical and topographical data has proposed the presence of a vertically extended pressure source between ~4 and 14 km depth (Gottsmann et al., 2020).

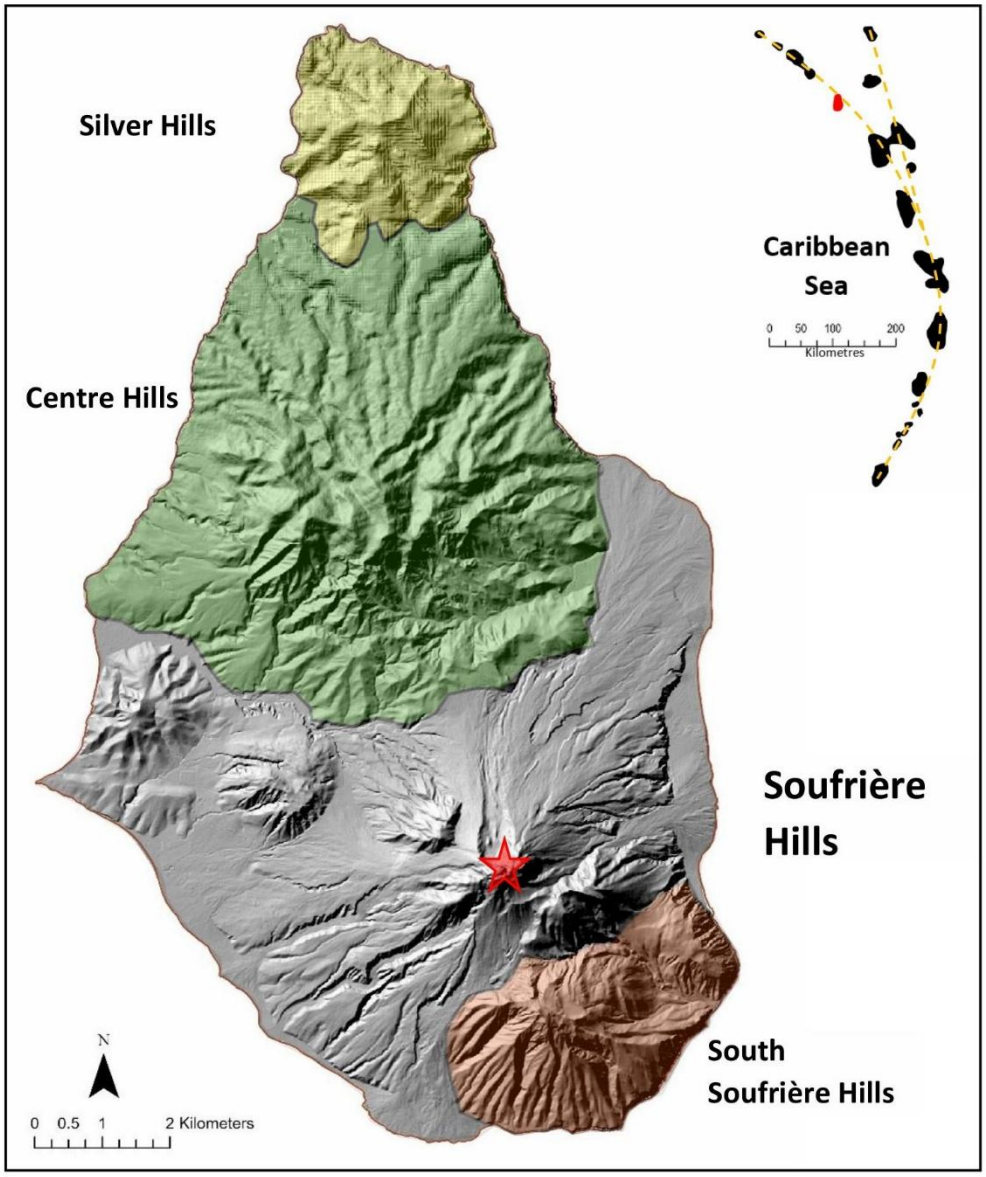

Figure 2.1 - Map of Montserrat showing location of the four stratovolcanoes. Soufrière Hills is located in the south, denoted by the red star. Inset map illustrates the Lesser Antilles Arc and the western and eastern arcs.

2.4 Methodology

2.4.1 Sample Details and Preparation

Samples from the five eruption phases were sourced from the Montserrat Volcano Observatory's rock catalogue and are listed in Table 2.2. They were crushed and separated into different sized fractions, and plagioclase and orthopyroxene phenocrysts were hand separated from the 500-1000 µm fraction under a binocular microscope. For this study, plagioclase and orthopyroxene were selected due to their abundance and optical properties allowing for easy preparation and analysis of melt inclusions.

Individual phenocrysts were mounted on glass slides and gently polished to a flat surface using 2400 silicon carbide lapping paper and inspected under a microscope. Samples containing glassy melt inclusions were further polished with 3 and 1 µm alumina paper until the inclusions were within ~20-30 µm of the surface in preparation for Raman spectroscopy. Glassy melt inclusions occurred in Phases 1, 2, 4 and 5, with Phase 3 inclusions being crystallised, likely reflecting a longer cooling history, and are therefore not considered for the analytical techniques applied in this study.

Inclusions analysed by Raman spectroscopy were 10-166 µm along their longest axis and were cuboidal (plagioclase-hosted) or ellipsoidal (orthopyroxene-hosted). All plagioclase-hosted inclusions contained at least one vapour bubble ranging from 3-52 µm, and orthopyroxene-hosted inclusions were either bubble free or contained at least one bubble, where bubble size ranged from 2-23 µm.

Following Raman spectroscopy, inclusions >25 µm and therefore large enough to be analysed by SIMS were polished with 3 and 1 µm aluminium oxide paper, (to avoid carbon contamination posed by diamond paste) until the inclusion glass was exposed at the surface. These samples were then washed in acetone to dissolve any adhesive resin, mounted in indium, and gold coated for SIMS analysis.

Following SIMS, samples were lightly polished with 0.25 µm diamond paste to remove the gold coat and carbon coated for EPMA.

Whole rock samples from all five phases were also crushed and separated into the 100 µm fraction in preparation for ICP-OES.

Phase	Sample ID	Date and Description
Phase 1	MVO1085	Glassy melt inclusions in pumice Trapped in plagioclase and orthopyroxene September/October 1997 explosion PDCs
Phase 2	MVO1243	Glassy melt inclusions in pumice Trapped in plagioclase 3rd March 2004
Phase 3	MVO1524	Crystallised melt inclusions in pumice 8th January 2007 PDCs
Phase 4	MVO1531	Glassy melt inclusions in pumice Trapped in plagioclase 28th July 2008 PDCs
Phase 5	MVO1548	Glassy melt inclusions in pumice Trapped in plagioclase and orthopyroxene 11th February 2010 pumice airfall

Table 2.2 - List of samples used in this study along with dates of production, brief descriptions and the analytical techniques applied.

2.4.2 Analytical Techniques

2.4.2.1 Raman Spectroscopy

Bubbles in melt inclusions were analysed at the Laboratoire Magmas et Volcans (LMV), Clermont-Ferrand, France using a Renishaw inVia confocal Raman microspectrometer. This was equipped with a 532.1 ± 0.3 nm diode-pulsed solid state laser, a Rayleigh rejection edge filter (cut-off at about 50 cm^{-1}), and a CCD detector of 1040 x 256 pixels. For each analysis, a slit aperture of 20 µm (high confocality setting) and a grating of 2400 grooves/mm was used. A Leica DM 2500 M optical microscope with a motorised XYZ stage was used to focus samples, and 50x or 100x microscope objectives were used, dependent on bubble size. A spectral resolution better than 0.4 cm^{-1}, and spatial resolutions of few µm were achieved based on the applied conditions. To calibrate peak positions and check the linearity of the spectrometer, the 520.5 cm^{-1} peak of Si and the two neon emission bands (568.982 and 576.442 nm) were used, as the neon bands bracket the peaks of CO_2, known as the Fermi diad (Δ, peaks at ~1388 and 1285 cm^{-1}). In order to acquire CO_2 spectra used for quantification of CO_2 concentration, spectra were collected in a single window ranging from ~725 to 1880 cm^{-1}, using the WiRE™ 4.4 software. Each measurement took 120 s (3 acquisitions of 40 s). Neon bands were measured before and after each analysis of CO_2 and the correction factor ($^{real}\Delta_{Ne}/^{measured}\Delta_{Ne}$) for each measurement lies between 0.9987 and 1.0003. In order to quantify CO_2 concentration in the bubbles, fluid inclusions of pure CO_2 with known densities were used as standards and were analysed three times during each analytical session (Boudoire et al., 2023). Uncertainties associated with the reproducibility of the measurement determined on standards are < 0.04 g/cc. The 60-1320 cm^{-1} wavenumber range was subsequently examined for the identification of mineral phases known to occur in the bubble (sulfates, carbonates, etc.). The presence of other fluid species (i.e., liquid or vapour H_2O, H_2S, HS^-) was also investigated by measuring the whole spectral range up to 4000 cm^{-1}.

2.4.2.2 Secondary Ion Man Spectrometry (SIMS)

The concentration of H_2O and CO_2 in melt inclusions glasses were measured at the Natural Environment Research Council (NERC) Ion-Probe Facility at University of Edinburgh, UK using a Cameca IMS 7f-GEO paired with a 5nA $^{16}O^-$ beam.

Prior to analysis, each sample was pre-sputtered for 180 seconds. $^{24}Mg^{2+}$, ^{26}Mg, ^{30}Si (counting times = 2s), ^{1}H (counting time = 1s) and ^{12}C (counting time = 10 s) were analysed over 10 cycles with an electron multiplier. In order to separate the mass interferences of $^{24}Mg^{2+}$ and ^{12}C, a mass resolving power of 2000 was applied. The curves of $^{1}H/^{30}Si$ vs H_2O and $(^{12}C/^{30}Si)*SiO_2$ vs CO_2 for H_2O and CO_2 respectively, were used for calibration based on a set of known glass standards (Supplementary Figure 2.S1; H_2O = 0.64-7.56 wt.%; CO_2 = 0-10,380 ppm). Eight of fifteen orthopyroxene-hosted, and one of sixty-one plagioclase-hosted inclusions required calculation of H_2O by difference, due to high measured H_2O contents which exceeded that of the standards (7.89-8.76 wt.%), leading to high total oxides of 102-104 wt.%. H_2O was calculated to achieve totals of 100.44 wt.%, the average total for the remaining orthopyroxene-hosted inclusions where the standard deviation is 0.54 wt.%. Calculation of CO_2 required SiO_2 which was measured via EPMA. H has a matrix correction and does not require further correction. Background concentrations for H_2O and CO_2 were measured on nominally anhydrous minerals (plagioclase and orthopyroxene) before final concentration calculations. Pressure in the sample chamber was $<6.80 \times 10^{-8}$ mbar over the analytical session. Reproducibility (2σ) on known standards amounts to <10% for both H_2O and CO_2, with a detection limit of 0.003 wt.% for H_2O, and 3 ppm CO_2.

2.4.2.3 Electron Probe Microanalysis (EPMA)

Melt inclusion glass and host major elements were analysed at the University of Cambridge, UK utilising a JEOL JXA-iHP200F HyperProbe with 15 kV accelerating voltage.

Major elements in the melt inclusion glasses were measured with a beam size of 5 µm. A 5µm and a defocused beam were respectively applied for major element analysis of plagioclase and orthopyroxene host crystals. Beam current of 6 nA was applied across all analyses, and alkalis were measured first to mitigate for loss or migration.

Reproducibility (2σ) of major elements is based on repeat measurements of known rhyolitic glass standard AthoG and are <5% for SiO_2, TiO_2, Al_2O_3, FeO and CaO, <10% for K_2O, <13% for MgO and Na_2O.

Counting times for each element along with standards and associated diffraction crystals used for glass analysis are listed in Supplementary Table 2.S1.

2.4.2.4 Inductively Coupled Plasma Optical Emission Spectrometry (ICP-OES)

Whole rock samples from Phases 1-5 were analysed for major element composition at LMV, France using an Agilent 5800 ICP-OES instrument.

An induction furnace was used to melt 100 mg of each sample together with 300 mg of $LiBO_2$. The resulting product was dissolved in 1M HNO_3 until a final volume of 200 ml was achieved. 'GH' and 'BR' from Centre de Recherches Pétrographiques et Géochimiques (CRPG), Nancy, France were used as standards for Si, Na and K, and Al, Ti, Fe, Mn, Mg, Ca and P respectively (Supplementary Table 2.S2). The errors on reproducibility of the standards are <10% (2σ).

2.5 Results

2.5.1 Whole rock and host compositions

Whole rock compositions across the five phases are andesitic, spanning 57.84-59.97 wt.% SiO_2 (Figure 2.2; Table 2.3) and contain the mineral assemblage outlined in section 2.1.1. Samples from this study are comparable to published data across the five phases (Murphy et al., 2000, Zellmer et al., 2003 and Plail et al., 2018), and are less evolved than groundmass glass compositions (70-80 wt.% SiO_2) published for Phases 1-3 (Edmonds et al., 2001; Edmonds et al., 2002; Harford et al., 2003; Buckley et al., 2006; Humphreys et al., 2010).

Fifty-eight of the melt inclusions across the four phases being studied are hosted in An_{48-58} plagioclase, with three being hosted at An_{61-62} and two at An_{68-71}. Orthopyroxene data are only available for Phases 1 and 5 due to a restricted number of melt inclusions that are sufficiently large, glassy and crystal-free. Orthopyroxene phenocrysts from both phases occupy restricted compositional range of En_{57-59}.

All plagioclase phenocrysts across the studied Phases are out of equilibrium with the whole rock, at a total K_D range of 0.16-0.54 (applicable K_D range for equilibrium = 0.05-0.15; section 4.2.1). However, equilibrium is achieved between 11 of 16 Phase 1 inclusions and the average groundmass glass composition for Phase 1 (Edmonds et al., 2001; Harford et al., 2003; Buckley et al., 2006). None of the fourteen Phase 2 inclusions are in equilibrium with the average groundmass glass composition for Phase 2 (Edmonds et al., 2002; Buckley et al., 2006; Humphreys et al., 2010). Equilibrium is unable to be calculated between inclusions and the average groundmass compositions for Phases 4 and 5 as there are no published values of Phase 4 and 5 groundmass glasses.

The five analysed orthopyroxene melt inclusions from Phase 1 are out of equilibrium with the average whole rock (K_D = 0.49-0.55; section 2.5.2.1), along with the groundmass glass (Edmonds et al., 2001; Harford et al., 2003; Buckley et al., 2006) at a K_D range of 0.18-0.19. Equilibrium is also not achieved between the nine Phase 5 inclusions and the average whole rock composition (K_D = 0.49-0.55), and equilibrium between mineral and groundmass glass for Phase 5 cannot be calculated due to lack of measured groundmass glass compositions for Phase 5.

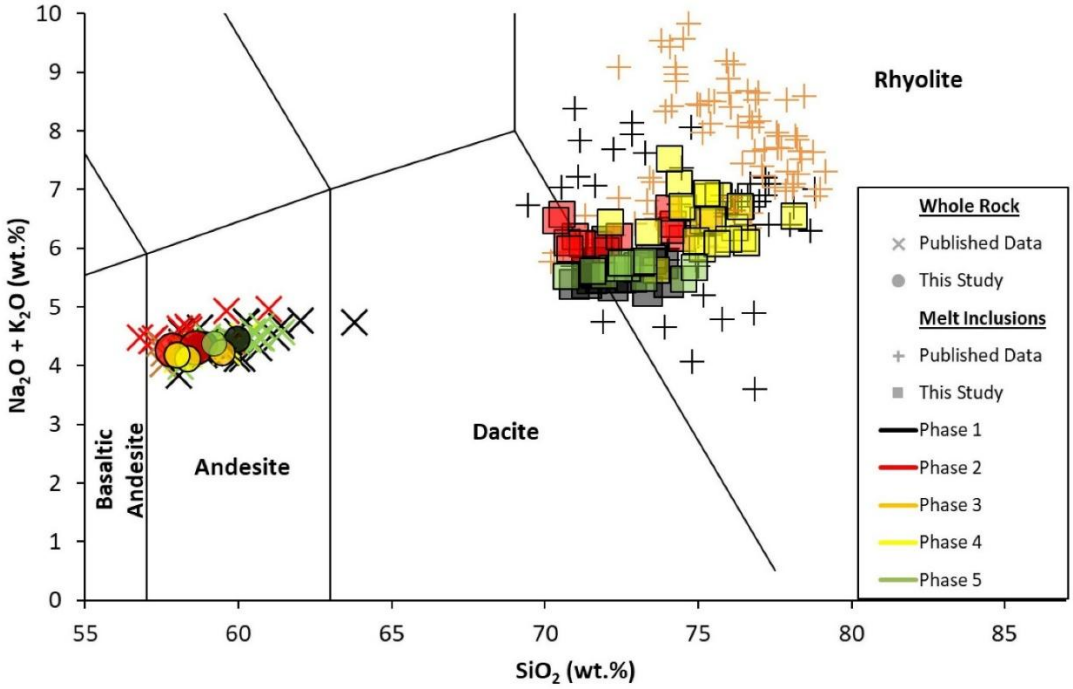

Figure 2.2 - Total alkali vs silica (TAS) plot of whole rock samples and melt inclusions from SHV. Whole rocks are predominantly andesite composition except for two samples. Melt inclusions are dacitic to rhyolitic. Published data for whole rock are from Murphy et al., 2000, Zellmer et al., 2003 and Plail et al., 2018. Published data for melt inclusions are from Barclay et al., 1998, Devine et al., 1998, Edmonds et al., 2001 and Humphreys et al., 2010.

	Whole Rock Samples								
	Phase 1	**Phase 1**	**Phase 1**	**Phase 2**	**Phase 2**	**Phase 3**	**Phase 4**	**Phase 4**	**Phase 5**
	MVO 1085	**MVO 1085**	**MVO 1085**	**MVO 1243**	**MVO 1243**	**MVO 1524**	**MVO 1531**	**MVO 1531**	**MVO 1548**
SiO_2	58.89	59.97	58.63	57.84	58.61	59.48	58.35	58.01	59.23
TiO_2	0.60	0.56	0.50	0.57	0.60	0.59	0.60	0.62	0.58
Al_2O_3	17.53	17.55	17.52	18.20	18.17	18.32	17.94	18.00	18.49
Fe_2O_3	7.10	6.78	6.56	6.89	7.34	7.29	7.09	7.29	6.93
MnO	0.16	0.16	0.18	0.15	0.17	0.17	0.15	0.16	0.16
MgO	2.92	2.54	3.05	2.76	3.04	2.80	3.04	3.06	2.93
CaO	7.44	7.08	7.35	7.73	7.84	7.76	7.73	7.81	7.85
Na_2O	3.51	3.59	3.53	3.51	3.51	3.41	3.37	3.43	3.54
K_2O	0.84	0.85	0.76	0.75	0.79	0.80	0.74	0.74	0.82
P_2O_5	0.13	0.12	0.12	0.12	0.13	0.13	0.12	0.13	0.13
Ba	0.02	0.02	0.02	0.02	0.02	0.02	0.02	0.02	0.02
Sr	0.03	0.03	0.03	0.03	0.03	0.03	0.03	0.03	0.03
H_2O	0.58	0.48	0.46	0.36	0.41	0.74	0.55	0.26	0.38
Total	99.74	99.73	98.70	98.92	100.65	101.53	99.72	99.55	101.09

Table 2.3 - Whole rock compositions of samples from Phases 1-5 in wt.%. Total iron is given as Fe_2O_3 and H_2O is loss on ignition.

2.5.2 Melt Inclusions

2.5.2.1 *Post-entrapment* modifications

Post-entrapment modification of melt inclusion compositions is common, and occurs via diverse processes, resulting in compositions not representative of the parental melt. These processes include post-entrapment crystallisation that modifies both major and volatile elements (Anderson and Brown, 1993; Danyushevsky et al., 2000; Kent, 2008), the formation of bubbles that can be empty (Schipper et al., 2010; Steele-Macinnis et al., 2011), or contain vapour (Anderson and Brown, 1993; Moore et al., 2015; Moore and Bodnar, 2019), or aqueous species and solids (Schiavi et al., 2020). Other processes include diffusion of H^+ into and out of inclusions (Gaetani et al., 2012), altering H_2O contents, and decrepitation leading to volatile loss (Neave et al., 2017). As these processes allow for misrepresentation of the major element and volatile composition of the melt, it is important to assess their extent in individual inclusions, and make corrections where possible, prior to further modelling.

Post Entrapment Crystallisation (PEC)

Assessment of PEC for plagioclase-liquid pairs was carried out by two methods. Firstly, we considered the anorthite-albite exchange between the inclusion and its host which varies with temperature, where $K_D = 0.10 \pm 0.05$ for inclusions trapped <1050°C and $K_D = 0.28 \pm 0.11$ for those trapped at ≥1050°C (Putirka, 2008). As magmatic temperature at SHV are ~850 °C based on petrological and experimental studies (Sparks and Young, 2002), the lower temperature K_D value of 0.10±0.05 was used to assess equilibrium. According to this equilibrium test, 52% of inclusions were in equilibrium with their hosts, with a total K_D range of 0.02-0.07. However, due to the hydrous nature of the inclusions, K_D may not be an accurate indicator of equilibrium for SHV inclusions, as equilibrium is affected by H_2O degassing (Humphreys et al., 2016), and a second method was employed. As an alternative test for equilibrium, the Al_2O_3-SiO_2, Al_2O_3-MgO, Al_2O_3-K_2O and MgO-K_2O systematics of the melt inclusions in relation to the established liquid line of descent (LLD) for SHV whole rock and groundmass glasses were assessed, as PEC leads to a decrease in Al_2O_3 and an increase in MgO (e.g. Figure 2.3; Nielsen, 2011). As no deviation from any of the tested LLDs occurred, this is interpreted as an indication of no PEC occurring in the plagioclase-hosted inclusions, and therefore no correction being required.

Orthopyroxene-liquid pairs were tested for equilibrium according to the K_D threshold of $K_{D_{px-liq}}^{Fe-Mg} = 0.29 \pm 0.06$ (Putirka, 2008). All inclusions were out of equilibrium with their hosts at a K_D range of 0.05-0.22, and PEC ranges from 0.96-3.33%. Due to the low amount of PEC, the compositions of orthopyroxene-hosted melt inclusions do not require correcting, as this process has been shown to have negligible effects on both major and volatile elements up to 11% PEC (Moretti et al., 2018).

Melt inclusion compositions are listed in Table 2.4.

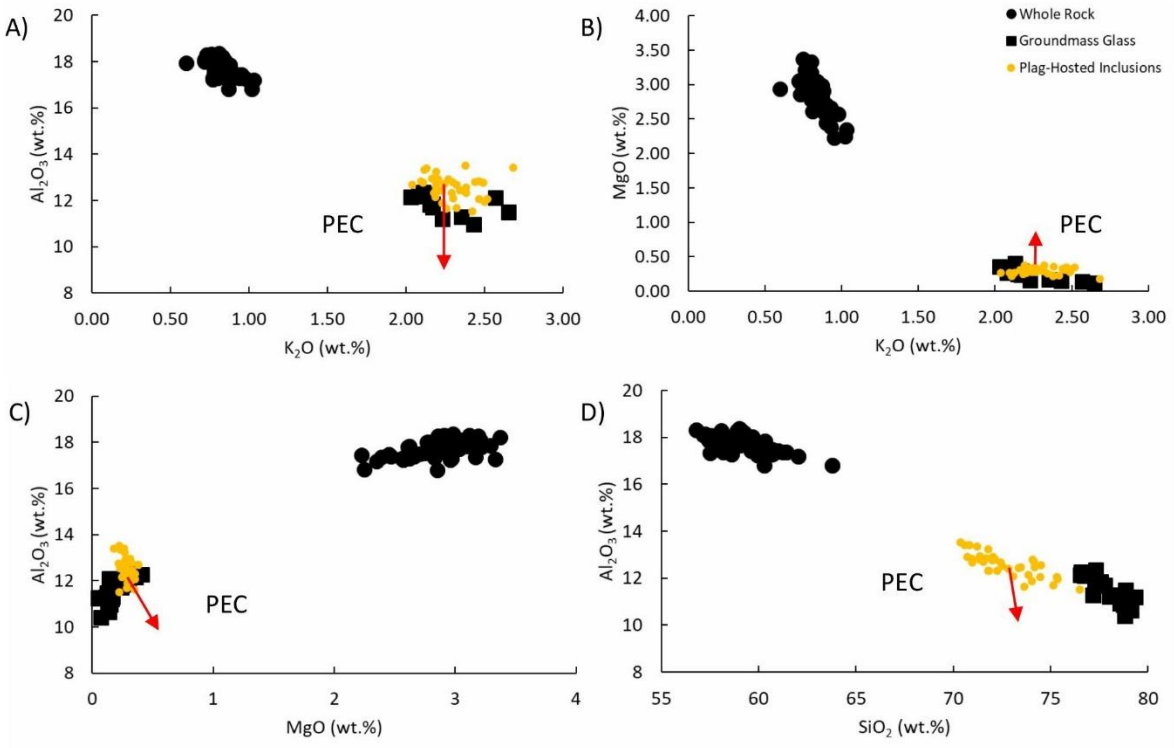

Figure 2.3 - Various liquid lines of descent for whole rock and groundmass glass compositions, in relation to melt inclusion compositions. Red lines indicate the amount (~15%) and direction that compositions of plagioclase-hosted inclusions would follow as a result of post-entrapment crystallisation. Therefore, SHV melt inclusions do not show any indication of post-entrapment crystallisation, as data do not follow the red lines. A) Al_2O_3 vs K_2O. B) MgO vs K_2O. C) Al_2O_3 vs MgO. D) Al_2O_3 vs SiO_2.

Melt Inclusion Compositions																	
Sample	Major Elements (wt.%)									Volatile Elements						Hosts	
	SiO_2	TiO_2	Al_2O_3	FeO	MgO	CaO	Na_2O	K_2O	Total	H_2O (wt%)	Error ±	Bubble CO_2 (ppm)	Error ±	Glass CO_2 (ppm)	Error ±	En	An
Orthopyroxene-Hosted Melt Inclusions																	
SHV_P1_OPX_005	71.08	0.16	12.18	2.34	0.28	1.64	2.86	2.48	93.65	6.67	0.67	n.d.	n.d.	84	8	58	-
SHV_P1_OPX_008_MI1	70.06	0.22	12.38	2.42	0.42	1.90	2.93	2.23	92.55	6.82	0.68	-	-	419	42	58	-
SHV_P1_OPX_011_MI2	71.78	0.18	11.85	2.52	0.40	1.88	2.64	2.10	93.49	6.29	0.62	188	41	399	40	57	-
SHV_P1_OPX_013_MI1	70.21	0.26	12.69	2.69	0.35	2.23	2.93	1.65	93.42	7.01	0.70	186	54	60	6	59	-
SHV_P1_OPX_020	71.54	0.20	11.79	2.37	0.39	1.73	3.00	2.13	94.03	5.58	0.56	9	9	192	19	57	-
SHV_P5_OPX_002_MI1	72.49	0.22	11.90	2.53	0.11	1.87	3.04	1.98	94.68	5.26	0.53	294	41	458	46	58	-
SHV_P5_OPX_002_MI2	70.89	0.15	11.88	2.66	0.39	1.84	2.91	2.06	92.95	7.11	0.71	37	14	175	18	58	-
SHV_P5_OPX_006_MI1	71.14	0.18	11.86	3.13	0.46	1.90	2.70	2.08	93.78	6.24	0.62	67	33	156	16	57	-
SHV_P5_OPX_009_MI2	70.23	0.21	12.34	2.92	0.38	2.33	3.06	1.81	93.49	6.48	0.65	102	27	344	34	59	-
SHV_P5_OPX_012_MI1	70.69	0.22	12.02	3.10	0.36	1.92	3.07	1.97	93.47	7.44	0.74	128	38	243	24	58	-
SHV_P5_OPX_013_MI1	70.78	0.24	12.12	2.84	0.36	2.17	2.93	2.00	93.43	6.57	0.66	87	26	468	47	58	-
SHV_P5_OPX_016	71.07	0.17	11.89	2.78	0.48	1.86	2.77	2.23	94.25	5.82	0.58	121	23	509	51	58	-
SHV_P5_OPX_018	69.31	0.22	11.99	3.48	0.81	2.01	2.53	2.08	92.30	-	-	-	-	216	22	58	-
SHV_P5_OPX_020	70.06	0.22	11.86	3.61	0.80	1.83	2.93	1.92	96.63	6.81	0.68	122	42	422	42	57	-
Plagioclase-Hosted Melt Inclusions																	
SHV_P1_PLAG_014_MI1	71.78	0.21	12.31	1.84	0.36	1.79	3.36	2.38	94.02	-	-	664	251	-	-	-	52
SHV_P1_PLAG_014_MI2	71.37	0.19	12.94	1.78	0.31	2.07	3.23	2.16	94.05	5.30	0.53	571	226	937	94	-	52
SHV_P1_PLAG_015_MI1	70.98	0.23	12.67	1.48	0.27	1.90	3.34	2.04	93.22	5.35	0.54	588	156	385	39	-	71
SHV_P1_PLAG_016_MI1	71.70	0.17	12.84	1.55	0.27	2.19	3.46	2.10	94.46	5.73	0.57	341	131	101	10	-	54
SHV_P1_PLAG_017_MI6	73.48	0.17	12.45	1.65	0.33	1.66	3.57	2.23	95.70	3.71	0.37	439	136	174	17	-	51
SHV_P1_PLAG_020_MI2	72.84	0.17	12.40	1.54	0.27	1.71	3.29	2.21	95.05	4.81	0.48	726	196	76	8	-	51

SHV_P1_PLAG_024_MI2	73.36	0.20	12.43	1.58	0.32	1.67	3.06	2.20	95.31	5.88	0.59	1434	318	111	11	-	55
SHV_P1_PLAG_024_MI3	71.84	0.21	12.32	1.59	0.30	1.67	3.18	2.29	93.67	5.05	0.51	737	247	59	6	-	57
SHV_P1_PLAG_028_MI3	71.54	0.22	12.70	1.95	0.38	1.87	3.27	2.19	94.13	6.26	0.63	665	200	104	10	-	49
SHV_P1_PLAG_030_MI1	72.50	0.17	12.54	1.38	0.28	1.91	3.29	2.19	94.27	6.06	0.61	440	157	111	11	-	52
SHV_P1_PLAG_032_MI1	72.04	0.17	12.91	1.42	0.30	1.92	3.92	2.21	95.73	5.82	0.58	745	213	147	15	-	52
SHV_P1_PLAG_032_MI2	73.87	0.15	12.14	1.41	0.25	1.82	3.55	2.19	95.38	4.96	0.50	777	245	69	7	-	53
SHV_P1_PLAG_036_MI3	71.37	0.19	12.80	1.74	0.31	1.73	3.29	2.29	93.86	6.13	0.61	1305	383	102	10	-	57
SHV_P1_PLAG_037_MI2	73.08	0.15	12.08	1.59	0.30	1.63	3.37	2.30	94.50	5.58	0.56	1127	248	230	23	-	55
SHV_P1_PLAG_040	74.04	0.21	11.89	1.63	0.29	1.64	3.18	2.23	95.10	5.65	0.57	451	204	82	8	-	52
SHV_P1_PLAG_048_MI1	72.24	0.18	12.31	1.75	0.29	1.88	3.17	2.18	94.30	6.25	0.63	567	266	104	10	-	51
SHV_P2_PLAG_010_MI1	74.48	0.19	12.06	1.67	0.35	1.50	3.70	2.47	96.41	3.65	0.37	1339	366	75	8	-	61
SHV_P2_PLAG_011	70.99	0.23	12.83	1.84	0.31	1.81	3.72	2.46	94.34	4.55	0.46	666	216	30	3	-	52
SHV_P2_PLAG_013_MI1	74.18	0.19	12.45	1.30	0.26	1.64	4.06	2.34	96.42	3.50	0.35	118	277	13	1	-	50
SHV_P2_PLAG_015_MI3	70.74	0.24	12.91	1.67	0.27	1.98	3.82	2.27	94.38	4.69	0.47	151	364	45	5	-	49
SHV_P2_PLAG_017	71.99	0.16	12.76	1.29	0.22	1.93	3.84	2.11	94.52	3.88	0.39	467	219	64	6	-	53
SHV_P2_PLAG_025	71.79	0.19	13.23	1.59	0.27	2.19	3.86	2.19	95.31	4.62	0.46	1451	289	116	12	-	50
SHV_P2_PLAG_029	70.57	0.17	13.41	1.36	0.18	1.89	3.89	2.68	94.15	4.78	0.48	3145	733	84	8	-	52
SHV_P2_PLAG_030_MI1	74.15	0.20	12.70	1.52	0.28	1.74	4.06	2.24	96.91	3.85	0.39	829	327	71	7	-	54
SHV_P2_PLAG_031_MI1	71.23	0.23	13.34	1.44	0.24	2.24	3.95	2.12	94.79	4.88	0.49	1149	296	57	6	-	50
SHV_P2_PLAG_031_MI2	70.83	0.22	13.40	1.44	0.27	2.20	3.85	2.13	94.34	4.94	0.49	1249	353	81	8	-	56
SHV_P2_PLAG_032_MI1	72.44	0.22	12.68	1.87	0.38	1.66	3.87	2.32	95.74	3.98	0.40	977	357	40	4	-	55
SHV_P2_PLAG_038_MI2	75.37	0.23	11.95	1.70	0.31	1.45	3.94	2.50	98.08	3.24	0.32	2016	557	34	3	-	50
SHV_P2_PLAG_039	70.36	0.46	13.51	1.55	0.22	2.32	4.09	2.38	95.05	5.26	0.53	328	191	43	4	-	52
SHV_P2_PLAG_049	74.06	0.21	12.78	1.52	0.28	1.60	4.18	2.49	97.85	3.07	0.31	1795	557	-	-	-	53
SHV_P4_PLAG_002_MI2	75.15	0.17	11.68	1.48	0.29	1.19	3.65	2.32	96.26	3.40	0.34	1152	770	32	3	-	49
SHV_P4_PLAG_004	74.51	0.21	12.55	1.62	0.23	1.45	4.30	2.38	97.25	2.85	0.29	415	258	-	-	-	51
SHV_P4_PLAG_006_MI1	76.48	0.25	11.51	1.48	0.23	1.15	3.73	2.42	97.26	3.38	0.34	412	151	32	3	-	55

SHV_P4_PLAG_008	73.66	0.21	11.63	1.65	0.35	1.29	3.36	2.26	94.54	4.58	0.46	3767	1372	30	3	-	57
SHV_P4_PLAG_009	75.31	0.24	12.06	1.87	0.35	1.40	4.35	2.52	98.30	2.89	0.29	1026	503	37	4	-	52
SHV_P4_PLAG_018_MI1	72.14	0.24	12.78	1.83	0.33	1.32	4.00	2.44	95.54	3.82	0.38	567	291	25	3	-	52
SHV_P4_PLAG_019_MI2	-	-	-	-	-	-	-	-	-	2.48	0.25	-	-	-	-	-	-
SHV_P4_PLAG_024_MI1	74.39	0.18	12.29	1.37	0.18	1.13	4.26	2.84	97.37	2.47	0.25	2136	541	29	3	-	46
SHV_P4_PLAG_024_MI2	74.07	0.20	12.78	1.27	0.21	1.34	4.71	2.80	97.38	2.97	0.30	3313	691	31	3	-	50
SHV_P4_PLAG_026_MI2	76.21	0.18	11.51	1.42	0.30	1.21	3.89	2.45	97.39	3.26	0.33	647	197	31	3	-	49
SHV_P4_PLAG_026_MI3	76.59	0.15	11.24	1.38	0.25	1.04	3.59	2.50	97.02	2.93	0.29	-	-	-	-	-	49
SHV_P4_PLAG_028_MI1	78.15	0.20	11.04	1.38	0.22	1.15	4.04	2.50	98.68	-	-	1456	421	-	-	-	48
SHV_P4_PLAG_035_MI1	75.66	0.19	11.99	1.46	0.31	1.30	4.46	2.43	97.79	2.81	0.28	2139	468	63	6	-	50
SHV_P4_PLAG_035_MI4	75.16	0.21	12.16	1.54	0.27	1.39	4.06	2.40	97.19	3.10	0.31	-	-	47	5	-	52
SHV_P4_PLAG_035_MI5	75.50	0.19	12.07	1.71	0.30	1.40	4.14	2.34	97.64	3.24	0.32	-	-	37	4	-	51
SHV_P4_PLAG_038_MI1	74.49	0.26	11.84	1.94	0.36	1.46	4.25	2.45	97.86	2.96	0.30	2653	519	32	3	-	53
SHV_P4_PLAG_040	73.38	0.24	12.23	1.91	0.36	1.55	3.99	2.28	95.95	3.46	0.35	1465	312	44	4	-	53
SHV_P4_PLAG_041_MI1	76.00	0.23	11.49	1.25	0.15	1.21	3.51	2.63	96.96	3.51	0.35	641	305	19	2	-	55
SHV_P4_PLAG_043_MI1	75.30	0.28	12.19	2.03	0.41	1.40	4.35	2.58	99.47	-	-	881	304	-	-	-	61
SHV_P4_PLAG_044_MI2	74.93	0.29	11.91	1.75	0.34	1.23	3.60	2.52	97.02	3.69	0.37	670	247	28	3	-	62
SHV_P4_PLAG_045_MI1	76.39	0.10	11.74	1.45	0.28	1.06	3.99	2.72	97.72	2.75	0.28	545	279	30	3	-	49
SHV_P4_PLAG_047_MI2	75.63	0.20	11.77	1.47	0.24	1.45	3.70	2.37	96.83	4.20	0.42	1517	363	40	4	-	49
SHV_P5_PLAG_002_MI4	70.71	0.24	13.07	1.81	0.34	2.26	3.32	2.19	93.94	6.39	0.64	884	257	1126	113	-	54
SHV_P5_PLAG_008_MI1	73.25	0.17	12.53	1.43	0.29	2.07	3.35	2.13	95.53	5.66	0.57	804	219	95	10	-	55
SHV_P5_PLAG_009_MI2	72.20	0.16	12.87	1.37	0.28	2.01	3.53	2.11	94.52	6.18	0.62	487	200	835	84	-	55
SHV_P5_PLAG_016_MI1	71.96	0.15	12.68	1.57	0.28	1.92	3.35	2.17	95.10	6.18	0.62	268	97	128	13	-	52
SHV_P5_PLAG_016_MI3	72.71	0.10	12.66	1.48	0.28	1.86	3.51	2.14	95.06	5.87	0.59	467	163	147	15	-	48
SHV_P5_PLAG_016_MI6	73.16	0.14	12.68	1.49	0.32	1.64	3.52	2.22	95.17	4.87	0.49	-	-	211	21	-	50
SHV_P5_PLAG_024_MI2	74.54	0.20	11.77	1.57	0.30	1.69	3.27	2.20	95.75	4.97	0.50	2347	691	206	21	-	48
SHV_P5_PLAG_025_MI1	72.45	0.21	12.27	1.69	0.32	1.66	3.37	2.28	94.25	5.80	0.58	720	241	96	10	-	55

SHV_P5_PLAG_034_MI2	71.58	0.18	12.83	1.61	0.31	2.16	3.37	2.23	94.28	5.98	0.60	1421	260	152	15	-	51
SHV_P5_PLAG_037_MI1	73.25	0.15	12.63	1.55	0.30	1.65	3.51	2.27	95.30	5.33	0.53	381	178	442	44	-	51
SHV_P5_PLAG_042_MI2	72.48	0.24	12.91	1.71	0.31	1.90	3.55	2.18	95.29	5.82	0.58	1384	417	1243	124	-	53
SHV_P5_PLAG_043_MI3	74.89	0.28	11.76	1.72	0.34	1.64	3.35	2.31	96.28	4.55	0.46	800	304	233	23	-	68

Table 2.4 - Compositions for seventy-eight melt inclusions across Phases 1 - 5 for Soufrière Hills Volcano. Major element oxides in wt.% are measured via EPMA. H_2O and CO_2 in the glass are measured by SIMS. CO_2 in the bubble is measured via Raman spectroscopy. PEC refers to post-entrapment crystallisation as assessed in section 4.2.1.

Bubble Growth

After entrapment of melt, bubbles can be formed in response to the pressure-volume-temperature relationship between host mineral and melt. Based on this relationship, bubbles can grow via (i) post-entrapment crystallisation, (ii) diffusive H^+ loss and (iii) differential thermal contraction (Roedder, 1979; Anderson and Brown, 1993; Lowenstern, 1995; Kent, 2008; Hartley et al., 2014; Wallace et al., 2015b; Aster et al., 2016; Hanyu et al., 2020; Wieser et al, 2021). The process with the largest effect occurs due to differing thermal expansivities between host mineral and melt during cooling from high trapping temperatures to the glass transition temperature, after which bubble growth is suppressed (Moore et al., 2015). However, bubbles are also known to nucleate in the melt prior to entrapment, and can grow by diffusion of volatiles from the inclusion glass into the bubble, coalescence, decompression during ascent or Ostwald ripening (Cashman and Mangan, 1994; Best, 2003). It is therefore necessary to identify bubbles that have grown homogenously post-entrapment, in order to prevent overestimation of the bubble volatile content caused by volatile-bearing bubbles being trapped at the time of melt inclusion formation. Homogenous bubble growth has been reported to be 5-12% for a range of volcanic systems (e.g. Hartley et al., 2014; Aster et al., 2016; Hanyu et al., 2020), and we adopt the lower end of 5% bubble volume to distinguish bubbles that nucleated and grew post-entrapment, in comparison to those trapped with the melt.

Previous studies combining CO_2 analysis in vapour bubbles and their host melt inclusions have shown that up to 90% of CO_2 can be sequestered to bubbles in the form of vapour (Hartley et al., 2014; Moore et al., 2015; Venugopal et al., 2020). However, CO_2 can exist in its liquid form and also as carbonates that can store up to 50% of CO_2 in the bubble. This is also true for sulphur-bearing minerals precipitated on bubble walls, which can store up to 60% of sulphur originally trapped in an inclusion (Esposito et al., 2016; Schiavi et al., 2020), and H_2O of which up to 16% can be sequestered (Esposito et al., 2016). Overall, melt inclusion bubbles have the ability to not only store large amount of CO_2 and S, but also H_2O and major and minor elements that constitute carbonates, sulphates, sulphides, halides and other minerals such as Na, Ca, Mg, Fe or Cu (Schiavi et al., 2020; Venugopal et al., 2020).

The concentration of CO_2 sequestered to bubbles post-entrapment is calculated by mass-balance equations (Moore and Bodnar, 2019), taking into consideration: (i) the volume fraction of the melt inclusion that is constituted by the bubble, and (ii) the density of CO_2 measured by Raman spectroscopy (attached supplementary data sheet 'C2'). Total inclusion and bubble volumes were estimated from photomicrographs, assuming a spherical shape for bubbles, an ellipsoid shape for orthopyroxene hosted

inclusions and cuboidal shapes for inclusions hosted in plagioclase, based on their 2D appearances from a polished surface (Figure 2.4). The two perpendicular axes were measured using a Leica DM4500 P LED microscope on the Leica Application Suite software, and the third unseen axis was calculated using the arithmetic mean of the measured axes. This method is associated with an average 5% error, but a 1σ error of -48 to 37% (Tucker et al., 2019). Uncertainty in bubble sizes was ±2 µm, which yielded bubble volume uncertainties of 6-24%. (Mean 11%; attached supplementary data sheet 'C2'). Density calculations were undertaken by firstly processing the Raman spectra of individual bubbles using the WiRE^{TM} 4.4 spectral analysis software. After baselines were applied to each spectrum with >500 counts using a polynomial curve, the Fermi diad was truncated at 1200 and 1500 cm^{-1}. Each peak was fitted with a mixed Gaussian-Lorentzian curve, and the Fermi diad split was calculated as the difference between the centres (in wave number) of the two peaks. In the absence of a CO_2 densimetry curve specifically calibrated for the instrument used, the experimental equation of Lamadrid et al. (2017) was adopted to calculate CO_2 density. Fermi diad peaks with counts <500 or asymmetrical peaks to which curves could not be readily fitted were not used to quantify CO_2.

H_2O loss

Loss of H_2O in melt inclusions was assessed from H_2O vs K_2O, which shows no significant variation of H_2O at a given K_2O (Figure 2.7), and thereby indicates no significant H_2O loss in SHV melt inclusions.

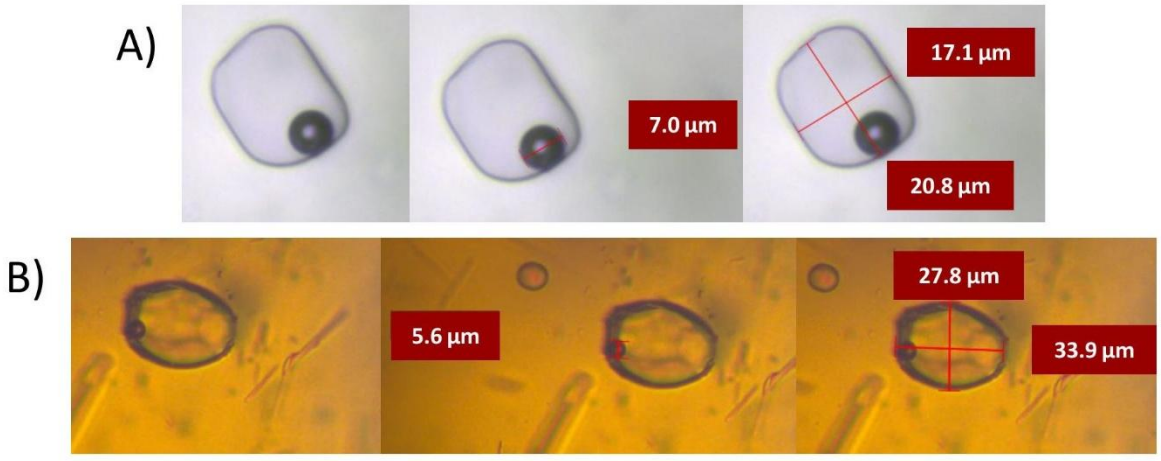

Figure 2.4 - Examples of melt inclusions adopting different shapes. A) SHV_P1_PLAG_010 is a plagioclase hosted inclusion taking the 2D shape of a rectangle, assumed to be cuboidal in 3D. B)

SHV_P5_OPX_006_MI1 is an orthopyroxene hosted inclusion taking the 2D shape of an oval, assumed to be ellipsoidal in 3D.

2.5.2.2 Major element compositions

The major element composition of seventy-seven SHV melt inclusions across phases 1, 2, 4 and 5 is plotted against K_2O as a representation of magma differentiation (Figure 2.5). There are trends in the overall dataset, and the dataset can also be divided into distinct groups, where the compositions differ based on Phase and host mineral. Overall, SiO_2 ranges from 69.63-78.15 wt.% with total alkalis of 4.48-7.51 wt.% across K_2O 1.61-2.84 wt.%, classifying the inclusions as dacite and rhyolite based on total alkali vs silica (Figure 2.2; Le Bas et al., 1986). Inclusions hosted in orthopyroxene are less evolved than those hosted in plagioclase, and inclusions are all more evolved than whole rock compositions. However, they overlap with groundmass glass compositions of 69.85-80.03 wt.% for Phases 1-3 (Edmonds et al., 2001; Edmonds et al., 2002; Harford et al., 2003; Buckley et al., 2006; Humphreys et al., 2010). Increasing trends with differentiation are seen in SiO_2 and Na_2O vs K_2O, while decreasing trends occur in CaO vs K_2O. Trends remain relatively constant for TiO_2, Al_2O_3, FeO and MgO vs K_2O.

In Phase 1, SiO_2 ranges from 70.06-74.04 wt.%, and is one of the least evolved Phases. Major element data exist only for plagioclase hosted inclusions in Phase 2. This group generally overlaps with Phases 1 and 5 with SiO_2 of 70.36-75.37 wt.%. Phase 4 stands out as the most evolved group, with SiO_2 ranging from 72.14-78.15 wt.% in plagioclase hosted inclusions. Inclusions in Phase 5 are similar to those of Phase 1, with 69.63-74.89 wt.% SiO_2. Overall, there is a trend of increasingly evolved melt compositions through Phases 1-4, before compositions revert to lower SiO_2 contents during Phase 5. Similar temporal evolution – with a distinction between the Phase 1-4 trend and Phase 5 – is also identified in CaO and Na_2O (Figure 2.5).

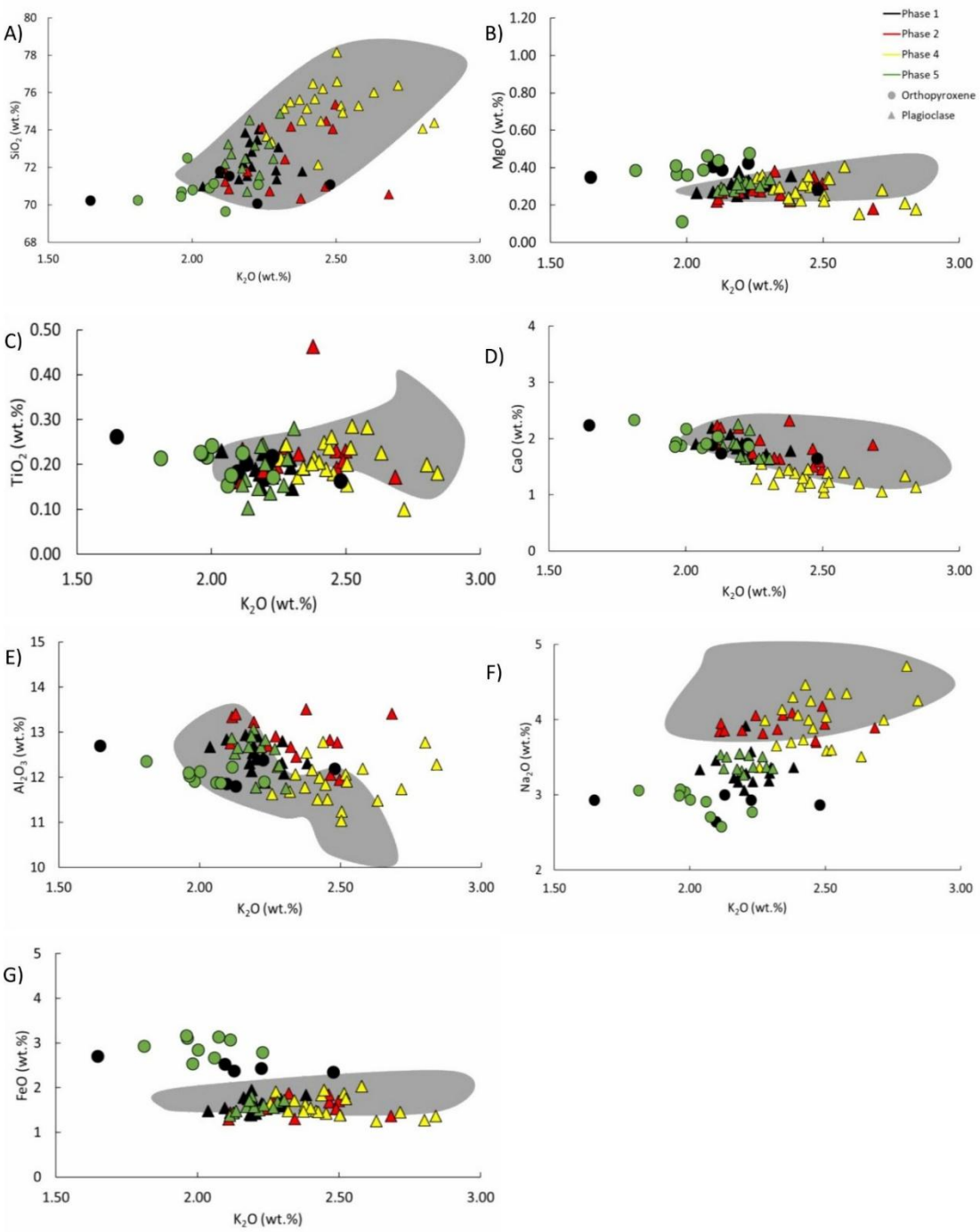

Figure 2.5 - Harker diagram showing major elements plotted against K_2O for assessment of variation with magma differentiation. The composition of inclusions differs with phase, where there is an increase in evolution through Phases 1 to 4, followed by less evolved inclusions at Phase 5. Grey zones are data reported in the literature for Phases 1-3 from Edmonds et al. (2001), Buckley et al., (2006),

Humphreys et al., (2010), Mann et al., (2013). (A) SiO_2 vs K_2O, (B) MgO vs K_2O, (C) TiO_2 vs K_2O, (D) CaO vs K_2O, (E) Al_2O_3 vs K_2O, (F) Na_2O vs K_2O, (G) FeO vs K_2O.

2.5.2.3 Volatile element compositions

2.5.2.3.1 Melt Inclusion Glass

SHV melt inclusions are rich in volatiles, with H_2O in the glass of seventy-five orthopyroxene-hosted inclusions ranging from 5.38-7.74 wt.%, and 2.47-6.40 wt.% in plagioclase-hosted inclusions (Figure 2.7A) throughout the eruption. Melt inclusion H_2O values across all Phases are similar to those recorded for Phase 1 and 2 plagioclase- and quartz-hosted inclusions (1.20-6.86 wt%, reported by Barclay et al., 1998; Mann et al., 2013), and are also similar to values reported by Humphreys et al., (2009) and Edmonds et al., (2014) where H_2O in plagioclase- and orthopyroxene-hosted inclusions measured 0.03-6.40 wt% for Phase 3 samples. Values from this study are also roughly similar to H_2O measured in orthopyroxene cores (6-9 wt%) for Phase 3 data of Edmonds et al., 2016.

H_2O across the eruption exhibits a decreasing trend with K_2O. This trend is also apparent in individual Phase groups, where plagioclase-hosted inclusions indicate degassing associated with crystallisation, except in Phase 1, where most of the data fall between a very restricted K_2O range, but are consistent with the overall degassing trend. Separating the dataset into Phase groups illustrates not only the degassing trend in the Phases, but also the difference in H_2O content as the eruption progresses. Similar to major elements, there is a decrease in H_2O contents from Phase 1, at the beginning of the eruption, to Phase 4, with a return to high H_2O in Phase 5 (Figure 2.7A). Based on their relationship with K_2O, the conclusion is made that SHV inclusions experienced at most negligible H_2O loss, as inclusions do not fall out of trend at a given K_2O.

This distinction in Phase groups is however not seen with melt inclusion glass CO_2 concentrations, where CO_2 across the eruption does not trend with K_2O except for Phase 2, and are typically <1000 ppm, with 67 of 69 inclusions containing 13-937 ppm, while two inclusions which contain 1126 (SHV_P5_PLAG_002_MI4) and 1243 (SHV_P5_PLAG_042_MI2) ppm.

2.5.2.3.2 Melt Inclusion Bubble

Bubbles at SHV contain CO_2 vapour along with solid phases crystallised on the bubble wall, identified via their main and other vibrations (Frezzotti et al., 2012; Figure 2.6). Solids are in the form of sulphates and are normally anhydrite and gypsum. No carbonates were observed.

Two groups can be identified from a total of 577 bubbles analysed by Raman spectroscopy. Group A consists of 91% of the bubble population, and are described as displaying a Fermi diad. Group B accounts for 9% of the bubble population, and their Raman spectra lack observable Fermi diads, indicating no CO_2 or CO_2 with very low densities. The 523 bubbles displaying Fermi diads have a CO_2 density range from 0.001-0.22 g cm^{-3}, with an upper limit of 0.13 (Figure 2.8B) for those with glass analysed via SIMS. Overall, bubble CO_2 density exists below the critical density of CO_2 (0.468 g cm^{-3}; Moldover, 1974), therefore, CO_2 exists solely as vapour and is not underestimated due to the presence of aqueous CO_2. In order to correct the total melt inclusion CO_2 to account for the bubble-hosted component, we take the mass of CO_2 in the bubble and add it back into the entire mass of glass in the MI and must thus account for their relative volumes. The contribution of the bubble-hosted CO_2 to the total inclusion CO_2 is based on the mass ratio between the bubble and the glass, and is therefore given by Equation 2.1:

$$[CO_2]_{bubble} = \frac{\rho_{CO_2} V_{bubble}}{\rho_{glass} V_{glass}} x\ 10^6 \qquad 2.1$$

where $[CO_2]_{bubble}$ is the amount that the concentration of CO_2 in the entire inclusion will be corrected when CO_2 in the bubble is accounted for. CO_2 density, volume of the bubble(s) and volume of the total inclusion are calculated according to section 4.2.1, and glass density is calculated for individual inclusions using DensityX (Iacovino and Till, 2019). Important sources of errors in calculating the amount of CO_2 that is contributed from the bubble are the estimation of bubble and inclusion volumes. For bubbles in the range 3 – 6 µm (majority orthopyroxene-hosted inclusions), volume errors are as large as 24%. However, the contribution of CO_2 from the bubble to total CO_2 in these inclusions are small in comparison to the concentration of CO_2 in the glass, and therefore the total error is small (~11%). For bubbles over 6 µm, errors on volume calculations are 5-10%. Additionally, large errors are introduced in calculation of the CO_2

density, especially at low densities (Attached supplementary data sheet 'C2'), calculated using the densimeter equation of Lamadrid et al., (2017) in the absence of a calibration curve specific to the Raman spectrometer used. Overall, errors on the calculation of total CO_2 amount to ~22%. Based on (i) CO_2 existing solely as vapour in the bubble(s), and (ii) carbonates being absent in the bubble, the contribution of CO_2 from the bubble of seventy-two inclusions for which there are SIMS and EPMA data ranges from 9-3767 ppm. However, for further calculations and models, we use bubbles that do not show signs of heterogeneous entrapment (bubbles <5% of total inclusion volume). The contribution of CO_2 from these bubbles to the total inclusion is 9 - 3145 ppm.

2.5.2.3.3 Total CO_2

The summation of CO_2 in the glass and CO_2 in the bubble (5% threshold applied) gives a total CO_2 budget of melt inclusions of 131-3230 ppm, with an average of 1006 ± 684 ppm at SHV (Figure 2.7C), the highest for the Northern Group islands where maximum CO_2 is 720 ppm for St Kitts (Melekhova et al., 2017), and is most comparable with islands in the Central Group where CO_2 values extend up to 1507 and 4012 ppm for bubble-free melt inclusions from Guadeloupe and Dominica respectively (Balcone-Boissard et al., 2018; d'Augustin et al., 2020; Metcalfe et al., 2022).

While the bubble comprised ≤5% of total inclusion volume, the percentage of CO_2 sequestered to the bubble amount to 5-76% for inclusions hosted in orthopyroxene, and 37-99% for those hosted in plagioclase (Figure 2.8A), in agreement with published data on CO_2 loss to the bubble (e.g Hartley et al., 2014; Wallace et al., 2015b; Moore and Bodnar, 2019; Venugopal et al., 2020). It is noted that orthopyroxene-hosted melt inclusions trapped less evolved and less differentiated magma and therefore contain more H_2O than the plagioclase-hosted melt inclusions. Following this trend, it is expected that these inclusions should also contain higher CO_2 contents, but this is not the case, and we are unable to adequately explain this phenomenon.

H_2O and total CO_2 do not show simple open- or closed-system degassing trends overall or when separated by Phases (Figure 2.7B). However, CO_2 during Phase 1 appears 1082-1685 ppm lower than Phases 2, 4 and 5. The case can be made for CO_2 degassing in each Phase as large variations in CO_2 exist at relatively constant H_2O while being hosted in phenocrysts with similar enstatite and anorthite contents. Due to its low solubility, CO_2 begins to exsolve at high pressures and is the first volatile species to be degassed (Best, 2003).

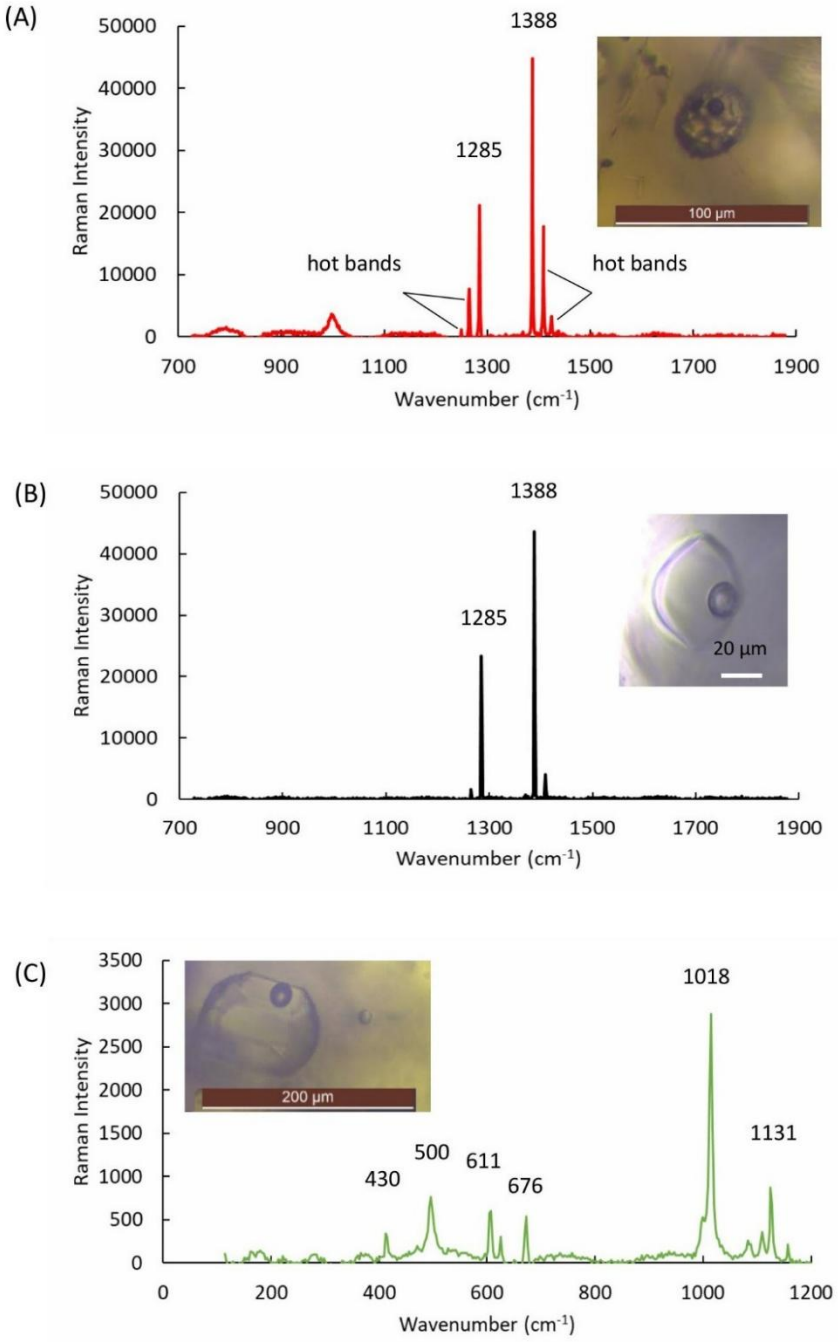

Figure 2.6 - Raman spectra of gaseous and solid phases found in Soufrière Hills bubbles. A) Raman spectra of bubble from SHV_P2_OPX_001_MI1 displaying Fermi diad indicating the presence of CO_2. B) Raman spectra of the bubble of plagioclase-hosted inclusion 'SHV_P1_PLAG_030_MI1' showing Fermi diad. C) Raman spectra of bubble in SHV_P5_OPX_002_MI1 showing presence of sulphate (anhydrite) crystals on bubble wall with peaks at 430, 500, 611, 629, 676, 1018 and 1131 cm^{-1}.

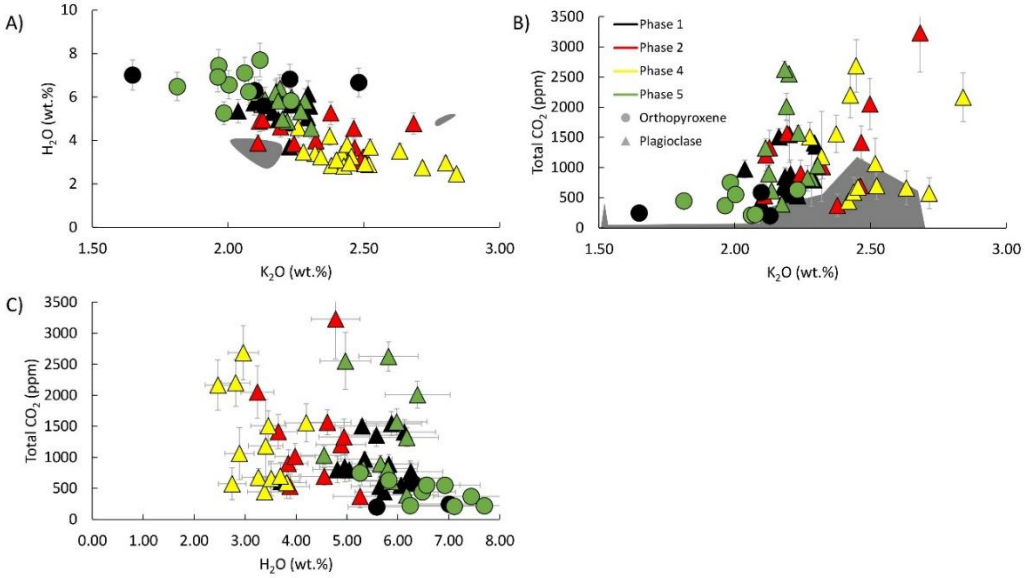

Figure 2.7 - A) H_2O vs K_2O in the glass shows degassing within Phases and an overall decrease of H_2O with time, reverting to high H_2O during the last Phase of eruption. B) Total CO_2 vs K_2O. C) Total CO_2 vs H_2O does not follow simple open or closed degassing trends. Grey areas are values reported in the literature. H_2O and CO_2 data from Barclay et al., (1998); Mann et al., (2013) and Edmonds et al., (2014). Error bars show 10% errors n H_2O, and are calculated individually for CO_2 based on the contribution from both the bubble and the glass. Where error bars are not shown, the error is smaller than the symbol size.

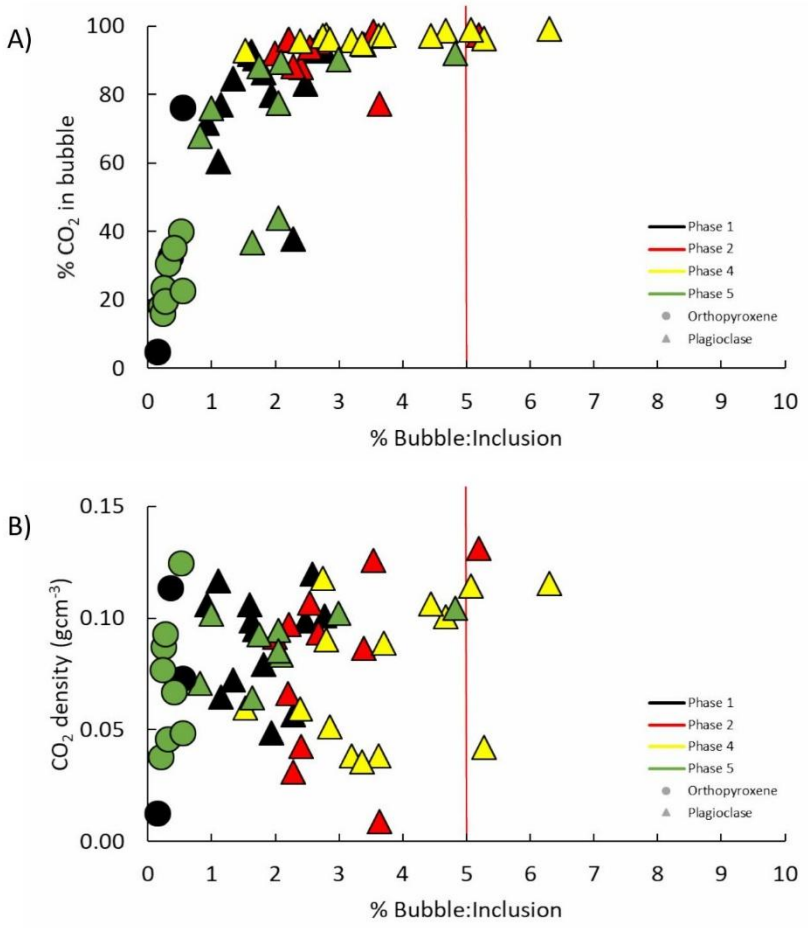

Figure 2.8 - A) Percentage of CO_2 contributed by the bubble vs bubble to inclusion ratio. In orthopyroxene-hosted inclusions, 5-76% of CO_2 in the total melt inclusion is contributed by the bubble. In plagioclase-hosted inclusions, this value is 37-99%. Overall, there is a median of 90% contribution from the bubble to the total inclusion CO_2 B) There is no correlation with CO_2 density as a function of bubble volume percentage. The red line on both plots denote the 5% bubble threshold of homogenous vs heterogeneous bubble growth.

2.6 Discussion

2.6.1 Magma Storage Conditions

The compositions of major and volatile elements are applied to models to facilitate connection between melt inclusion data and crystallisation temperatures, magma storage depths, degassing systematics and magmatic CO_2 budgets.

2.6.1.1 Geothermometry

The temperatures calculated represent magmatic temperatures at the time of melt inclusion trapping. For orthopyroxene-hosted inclusions from Phase 1 and Phase 5, the temperature calculation was based on orthopyroxene-liquid equilibria using Equation 28a of Putirka, (2008). Temperatures from the two Phases are not highly varied, with a total range of 880-916 °C, and a standard error of estimate (SEE) of 28 °C. Phase 1 and 5 results are not significantly different, being 880-898 °C for Phase 1 (three melt inclusions) and 884-916 °C for eight Phase 5 inclusions. Plagioclase-liquid equilibria are applied to fifty-two plagioclase-hosted inclusions where H_2O was measured via SIMS, to reduce overestimation of temperature due to its strong dependence on H_2O. Applying Equation 24a of Putirka, (2008) yields a narrow temperature range across Phases, with temperatures ranging from 828-893 °C and SEE of 36 °C. However, the plagioclase melt inclusion data do reveal a significant difference in temperature between Phases, where Phase 2 inclusions yield the hottest temperatures from 875-893 °C along with Phase 4 (849-891). Phases 1 and 5 are cooler, with temperatures of 828-881 °C and 836-864 °C respectively (Figure 2.9). While Phase 5 inclusions are more primitive than Phase 2 and 4, based on SiO_2, FeO and MgO contents (Figure 2.5), their temperatures are lower. This may indicate a lack of hotter, more mafic magma input, correlating with evidence from uranium-series disequilibria in mafic enclaves and their hosts that suggest the intrusion of mafic magma had halted by Pause 2 (McGee et al., 2019).

Temperatures calculated in this study are the first temperature estimates for Phases 2, 4 and 5 using melt inclusion data and are similar to those of Phase 1 (812-891 °C) obtained via geothermometry and experimental phase equilibria (e.g. Barclay et al., 1998; Devine et al., 1998; Murphy et al., 2000).

Constraints on hornblende stability have been used to infer that the andesitic magma was originally cooler (≤ 840 °C), before being reheated by injection of deeper basalt, which elevated the andesite temperature to ~880 °C (Barclay et al., 1998; Devine et al., 1998).

2.6.1.2 Saturated pressures and associated depths

The crustal depth and thus pressure at which magma accumulates is a key influence on volcanic system behaviour, including exsolution of volatiles, crystallisation, and mineral growth (Huber et al., 2019). The mush model, whereby melt exists within a continuous crystalline framework (Marsh, 2004; Cashman et al., 2017) has been proposed for arc volcanoes including those of the Lesser Antilles, with storage regions being continuous (Dominica and Kick 'em Jenny) or multi-leveled (Guadeloupe, Martinique and St Lucia; Metcalfe et al., 2022). Storage depths at SHV, Montserrat have been previously estimated using volatiles in melt inclusion glasses alone (e.g. Edmonds et al., 2014; Edmonds et al., 2016) and are clearly underestimated as bubble-hosted CO_2 was neglected. Recalculation is now possible with the new whole melt inclusion glass + bubble CO_2 results provided here, providing a better understanding of the plumbing system.

After accounting for bubble growth, the values of total CO_2, H_2O, melt inclusion composition, and temperature were input into the H_2O-CO_2 solubility model MagmaSat (Ghiorso and Gualda, 2015), hosted in VESIcal (Iacovino et al., 2021). MagmaSat permits calculation of saturation pressures for each melt inclusion based on specific composition-relevant pressure-solubility relations, and its usefulness is underpinned by the assumption that the melt trapped within inclusions is representative of the magma storage regions from which the crystals are derived (Cannatelli et al., 2016). Model results indicate that melt inclusion saturation pressures over the duration of eruptions at SHV are highly variable, with plagioclase-hosted inclusions yielding entrapment pressures spanning 1000-6800 bars (100-680 MPa). Pressures for orthopyroxene-hosted inclusions are more restricted in range, between 1900-3200 bars (190-320 MPa).

To correlate entrapment pressures to depths (MI_{depth}), Equation 2.2 is applied:

$$MI_{depth} = \frac{p}{\rho g} \quad 2.2$$

where MI_{depth} (m), is based on pressure *'p'* (in Pascals) calculated above, Lesser Antilles crustal density 'ρ' of 2660 kgm^{-3} (Christeson et al., 2008) and g = 9.81 ms^{-2}.

Therefore, the pressures derived here indicate that SHV melt inclusions were trapped in orthopyroxenes and plagioclases at upper to mid crustal depths (5.7±0.8 to 17±2.5 km), with four plagioclase-hosted inclusions in the lower crust (20±2.8 to 23±1.3 km), and one deeper inclusion plotting at 26±4.0 km. While plagioclase-hosted inclusions span the entire calculated range, orthopyroxene-hosted inclusions are restricted to 7.4±0.1 to 12±0.3 km, similar to depth estimates from the H_2O content of enstatites (mean of 10 km, over a total range of 4-16 km; Edmonds et al., 2016).

The depth of magma storage has been linked to (i) the depth of neutral buoyancy where the density of magma and country rock are similar (Hooft and Detrick, 1993), (ii) rheological conditions of the crust (Mazzarini et al., 2010), and (iii) to the location of pre-existing zones of crust weakness (Chaussard and Amelung, 2014). Alternatively, inferred magma storage depths may instead merely reflect the magmatic water concentrations (Rasmussen et al., 2022), where the maximum H_2O content of SHV magmas correlates to ~13 km depth. However, melt inclusion data at SHV resolve depths greater than 13 km for 20% of inclusions, and are outside of the mafic-intermediate dataset range used in the study. This H_2O limit does not appear to apply to this volcanic system - perhaps due to the higher silica content of the SHV magma.

Our new melt inclusion H_2O and CO_2 data support a vertically extensive transcrustal magmatic system (Figure 2.9; Figure 2.10; e.g. Cashman et al., 2017). The wide range of pressures and depths relate to inclusion trapping during crystal growth within a vertically extensive magma storage system that spans 5-17 km, with no distinct gaps in crystallisation depths. The transcrustal model can also explain the wide range of entrapment pressures inferred from H_2O and Al_2O_3 contents of Phase 3 orthopyroxenes (Edmonds et al., 2016), and 3D modelling of the ground deformation during Pause 5, where best solutions require melt injection into the base of a mush-based reservoir at ~17 km depth (Gottsmann et al., 2020; Alshembari et al., 2024). Vertically extensive mush systems are the proposed magma storage types in arc environments, including the Lesser Antilles (Metcalfe et al., 2022), and are more importantly not uncommon to Montserrat, where melt inclusions from South Soufrière Hills reveal trapping pressures

equivalent to 3-17 km depth using vapour-bubble-free melt inclusions hosted in olivine and clinopyroxene (Cassidy et al., 2015a; Cassidy et al., 2015b).

Phase 1 inclusions are evenly spread at 9.7±0.7 to 16±1.3 km, with one shallower at 7.3±0.5 km. In Phase 2, depths span 7.2±1.3 to 16±2.7 km, with one deeper at 26±4.0 km. Phases 4 and 5 also have similar depths to the first two phases at 5.7±0.8 to 17±2.5 and 9.9±0.4 to 17±1.3 km respectively, however, with deeper depths at 20±1.2 to 23±1.3 km.

Geochemical, geodetic and Fe-oxide data place a lower limit of ~17 km for the SHV magma storage region in both dual and mush reservoir scenarios (Foroozan et al., 2010; Edmonds et al., 2016; Alshembari et al., 2024), consistent with the inferred entrapment pressure of 58 of the 63 melt inclusions characterised in this study. Thus, the overwhelming majority of the inclusions, which resolve depths <17 km, are taken as representative of a melt undergoing crystallisation, degassing, and thus differentiation.

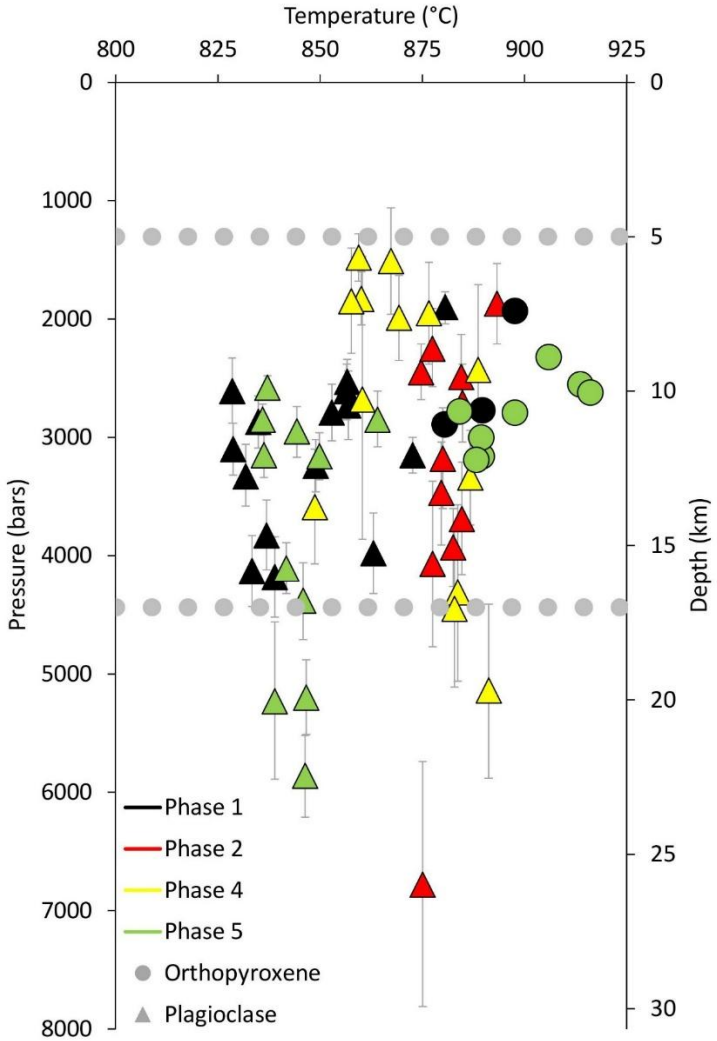

Figure 2.9 – Pressure vs temperature graph for inclusions at SHV showing the magmatic conditions at the time of plagioclase and orthopyroxene crystal growth. Grey horizontal dashes represent the depths of magma storage based on deformation modelling (Foroozan et al., 2010). Error bars represent the uncertainty in depths based on uncertainties in total CO_2. Error bars for orthopyroxene-hosted melt inclusions are not shown as the uncertainty is smaller than the size of the symbol.

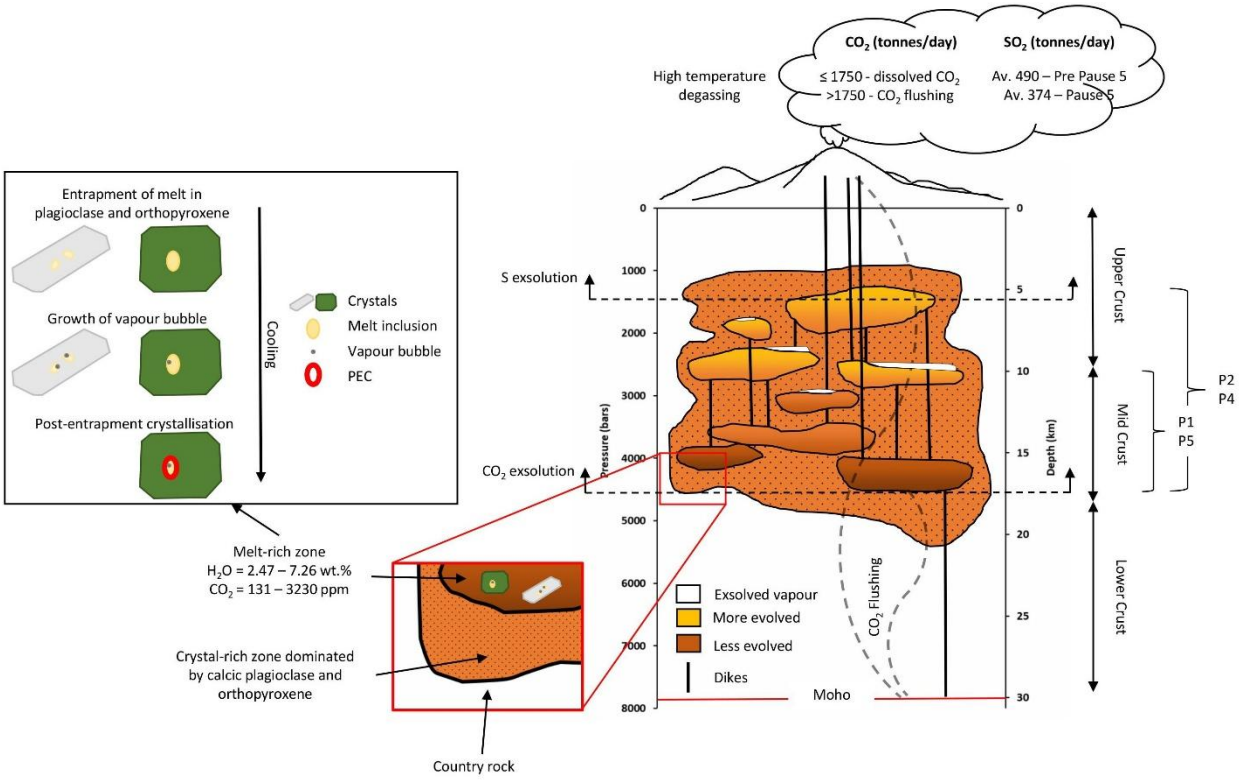

Figure 2.10 - Schematic of the plumbing system beneath Soufrière Hills Volcano, exhibiting mush properties similar to other arc volcanoes. This is a vertically extensive transcrustal magmatic system consists of a melt-rich zone with high H_2O and CO_2 contents and a crystal rich zone dominated by calcic plagioclase and orthopyroxene spanning ~5 - 17 km, and is periodically flushed with CO_2 from deeper in the system. Melt inclusions from Phases 1 and 5 plot in the mid crustal region whereas Phases 2 and 4 span the upper to mid crustal regions.

2.6.2 CO_2 volatile budget

The maximum measured CO_2 concentration in melt inclusion glass and bubble, representing the least degassed CO_2 trapped in melt inclusions is compared to estimates of CO_2 degassed through the plume using the petrological method (Devine, et al., 1984), assuming that the concentration of volatiles in melt inclusions represents the concentration of volatiles dissolved in the magma at depth. A total of 4.5 Mt of CO_2 (M_{dv}) is calculated to have been contained in SHV magma during Phases 1, 2, 4 and 5 based on Equation 3

$$M_{dv} = X_{MI} V \rho \quad (3)$$

where X_{MI} is the maximum concentration of CO_2 measured in melt inclusions (3230 ppm) in the studied Phases, V is the volume of erupted magma (Wadge et al., 2014), and ρ refers to the magma density of 2400 kg m^{-3} Dense Rock Equivalent (Melnik and Sparks, 2002). Phases 1 and 2 held more dissolved CO_2 in their magmas with maxima of 1.2 and 2.6 Mt respectively, exceeding the corresponding figures for Phases 4 and 5 (0.25 and 0.44 Mt respectively). This total of 4.5 Mt of CO_2 dissolved in the magma is however much less than the 7.7-12 Mt total plume-emitted CO_2 estimated by Edmonds et al., (2014) during the period 1995-2009, using an average molar CO_2/SO_2 ratio of 5.1. However, the ratio of 5.1 used in their estimation introduces a large error, as it is derived from five days of measurements during Pause 3, and assumes a constant ratio over fourteen years of activity. This mismatch of petrological estimates in comparison to direct measurements is often seen in SO_2 fluxes, and is a feature common to arc settings where magmas are more oxidized, and is not generally observed in non-arc magmas (e.g. Sigurdsson, et al., 1990; Westrich and Gerlach, 1992; Gerlach et al., 1994; Blake et al., 2003; Sharma et al., 2004).

Applying the five days of CO_2 measurements (Edmonds et al., 2014) in the plume taken during July 2008 to a shorter time period of Phase 4 (July 2008-January 2009), we calculate that 0.24 Mt was released in the plume over 158 days. Therefore 96% of the CO_2 dissolved in Phase 4 magma was emitted during the eruption. Applying the calculations to Phase 5 (October 2009-January 2010), an average of 2297 tonnes/day of CO_2 emitted from June-November 2010 (Edmonds et al., 2014) amounts to 0.29 Mt or 66% of the CO_2 dissolved in the magma being released over 125 days. While these estimates are termed 'maxima' based on the maximum CO_2 considered for each Phase, it is noted that masses calculated can be underestimated due to (i) unerupted volumes of magma which are not taken into account, and (ii)

entrapment of already degassed melt (Moune et al., 2007). The percentage of CO_2 released during Phases 1 and 2 is unable to be estimated due to lack of published CO_2 fluxes.

Original magmatic CO_2 contents can also be estimated using the CO_2 flux derived by combining SO_2 fluxes measured using UV spectrometer and CO_2/SO_2 ratio acquired via Multisensor Gas Analyser System (MultiGAS) over the five days in July 2008 and fifteen days during June to October 2009. The highest CO_2 flux reported (Edmonds et al., 2014) of 5494 tonnes/day measured on October 1 2010 is used to calculate a maximum mass of CO_2 for a period of 125 days during Phase 5, amounting to 0.69 Mt, and magma masses are calculated from reported magma volume estimates and magmatic density of 2400 kgm^{-3}. We can therefore use equation 3 to estimate the required melt inclusion CO_2 concentration to match the measured CO_2 emissions. This value of 4107 ppm is 877 higher than the initial CO_2 from the least degassed melt inclusions measured across the eruption. This value correlates to a pressure of 8090 bars or 31.0 km depth assuming a H_2O content of 6.39 wt.%, the highest of the Phase 5 inclusions. As a result, we attribute this high CO_2 flux to CO_2 flushing (e.g. Blundy et al., 2010; Caricchi et al., 2018) from degassing deeper in the system, a process that is commonplace in the arc, and occurs in all island groups (Metcalfe et al., 2023a). The related depth would extend into the Moho situated ~30 km under Montserrat, based on crustal xenolith petrology and seismic data (Melekhova et al., 2019). Based on fluxes generated during June to October, and compared to Phase 5, a CO_2 flux greater than ~1500-1750 tonnes/day cannot be accounted for by the dissolved CO_2 in this batch of magma, and therefore relate to CO_2 flushing from mantle depths.

2.6.3 CO_2 controls on explosivity and implications for the future

Quantification of dissolved magmatic gases as well as their emissions is essential for understanding the influence of volatiles on volcanic system dynamics and the related hazards. The dissolved magmatic CO_2 concentration can, alongside more abundant H_2O, drive eruptions, dictate eruptive style or impact both in volcanic settings (e.g. Burton et al., 2007; Allard, 2010; Allison et al., 2021). The eruptive style at SHV can be described as transitioning, with both effusive and explosive eruptions occurring during each Phase, producing lava domes and explosions (e.g. Druitt et al., 2002; Edmonds and Herd, 2007; Ryan et al., 2010). However, at SHV, microlite petrology from Phase 3 samples has demonstrated that shallow conduit processes determine eruptive style, with similar decompression pathways within the deeper magmatic system resulting in both lava dome growth and explosions (Murch and Cole, 2019). Nevertheless, melt inclusion analysis conducted in this study shows that while each Phase produced VEI 2-3 events, their SiO_2 content, H_2O content, CO_2 content, duration, and the number of explosions differ. Particularly, Phase 1 and 5 are similar in silica content, H_2O and also have similar pressures and depths based on solubility modeling of melt inclusion H_2O and CO_2 concentrations. While these Phases exhibit similar chemistry, their explosive behaviours have differed, with Phase 5 producing more Vulcanian explosions within a shorter timeframe (125 days) than Phase 1 (846 days). This is likely due to the amount of CO_2 in the system during these Phases as Phase 1 had ~1000 ppm less CO_2 dissolved within its melt and Phase 5 was influenced by CO_2 flushing. However, due to the limited availability of CO_2 flux data at SHV, it is unclear if CO_2 flushing occurred during either Phases.

The monitoring of volatile release at SHV has primarily focused on SO_2 flux (e.g. Young et al., 1998; Carn and Prata, 2010; Nicholson et al., 2013; Christopher et al., 2015), however trends in SO_2 have not correlated with the eruptive Phases, but instead occur on multi-year (~2 years) and multi-week cycles (~50 days and ~5 months), independent of lava extrusion and dome building (Nicholson et al., 2013; Christopher et al., 2015), upon which Phases are determined. We recommend that CO_2 should also be routinely monitored as it provides insight into movement of magma in the deep system, and also has the ability to drive eruptions through processes such as CO_2 flushing, which can alter the physical properties of the magma - increasing magma volume, leading to overpressure and potentially eruptions (Caricchi et al., 2018). While data are severely limited, instances of CO_2 flushing at SHV are evident at the transition between Pause 3 and Phase 4, and ~6 months after the cessation of Phase 5. As the crystallinity of SHV magma, at 30-45%, is at or beneath the threshold at which magmas reach their rheological locking point

(40-50%), flushing at SHV can potentially trigger eruptions. This further highlights the importance of monitoring of CO_2 flux at SHV, especially during the current period of unrest.

2.7 Conclusions

We have provided the most comprehensive study published to date of magmatic carbon in the Soufrière Hills Volcano magmatic system, providing the first measurements to include bubble-hosted CO_2 in melt inclusions and the first pre-eruptive CO_2 measurements for the most recent eruptive phases. H_2O and total CO_2 contents for melt inclusions hosted in plagioclase from pumice erupted during four phases of eruption are 2.47-6.40 wt.% H_2O and 131-3230 ppm CO_2. Those hosted in orthopyroxene are 5.15-7.26 wt.% and 199-736 ppm CO_2. The sequestration of CO_2 to the bubble has proven to be an important post-entrapment modification at SHV, with 5 -99% (median 90%) of CO_2 contained in bubbles and thus excluded in earlier analyses. Our measurements therefore provide unprecedented insight into the magmatic CO_2 concentrations within the SHV system and indicate higher concentrations than previous studies. Our volatile solubility-based estimates of magma storage depths (5.7-17 km) indicate that a transcrustal magmatic system was persistent throughout the eruption, consistent with geodetic modelling (Alshembari et al., 2024).

We use melt inclusion compositions to estimate magmatic temperatures at entrapment, based on liquid-mineral pairs. Temperature results (828-916 °C) are similar to published estimates for Phase 1 (812-891 °C) and are the first temperature estimates for Phases 2, 4 and 5.

The total amount of CO_2 contained in magma from Phases 1, 2, 4 and 5 is ~4.5 Mt, using the petrological method. We calculate that 96% of the dissolved CO_2 in Phase 4 magma was released to the atmosphere during Phase 4, and 66% of the dissolved CO_2 in Phase 5 was released. Our results indicate that ~1500-1750 tonnes/day CO_2 can be emitted from the magma, and thus any CO_2 fluxes higher than 1750 tonnes/day are likely the result of CO_2 flushing from deeper in the magmatic system. Pauses 4 and 5 therefore experienced CO_2 flushing, with up to 5494 tonnes/day being released (Edmonds et al., 2014), and are the only Phases with reported CO_2 fluxes.

Our new melt inclusions dataset covers four of five Phases of eruptive activity at SHV, and provides the first account of total (glass + bubble hosted) CO_2. Our data indicates that the magmatic system feeding SHV is a vertically elongated mush system, as corroborated by geophysics and geochemistry.

2.8 Supplementary Material C2

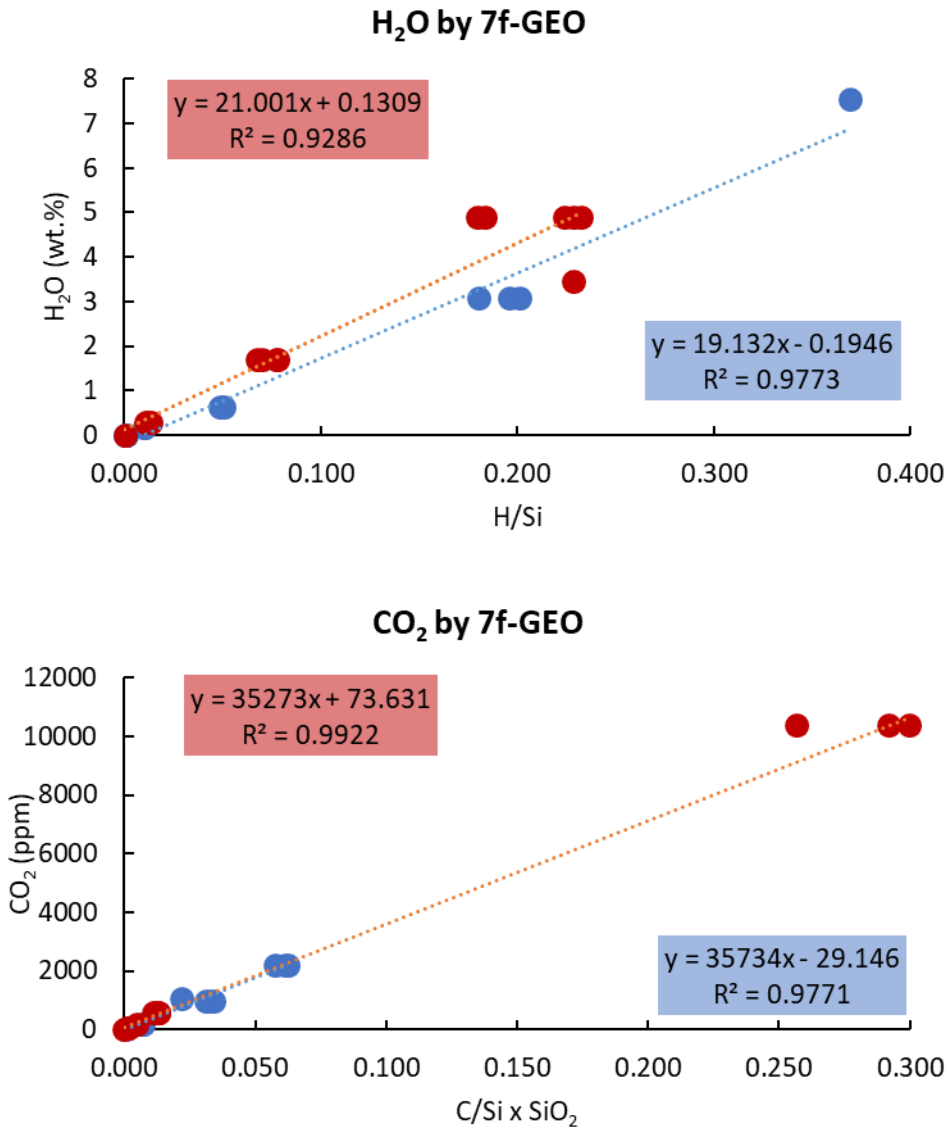

Supplementary Figure 2.S1 - Calibration curves used to calculate H_2O and CO_2 using Cameca IMS 7f-GEO. H_2O is calculated using the curve of H/Si vs H_2O where standards range from 0.64–7.56 wt.%. CO_2 is calculated using the curve of (C/Si)*SiO_2 vs CO_2 where standards range from 0–10380 ppm. Basaltic standards are blue and rhyolite standards are red.

Major & Volatile Elements	Standard	Diffraction Crystal	Counting Time (s)
Si	Diopside	TAP	10
Ti	Rutile	PETL	30
Al	K-Feldspar	TAPL	10
Fe	Fayalite	LIFL	20
Mn	Mn metal	LIFL	40
Mg	Periclase	TAP	40
Ca	Diopside	PETL	30
Na	Jadeite	TAPL	10
K	K-Feldspar	PETH	10

Supplementary Table 2.S1 - Analytical conditions for major and volatile element composition analysis of melt inclusion glass.

Elements	Standard 'BR'	Standard 'GH'
SiO_2	38.20	75.80
Al_2O_3	10.20	12.50
Fe_2O_3	12.88	1.34
MgO	0.20	0.05
CaO	13.28	0.03
Na_2O	13.80	0.69
K_2O	3.05	3.85
TiO_2	1.40	4.76
MnO	2.60	0.08
P_2O_5	1.04	0.01
Ba	0.1050	0.0002
Sr	0.1320	0.0001
H_2O+	2.30	0.46
H_2O-	0.50	0.14
Total	99.7	99.7

Supplementary Table 2.S2 - Reference values for standards 'BR' and 'GH' from Centre de Recherches Pétrographiques et Géochimiques used for calibration in whole rock analysis.

Melt inclusion bubble CO_2 reconstruction

Sample ID	Bubble Volume	Total Inclusion Volume	Bubble Volume Fraction	Fermi Diad	Neon correction factor	Corrected Fermi Diad	CO_2 density	Glass density	CO_2 in bubble (ppm)	CO_2 in glass (ppm)	Total CO_2 (ppm)
Plagioclase Hosted											
SHV_P1_PLAG_014_MI1	1.35E-09	6.11E-08	0.02	102.66	1.00	102.84	0.07	2.31	664	n.d.	n.d.
SHV_P1_PLAG_014_MI2	3.74E-09	1.64E-07	0.02	102.63	1.00	102.81	0.06	2.32	571	937	1507
SHV_P1_PLAG_015_MI1	1.14E-09	1.04E-07	0.01	102.80	1.00	102.98	0.12	2.21	588	385	973
SHV_P1_PLAG_016_MI1	1.65E-09	1.45E-07	0.01	102.65	1.00	102.83	0.06	2.19	341	101	442
SHV_P1_PLAG_017_MI6	6.85E-10	7.42E-08	0.01	102.77	1.00	102.95	0.11	2.25	439	174	613
SHV_P1_PLAG_020_MI2	2.18E-09	1.31E-07	0.02	102.73	1.00	102.91	0.09	2.22	726	76	803
SHV_P1_PLAG_024_MI2	2.51E-09	9.72E-08	0.03	102.80	1.00	102.98	0.12	2.21	1434	111	1545
SHV_P1_PLAG_024_MI3	1.25E-09	7.72E-08	0.02	102.75	1.00	102.93	0.10	2.21	737	59	796
SHV_P1_PLAG_028_MI3	4.70E-09	2.59E-07	0.02	102.69	1.00	102.87	0.08	2.20	665	104	769
SHV_P1_PLAG_030_MI1	3.87E-09	2.00E-07	0.02	102.60	1.00	102.78	0.05	2.18	440	111	551
SHV_P1_PLAG_032_MI1_B1	1.70E-09	1.45E-07	0.01	102.77	1.00	102.95	0.11	2.17	597	147	892
SHV_P1_PLAG_032_MI1_B2	8.09E-10		0.01	102.63	1.00	102.81	0.06	2.17	148		
SHV_P1_PLAG_032_MI2	7.77E-10	4.86E-08	0.02	102.77	1.00	102.95	0.11	2.21	777	69	846
SHV_P1_PLAG_036_MI3	9.61E-10	3.47E-08	0.03	102.75	1.00	102.93	0.10	2.20	1305	102	1407
SHV_P1_PLAG_037_MI2	5.18E-09	2.10E-07	0.02	102.75	1.00	102.93	0.10	2.21	1127	230	1357
SHV_P1_PLAG_040	1.06E-09	7.95E-08	0.01	102.67	1.00	102.85	0.07	2.18	451	82	533
SHV_P1_PLAG_048_MI1_B1	6.65E-10	6.34E-08	0.01	102.72	1.00	102.90	0.09	2.18	433	104	672
SHV_P1_PLAG_048_MI1_B2	1.76E-10		0.00	102.53	1.00	102.71	0.02	2.18	29		
SHV_P1_PLAG_048_MI1_B3	1.10E-10		0.00	102.67	1.00	102.85	0.07	2.18	59		
SHV_P1_PLAG_048_MI1_B4	1.10E-10		0.00	102.63	1.00	102.81	0.06	2.18	46		
SHV_P2_PLAG_010_MI1	1.92E-09	5.68E-08	0.03	102.71	1.00	102.89	0.09	2.26	1339	75	1414
SHV_P2_PLAG_011	7.36E-10	3.35E-08	0.02	102.65	1.00	102.83	0.07	2.23	666	30	695
SHV_P2_PLAG_013_MI1_B1	4.71E-10	3.25E-08	0.01	102.48	1.00	102.66	0.01	2.23	67	n.d.	n.d.
SHV_P2_PLAG_013_MI1_B2	4.46E-10		0.01	102.51	1.00	102.69	0.01	2.23	162		
SHV_P2_PLAG_015_MI3	1.70E-09	4.70E-08	0.04	102.49	1.00	102.67	0.01	2.21	151	45	196
SHV_P2_PLAG_017	1.11E-09	4.63E-08	0.02	102.59	1.00	102.77	0.04	2.23	467	64	531

SHV_P2_PLAG_025_B1	6.83E-08	2.94E-06	0.02	102.75	1.00	102.93	0.10	2.25	1051	116	1566
SHV_P2_PLAG_025_B2	2.44E-08		0.01	102.77	1.00	102.95	0.11	2.25	400		
SHV_P2_PLAG_029	8.56E-09	1.65E-07	0.05	102.84	1.00	103.02	0.13	2.28	3145	84	3230
SHV_P2_PLAG_030_MI1	4.60E-10	2.30E-08	0.02	102.73	1.00	102.91	0.09	2.25	829	71	900
SHV_P2_PLAG_031_MI1	8.79E-09	3.29E-07	0.03	102.73	1.00	102.91	0.09	2.23	1149	57	1206
SHV_P2_PLAG_031_MI2	2.48E-09	9.75E-08	0.03	102.77	1.00	102.95	0.11	2.23	1249	81	1330
SHV_P2_PLAG_032_MI1	4.27E-10	1.93E-08	0.02	102.74	1.00	102.92	0.10	2.25	977	40	1017
SHV_P2_PLAG_038_MI2	1.95E-09	5.49E-08	0.04	102.82	1.00	103.00	0.13	2.29	2016	34	2050
SHV_P2_PLAG_039	6.43E-09	2.82E-07	0.02	102.56	1.00	102.74	0.03	2.21	328	43	371
SHV_P2_PLAG_049	6.74E-10	2.19E-08	0.03	102.83	1.00	103.01	0.13	2.27	1795	n.d.	n.d.
SHV_P4_PLAG_002_MI2	1.94E-09	6.92E-08	0.03	102.57	1.00	102.72	0.03	2.26	1152	32	1184
SHV_P4_PLAG_004	4.18E-10	1.41E-08	0.03	102.58	1.00	102.73	0.03	2.26	415	n.d.	n.d.
SHV_P4_PLAG_006_MI1	1.13E-09	7.42E-08	0.02	102.67	1.00	102.82	0.06	2.24	412	32	445
SHV_P4_PLAG_008	6.25E-09	4.25E-08	0.15	102.63	1.00	102.78	0.05	2.23	3767	30	3796
SHV_P4_PLAG_009	5.71E-10	1.08E-08	0.05	102.62	1.00	102.77	0.04	2.28	1026	37	1064
SHV_P4_PLAG_018_MI1	6.30E-10	1.97E-08	0.03	102.61	1.00	102.76	0.04	2.24	567	25	592
SHV_P4_PLAG_019_MI2	1.59E-10	4.44E-09	0.04	102.79	1.00	102.94	0.10	n.d.	n.d.	n.d.	n.d.
SHV_P4_PLAG_024_MI1	2.42E-09	5.17E-08	0.05	102.78	1.00	102.93	0.10	2.31	2136	29	2165
SHV_P4_PLAG_024_MI2	5.66E-09	8.98E-08	0.06	102.82	1.00	102.97	0.12	2.34	3313	31	3344
SHV_P4_PLAG_026_MI2	1.12E-09	4.69E-08	0.02	102.75	1.00	102.90	0.09	2.25	647	31	678
SHV_P4_PLAG_026_MI3	n.d.	n.d.	n.d.	n.d.	n.d.	n.d.	n.d.	n.d.	n.d.	n.d.	n.d.
SHV_P4_PLAG_028_MI1	1.31E-09	3.92E-08	0.03	102.77	1.00	102.92	0.10	2.27	1456	n.d.	n.d.
SHV_P4_PLAG_035_MI1	5.27E-09	1.19E-07	0.04	102.80	1.00	102.95	0.11	2.31	2139	63	2201
SHV_P4_PLAG_035_MI4	n.d.	n.d.	n.d.	n.d.	n.d.	n.d.	n.d.	n.d.	n.d.	47	n.d.
SHV_P4_PLAG_035_MI5	n.d.	n.d.	n.d.	n.d.	n.d.	n.d.	n.d.	n.d.	n.d.	37	n.d.
SHV_P4_PLAG_038_MI1	9.62E-09	1.90E-07	0.05	102.82	1.00	102.97	0.11	2.3	2653	32	2685
SHV_P4_PLAG_040	4.65E-09	1.70E-07	0.03	102.83	1.00	102.98	0.12	2.27	1465	44	1508
SHV_P4_PLAG_041_MI1	1.62E-09	4.49E-08	0.04	102.61	1.00	102.76	0.04	2.24	641	19	660
SHV_P4_PLAG_043_MI1	2.15E-09	6.41E-08	0.03	102.66	1.00	102.81	0.06	2.29	881	n.d.	n.d.
SHV_P4_PLAG_044_MI2	2.70E-09	9.49E-08	0.03	102.64	1.00	102.79	0.05	2.24	670	28	698
SHV_P4_PLAG_045_MI1	1.34E-09	4.00E-08	0.03	102.60	1.00	102.75	0.04	2.26	545	30	575
SHV_P4_PLAG_047_MI2	5.64E-09	1.52E-07	0.04	102.75	1.00	102.90	0.09	2.25	1517	40	1556
SHV_P5_PLAG_002_MI4	1.41E-09	6.92E-08	0.02	102.73	1.00	102.91	0.09	2.23	884	1126	2010

SHV_P5_PLAG_008_MI1	1.14E-09	5.49E-08	0.02	102.70	1.00	102.88	0.08	2.2	804	95	899
SHV_P5_PLAG_009_MI2	3.45E-10	2.10E-08	0.02	102.65	1.00	102.83	0.06	2.2	487	835	1322
SHV_P5_PLAG_016_MI1	5.21E-10	6.36E-08	0.01	102.67	1.00	102.85	0.07	2.18	268	128	396
SHV_P5_PLAG_016_MI3	4.24E-10	4.26E-08	0.01	102.75	1.00	102.93	0.10	2.19	467	147	614
SHV_P5_PLAG_016_MI6	n.d.	n.d.	n.d.	n.d.	n.d.	n.d.	n.d.	n.d.	n.d.	211	n.d.
SHV_P5_PLAG_024_MI2	1.08E-09	2.23E-08	0.05	102.76	1.00	102.94	0.10	2.25	2347	206	2553
SHV_P5_PLAG_025_MI1	5.03E-10	2.87E-08	0.02	102.73	1.00	102.91	0.09	2.29	720	96	816
SHV_P5_PLAG_034_MI2	9.58E-09	3.21E-07	0.03	102.76	1.00	102.94	0.10	2.21	1421	152	1573
SHV_P5_PLAG_037_MI1_B1	2.29E-10	3.54E-08	0.01	102.65	1.00	102.83	0.07	2.21	193	442	823
SHV_P5_PLAG_037_MI1_B2	1.46E-10		0.00	102.75	1.00	102.93	0.10	2.21	188		
SHV_P5_PLAG_042_MI2_B1	8.19E-10	2.76E-08	0.03	102.74	1.00	102.92	0.10	2.25	1327	1243	2627
SHV_P5_PLAG_042_MI2_B2	1.08E-10		0.00	102.56	1.00	102.74	0.03	2.25	57		
SHV_P5_PLAG_043_MI3	3.25E-10	1.59E-08	0.02	102.71	1.00	102.89	0.09	2.23	800	233	1033
Orthopyroxene Hosted											
SHV_P1_OPX_005	n.d.	n.d.	n.d.	n.d.	n.d.	n.d.	n.d.	n.d.	n.d.	83	n.d.
SHV_P1_OPX_008_MI1	no bubble	9.59E-08	-	-	-	-	-	n.d.	0	415	415
SHV_P1_OPX_011_MI2	1.71E-10	4.73E-08	0.01	102.74	1.00	102.97	0.11	2.19	188	394	582
SHV_P1_OPX_013_MI1	7.24E-11	1.30E-08	0.01	102.62	1.00	102.85	0.07	2.18	186	59	244
SHV_P1_OPX_020	4.03E-10	2.61E-07	0.00	102.45	1.00	102.68	0.01	2.19	9	190	199
SHV_P5_OPX_002_MI1	5.37E-09	1.02E-06	0.01	102.87	1.00	103.00	0.12	2.23	294	442	736
SHV_P5_OPX_002_MI2	1.28E-10	5.94E-08	0.00	102.65	1.00	102.77	0.04	2.16	37	172	210
SHV_P5_OPX_006_MI1	9.31E-11	2.90E-08	0.01	102.66	1.00	102.78	0.05	2.19	67	153	220
SHV_P5_OPX_009_MI2	1.20E-10	4.65E-08	0.00	102.77	1.00	102.89	0.09	2.2	102	336	438
SHV_P5_OPX_012_MI1	1.06E-10	2.54E-08	0.01	102.77	1.00	102.83	0.07	2.17	128	237	365
SHV_P5_OPX_013_MI1	1.08E-10	4.37E-08	0.00	102.74	1.00	102.86	0.08	2.19	87	458	545
SHV_P5_OPX_016	1.12E-09	3.91E-07	0.01	102.83	1.00	102.91	0.09	2.2	121	502	624
SHV_P5_OPX_020	1.28E-10	2.32E-08	0.01	102.72	1.00	102.78	0.05	2.19	122	422	544

n.d. - not determined
correct. value from standard fluid inclusions for plagioclase hosted bubbles in Phases 1, 2, 5 and clinopyroxene hosted bubbles in Phase 5 - 0.18
correct. value from standard fluid inclusions for plagioclase hosted bubbles in Phase 4 - 0.15
correct. value from standard fluid inclusions for clinopyroxene hosted bubbles in Phase 1 - 0.23

Supplementary Table 2.S3 – Calculation of CO_2 contribution from the bubble to the total melt inclusion

3 Volatile emissions and magma storage conditions for the 2021 explosive eruption at La Soufrière volcano, St Vincent from melt inclusions

3.1 Abstract

The VEI 4 eruption of La Soufrière volcano underwent a dramatic transition in style from initial lava dome effusion in December 2020 to hazardous explosive activity in April 2021. Understanding the magmatic processes underpinning such transitions is critical. We provide the first comprehensive dataset of the compositions and volatile contents of melt inclusions from the 2021 explosive activity, including the first measurements of pre-eruptive total CO_2 at La Soufrière and estimates of magmatic temperature. We use the petrological method to quantify volatile fluxes to the atmosphere of 2.99 Mt H_2O, 0.14 CO_2, 0.39 Mt SO_2, and 0.18 Mt HCl. Modelling of volatile saturation pressures indicates final magma storage depths of 2.4-8.9 km (mean 6.4 km) throughout four phases of explosive activity after migration of magma in the lower storage region within the transcrustal mush system. Inferred depths are consistent with recorded seismicity and deformation before and during the explosions.

3.2 Introduction

Volatiles are a key component of magmatic systems, influencing magma storage and ascent, mechanisms and the characteristics of volcanic eruptions at the surface (e.g. Cashman and Scheu, 2015), and are also important for their environmental effects, including climate perturbation and impacts of gas and aerosol emissions. Volatiles are exsolved from ascending magmas upon reaching saturation, which can be influenced by pressure, temperature, composition, crystallisation and the solubility of specific volatile species in magmas (Cashman and Mangan, 1994; Johnson et al., 1994; Roggensack et al., 1997; Edmonds and Wallace, 2017; Edmonds and Woods, 2018). The explosive-effusive nature of eruptive activity (e.g. Cassidy et al., 2018), can be influenced by volatiles, with retention of magmatic volatiles favouring violent acceleration and fragmentation of ascending magma, and thus explosive events, whereas in situations where gases can exsolve and physically separate from the magma, effusive activity is mostly favoured.

While large eruptions often release sizeable amounts of volatiles into the atmosphere, ground based measurements of these volatile emissions are often sparse, or unachievable during eruptions, and are supplemented by other techniques such as satellite measurements (e.g. Theys et al., 2019; Queißer et al., 2019; Burton et al., 2021; Cofano et al., 2021). Additionally, quantification of emitted magmatic volatiles can be complicated by the scrubbing effect of hydrothermal systems, where emissions of certain volatile species may be reduced by interactions between magmatic gas and water or rock (e.g. dissolution of SO_2 into water; Symonds et al., 2001) or be lost to the atmosphere. Within this context, there is much value in petrological methods for determining overall volatile budgets of eruptions, which can provide a minimum estimate of the concentrations and flux of volatiles by comparing the pre-eruptive volatile concentrations of magma as recorded by the melt (Moore and Bodnar, 2019) with those of erupted material, taking into account the emitted volume of magma (Devine et al., 1984). The difference indicates the amount of gas released to the environment (both at the surface and subsurface of the Earth).

La Soufrière Volcano (Lindsay et al., 2005; Cole et al., 2019; Robertson et al., 2023) has been one of the most historically active subaerial volcanoes in the Lesser Antilles arc (Wadge, 1984) and is known for displaying both effusive and explosive styles. Like many arc volcanoes capable of producing large explosive eruptions, a considerable population exists in close proximity to the volcano and improved constraints on volatile systematics underpins improved hazard management, and volatile systematic constraints also advances our understanding of global volatile cycles, including carbon exchange between the inner Earth and the atmosphere. The volcanic hazards at St Vincent were evident in the 2020-2021 eruptions, which

involved roughly three months of crater contained lava effusion followed by an abrupt transition to explosive activity on April 9th 2021 (Joseph et al., 2022; Camejo-Harry et al., 2023; Latchman and Aspinall, 2023; Robertson et al., 2023)

A key challenge at St Vincent and at other arc volcanoes worldwide is to understand the physicochemical processes underpinning the transitions in eruptive styles, similar to the 2020-21 La Soufrière eruption, and specifically how they relate to the plumbing system of the volcano and the nature of its unrest. Previous estimates on magma storage pressures and corresponding depths at La Soufrière have been estimated using mineral thermobarometry and experimental petrology (e.g. Melekhova et al., 2015; Fedele et al., 2021; Weber et al., 2023), and whilst valuable, some petrological techniques involve significant uncertainties (Wieser et al., 2023). However, parcels of melt trapped in crystallising minerals (melt inclusions) represent the magma at the time of entrapment/crystallisation and can be used to provide additional constraints on magmatic conditions such as pressure and depth if any subsequent changes during ascent are accounted for, and together with groundmass glass, calculate volatile flux during eruptions.

In this study, we quantify the concentration of major and volatile elements (H_2O, S, Cl and F) in pyroclasts emitted in the April 2021 explosive activity and provide the first measurements of total magmatic CO_2 at La Soufrière volcano. The chemical composition of magma trapped as melt inclusions found in the olivine, plagioclase, orthopyroxene and clinopyroxene phenocrysts of the 2021 explosive activity allows for the reconstruction of magma storage conditions, magma evolution, La Soufrière's pre-eruptive budget, and an estimation of volatile loading into the atmosphere.

3.3 Geological Setting and History of La Soufrière Volcano

3.3.1 Geological Setting

The Lesser Antilles Arc is the surface manifestation of subduction of an oceanic portion of the western Atlantic Plate (North and South American Plates) beneath the eastern boundary of the Caribbean plate, forming an island arc subduction zone (Macdonald et al., 2000; Evain et al., 2013; Melekhova et al., 2019).

The arc is approximately 850 km long and is aligned submeridionally (Christeson et al., 2008; Evainn et al., 2013; Kopp et al., 2011). Geophysical data suggests a convergence rate of ~2cm /year in a 67° ENE trend (DeMets, et al., 2000), which is slow in comparison to other island arcs on Earth such as Java and the Philippines (~8 cm/year). The slow convergence rate of the Lesser Antilles arc leads to relatively low magma production rates (Macdonald et al., 2000), which inexorably leads to a lower tempo of eruptions along the arc. For instance, in the 300-year period from 1680-1980, only three Lesser Antilles volcanoes produced magmatic eruptions (Wadge 1984); these are La Soufrière (St Vincent), Mt Pelee (Martinique) and Kick 'em Jenny.

3.3.2 La Soufrière Volcano

St Vincent is located in the southern section of the Lesser Antilles arc and is situated around latitude 13°15' and longitude -61°10'. The island is made up of Pliocene to Recent lava and pyroclasts of basalt and basaltic andesite composition (Aspinall et al., 1973) which are the products of four stratovolcanoes (Le Friant et al., 2009, Cole et al., 2019). All are extinct except La Soufrière volcano. Based on K-Ar dating, the major centres show progression from south to north over time, with the earliest construction of La Soufrière beginning during the late Pleistocene, around 700 ka (Briden et al., 1979). Presently, La Soufrière Volcano (Figure 3.1) is a 1220 m high stratovolcano whose base extends outwards to 11km (Aspinall et al., 1973; Shepherd et al., 1979) and is one of the twenty-one potentially active volcanoes in the Lesser Antilles Arc (Lindsay et al., 2005).

Over the last 600 years, La Soufrière has experienced at least 7 explosive eruptions, along with 6 possible effusive eruptions (Shepard et al., 1979; Cole et al., 2019). These have either been effusive only, generally associated with no pre- or syn-eruptive seismicity, lower magma effusion rate and lower volume of erupted material, producing lava domes, explosive only, associated with high explosivity, strong earthquakes, high magma production rate and large volumes of ejecta, or transitional eruptions where the eruption style changes from effusive to explosive or vice versa (Aspinall et al., 1973; Lindsay et al., 2005; Le Friant et al., 2009). At La Soufrière, there have only been two recorded instances of transitional eruptions – the explosive to effusive eruption of 1979 and the effusive to explosive 2020–2021 eruption. Over the 600-year period, the repose period between explosive events has spanned 140 and 77 years, and decreased with each event (Cole et al., 2019). The repose period between the two most recent eruptions in 1979 and 2020-2021 is 41 years, a continuation of this shortening trend of repose periods between eruptions observed at the La Soufrière volcano.

3.3.2.1 27th December 2020 – 22nd April 2021 Eruption

The 2020-2021 eruption of La Soufrière is extensively described in Joseph et al., (2022) and Robertson et al., (2023); however, a brief overview is provided here for context.

Pre-Explosive Activity

On 27th December 2020, satellite observations noted a hotspot in the La Soufrière crater, as a new dome began to grow adjacent to the 1979 dome (Joseph et al., 2022). The formation of the dome spanned 103 days, emplacing 16-19 million m^3 (Dualeh et al., 2023; Stinton et al., 2023) of basaltic andesite (Joseph et al., 2023). Notably, the first 13 days of dome emplacement were aseismic, suggesting unobstructed flow of degassed magma to the surface (Latchman and Aspinall, 2023).

Deformation monitoring conducted at La Soufrière showed two distinct phases of pre-eruptive deformation occurred (Camejo-Harry et al., 2023). The first is a deep source of inflation (~18 km depth) beginning 1st July 2020, and continuing into the effusive phase, ending in March 2021, recorded by the Global Positioning System (GPS) network. The second, occurring between 19th – 31st December 2020, a shallow source of inflation recorded by Interferometric Synthetic Aperture Radar (InSAR), was modelled to be an intrusive dike at depths of about 700-600 m (Joseph et al., 2022; Camejo-Harry et al., 2023).

Volatile concentrations (H_2O, CO_2, SO_2 and H_2S) in the plume were measured using Multi-component Gas Analyser System (MultiGAS) and Differential Optical Absorption Spectroscopy (DOAS) UV spectrometers measured SO_2 fluxes. The first gas measurements post-dome emplacement taken in January 2021 revealed no detectable SO_2 in the plume, and on 1st February, the first signal of SO_2 was detected by the MultiGAS (Joseph et al., 2022). Throughout the effusive phase, the ratios were indicative of deep magmatic and deep hydrothermal degassing (>10km; based on their occupied positions in a ternary diagram of SO_2*3-CO_2/2-H_2S*5; Joseph et al., 2022), except for one measurement taken on 23rd March, which indicates hydrothermal degassing, together with an increase in CO_2. Remote sensing carried out using the UV spectrometer to detect SO_2 in the plume was done in January, February and March, and no SO_2 was detected (Joseph et al., 2022). The change in the degassing signal from deep magmatic and deep hydrothermal to hydrothermal degassing was also marked by a swarm of volcano-tectonic (VT) earthquakes occurred at depths <5 km on 23rd – 24th March, followed by a second swarm during 5th-6th April occurring at ~10 km depth. The swarm of deeper VTs was inferred to accompany pathway opening for a new batch of ascending magma (Joseph et al., 2022). Beginning on 8th April 2021, banded tremor (bursts of seismic activity lasting hours) for an interval of ~2.5 hours with increasing magnitude was recorded, consisting of multiple VT events. This progressed into continuous tremor with increasing amplitude (Joseph et al., 2022).

The first detection of SO_2 in the plume occurred on 8th April 2021 by DOAS and also by the TROPOspheric Monitoring Instrument (TROPOMI) on board the Sentinel-5 Earth observation satellite (Joseph et al., 2022; Esse et al., 2023) and roughly coincided with the emergence of banded tremor. The total mass of SO_2 measured on that day was 80 (±) 6 tonnes/day measured via ground-based traverses with a UV spectrometer (Joseph et al., 2022) or 121 (±) 86 tonnes/day as measured via TROPOMI (Esse et al., 2023).

Explosive Eruptions

On 9th April 2021, the eruption style of La Soufrière transitioned from lava effusion to a series of near continuous sub-Plinian activity that lasted until 10th April (Joseph et al., 2022). Toward the end of 10th April, the style changed to discrete Vulcanian explosions, with increasing inter-explosive intervals, and a general decrease in both intensity and magma discharge rate, culminating on 22nd April, 2021 (Esse et al., 2023; Sparks et al., 2023). The transition in style from dome growth to explosions coincided with a rapid

deflation of the volcano, modelled as the migration of ~50 x 10^6 m^3 of magma, from a storage region at ~6 km depth (Camejo-Harry et al., 2023). During the explosive phase, SO_2 emissions measured by TROPOMI were as high as 56 × 10^4 tonnes/day on 9th April (Esse et al., 2023), and as low as 331 tonnes/day as measured on 22nd April using DOAS (Joseph et al., 2022). Following the cessation of explosive activity on 22nd April 2021, seismicity decreased from an average of 354 events/day, to 24 events/day in early May 2021. Between May and November 2021, seismicity remained sparse (Joseph et al., 2022).

3.4 Methods and Materials

3.4.1 Sample Characteristics

The samples were collected from around La Soufrière during two field campaigns in January and May 2022 by Paul Cole, and are characterised as vesicular scoria 1-3 cm in diameter produced via Vulcanian and sub-Plinian eruptions from 9th–11th April 2021. The locations of sample collection and a brief description of each unit are outlined in Table 3.1 and Figure 3.1. During the explosive phase, seven stratigraphic units of material were produced in the form of ash, lapilli and scoria, which are described extensively in Cole et al., (2023). Of the seven units, only units 1, 2, 3 and 5 contained scoria and are the focus of this study. Clast size in unit 4 was too fine to permit sample preparation. Melt inclusions in the samples from the effusive phase (lava dome) were crystallised and were therefore not suitable for the methods employed (Raman spectroscopy, SIMS, EPMA as outlined below) in order to determine the chemical composition (major and volatile elements) of phenocryst-hosted melt inclusions. Studying the uncrystallised inclusions in the scoria samples from units 1-3, and 5 which all had typical scoria characteristics, allows for reconstruction of the melt at depth such as its pre-eruptive volatile concentrations, and thus sheds light on magma storage conditions such as pressure and temperature.

La Soufrière melt inclusions are hosted in olivine, plagioclase, orthopyroxene and clinopyroxene phenocrysts, which generally range from 2500 to 1000 µm along their longest axes. Plagioclase represents the greatest fraction of the phenocryst assemblage and crystals are typically euhedral, with lesser amounts of euhedral pyroxenes and subhedral olivine crystals. Phenocrysts appear as individual crystals, with small clusters and larger glomerocrysts present. Overall, the petrology of the samples studied is similar to scoria and dome samples from previous studies of the 2020-2021 eruption (e.g. Frey et al., 2023; Weber et al., 2023).

Sample Specifications				Characteristics of Unit
Unit	**Duration/Time (UTC)**	**Sample**	**Distance to vent (km)**	
Unit 1	1241 April 9th – 0724 April 10th	LS21-99a	2.0	• Basal deposit • Plume heights of 13 – 16 km • 3.3 x 10^{10} kg of material ejected at maximum rate of 830 m^3 s^{-1} • Formation of 2021 crater
		LS21-97	6.2	
		LS21-76	1.3	
Unit 2	0935 – 1620 10th April	LS21-89	1.6	• Plume heights 13 – 16 km • 3.1 x 10^{10} kg of material ejected at maximum rate of ~400 m^3 s^{-1} • Ash rich with 7 lapilli layers
		LS21-98	6.2	
Unit 3	1830 – 2120 10th April	LS21-83	1.6	• Plume heights up to 16 km • First occurrence of PDC activity • Magma ejection rate of 200 – 300 m^3 s^{-1}
		LS21-87	1.6	
Unit 5	0051 – 0755 11th April	LS21-96	4.6	• Final scoria bearing unit • Plume heights up to 16 km • Magma discharge rate – 100 – 200 m^3 s^{-1}

Table 3.1 - Sample details including time of formation of individual units deposited, along with brief characteristics. Compiled from Cole et al., (2023); Esse et al., (2023); Sparks et al., (2023).

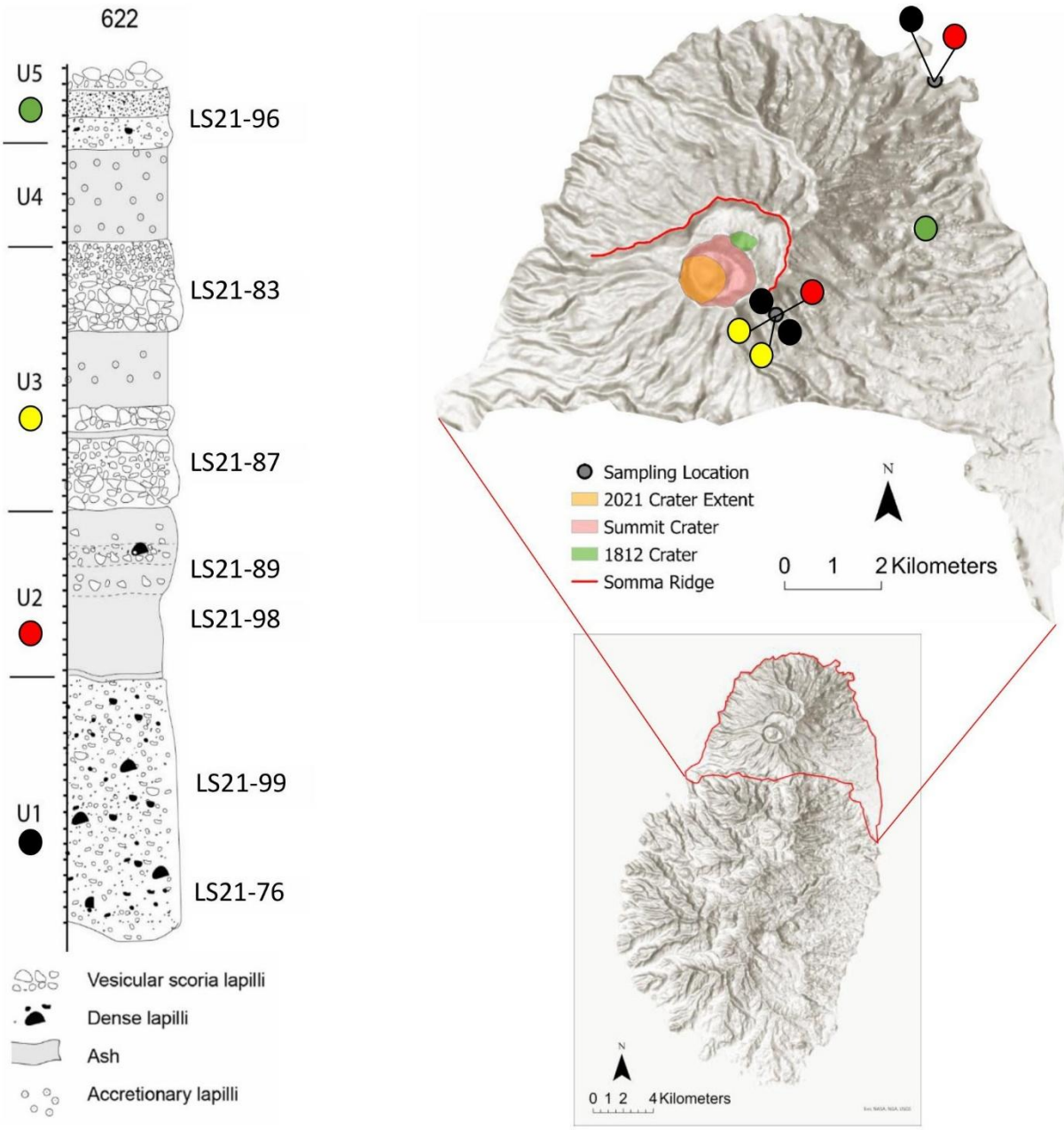

Figure 3.1 – Stratigraphic column showing units 1 to 5 and samples used for analysis, and map of the La Soufrière edifice with sampling locations. Stratigraphic column from Cole et al., (2023).

3.4.2 Sample Preparation

Scoria clasts from each unit were prepared for Raman spectroscopy, SIMS and EPMA by separating and crushing clasts using a mortar and pestle and sieved into different sized fractions. Olivine, plagioclase, orthopyroxene and clinopyroxene crystals were then hand-picked from the 250-500 µm and 500-1000 µm fractions under a binocular microscope. Crystals were individually mounted on glass slides using Crystalbond 509 resin, lightly polished and inspected for non-crystallised melt inclusions (MI). Crystals containing appropriate melt inclusions were then polished using 2400 grade SiC paper and 3 and 1 µm aluminium oxide lapping paper, bringing the inclusion close to the surface (~20 µm) without exposing it, in order to avoid compromising the bubble for Raman analysis. Along their longest axes, inclusions ranged in size from 6 to 150 µm.

Melt inclusions (Figure 3.2) were glassy, with some, especially those hosted in pyroxenes, containing trapped pre-existing crystals such as iron oxides and/or daughter crystals grown from the melt after entrapment, and these latter inclusions were not used in this study. Of 339 prepared melt inclusions, all but three contained bubbles. The 336 melt inclusions with bubbles occurred in three groups, as shown in Figure 3.2: (i) bubbles occupying <10% of the inclusion (76% of the population), (ii) bubbles occupying 10-60% of the inclusions (20% of the measured population), and (iii) multiple bubbles occupying a single inclusion (3% of the population). Inclusions hosted in olivine and pyroxene crystals displayed ellipsoidal shapes, whereas plagioclase hosted inclusions were predominantly cuboidal.

Following Raman spectroscopy, thirty-nine melt inclusions >25 µm (large enough to be analysed by SIMS) were polished further with 3 and 1 µm aluminium oxide paper, exposing the inclusion at the surface in order to measure the volatile elements CO_2, H_2O, S, Cl and F, and major elements in the glass by SIMS and EPMA. Samples were then removed from the glass slide and washed in an acetone bath to dissolve remaining resin.

Ahead of SIMS analysis, they were mounted in indium, oven-dried at 70°C, gold coated and equilibrated in the SIMS vacuum. Following SIMS analysis, the gold coating was removed with light polishing using a 0.25 µm diamond polishing pad and samples were carbon coated in preparation for EPMA.

Thirty-five additional inclusions between 10-25 µm were prepared for EPMA by polishing with 3 and 1 µm paper to expose the inclusion at the surface, removed from the glass slide and washed in an

acetone bath. They were then embedded in a non-acetone soluble resin, placed in a 1-inch brass or aluminium holder and carbon coated in preparation for analysis.

Thin sections of scoria from each unit were also created and were carbon coated (i) for EPMA in order to measure major and volatile (S, Cl, F) elements of the groundmass glass, and (ii) for SEM-EDX analysis of plagioclase compositions.

Five samples representative of the four scoria bearing units along with dense clasts of Unit 5 were crushed and sieved into the 100 μm size, until 100 mg of powder was obtained, in preparation for ICP-OES.

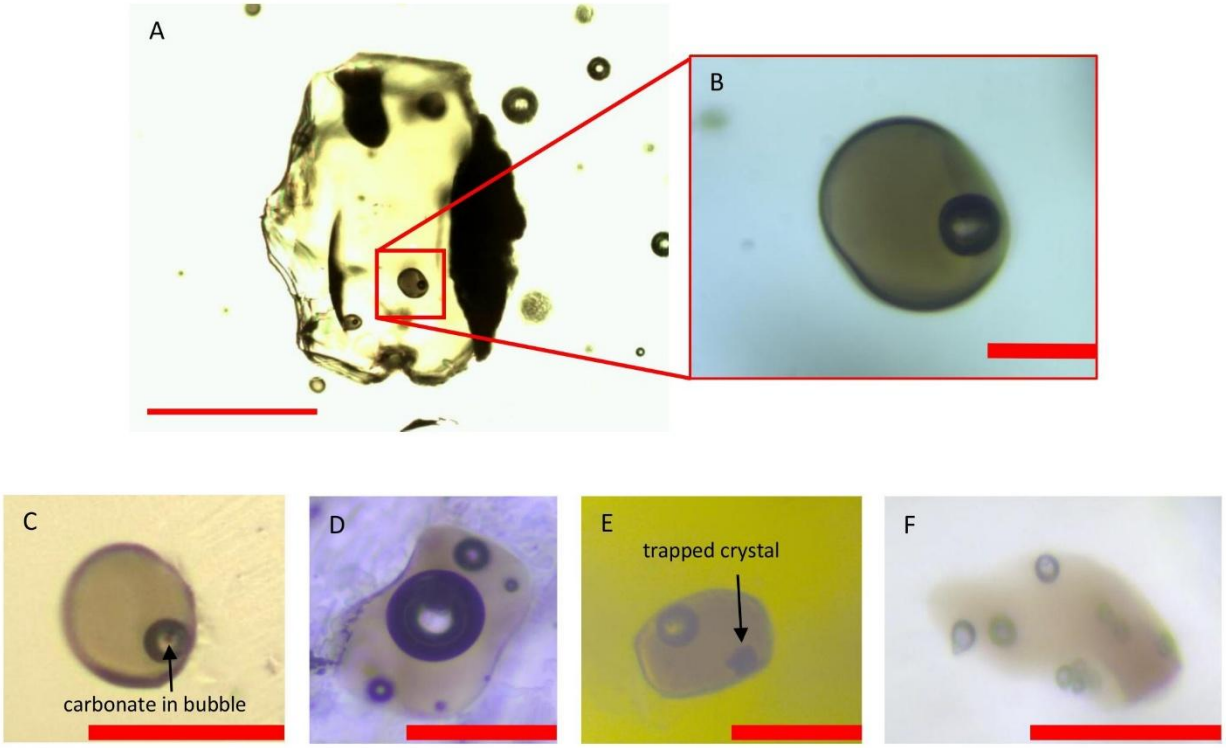

Figure 3.2 – Types of melt inclusions found in La Soufrière explosive products. [A] LSS_U3_OL_001 shows an olivine phenocryst hosting melt inclusions. [B] An ideal melt inclusion for this study based with bubble, crystal free glass, and large enough to accommodate SIMS and EPMA analysis. [C] LSS_U3_OL_001 - example of an inclusion with carbonate crystals in the bubble. [D] LSS_U2_PLAG_003_MI4 - example of an inclusion with large bubble >10% of inclusion volume along with multiple smaller bubbles. Due to high bubble volume ratio and irregularity in the glass, this is not ideal for analysis. [E] LSS_U1_CPX_010 is an example of an inclusion with a trapped crystal making it unsuitable for analysis. [F] LSS_U5_OL_025 is an example of an inclusion with multiple bubbles. Scale bar on [A] represents 200 µm. Scale bars on [B], [C], [D], [F] represent 50 µm. Scale bar on [E] represents 15 µm.

3.4.3 Analytical Techniques

3.4.3.1 Raman Spectroscopy

Raman spectra of individual bubbles were collected using a Renishaw inVia confocal Raman micro-spectrometer at Laboratoire Magmas et Volcans (LMV), Clermont-Ferrand, France. The instrument was equipped with a 532.1 ±0.3 nm diode-pulsed solid-state laser delivering ~150 mW power to the sample, a Rayleigh rejection edge filter (cut-off at about 50 cm^{-1}), a CCD detector of 1040 x 256 pixels, a slit aperture of 20 µm (high confocality setting) and 2400 l/mm diffraction grating. The spectrometer uses a Leica DM 2500M optical microscope to focus on the sample; ×50 or ×100 microscope objectives were used, depending on the size of the bubble. These conditions result in a spectral resolution better than 0.4 cm^{-1}, and spatial resolutions of few µm. This was paired with 10% laser power, so as to not damage bubbles close to the surface, allowing for repeat, or further measurements. A higher laser power of 50% was used on occasion in an attempt to increase the Raman signal where necessary.

Each spectrum was collected in the 725-1880 cm^{-1} wavenumber range during 120 seconds of acquisition time (3 acquisitions of 40s), using the WiRE™ 4.4 software, allowing for CO_2, which has two peaks at ~1285 and ~1388 cm^{-1}, dubbed the Fermi diad doublet, to be visible along with the peaks of the host phases. Identification of potential mineral phases, such as carbonates or sulphates, in bubbles required analysis in the 60 – 1320 cm^{-1} window. In a random selection of samples, an extended range was taken from 2400 to 4000 cm^{-1} in order to identify the presence of other liquid/gas species such as H_2S and HS^- (2550 – 2610 cm^{-1}) and H_2O at 2800 – 3900 cm^{-1}.

The 520.5 cm^{-1} peak of Si and two neon emission bands (568.982 and 576.442 nm) were used to perform the spectrometer alignment and to calibrate peak positions. Neon bands were measured prior to and after each acquisition, and the distance between the two emission lines (bracketing the Fermi diad) was used to calibrate the splitting of the Fermi diad. During the post-processing of the Raman spectra, a correction factor ($^{real}\Delta_{Ne}/^{measured}\Delta_{Ne}$) between 0.9990 and 1.0006 was applied to each measurement. To quantify CO_2 concentration in the bubbles, fluid inclusions standards of pure CO_2 of known densities were analysed three times during each analytical session. Uncertainties associated with the reproducibility of the measurement determined on standards are <0.04 g/cc. The errors associated with the measurement

of CO_2 density in the studied bubbles are reported in Supplementary Table 3.S4 and become relatively larger as CO_2 density decreases, mainly due to the greater uncertainty in the fitting of weak Raman peaks.

To calculate the concentration of vapour CO_2 sequestered to the bubble using mass balance equations, the volume fraction occupied by the bubble in the melt inclusion and the density of the CO_2 vapour must be known. Volumes of both the bubble and the total inclusion were estimated using photomicrographs of the polished surface, assuming a spherical shape for the bubble, an ellipsoid for the melt inclusions hosted in olivine and pyroxene phenocrysts and a cuboid for plagioclase hosted inclusions, based on their 2D shapes. The x and y axes of melt inclusions were measured using a Leica DM4500 P LED microscope with Leica Application Suite software, with 0.2-micron uncertainty. The third unseen axis was calculated using the arithmetic mean of the x- and y-axis, which introduces a 5% error (with 1σ errors of -48 to 37%) on the calculation (Tucker et al., 2019). In order to calculate the density of CO_2 in bubbles (ρ_{CO_2}), each Raman spectrum was first processed using WiRE™ 4.4 spectral analysis program. Polynominal baselines were applied to spectra, which were truncated at 1200 and 1500 cm^{-1} to focus on the area known to contain the Fermi diad, and the peaks were fitted with a mixed Gaussian-Lorentzian curves. The centre of each peak was identified and the Fermi diad (Δ) calculated by subtracting their wavenumbers. The densimeter of Lamadrid et al., (2017) was used to calculate CO_2 density, as the instrument used does not have a specifically calibrated densimetry curve. The relationship between the Fermi diad (Δ) and CO_2 density (ρCO_2) is given by Equation 3.1:

$$\rho_{CO_2} = -39.737 + (0.387 * \Delta) \quad 3.1$$

Fermi diad peaks with low intensity (<500 counts) or with asymmetrical peaks that evade ready curve-fitting could not be fitted with curves and thus could not be used to quantify ρ_{CO_2}, but were noted as they indicate a bubble containing a low density of CO_2.

The CO_2 contribution from the bubble can therefore be calculated by the ratio of the relationship between volume and density in the bubble and in the glass using Equation 3.2:

$$[CO_2]_{bubble} = \frac{\rho_{CO2} V_{bubble}}{\rho_{glass} V_{glass}} \quad 3.2$$

where $[CO_2]_{bubble}$ is the amount that the concentration of CO_2 in the total inclusion will increase by once any CO_2 in the bubble is accounted for, bubble and glass volumes are as described above, and glass density is quantified with the DensityX model (Iacovino and Till, 2019). Total CO_2 of the melt inclusion is therefore the sum of the corresponding amount of CO_2 in the bubble and that in the glass.

H_2O and sulphur or carbon bearing species in the bubble identified by their Raman vibrations could not be quantified due to a lack of appropriate standards.

3.4.3.2 Secondary Ion Mass Spectrometry (SIMS)

SIMS analysis was carried out prior to EPMA in order to (i) avoid the contamination of C from the carbon coat necessary for EPMA, which makes the surface conductive and (ii) avoid beam damage in (especially hydrous) glasses due to EPMA which can cause the migration of mobile elements such as Na, K and H, and can also cause an increase in measured concentrations of immobile elements such as Si and Al (Humphreys et al., 2006; Rose-Koga et al., 2021).

The H_2O and CO_2 concentrations in 46 melt inclusion glasses were measured at both the Natural Environment Research Council (NERC) Ion Micro-Probe Facility, University of Edinburgh, Scotland and at the Centre de Recherches Pétrographiques et Géochimiques (CRPG), Nancy, France.

The H_2O and CO_2 concentrations of melt inclusion glass from Unit 5 were measured at the NERC facility using a Cameca IMS 7f-GEO equipped with a 5 nA $^{16}O^-$ primary beam. Pressure in the chamber was 3.30 x 10^{-8} mbar. Samples were pre-sputtered for 180 seconds over an area of 20 x 20 µm for the removal of surface impurities before analysis. The isotopes of $^{24}Mg^{2+}$, ^{26}Mg, and ^{30}Si were analysed with a counting time of 2 seconds, whilst ^{1}H had a counting time of 3 seconds and ^{12}C of 10 seconds, over 10 cycles using an electron multiplier. A mass resolving power of 1200 was used in order to separate the mass interferences of $^{24}Mg^{2+}$ and ^{12}C. Background concentrations of ^{12}C and ^{1}H were measured using host phenocrysts and were subtracted from all analyses before final concentration calculations. H_2O and CO_2 concentrations were calculated using the calibration curves (Supplementary Figure 3.S1, Supplementary

Material C3) of $^{1}H/^{30}Si$ vs H_2O and $(^{12}C/^{30}Si)*SiO_2$ vs CO_2 for a set of known basaltic and rhyolitic glasses analysed under the exact conditions of melt inclusion analysis, and SiO_2 is determined by EPMA subsequent to SIMS. The reproducibility of the standards amounted to 10% for H_2O which has a detection limit of 0.01 wt.%, and 10% for CO_2 which has a detection limit of 60ppm.

At the CRPG facility, H_2O and CO_2 were measured in melt inclusion glasses from Units 1 – 3 using a Cameca IMS 1280 HR2 instrument which utilises a 10 kV Cs^+ primary beam with a current of 1 nA, coupled with an electron gun for charge compensation. H_2O and CO_2 were measured using a mass resolving power of ~7000 to separate mass interferences. Prior to analysis, an area of 15 x 15 µm was pre-sputtered for 300 seconds. Pressure in the chamber ranged from 1.1 x 10^8 to 1.0 x 10^8 mb over the analytical session. Background concentrations were measured using San Carlos olivine and were subtracted from all analyse prior to final concentration calculations. CO_2 concentrations were calculated using calibration curves of CO_2/SiO_2 vs $^{12}C/^{30}Si$ for several basalt, andesite and dacite standards. Repeat analyses indicates a 2σ standard deviation dependent on CO_2 content. Reproducibility on standards with low CO_2 (~5 ppm) is <53%, while standards with higher CO_2 contents (hundreds to thousands of ppm) have a reproducibility of 20%, and the detection limit is 33 ppm. H_2O was calculated using the weighted mean of the two calibration curves of H_2O vs $(^{16}O^{1}H/^{30}Si)*SiO_2$ produced by basaltic and rhyolitic glass standards, as a function of SiO_2. The reproducibility on the set of used standards is 5%, and the detection limit is 0.006 wt.%.

To be able to compare H_2O and CO_2 measured in different labs, values are compared to M40, an international standard of known composition used by both labs during the analytical sessions. The difference in H_2O for measurements of M40 at CRPG vs the known concentration amounts to 6%, while the difference for NERC vs M40 is 1%. The difference in H_2O for standard M40 measured at CRPG vs NERC is 7%. For CO_2, the difference between CRPG vs M40 is 6%, while NERC vs M40 is 3%, which validates the coherence between our analyses in both laboratories. The difference between CO_2 values measured for M40 at CRPG vs NERC is 3%. As the differences are <10%, H_2O and CO_2 from units 1-3 and unit 5 are directly comparable.

3.4.3.3 Electron Probe Microanalysis (EPMA)

The major element composition of crystals hosting melt inclusions, plus major and volatile (S, Cl, F) element compositions of the inclusion glasses were measured using a Cameca SX-100 electron microprobe at the Laboratoire Magmas et Volcans, Clermont-Ferrand, France, with 15kV accelerating voltage. The conditions applied when measuring melt inclusion glasses consisted of a beam current of 4nA for major elements or 40 nA for volatile elements, paired with a defocused beam of 10 µm. In inclusions with limited glass surface area, a focused beam of 1 µm was applied. Two to three spot measurements per inclusion were taken in order to improve analytical precision in the minority of sufficiently large inclusions. Detection limits for volatiles are 40 ppm for S, 49 ppm for Cl and 200 ppm for F. The compositions of olivine, plagioclase, orthopyroxene and clinopyroxene phenocrysts were measured using a 15nA beam current and focused beam pair. Additional information on standards used for calibration are given in Tables S1 and S2, Supplementary Material 'C3'. The 2σ uncertainty for major elements based on known standards is <5% for SiO_2, Al_2O_3, FeO and CaO, <10% for TiO_2 and MgO, 11% for Na_2O and 20% for K_2O. The 2σ uncertainty for volatile element compositions based on repeat measurements on the inclusion was 35% for S, 6% for Cl and 44-61% for F based on the F content.

3.4.3.4 Inductively Coupled Plasma Optical Emission Spectrometry (ICP-OES)

The major elements of whole rock samples from U1, U2, U3 and U5 were determined using an Agilent 5800 ICP-OES instrument at the Laboratoire Magmas et Volcans, Clermont-Ferrand France.

100 mg of each sample was melted together with three times the amount of $LiBO_2$ in an induction furnace at 1100°C for five minutes, after which, the melted product was dissolved in 1 M HNO_3, until a final volume of 200 ml was achieved. Standards used for reference are GH for Si, Na and K, and BR for Al, Ti, Fe, Mn, Mg, Ca and P, provided by CRPG, Nancy, France, and uncertainty is not greater than 10% (2σ).

3.4.3.5 SEM-EDX

In addition to EPMA spot analyses of phenocrysts hosting melt inclusions, line traverses of the major element compositions of the plagioclase hosts were measured via a JSM-7800F Scanning Electron Microscope (SEM) fitted with an energy-dispersive X-ray spectrometer (EDX), using 15 kV accelerating voltage at Lancaster University, UK in order to establish zoning patterns by calculating anorthite contents across the entire crystal.

3.5 Results

3.5.1 Whole rock composition

Scoria produced in the 2021 explosive eruption are basaltic andesite in composition with 53.64 – 54.81wt% SiO_2 (Table S3, Supplementary Material 1), comparable to analyses of Joseph et al., 2022. They overlap with historical and pre-historical eruptions, although whole rock analyses from the suite of historical and pre-historical eruptions spanned a wider compositional field (Figure 3.3; from Graham and Thirlwall, (1981); Heath et al., (1998); Cole et al., (2019); Fedele et al., (2021).

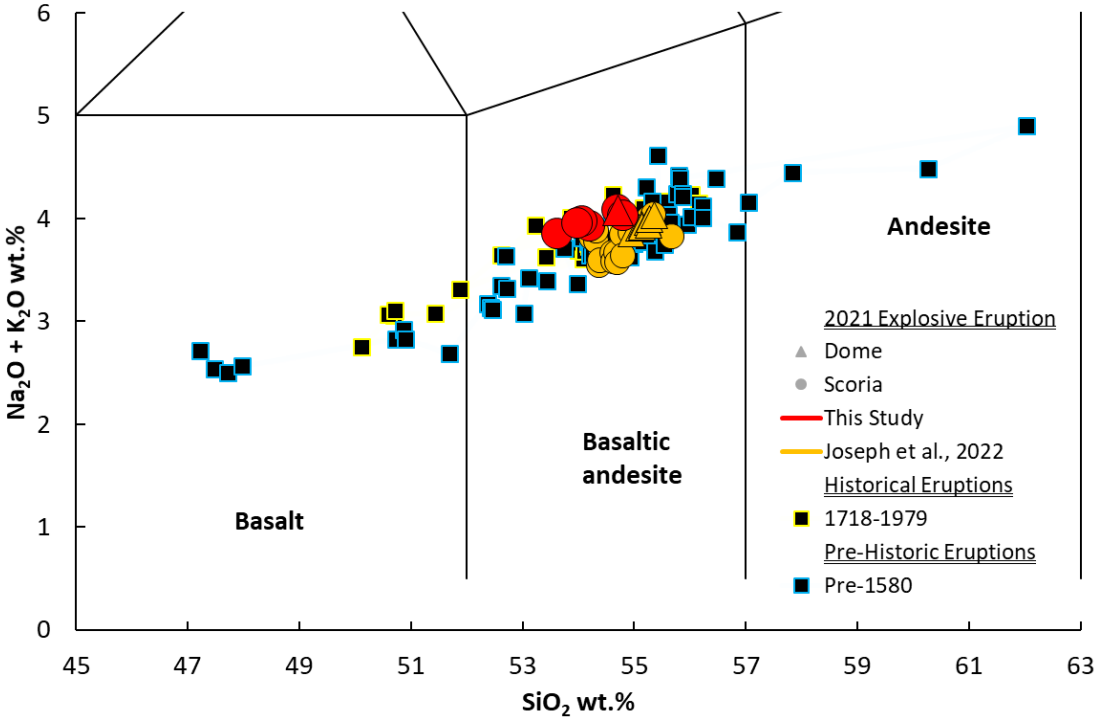

Figure 3.3 – Total Alkali vs Silica (TAS; Le Bas et al., 1986) plot showing the basaltic andesite composition of the 2020-2021 whole rock products in comparison to historic and pre-historic compositions compiled from Graham and Thirwall, (1981); Heath et al., (1998); Cole et al., (2019); Fedele et al., (2021).

3.5.2 Melt inclusion host compositions and texture

The compositions of the olivine hosts range from Fo_{65-76}, indicating evolved crystals, similar to the 1979 (Fo_{64-77}) and pre-historic eruptions (Fo_{55-85}) of La Soufrière (Graham and Thirwall, 1981; Heath et al., 1998). There is no significant difference between the forsterite (Fo) contents of olivines in different units. Olivine Fo contents have a general negative correlation with melt inclusion SiO_2 compositions, indicating that they are phenocrysts of the carrier melt, except for two crystals which have higher SiO_2 contents than the established trend, at given Fo contents of Fo_{73} and Fo_{75}, indicating that these may be antecrysts (Supplementary Figure 3.S2 in Supplementary Material C3). Within the olivine population exists two groups – the first being Fo_{72-76}, accounting for 79% of analysed phenocrysts, and the second group being Fo_{65-69}, accounting for 21% of the population (Supplementary Figure 3.S2 in Supplementary Material C3). Twenty-four of twenty-eight crystals are in equilibrium with the whole rock total K_D range = 0.25–0.43; K_D is described in the following section), whilst none are in equilibrium with the groundmass glass (total K_D range = 0.07–0.16) which has an average composition (Frey et al., 2023) equivalent to rhyolite. In comparison, olivine phenocrysts display <5 µm wide rims of different Fe contents than the cores (Frey et al., 2023).

Plagioclase compositions are similar across units 1–3, with anorthite (An) contents ranging from An_{65-95}. There are no plagioclase compositions available for unit 5. They comprise of normally zoned crystals with high anorthite cores ($An_{>80}$), becoming less calcic towards the rim, down to An_{60} (Figure 3.4). Oscillatory zoning on the spatial scale of tens of microns is also present and occurs in mostly normally zoned crystals that can be either high or low An (65–75). Eight of ten melt inclusions measured for volatiles were located in high An zones, with no difference observed in volatile content based on melt inclusions local An content. Eleven of nineteen plagioclase hosts are in equilibrium with the whole rock, with a total K_D range of 0.03–0.44, and five of nineteen are in equilibrium with the groundmass glass based on K_D for temperatures <1050 °C.

Two pyroxene groups exists in the La Soufrière explosive products, each having very restricted enstatite (En) ranges. Orthopyroxenes are En_{63-67} and clinopyroxenes En_{41-43}. 25% of orthopyroxenes are equilibrium with the whole rock, having a total K_D range of 0.30 – 0.43. Clinopyroxenes, however, are all in equilibrium with the whole rock, having K_D between 0.24 and 0.34. This is comparable to textural equilibrium shown by sharp euhedral edges in unzoned ortho- and clinopyroxenes (Frey et al., 2023). Neither pyroxene group

are in equilibrium with the groundmass at K_D 0.11-0.17 for orthopyroxene and 0.07-0.13 for clinopyroxene. Orthopyroxenes have Mg# [$(Mg/Mg+Fe^{2+})*100$ moles] of 65 – 72, whilst clinopyroxenes Mg# are 71 – 76.

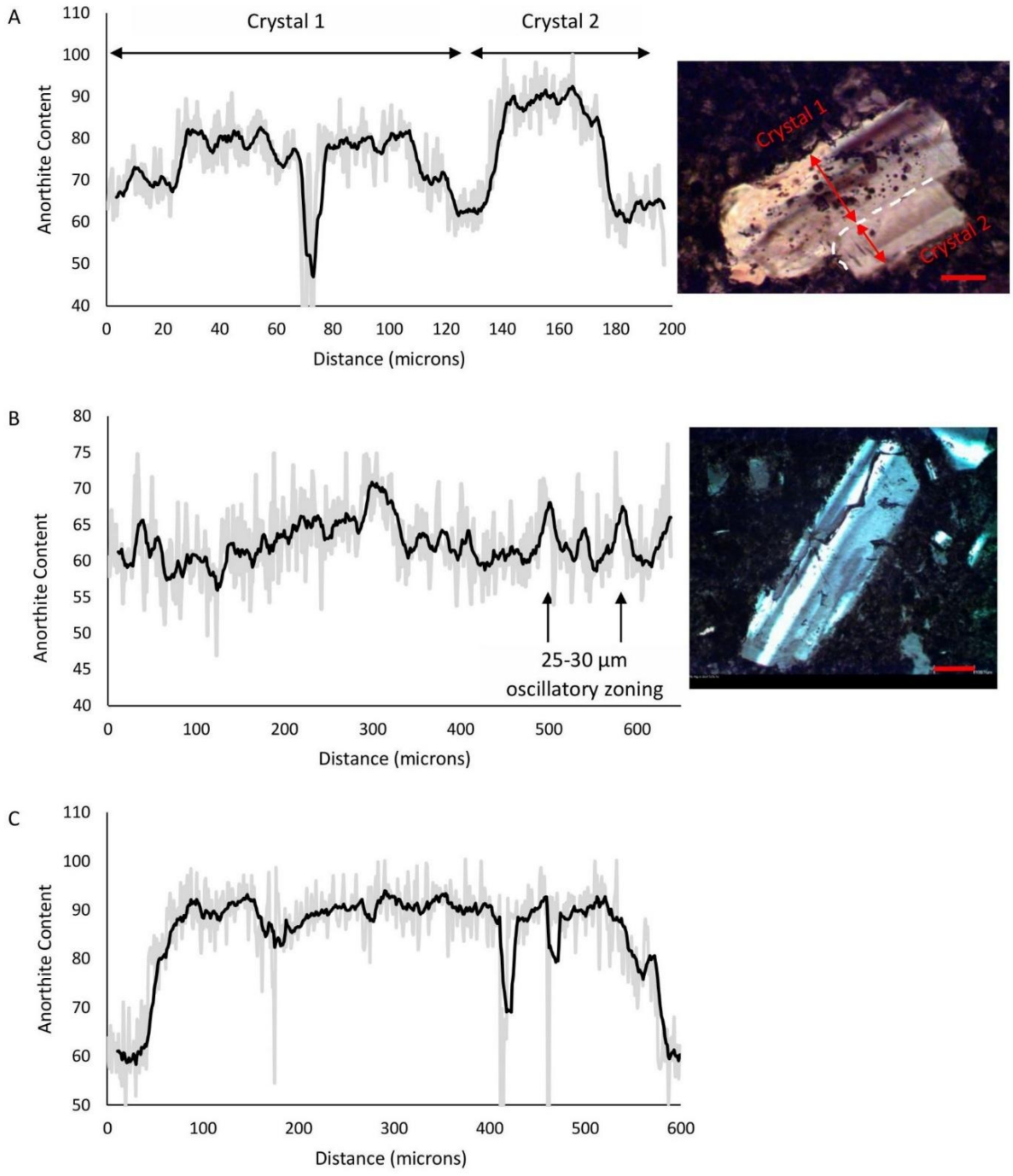

Figure 3.4 – Zoning profiles of plagioclase phenocrysts found in La Soufrière explosive products. [A] Example of normal zoning of a group of two plagioclase crystals with melt inclusions in the core and rim of Crystal 1 found in thin section. [B] Example of overall weakly normal zoning together with oscillatory zoning on the scale of 10s of microns found in thin section. [C] Example of normal zoning with high

anorthite core and low anorthite rims from LSS_U1_PLAG_006 which was analysed for volatiles by SIMS. Scale bars represent 100 µm.

3.5.3 Melt inclusion compositions

3.5.3.1 Post-entrapment modification and reconstruction

Melt inclusions that have undergone post-entrapment modification follow a separate evolution line to their parent magma outside of the host crystal. This includes diffusion of water into or out of inclusions (Gaetani et al., 2012), post-entrapment crystallisation (PEC; Kent, 2008), diffusion of major elements compatible to the host (Kent, 2008), volatile loss due to decrepitation (Neave et al., 2017; Maclennan, 2017), growth of crystals from the inclusion melt before quenching, or the formation of vapour bubbles (Steele-Macinnis et al., 2011; Moore and Bodnar, 2019). These processes can change the original composition of the melt, in both major/minor elements and volatile species. Therefore, assessment of the degree of modification is required prior to using the data in models.

Post-Entrapment Crystallisation

The extent of post-entrapment modification of olivine-hosted melt inclusions was assessed by calculating equilibrium between each olivine-melt pair using the $K_{D}{}^{Fe-Mg}_{ol-liq}$ model of Toplis (2005), which considers pressure, temperature, and olivine and liquid compositions. At La Soufrière, olivine-liquid pairs are in equilibrium at K_D = 0.33±0.02. Further testing for Fe/Mg diffusion showed Fe loss in some inclusions when compared to the La Soufrière whole rock and groundmass glass liquid line of descent (Graham & Thirlwall, 1981; Heath et al., 1998, Cole et al., 2019; Fedele et al. 2019). If inclusion-host pairs are in equilibrium, this indicates that the inclusion has experienced little to no PEC, and the measured glass composition represents that at entrapment (Putirka, 2008). $K_{D\,ol-liq}$ for this suite of La Soufrière melt inclusions ranges from 0.13-0.30, indicating PEC, with some inclusions experiencing Fe loss, as FeO contents are ~2wt.% lower than the liquid line of descent (Supplementary Figure 3.S3, Supplementary Material C3).

All olivine-hosted melt inclusions were therefore corrected for both post-entrapment crystallisation/melting and Fe-Mg exchange using MiMiC (Rasmussen et al., 2022) by incrementally adding

or subtracting olivine from the inclusion until equilibrium is achieved at an initial FeO dictated by the liquid line of descent (LLD). FeO and Fe_2O_3 are calculated using Fe^{3+}/Fe_{total} of 0.4, based on a plausible fO_2 of NNO +1.4 (Bouvier et al., 2008). PEC required the addition of 0.60–6.79 wt.% olivine to achieve equilibrium, while post-entrapment melting required the subtraction of 0.28–3.92 wt.% olivine. Corrected compositions are presented in Supplementary Table 3.S5 and Supplementary Table 3.S6, Supplementary Material 'C3'.

Assessment of equilibrium between orthopyroxene-liquid pairs, which is obtained at $K_D{}^{Fe-Mg}_{px-liq} = 0.29 \pm 0.06$ (Putirka, 2008), was carried out using Fe-Mg ratios between host and inclusion. While Fe-Mg exchange can occur in pyroxene-melt pairs, diffusion through pyroxene crystals is slower than that of olivine (Müller et al., 2013; Dohmen et al., 2016). Orthopyroxene-hosted inclusions had K_D of 0.13–0.25, and those out of equilibrium (six of nine inclusions) were corrected for PEC by incrementally adding orthopyroxene back into the inclusion until $K_D{}^{Fe-Mg}_{px-liq}$ of 0.29 was achieved. All reconstructed inclusions behaved as expected in relation to the LLD. Reconstructed inclusions required the addition of 3.10–6.45% orthopyroxene to achieve equilibrium.

Experimental data show that clinopyroxene-liquid pairs are in equilibrium at $K_D{}^{Fe-Mg}_{px-liq} = 0.28 \pm 0.08$ (Putirka, 2008). Measured K_D was 0.12–0.24, with eight of seventeen clinopyroxene-inclusion pairs being within equilibrium range. Inclusions out of equilibrium with their hosts were therefore corrected for PEC by incrementally adding the clinopyroxene until $K_D{}^{Fe-Mg}_{px-liq} = 0.28$, and predicted and observed clinopyroxene components (DiHd, EnFs, CaTs, Jd, CaTi, CrCaTs) were within 15%. This required the addition of 7.3-13% of clinopyroxene. Corrected compositions are presented in Supplementary Table 3.S5 and Supplementary Table 3.S6, Supplementary Material 'C3'.

In plagioclase-liquid pairs, partition coefficients vary with temperature, such that two K_D ranges exist based on temperature. For inclusions trapped at ≥1050°C to exist in equilibrium with their hosts, calculated K_D must fall within the range 0.28±0.11. Those inclusions trapped at T<1050 °C are in equilibrium with their hosts when K_D =0.10±0.05. However, due to the high water contents of the La Soufrière melt inclusions, and the fact that equilibrium in plagioclase-hosted melt inclusions is affected by degassing, assessing K_D is not an accurate indicator of equilibrium (Humphreys et al., 2016) and we do not use this method.

Instead, there is another indication of post-entrapment crystallisation - the resulting increase in MgO and decrease in Al_2O_3 in inclusions (e.g. Nielsen, 2011) in relation to an established liquid line of

descent. At La Soufrière, plagioclase hosted inclusions can be divided into two groups, based on PEC and diffusion of elements. The first defines a group at K_2O<1.0, consisting of 14 inclusions. Harker plots of Al_2O_3 vs K_2O and MgO vs K_2O indicate that this group is characterised by low Al_2O_3 (up to 3 wt.% lower than the trend exhibited by olivine- and pyroxene-hosted inclusions; Supplementary Figure 3.S4, Supplementary Material C3) and high MgO (up to 3 wt.% higher), indicating PEC. However, two inclusions fall within the accepted K_D range given by Putirka (2008). The second group consists of six inclusions at >1.0 K_2O. In this group, four of five inclusions are in the accepted K_D range, and all fall within the trend exhibited by olivine- and pyroxene-hosted inclusions. Inclusions were assessed for PEC based on the Al_2O_3-K_2O relationship defined by olivine and pyroxene hosted melt inclusions (Supplementary Figure 3.S4 in Supplementary Material C3), regardless of equilibrium state. Plagioclase (9.88–23.53%; average 16.74%) was incrementally added back into inclusions until Al_2O_3 values equalled the predicted value at a given K_2O based on regression data (R^2=0.62). The plagioclase-liquid model of Namur et al. (2012) and Fe^{2+}/Fe_{total} of 0.6, based on fO_2 (NNO +1.4; Bouvier et al., 2008) was used.

Bubble growth

The growth of bubbles in melt inclusions occurs as a result of changes in the pressure, volume and temperature in the liquid-host crystal system, with contributing processes including PEC, H^+ loss from the inclusion, and differing thermal expansivities of the host and inclusion (Roedder, 1979; Anderson and Brown, 1993; Lowenstern, 1995; Kent, 2008; Wallace et al., 2015; Hanyu et al., 2020). Bubble growth can sequester large amounts of volatiles trapped in inclusions. Up to 99% of CO_2, 60% of S and 16% of H_2O has been found to be held in melt inclusion bubbles as vapour or as an aqueous solution, as well as major and minor elements which together with volatile elements forms solids in the form of carbonates, sulphates and other mineral groups (e.g. Moore et al., 2015; Esposito et al., 2016; Schiavi et al., 2020; Venugopal et al., 2020; Howe et al., 2025). Therefore, element diffusion into the bubble has the ability to affect a range of magma and magma storage properties.

3.5.3.2 Major element composition

Seventy-eight La Soufrière melt inclusions show compositional variation from basaltic (48.45 wt.% SiO_2) to andesitic (61.62 wt.% SiO_2), except for two dacitic inclusions. Overall, there are two groups of data separated by a compositional break between 0.6-0.8 wt.% K_2O (Figure 3.5). Olivine hosted inclusions exist at lower K_2O (<0.6 wt.%), are the least evolved being basaltic to andesitic in composition (48.45–57.46 wt.% SiO_2). Within this inclusion subset, those with highest Mg# and lowest SiO_2 exhibits the highest Fo contents. Conversely, those inclusions in the group >0.8 wt.% K_2O contain the most evolved inclusions and are orthopyroxene-hosted, ranging from andesitic to dacitic in composition (58.12–65.13 wt.% SiO_2). In these inclusions, the lowest Mg# corresponds with the highest SiO_2. Plagioclase and clinopyroxene-hosted inclusions span both low and high K_2O groups, where the plagioclase-hosted inclusions are basaltic to dacitic, with 50.91–63.40 wt.% SiO_2, whilst clinopyroxene-hosted inclusions span a narrower compositional range from basaltic andesite to andesite.

Major element oxides are plotted against K_2O due to its mostly incompatible behavior, which allows potassium to be used as a proxy for magma differentiation. No apparent trend exists between units (Figure 3.5), as in all inclusions, SiO_2, Na_2O and P_2O_5 increases with K_2O, whilst Al_2O_3, FeO, MgO, CaO decreases, and TiO_2 and MnO are relatively constant with increasing K_2O. Olivine, plagioclase and clinopyroxene melt inclusion major element compositions overlap with whole rock compositions, whilst groundmass glass (Frey et al., 2023) represents the final crystallisation phase, with a measured maximum of 69.31 wt.% SiO_2 content. Melt inclusions in equilibrium with their host, and those corrected for PEC are detailed in Supplementary Table 3.S5 and Supplementary Table 3.S6, Supplementary Material ‘C3’.

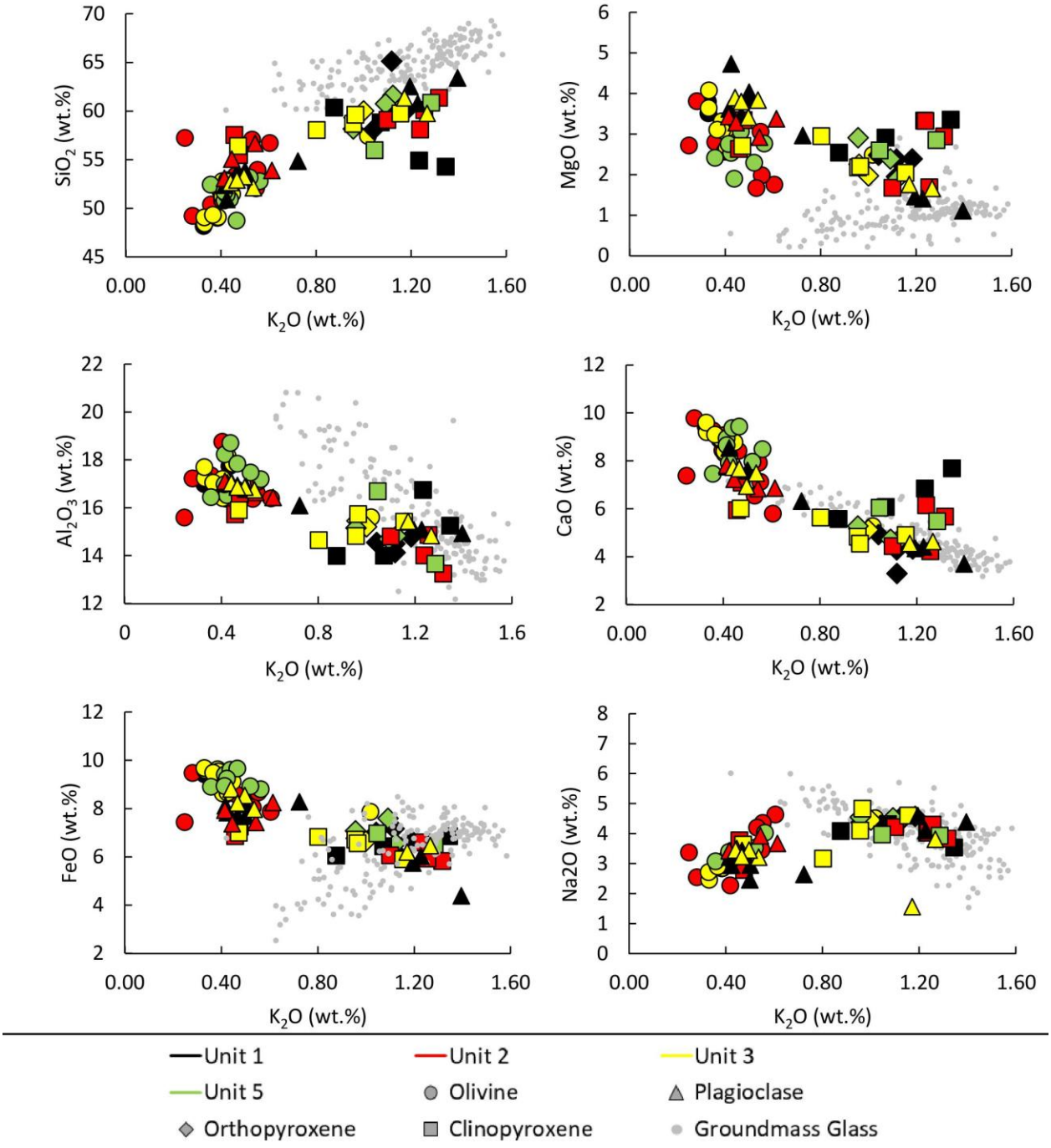

Figure 3.5 – Major element compositions versus K_2O for La Soufrière melt inclusions showing a compositional gap between ~0.6–0.8 wt % K_2O. Groundmass glass are plotted as grey circles, showing compositional evolution and is from Frey et al., (2023) for the 2021 eruption.

3.5.3.3 Volatile element composition

The volatile contents in La Soufrière melt inclusions are comparable to other Lesser Antilles Arc volcanoes (e.g. Mann et al., 2013; Gurenko et al., 2005) and volcanoes from other arcs (Wallace, 2005). On average, La Soufrière melt inclusions contain 4.25 ± 0.76 wt.% total volatiles. Three of the four most primitive inclusions (3.65 – 4.08 wt.% MgO) have a complete volatile dataset (CO_2, H_2O, S, Cl, F) comprising 5.40 ± 0.05 wt.% total volatiles.

3.5.3.3.1 Melt Inclusion Glass

H_2O and CO_2

H_2O contents in thirty-nine melt inclusions across the four units vary from 2.61–5.37 wt.% (Figure 3.6), making up the majority of dissolved volatiles. These concentrations are comparable to published values of 4.90 – 5.30 wt.% for St Vincent products (n=3; Cooper et al., 2020) and 0.83-5.23 wt.% for primitive melt inclusions (Bouvier et al., 2008; Bouvier et al., 2010b), but are greater than the 1.5-3.9 wt.% estimated from volatile by difference method for plagioclase and pyroxene hosted melt inclusions (Weber et al., 2023) and the 2.8-3.1 wt.% estimated based on plagioclase microlite hygrometry (Frey et al., 2023). H_2O decreases with increasing K_2O, most likely due to degassing and crystallisation of the H_2O-saturated magma. The highest H_2O concentrations occur in olivine-hosted inclusions (3.42–5.37 wt.%, n=18), which also have the least evolved compositions, while plagioclase-hosted inclusions contain 2.61-4.11 wt.% (n=10). The two pyroxenes have similar H_2O contents – orthopyroxene with 3.34–3.66 wt.% (n=2) and clinopyroxene with 3.10–4.51 wt.% (n=9). There is no distinct trend between erupted units, however the presence of two compositional groups are also evident where H_2O contents show a decrease with increasing K_2O up to 0.6 wt.%, while they remain constant for K_2O >0.8 wt.% (Figure 3.6). H_2O contents are taken as representative of the magma at melt inclusion entrapment, as there is no evidence of H_2O loss at any given K_2O.

CO_2 concentrations in 29 melt inclusions hosted in all four crystal phases generally range from 3–661 ppm (Figure 3.6). Two inclusions, however, have much higher CO_2, of >2000 ppm. One olivine-hosted inclusion has 2506 ppm CO_2, and one plagioclase-hosted inclusion 3567 ppm. There are no trends in CO_2/K_2O, and

no significant differences between units, as Unit 1 CO_2 ranges from 8–661 ppm, Unit 2 3–434 ppm, Unit 3 12–139 ppm (3567 ppm if the two >1000 ppm outliers are taken into consideration), and Unit 5 20–162 ppm (Figure 3.6). Twenty-eight of twenty-nine melt inclusion glass concentrations represent the total CO_2 in the inclusions at trapping, as their bubbles lacked Fermi diads or carbonates. Sample LSS_U3_OL_011_MI2 lacked CO_2 in its bubble, but the presence of carbonate was detected. Unlike H_2O, there does not appear to be a clear difference in CO_2 contents at high and low K_2O groups, however, the low K_2O group contains the two highest measurements.

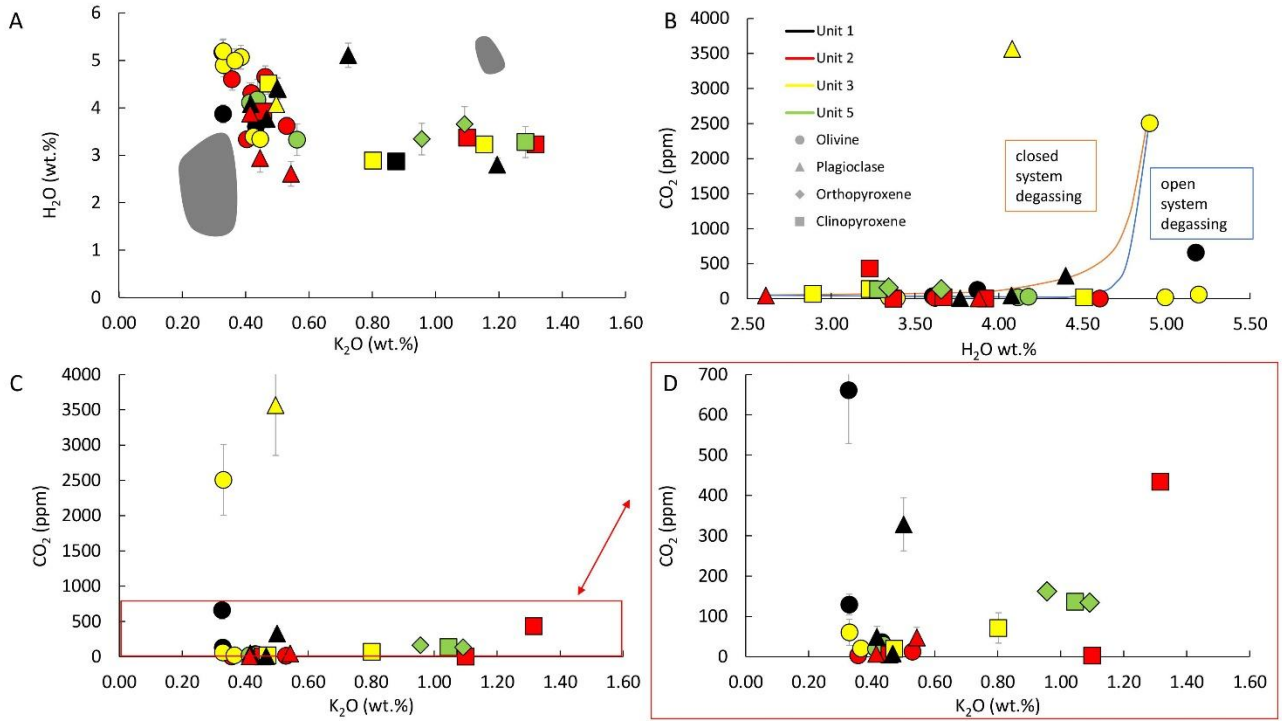

Figure 3.6 – H_2O and CO_2 in La Soufrière melt inclusions. [A] H_2O vs K_2O showing degassing up to ~0.6 K_2O after which the trend levels. [B] CO_2 vs H_2O does not follow simple open or closed degassing trends modelled using melt inclusion LSS_U3_OL_003 which had high CO_2 and H_2O. [C] CO_2 vs K_2O indicates very low CO_2 in the majority of inclusions and no systematic variation in CO_2 with K_2O. [D] CO_2 vs K_2O at CO_2 values up to 700 ppm as an extension of panel [C]. Error bars are 2σ, and where error bars on [A], [B] and [C] are not shown, the error is smaller than the symbol. Grey shaded areas represent published values from Bouvier et al., (2008); Bouvier et al., (2010b) and Cooper et al., (2020).

Sulphur (S), Chlorine (Cl) and Fluorine (F)

Seventy-four inclusions were analysed for S and range from 59–836 ppm. In all units, S decreases with increasing K_2O (Figure 3.7A) and S contents are generally consistent between units. However, there also exists a compositional break in S, as with the major elements, showing higher S contents in the low K_2O group, with a steep S/K_2O gradient and lower S contents at higher K_2O with a shallow S/K_2O gradient. The highest S concentrations are also present in olivine-hosted inclusions, ranging from 162-620 ppm, with one outlier inclusion at 836 ppm. Lower S concentrations occur in melt inclusions within other crystal hosts, with ranges from 92–285 ppm for plagioclase, 90–306 ppm for orthopyroxene, and 59–293 ppm for clinopyroxene-hosted inclusions. The melt inclusion S data for this 2021 explosive eruption of La Soufrière are broadly similar to the only other published data for this volcanic system which is the 1979 explosive eruption, where S measured below detection limit (<50) to 558 ppm, at 0.45–0.96 K_2O (Figure 3.7A; Devine and Sigurdsson, 1983). In the context of the arc, S values are similar to volcanoes such as South Soufrière Hills Volcano, Montserrat (Cassidy et al., 2015) and La Soufrière de Guadeloupe, Guadeloupe (Metcalfe et al., 2022) where S also ranges from below detection limit to ~780 ppm. These volcanic systems are all more S-rich than both Soufrière Hills Volcano, Montserrat (Edmonds et al., 2001) and Morne Trois Pitons-Micotrin, Dominica (d'Augustin et al., 2020) where maximum S is ~70 and ~150 ppm respectively.

Cl behaves incompatibly, with concentrations rising as magma differentiates, as indicated by the overall positive trend of Cl vs K_2O (Figure 3.7B). Cl vs K_2O in olivine (Figure 3.7B circles) has a strongly positive correlation (R^2 of 0.91), however, there is a decrease in the gradient of Cl vs K_2O in plagioclase, orthopyroxene and clinopyroxene hosts, particularly above 0.8 wt% K_2O, as well as a wider variation in the data (Figure 3.7B). The trend also highlights two groups of melt inclusions as seen in other elements. In Cl, concentrations increase in the low K_2O group, and after the compositional gap at 0.6-0.8 wt.% K_2O, Cl values become more stable. This trend is also seen in pre-historic La Soufrière inclusions (Heath et al., 1998). Overall, Cl concentrations span 981–5083 ppm, comparable to values from pre-historic eruptions of La Soufrière (Heath et al., 1998; Bouvier et al., 2010b), and other Lesser Antilles volcanoes more broadly (e.g. Edmonds et al., 2001; Gurenko et al., 2005; Metcalfe et al., 2022).

Similarly, fluorine generally increases with K_2O up to 0.6 wt %, after which the concentration remains stable in the >0.8 wt.% K_2O group (Figure 3.7C). F concentrations in all melt inclusions range from below

detection limit to 880 ppm, roughly comparable to pre-historic La Soufrière eruptions (100-1600 ppm; Heath et al., 1998; Figure 3.7C) and to other Lesser Antilles volcanoes where F extends up to 500 ppm (Edmonds et al., 2001; d'Augustin et al., 2020; Metcalfe et al., 2022). Like other volatiles, F does not vary systematically between Units but does vary by host crystal. Measured ranges are 200-769 ppm (olivine-hosted), 372–880 ppm (plagioclase-hosted), 286–633 ppm (clinopyroxene-hosted) and 451–560 ppm for orthopyroxene-hosted MI.

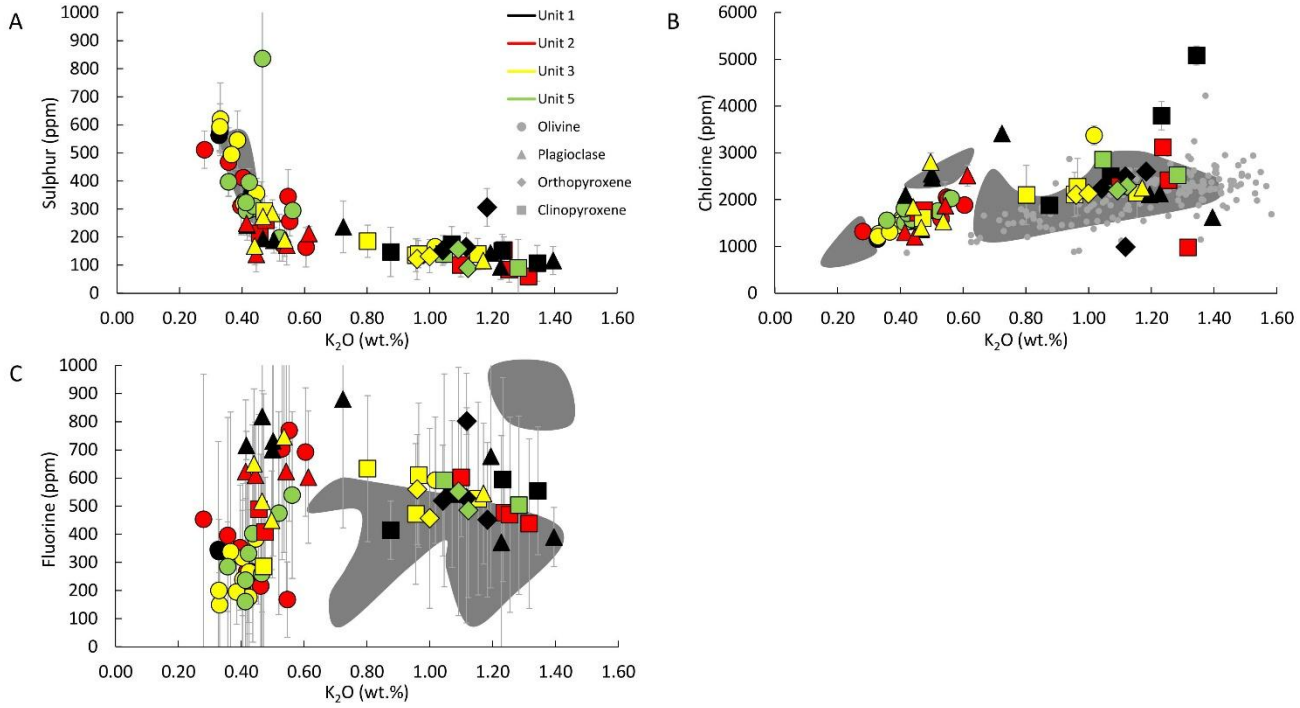

Figure 3.7 – Sulphur and halogen compositions of La Soufrière melt inclusions. [A] Sulphur vs K_2O exhibiting degassing behaviour. Areas shaded in grey are compositions measured in products from the 1979 eruption from Devine and Sigurdsson, (1983). [B] Chlorine vs K_2O shows a steady increase between K_2O of 0.2-0.6, after which the gradient of increase decreases. Grey circles are groundmass glass compositions for the 2021 explosive products from Frey et al., (2023). Grey shaded areas are pre-historic melt inclusions from Heath et al., (1998) and Bouvier et al., (2010b). [C] Fluorine vs K_2O also showing an increase from 0.20-0.60 K_2O, followed by a decrease in F content. Grey shaded areas are pre-historic melt inclusions from Heath et al., (1998) and Bouvier et al., (2010b) which generally overlap with 2021 inclusions. Error bars are 2σ and where error bars are not shown, the error is smaller than the symbol.

3.5.3.3.2 Melt Inclusion Bubbles

The population of 394 measured bubbles in the La Soufrière melt inclusions can be divided into two groups: (i) those with a discernible Fermi diad, indicating the presence of vapour CO_2, accounting for 7% of the population, and (ii) those without a Fermi diad (the remaining 93%). Raman spectra with low counts (<500) and those with skewed peaks unsuitable for mixed Gaussian-Lorentzian curve fitting could not be used to accurately calculate CO_2 densities or concentrations and so are not considered. All melt inclusions with a discernible Fermi diad contain a singular bubble.

The 28 bubbles yielding measurable Fermi diads have CO_2 densities of 0.003–0.147 g cm^{-3} (Supplementary Figure 3.S5, Supplementary Material C3). As the measured densities are less than the critical density of CO_2 (0.468 g cm^{-3}; Moldover, 1974), the bubbles contain purely vapour CO_2, and CO_2 is therefore not underestimated due to the presence of a liquid phase. CO_2 densities across all units are similar. Unit 1 has the widest range of CO_2 densities, from 0.003–0.147 g cm^{-3}, with twelve bubbles presenting Fermi diads, while in Unit 2, five bubbles have measurable CO_2 densities of 0.023–0.086 g cm^{-3}. There was only one bubble in Unit 3 presenting a Fermi diad, with measured CO_2 density of 0.028 g cm^{-3}. Unit 5 had six bubbles with densities spanning 0.004–0.126 g cm^{-3}. There is no correlation between CO_2 density and bubble volume.

Additionally, there is no distinction between bubbles containing vapour CO_2 and carbonates and bubbles with only vapour CO_2, suggesting insignificant CO_2 precipitation as carbonates (Supplementary Figure 3.S5, Supplementary Material C3). Carbonates were identified in twenty-eight of three hundred ninety-four bubbles analysed and were present in all crystal phases and units. In unit 1, seven bubbles contained carbonates. In unit 2, there were ten, and in units 3 and 5, there were four and seven bubbles containing carbonates respectively. However, carbonates could occur on the rim of other bubbles, as a comprehensive characterisation of solid phases was not conducted and is outside the scope of this research. Carbonates occur in the form of calcite, nahcolite, natrite, and gaylussite, identified by their main and other vibrations in the Raman spectra (Frezzotti., et al., 2012). It is important to note that carbonates were present in both bubbles with and without Fermi diads, indicating that the amount of CO_2 measured in the bubble should be considered minimum values.

Along with CO_2 and carbonates, other volatile species in the form of gases, solids and solutes were present in bubbles at La Soufrière. H_2O was present in twelve bubbles from all four units, in both aqueous and gaseous phases. This includes three inclusions measured for H_2O at the SIMS - two hosted in olivine –

LSS_U1_OL_003 (aqueous H_2O) and LSS_U2_OL_006 (aqueous H_2O), and one hosted in clinopyroxene – LSS_U3_CPX_007 (gaseous H_2O). While the sequestration of H_2O to these three bubbles suggests that concentrations are underestimated in the glass, their glass H_2O analysed are within the range defined by other, non-bubble bearing H_2O samples. Sulphur bearing species in the form of H_2S vapour and HS^- and H_2S dissolved as solutes in water were also present in seven bubbles from unit 1, 3 and 5, including two samples measured with EPMA. These two samples yielded glass S concentrations that were within range of those for non-bubble bearing inclusions. Raman peaks at 984 and 1000 cm^{-1} likely indicate the presence of sulphates in two olivine hosted inclusions in unit 3 (Frezzotti et al., 2012).

Mass balance calculations show that bubbles in La Soufrière melt inclusions contain 68 – 1807 ppm CO_2 (Supplementary Figure 3.S6, Supplementary Material C3). In Unit 1, the eight inclusions that pass the bubble volume threshold test have CO_2 concentrations of 72 – 1014 ppm. Unit 2 bubbles are within similar range, with four bubbles ranging from 205 – 1007 ppm. The lone Unit 3 bubble has a concentration of 572 ppm, whilst five such bubbles in Unit 5 range from 68 – 1807 ppm. Of these eighteen bubbles which grew homogenously in the inclusion, twelve contain CO_2 higher than that measured in the glass. However, these bubbles were hosted in inclusions that were not acceptable for SIMS analysis due to small size or the presence of crystals. We are therefore unable to calculate total CO_2 for these 28 melt inclusions.

3.6 Discussion

3.6.1 Magma Storage Conditions

CO_2 solubility in magma is pressure-, temperature- and major element composition-dependent. Several models exist, allowing for calculation of magma storage conditions such as melt inclusion entrapment pressure, based on CO_2-H_2O systematics (e.g. Newman and Lowenstern, 2002; Ghiorso & Gualda, 2015; Allison et al., 2022). To do this, the total CO_2 concentration (bubble + glass) in melt inclusions must be known. Several studies have highlighted the fact that bubbles grown in trapped inclusions can contain up to 99% of total inclusion CO_2 (e.g. Hartley et al., 2014; Moore et al., 2015; Aster et al., 2016; Venugopal et al., 2020; Howe et al., 2025) leading to an underestimation if only glass-held CO_2 is considered.

Several inclusions contain multiple bubbles, often with small diameters <10 µm (e.g. LSS_U5_OL_025_MI2 containing nine bubbles, all <7 µm). This suggests that the melt was supersaturated with volatiles, leading to a high nucleation rate, with the small size of the bubbles indicating nucleation occurring up until the point of magma fragmentation and quenching (Le Gall and Pichavant 2016; Feignon et al., 2022). However, in the 2021 explosive eruption at La Soufrière, no CO_2 was detected in the vast majority of bubbles. This suggests that either (i) bubbles contained low density vapour CO_2 undetectable by the instrument, (ii) bubbles grew by differential thermal contraction followed by rapid cooling, which provided insufficient time for CO_2 diffusion into the bubble, and are therefore vacuums (e.g. Schipper et al., 2010; Steele-Macinnis et al., 2011), (iii) CO_2 vapour present in bubbles crystallised to form carbonates (e.g. Schiavi et al., 2020), although carbonates only appear in a small percentage of La Soufrière inclusions, (iv) CO_2 was lost due to re-equilibration of the melt inclusion, or (v) CO_2 was lost due to decrepitation . Given the low detection limit for vapour CO_2 by Raman spectroscopy, the fact that there are carbonates in some bubbles and due to the low diffusivity of CO_2 in mineral phases (e.g. 1×10^{-19} in olivine at 800°C), rapid cooling prohibiting diffusion of CO_2 into bubbles (model ii) or decrepitation where the melt inclusions ruptures and loses CO_2 (model iv) can both explain the presence of some empty bubbles.

A total of 394 analysed bubbles across the four units were found to have a wide range of sizes, accounting for <1–32% of total inclusion volume (Supplementary Figure 3.S7, Supplementary Material C3). To ascertain which bubbles were formed post-entrapment, the model of Moore et al., (2015) was adapted. The volume change in inclusion glass and host crystal were calculated using average inclusion

compositions in each host type, along with entrapment temperatures (see section 5.1.1) and glass transition temperatures of 425–450°C, calculated using melt viscosity models (Giordano et al., 2008). For olivine-hosted inclusions at La Soufrière, olivine contracts by 2% and the melt by 8% at a calculated glass transition temperature of 440°C. This allows for the growth of a bubble occupying 6% of the inclusion volume. Similar calculations for plagioclase- orthopyroxene and clinopyroxene-hosted inclusions indicate that homogenously grown bubbles should occupy 6%, 4% and 5% of the melt inclusion volume respectively. Therefore, melt inclusions with bubbles larger than this 4-6% volume threshold are likely trapped melt and vapour already present in bubble(s) entrapment, and adding their CO_2 to the measured glass values would lead to an overestimation of calculated total melt inclusion CO_2 concentration. Orthopyroxene-hosted inclusions are calculated to grow the smallest bubbles, as the inclusions are generally more evolved, and therefore contract less during cooling than the lesser-evolved olivine-hosted compositions. Across the four units, bubble volume is predominantly 1-3%, particularly in unit 5. This shows that the majority of bubbles were grown from the same process of differential thermal contraction, with others showing evidence of bubble growth and entrapment. Bubble sizes range from <1–32% in Unit 1 (average = 5%), 1–24% (average = 4%) in Unit 2, 1–25% in Unit 3 (average = 6%), and <1–14% (average = 4%) in Unit 5.

Since no bubbles in melt inclusions analysed by SIMS contained CO_2, the total CO_2 used in models from this point forward is equivalent to the CO_2 measured in the glass. However, we recognise that a small proportion of the melt inclusion bubbles that were analysed by Raman spectroscopy but not SIMS did contain measurable CO_2, and we therefore consider the glass-only CO_2 concentrations measured by SIMS to be minimum values.

After correction for post-entrapment processes, melt inclusion H_2O, CO_2 and major element compositions can be used to estimate magma storage conditions such as temperature, pressure and inferred depth, and thus better constrain magmatic generation and evolution.

3.6.1.1 Temperature

Magmatic temperatures were calculated for olivine-, plagioclase-, orthopyroxene- and clinopyroxene-hosted melt inclusions across the four scoria-bearing units using several different geothermometers and are shown in Figure 3.8. Temperatures of olivine-hosted melt inclusions were calculated using the MgO thermometer of Sugawara, (2000), built on experimental results showing a linear relationship between mol% MgO and temperature. This method is associated with a standard estimate of error (SEE) of 30 °C. Temperatures of plagioclase-hosted inclusions were assessed using two methods. Firstly, the thermometer of Waters and Lange (2015) was used to assess magmatic temperatures of the ten plagioclase-hosted inclusions for which H_2O was measured by SIMS, as plagioclase composition is strongly dependent on magma H_2O content (Waters and Lange, 2015). Secondly, plagioclase-liquid thermometry was used, based on Equation 24a from Putirka, 2008 (SEE 36°C). Temperatures for nine orthopyroxene hosted inclusions were calculated using Equation 28a of Putirka, 2008 (SEE 28 °C), based on orthopyroxene-liquid equilibria. Clinopyroxene-liquid thermometry based on Putirka, (2008) Equation 33 (SEE 45 °C), was applied to seventeen inclusions. Overall, temperatures for the 2021 explosive eruption generally overlap with temperatures from the 1979 and pre-historic eruptions (Figure 3.8). However, it is noted that similarly to the major and volatile elements, there are two groups of temperatures – higher temperatures associated with the olivine and plagioclase hosted melt inclusions, and lower temperatures associated with the pyroxene-hosted melt inclusions.

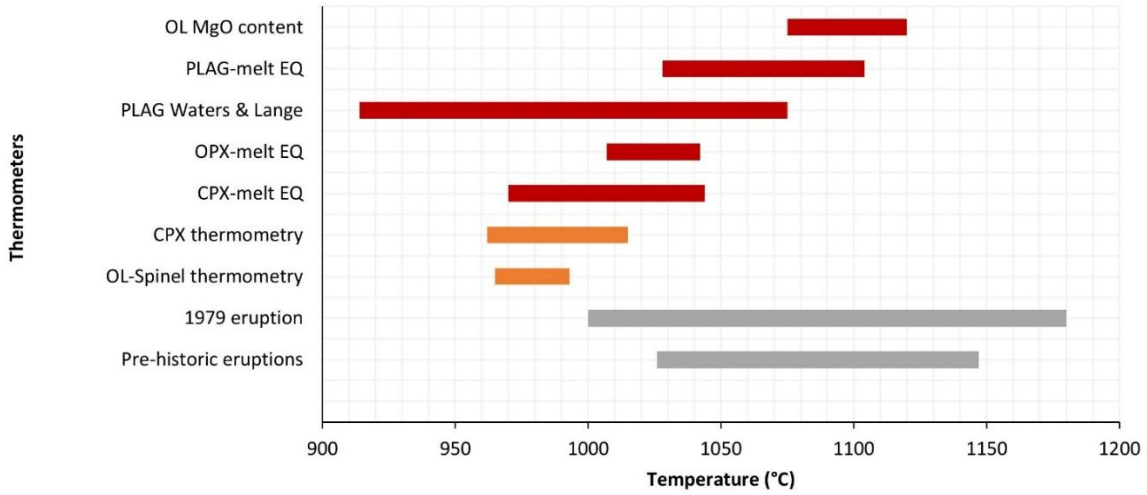

Figure 3.8 – Range of temperatures calculated for the explosive products of the 2021 eruption in comparison to published values. Temperatures in red are calculated in this study. Temperatures in orange are calculated using CPX thermometry by Weber et al., (2023) and by olivine-spinel thermometry (Camejo et al., 2025). Temperature data for the 1979 eruption is in grey and is estimated using plagioclase-melt equilibria of Kudo and Weill, (1970), 2-pyroxene equilibria of Wood and Banno, (1973), fusion of devitrified melt inclusions and two-liquid consolution curve, range from 1000–1180 °C (Devine and Sigurdsson, 1983; Bardintzeff, 1984; Martin-Lauzer et al., 1986). For prehistoric eruptions, also in grey, Heath et al., (1998) applied the olivine-spinel exchange thermometer of Ballhaus et al., (1991) and the two-pyroxene thermometer of Lindsley, (1983). Temperatures for the 2021 explosive eruption generally overlap with temperatures from previous eruptions. OL, PLAG, OPX, CPX and EQ refer to olivine, plagioclase, orthopyroxene, clinopyroxene and equilibria respectively.

3.6.1.2 Saturation Pressures and Depths

Melt inclusion entrapment pressures were estimated using the H_2O-CO_2 solubility model MagmaSat (Ghiorso and Gualda, 2015), hosted in VESIcal (Iacovino et al., 2021), assuming (i) vapour saturation, as H_2O and CO_2 do not behave compatibly based on their relationship with K_2O and (ii) that post-entrapment modifications such as bubble formation, PEC, and H_2O loss are accounted for, as discussed previously. Based on melt inclusion composition, H_2O and CO_2 contents, and temperature, entrapment pressures for olivine-, plagioclase-, orthopyroxene-, and clinopyroxene-hosted inclusions are 100-230, 62-160, 110-120, and 85-160 MPa respectively. Two higher pressures are present for olivine- and plagioclase-hosted inclusions at 320-620 MPa.

Inferred entrapment depths beneath the surface of La Soufrière were calculated assuming a crustal density of 2660 kg m^{-3}, based on gravity modelling data for the Lesser Antilles crust (Christeson et al., 2008). Twenty-five of twenty-eight inclusions recovered depths of 2.4–8.9 km depth (mean 6.4 km), with one inclusion at 12 km depth, and two high CO_2 inclusions at 21 and 24 km depth (Figure 3.9). While the mean depth of the entire melt inclusion population is 6.4 km, there are two discrete groups of melt inclusions based on the major element (Figure 3.5), volatile element (Figure 3.6; Figure 3.7) and temperature data (Figure 3.8) presented here, and on the petrology of the 2020/2021 eruptive products (Frey et al., 2023; Weber et al., 2023). It is proposed, based on an extensive range of methods (e.g. experimental petrology, mineral petrology, xenolith petrology, geophysical studies) applied to various eruptions and their products from pre-historic to present times, that the La Soufrière plumbing system consists of two main magma storage regions situated at ~6 km and 13-20 km depths (Tolan et al., 2011; Fedele et al., 2021; Camejo-Harry et al., 2023; Latchman and Aspinall, 2023), where the deep region is dominated by a basalt-basaltic andesite melt, and the shallow region by andesite-dacite melt within a crystal mush (Weber et al., 2023). The volatile-derived melt inclusion entrapment depths here mostly coincide with residence in the shallower storage region, with some inclusions sampling the deeper region.

While we acknowledge that our melt inclusion bubbles with measured H_2O and CO_2 in the glass (those measured at SIMS) lack CO_2 in their bubbles, this can be attributed to CO_2 loss as discussed above. Therefore, in order to model the effect of bubble-hosted CO_2 on pressure prior to CO_2 loss, we use average and maximum CO_2 values in the bubble to calculate pressure and infer depths (Figure 3.9). Here, we find that when an average bubble CO_2 concentration (472-875 ppm across U1-U5, Supplementary Table 3.S4) is added to the total inclusion excluding those at >20 km, pressures increase to 110 to 370 MPa or 4 to 14

km depth. Applying this concept using the maximum bubble-hosted CO_2 (1014-1807 ppm across U1-U5) further increases pressures to 280-330 MPa or 11 to 17 km depth. This addition of CO_2 to the melt inclusions correspond with the deeper storage region at 13-20 km (Fedele et al., 2021; Camejo-Harry et al., 2023; Weber et al., 2023), and together with the presence of carbonates in empty bubble further solidifies the theory of CO_2 loss from the bubble.

To further investigate the inferred depth of melt inclusion entrapment and depths of crystallisation using their compositions as at eruption, we compare volatile solubility relationships with independent depth constraints from clinopyroxene-only barometry and liquid-crystal equilibria. Clinopyroxene-only barometry is carried out using two barometers. Firstly, Equation 30 of Putirka, (2008) enables direct comparison with values published by Weber et al., (2023). This model yields pressures of 350-530 MPa (6.1-20.3 km) for sixteen clinopyroxene compositions, in comparison to 280-400 MPa (10.7-15.3 km) reported by Weber et al., assuming a crustal density of 2660 kg m^{-3} (Christeson et al., 2006). The two datasets largely overlap, and there is no significant difference as the root mean square error (RSME) on this method is 450 MPa or 17.2 km depth (Wieser et al., 2021). We also use the clinopyroxene-only barometric model of Wang et al., (2021) Equation 1, appropriate for clinopyroxenes crystallized within <60 wt.% SiO_2 melts. This accounts for 15 of the 17 crystals, and has a lower error of 180 MPa (6.9 km). The two more evolved melt inclusions are of 60-61 wt.% SiO_2. Results yield pressures of 30-210 MPa (average 110 MPa), corresponding to depths of 1.1-8.0 km (average 4.2 km), with the two inclusion >60 wt.% SiO_2 also falling within this range. These depths are much shallower than the results from Putirka, (2008), but within error, and match more closely with the volatile-derived pressure/depth constraints. We therefore rely on the Wang (2021) model, and deduce that the majority of clinopyroxene crystallisation occurred in the shallow storage region between 4-6 km depth.

We additionally employ liquid-crystal equilibria to identify the melt composition in equilibrium with the remaining host minerals and thus provide additional constraints on the magmatic plumbing system. Weber et al., (2023) infers an andesitic-dacitic carrier melt, with 60-64 wt.% SiO_2 based on mass balance calculations on phase proportions, whole rock, groundmass glass, melt inclusions and mineral chemistry. Here we apply orthopyroxene-liquid equilibria to whole rock compositions (basaltic andesite) and groundmass glass (andesite to dacite). Equilibrium is achieved between an andesitic (62 wt.% SiO_2) liquid and six of nine orthopyroxene crystals. The remaining three crystals are in equilibrium with a basaltic andesite liquid (54 wt.% SiO_2). These results, together with the low calculated temperatures for orthopyroxene-hosted melt inclusions, indicate that orthopyroxene most likely crystallised in the cooler

andesitic reservoir situated at shallow depths similarly to the clinopyroxene (based on clinopyroxene compositions).

Plagioclase-liquid equilibrium models are applied to nineteen low ($An_{<80}$) and high ($An_{>80}$) anorthite plagioclase-whole rock and plagioclase-groundmass glass pairs to test chemical equilibrium. Eleven of fourteen high An plagioclase crystals are in equilibrium with a basaltic andesite melt, whereas the five low An plagioclases are all in equilibrium with an andesite liquid. This suggests that high An plagioclases predominantly derive from the deeper, hotter basaltic andesite reservoir, while low An plagioclases formed in the shallow, cooler andesitic reservoir.

Chemical equilibrium is tested between twenty-eight olivine-liquid pairs in the average whole rock and andesite compositions as above. The overwhelming majority (26) are not in equilibrium with an andesitic melt, while 17 of 28 are in equilibrium with a basaltic-andesite melt. Based on the high temperatures yielded, textural disequilibrium in the whole rock shown by thin rims of differing compositions than cores (Frey et al., 2023) and the chemical equilibrium test, we ascribe olivine crystallisation to the deeper, hotter basaltic-andesite storage region.

In summary, our melt inclusion and mineral dataset indicate two separately crystallising magma bodies forming a transcrustal mush system beneath La Soufrière volcano (Figure 3.10). Between July and December 2020, there was the injection of magma into a storage region 18±1.9 km inferred from GPS and InSAR (Camejo-Harry et al., 2023). Over the next 3-9 months, high An plagioclase and olivine crystallised from this deep, hotter region in the mid-lower crust, while the shallow, cooler, andesite melt in the upper crust crystallised low An plagioclase along with clinopyroxene and orthopyroxene. In the weeks leading up to the transition from effusive to explosive activity, there is seismic evidence of migration of magma from the mid-lower crust into the shallow crust at the base of the shallow reservoir at ~7-8 km depth (Latchman and Aspinall, 2023). We acknowledge that despite the overwhelming evidence for polybaric crystallisation, there is a surprising lack of melt inclusions clustered at ~18 km on Figure 3.9. Instead, the entire melt inclusion dataset clusters around 6 km, with only three inclusions spread between 12-24 km. This can be caused by decrepitation and CO_2 loss from both melt inclusions after upward migration and stalling of the deeper magma, which would erase the deep CO_2 signature in particular, however, (i) there is no physical evidence for decrepitation (for example fluid filled cracks) and (ii) there is no difference in CO_2 content in olivine which is weakly cleaved and likely to be less affected by decrepitation, and plagioclase which is highly cleaved and more susceptible to decrepitation.

While clinopyroxene barometry using Equation 1 from Wang et al., (2021) fits the volatile data presented here, it is associated with large errors that span much of the upper crust (Wieser et al., 2023), and we therefore emphasise the importance of also using H_2O-CO_2 solubility constraints to estimating depth of magma storage. However, we recognize that this relationship may be subject to decrepitation and CO_2 loss, therefore, H_2O-CO_2 contents reflect the minimum depth of magma storage prior to eruption. This study provides the first pressure and depth estimates based on H_2O-CO_2 solubility at La Soufrière volcano, providing an important independent estimate of magma storage within the crust.

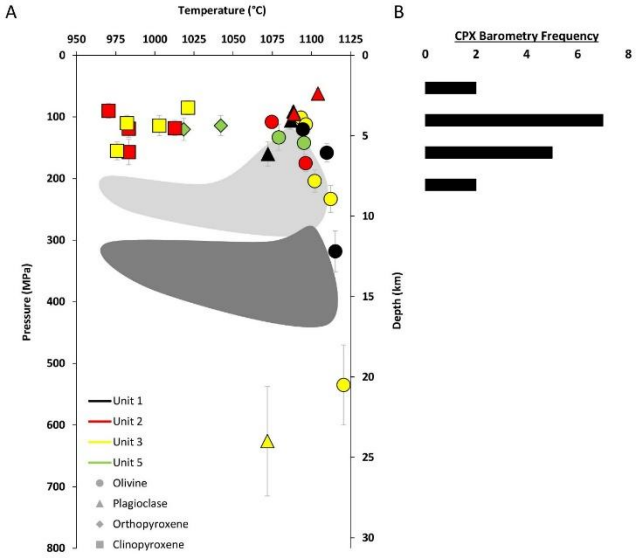

Figure 3.9 – Comparison of depths calculated from H_2O-CO_2 contents of melt inclusions and clinopyroxene-only barometry. [A] Pressure vs temperature graph based on solubility models calculated for the explosive phase of the 2021 La Soufrière eruption. Depth is converted from pressure using a crustal density of 2660 kg m^{-3} (Christeson et al., 2008). There are no variations between units. Error bars are 2σ and represent total error on H_2O and CO_2 contents which are then extrapolated to pressures and depths. Where error bars cannot be seen, the error is smaller than the symbol. The light grey shaded area represents pressures estimated by using average bubble-hosted CO_2 concentrations in each unit while the dark grey shaded area represents pressures calculated using the maximum CO_2 concentration in bubbles in each unit. [B] Depths yielded by clinopyroxene-only barometry using Equation 1 of Wang et al., (2021).

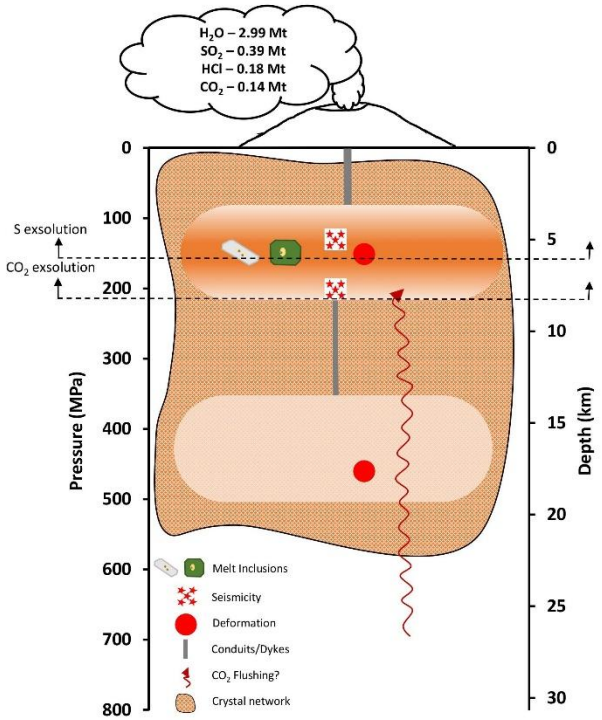

Figure 3.10 – Schematic model of the La Soufrière plumbing system. The 2020-2021 eruption involved two magma storage regions in the upper and mid-lower crust. Inflation at ~18 km occurred from July-December 2020, and seismicity occurring weeks before the transition from effusive to explosive behaviour infer transfer of hot, basalt to basaltic-andesite material from the deep storage region into the base of the shallow storage region where melt inclusions decrepitated, resulting in CO_2 loss where modelled depths yield ~6km depth, matching syn-explosive deflation.

3.6.2 Magma Degassing

During degassing, the CO_2/H_2O ratio should decrease due to the low solubility of CO_2, until depths at which H_2O degassing becomes prominent (Blundy et al., 2010; Witham, 2011), as shown by degassing models (e.g. Ghiorso and Gualda, 2015). The relationship between CO_2 and H_2O in this suite of La Soufrière melt inclusions is not well explained by either open or closed system degassing. For example, inclusion LSS_U3_OL_003 is the most primitive sample in the dataset, and has one of the highest CO_2 concentrations (2506 ppm), but not the highest H_2O. LSS_U3_OL_004 which has the highest H_2O value of 5.19 wt.% (but very low CO_2 of 60 ppm).

The solubility of S in the melt, like that of H_2O and CO_2, depends on parameters such as pressure, temperature, and major element composition, but additionally the fugacity of sulphur and oxygen, which dictates its dissolving speciation (Carrol and Webster, 1994). The compositional effect is particularly important, and Figure 3.11 shows the positive correlation with FeO, demonstrating the behaviour of S under oxidising conditions, as experimentally calculated for La Soufrière by Pichavant et al., (2002) and as calculated from pre-historic samples from Heath et al., (1998). We calculate the sulphur content at sulphide saturation (SCSS; Figure 3.11A) for this suite of melt inclusions at La Soufrière, and determine that sulphide saturation is not achieved, and therefore, the decreasing trend of S with K_2O in Figure 3.7A above is due to exsolution depth degassing. Modelling of S degassing at Etna volcano, similarly in an arc setting, shows that S begins to exsolve from the melt at ~140 MPa (Spilliaert et al. 2006b), equivalent to 5.4 km at La Soufrière based on a crustal density of 2660 kg m^3 (Christeson et al., 2008). However, we model S degassing for our suite of melt inclusions from La Soufrière volcano using Sulfur_X (Ding et al., 2023), and find that S begins to degas deeper than Etna magmas at ~220 MPa or 8.4 km. In Figure 3.11B, both S and H_2O are positively correlated, demonstrating degassing of both volatiles, as modelled by Sulfur_X (Ding et al., 2023), and Figure 3.11C justifies calculations of magma storage depths in the shallow storage region since S starts to degas at ~9 km at La Soufrière. S modelling also correlates well with pressures and depths inferred from H_2O-CO_2 solubility as modelled using MagmaSat (Ghiorso and Gualda, 2015), and shows that by 5 km depth, the magma lost ~60% of its S. The maximum measured H_2O content of 5.19 wt.% and S concentration of 620 ppm are therefore considered minimum values for the parental magma.

Cl and F lack a degassing signature in this suite of inclusions, implying that magma entrapment pressures are not as shallow as ~100 MPa or 3.8 km, as calculated for the onset of Cl (or 10 MPa/0.4 km for F)

degassing in arc settings (Spillaert et al., 2006b). Therefore, the general decrease in S/Cl ratios with differentiation is solely due to degassing of S.

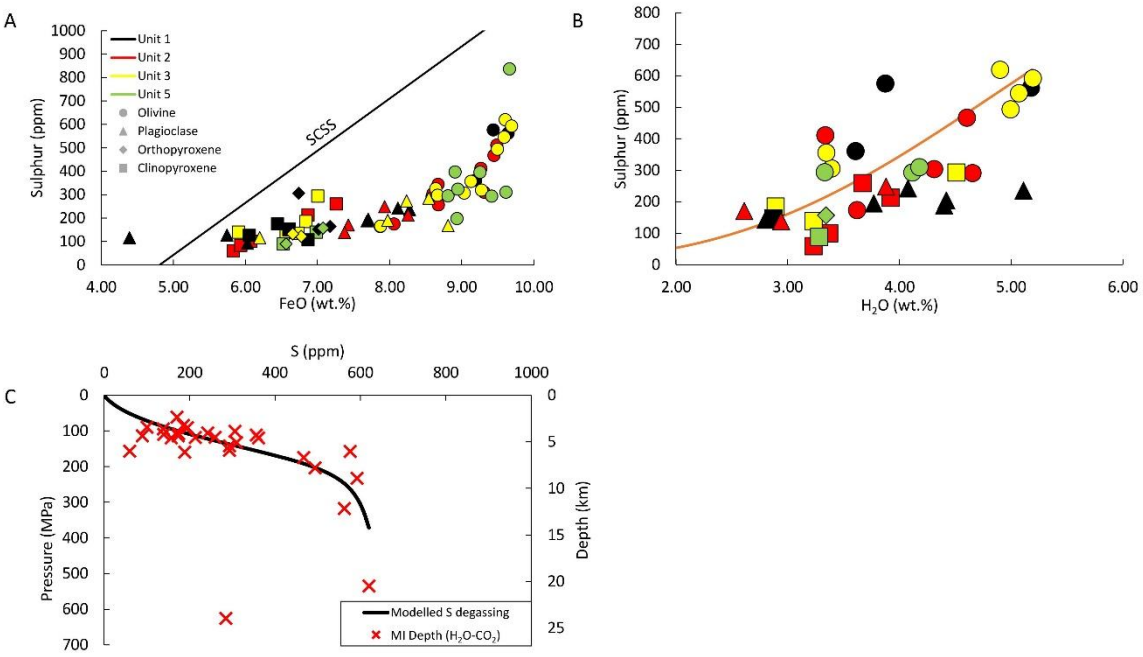

Figure 3.11 – [A] Sulphur vs FeO for this suite of melt inclusions from the 2021 explosive phase of La Soufrière volcano exhibiting an increasing trend of S with FeO under oxidising conditions. Sulphide saturation has not been achieved as this suite of melt inclusions is below the Sulphur Content at Sulphide Saturation (SCSS) line. [B] Sulphur vs H_2O showing an overall degassing trend of both volatile species, and modelling of sulphur degassing using Sulfur_X (Ding et al., 2023). [C] Modelling of S degassing with pressure shows that at La Soufrière, S begins to degas at depths <9 km and that by ~5km, 60% of S is lost.

In addition to modelling the degassing path of S, we use Sulfur_X to model the evolution of CO_2 and S from gas introduction to the system to the surface in order to better understand CO_2/S_T ratios measured in the plume and the depths at which the magma degases (e.g. Burton et al., 2007; Aiuppa et al., 2017). CO_2/S_T molar ratios (where S_T is the total sulphur, achieved by summing the SO_2 and H_2S gases) at La Soufrière were measured using MultiGAS in 2018 (Joseph et al., 2022) and ranged from 22-36. Following the extrusion of the lava dome in the 2020/2021 eruption, the MultiGAS was employed for the first time since 2018, and during the effusion phase, measurements covered a wide range of ratios from 9-75 (14th January to 23rd March 2021; Joseph et al., 2022).

We present five models in order to represent the range of pressures and depths obtained from melt inclusion H_2O-CO_2 solubility relationships (Figure 3.12; Table 3.2). Cluster 1 represents the group of melt inclusions with low CO_2 plotting at an average of ~5 km depth. The second cluster represents inclusions in the intermediate-depth group, plotting at ~9 km, and the third cluster represents the group of inclusions plotting in the lower crust at ~22 km (Figure 3.9). Average compositions of the parameters are calculated for Clusters 1, 2, 3A and 3B. Cluster 3C represents the olivine hosted melt inclusion (LSS_U3_OL_003) in the 22 km group which has the highest S in the dataset. The input parameters used in the five models are shown in Table 3.2. All models were ran at ΔFMQ of +2.08 as defined for the La Soufrière system by Bouvier et al., (2008).

As shown on Figure 3.12, Clusters 1 and 2 show magma injection, (calculated using Iacono-Marziano et al., 2012 H_2O-CO_2 solubility model within Sulfur_X) at ~160 and 230 MPa respectively, however, CO_2/S_T modelled in melt inclusions from these groups do not correspond to ratios in the plume.

In Cluster 3, all three models show magma injection at >350 MPa, and corresponds with plume CO_2/S_T ratios. Since high plume ratios likely occurred as a result of a lack of detectable SO_2 in the plume following the scrubbing effect into the hydrothermal system (Joseph et al., 2022), they therefore do not represent gas chemistry at depth. In order to compare CO_2/S_T ratios modelled using our melt inclusion dataset to CO_2/S_T emitted via the plume, we use the lowest ratio to combat contamination of the scrubbing effect. Taking this into account, the lowest ratio of 9 measured on February 1st 2021 suggests degassing between 140 and 190 MPa or 5.4 and 7.3 km depth, and broadly agrees with our estimates of the shallow reservoir at depths of 1.1-8.0 km using clinopyroxene-only barometry, and melt inclusion H_2O-CO_2 barometry at depths of 2.4-8.9 km. The modelling of CO_2/S_T from our melt inclusions in comparison to those measured in the plume further solidifies our placement of all melt inclusion-hosted minerals at a final magma residence in the upper crust prior to eruption.

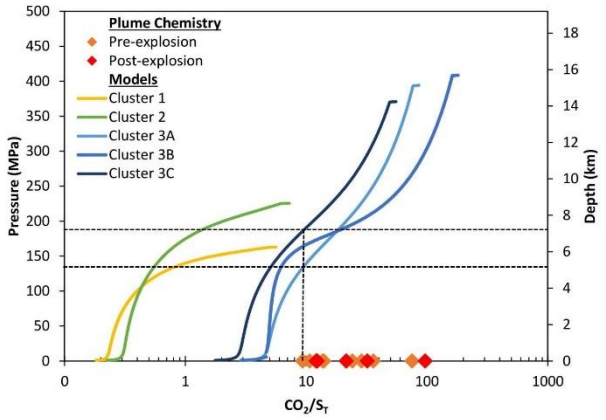

Figure 3.12 – Comparison of CO_2/S_T measured in the plume and CO_2/S_T modelled based on our melt inclusion dataset as a function of pressure and depth suggests magmatic degassing situated between 5.4 and 7.3 km.

	H_2O **(wt.%)**	CO_2 **(ppm)**	**S (ppm)**	**ΔFMQ +**	**Temp (°C)**	**Crystallisation**
Cluster 1	4.20	79	245	2.08	1050	no
Cluster 2	5.20	245	567	2.08	1110	no
Cluster 3A	4.46	3037	452	2.08	1096	no
Cluster 3B	4.46	3037	452	2.08	1096	yes
Cluster 3C	4.88	2506	620	2.08	1120	no

Table 3.2 – Input parameters for the modelling of CO_2/S_T using Sulfur_X (Ding et al., 2023). The three main groups of melt inclusions within our dataset are represented, and an average composition is used for Clusters 1-3B. 3C represents an olivine-hosted melt inclusion with the highest S from Cluster 3.

3.6.3 Magmatic Volatile Budget

The quantity of volatiles residing in the pre-eruptive magma determines the volatile budget of the system, which can help monitoring and modelling of degassing and eruption dynamics (Gerlach & Graeber, 1985), and constraining potential volatile loading into the atmosphere during eruptions (e.g. Devine, et al., 1984). Equation 3.3 was used to estimate the masses of H_2O, CO_2, S, Cl and F in the explosively erupted 2021 magma using the petrological method of Devine et al., (1984), whereby:

$$M_{dv} = X_{MI} V \rho \varepsilon \quad 3.3$$

where M_{dv} is the mass of the dissolved volatile compound, X_{MI} is the concentration of the volatile element measured from melt inclusions, being pre-eruptive volatile contents, V is the volume of erupted magma at 38.5 x 10^6 m^3 (Sparks et al., 2023), ρ is the density of the La Soufrière magma (2671 kg m^{-3}) calculated using the average of the whole rock compositions via DensityX (Iacovino and Till, 2019), ε refers to the factor for converting the volatile elements into their respective compounds, and assuming a crystal free magma. The application of this method reveals that the melt contained at maximum 5.64 Mt H_2O, 0.26 Mt CO_2, 0.13 Mt SO_2, 0.42 Mt HCl, and 0.85 Mt HF, assuming a crystal free melt. These values are deemed conservatively maximum values due to the possibilities of unerupted volumes of magma not taken into account, and due to the entrapment of already degassed magmas (Moune et al., 2007; Figure 3.11C).

The mass of volatiles released to the atmosphere during eruption is calculated as 2.99 Mt for H_2O, 0.14 for CO_2, 0.07 Mt for SO_2, and 0.18 Mt for Cl, based on the difference in volatile contents at entrapment against those during shallow ascent, corrected for the degree of crystallisation using Equation 3.4:

$$M_{dv} = (X_{MI} - X_{GG}) V \rho \varepsilon (1 - C) \quad 3.4$$

where X_{GG} is the concentration of the volatile element in the groundmass glass, and C is the crystal fraction of the magma (45%; Frey et al., 2023). Since S was not measured in the groundmass glass, and because of the degassing trend of S in melt inclusions, the minimum S value of 59 ppm in the melt inclusions was

used as a maximum concentration likely to be contained in the groundmass. The minimum Cl concentration of 846 ppm (Frey et al., 2023), and the average H_2O concentration of 0.2 wt.% (Phillips, 2023) measured in the groundmass glass was used, and we assume that CO_2 is totally degassed in the groundmass at 0 ppm. As F was not measured in the groundmass, and does not have a degassing signature with differentiation, F release from the magma cannot be estimated. Comparing the mass of H_2O, CO_2, SO_2 and HCl dissolved in the melt vs the amount released during eruption indicates that a minimum of 51% H_2O, 54% CO_2, 54% of SO_2, and 41% of HCl in the magma were released into the atmosphere during the explosive phase of the eruption.

In these calculations, SO_2 is assumed to be the only S species. However, S also exists as H_2S, with their relative proportions being dependent on factors such as temperature, pressure and redox conditions. In hydrous magmas, SO_2 exists primarily in oxidised conditions, at values above FMQ+1, whilst H_2S dominates in reduced conditions, below FMQ+1 (Carrol and Webster, 1994). The oxygen fugacity at La Soufrière exists around FMQ+2 (Bouvier et al., 2008), indicating S should exist mainly as SO_2, and that SO_2 mass calculated in the magma is not greatly overestimated. Assuming SO_2 = total S, the mass of calculated SO_2 dissolved in the magma using the petrological method accounts for only 34% of that released during the eruption, estimated using total plume SO_2 emission rates based on satellite observations from TROPOMI (Esse et al., 2023).

This issue of "excess S", where the amount of SO_2 being released during eruptions cannot be accounted for by the low amount of SO_2 dissolved in the melt, as represented by melt inclusions and the groundmass glass, has been identified at arc volcanoes globally, starting with the 1991 eruption of Mount Pinatubo (e.g. Mount Pinatubo, Westrich and Gerlach, 1992; Wallace, 2001; Wallace, 2003; Soufrière Hills Volcano, Christopher et al., 2010). However, it is recognised that there is a large source of error associated with the petrological method. An explanation for this discrepancy is that instead of the melt, there is an alternative main source of S at depth in arc magmas where higher oxygen fugacities and volatile contents enable the exsolution of a S rich gas phase co-existing with the melt (Westrich and Gerlach, 1992; Sharma et al., 2004). In mafic magmas, the amount of S in the gas phase has an upper limit of 1 wt.% due to the low viscosity of the magma, allowing bubbles to escape, while in silicic magmas, the amount of S in the gas phase can range from 0-6 wt.% as the higher viscosity retains bubbles (Scaillet et al., 2003).

We therefore apply the improved petrological method of Scaillet et al., (2003) to estimate the release of SO_2 during the 2021 explosive phase of La Soufrière volcano, taking into account the gas phase. In order

to estimate the amount of S in the gas phase, we use Equation 3.5, following the assumption that S partitioning in magma is dependent on SiO_2 content:

$$\frac{S_{gas}}{S_{melt}} = K_s \,, \qquad 3.5$$

where S in the melt is 620 ppm and K_s is the partition coefficient (Scaillet et al., 2003) for S based on the basaltic andesite compositionof the La Soufrière whole rock products, due to the inability to calculate K_s thermodynamically for this volcano due to the low S contents which inhibit S speciation measurements.

We therefore estimate that, when the amount of S in both the melt and gas phases are taken into consideration, the total SO_2 release from La Soufrière volcano is 0.39 Mt. This is a marked increase from 0.07 Mt when only the melt is accounted for, and our revised estimate is now comparable to satellite-derived measurements of 0.38 Mt of S release over the first few days of the eruption (using TROPOMI; Esse et al., 2023), when 80-90% of the total magma volume was erupted (Sparks et al., 2023). Using this SO_2 release and the mass of magma erupted (103 Mt), we estimate an average magma S content of 0.38 wt.% or 3800 ppm, where a maximum of 620 ppm of that total is dissolved in the melt.

A similar mass of SO_2, calculated using the improved petrological method was released during the 1979 eruption at 0.46 Mt (Figure 3.13A; Scaillet et al., 2003), which was also transitional in style, but from explosive to effusive, and which produced a similar volume of material of 0.05 km^3 compared to 0.04 km^3 in 2021.

In a broader context of the Lesser Antilles arc, the 2021 La Soufrière SO_2 emissions are most comparable to those of Guadeloupe (1010 and 5680 eruptions; Metcalfe et al., 2023b) and Martinique (Scaillet et al., 2023) where SO_2 released ranged from 0.2-0.34 Mt, although their eruptions produced larger volumes of erupted material (Figure 3.13A). Our SO_2 results are however far less than those produced by Soufrière Hills Volcano, Montserrat (2.34 Mt; Scaillet et al., 2003) and the Roseau Tuff of Dominica (180 Mt), both of which have greater eruptive volumes. Overall, SO_2 emissions at La Soufrière and the arc generally fit with emissions from global arc volcanoes.

We also compare HCl emissions calculated above (0.18 Mt) to the 1979 eruption of La Soufrière, as well as volcanoes in the Lesser Antilles and global arcs (Figure 3.13B). The 2021 eruption of La Soufrière saw

the release of an order of a magnitude less HCl than the 1979 eruption (1.16 Mt), despite its similar erupted volume. Our values are, however, broadly similar to those from eruptions at Guadeloupe (0.3-0.4 Mt). Like that of SO_2, HCl emissions from Dominica (11.5 Mt) are much higher than those of other Lesser Antillean volcanoes, likely owing to great volumes of magma erupted as can be seen in Figure 3.13. Of the four global arc volcanoes for which we compare our HCl results (Agung, Mt St Helens, Krakatau, Tambora), La Soufrière and the Lesser Antilles arc fall outside of the trend set by these volcanoes, producing comparable HCl at lower eruptive volumes than Agung and greater HCl emissions at lower eruptive volumes than Mt St Helens (Figure 3.13B).

In terms of global arc volcanoes, La Soufrière is not a significant contributor of volatiles to the atmosphere, and together with other Lesser Antillean volcanoes, has released volatiles on the order of minimum 5.5 Mt of SO_2 and HCl over the last 1000 years (based on the limited calculations available in the literature), which rivals the SO_2 release of the 181 AD eruption of Taupo volcano at 4.93 Mt for a similar erupted volume.

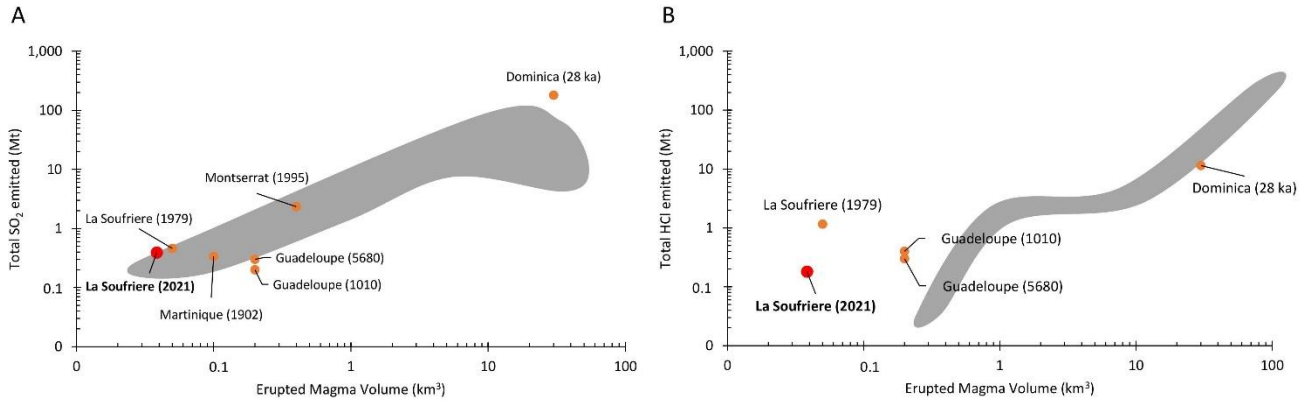

Figure 3.13 – Volatile release vs magma volume at arc volcanoes globally. [A] Total SO_2 taking into account the gas phase for Lesser Antillean volcanoes. La Soufrière is generally comparable with other volcanoes in the arc, except for Dominica with high SO_2 and erupted material. [B] HCl emissions from the melt phase for Lesser Antillean volcanoes. On both graphs, the grey shaded areas represent literature data on arc volcanoes outside of the Lesser Antilles. Data for SO_2 from Scaillet et al., (2003) are presented for La Soufrière's 1979 eruption, Soufrière Hills Volcano, Montserrat, Roseau Tuff, Dominica and Mt Pelée, Martinique in the Lesser Antilles, and Agung, Bezymianny, Coseguina, El Chichon, Fuego, Huaynaputina, Katmai, Krakatau, Minoan, Mt St Helens, Pinatubo, Rabaul, Redoubt, Ruiz, Santa Maria, Tambora, Tarawera, Taupo and Unzen for global arcs. SO_2 data from Guadeloupe are from Metcalfe et al., (2023b) for the 1010 and 5680 eruptions. HCl data is from Devine et al., (1986) for Agung, Ht St Helens, Krakatau and Tambora volcanoes.

3.7 Conclusions

We have provided the full suite of volatile element compositions for the 2021 explosive products of La Soufrière (St Vincent), including the first measurements of total magmatic CO_2 in melt inclusions at this volcano. Concentrations of H_2O, S, Cl and F are generally comparable with previous measurements and estimates at La Soufrière, and the first measurements of total CO_2 (where total CO_2 = CO_2 in the glass due to empty bubbles) range 3-661 ppm, with two measurements of 2506 and 3567 ppm. Based on the solubility relationship between H_2O and CO_2, melt inclusions yield minimum depths of 2.4-8.9 km (mean 6.4 km) beneath La Soufrière. This depth range is similar to estimates from geophysical data (deformation and seismicity) during the course of the 2021 eruption, and to petrologically-derived depths for pre-historic and the majority of historic eruptions. The depth range also corroborates the evidence for S degassing, which begins at <9 km depth at La Soufrière, and is the depth of final residence within the crust after migration and mixing of magma froma deeper storage region.

Independent barometric estimates based on clinopyroxene-only compositions either yield a similar depth range (1.1-8.0 km) to the melt inclusions volatiles when the Wang (2021) model is employed, or greater depths (6.1-20.3 km) using Equation 30 of Putirka, (2008) that more closely match earlier studies of clinopyroxene from this eruption. However, significant depth uncertainties in clinopyroxene-only barometry (±~7km) mean that this technique cannot reliably differentiate between mid-crustal reservoirs.

We used several geothermometers to calculate magma temperature based on major element and H_2O contents, and show that temperatures of the 2021 eruptions are 970-1120 °C using the best fit thermometers, similar to published data for pre-historic and the 1979 eruptions. The release of H_2O, S and Cl were also quantified using the petrological method, which revealed that 2.99 Mt H_2O, 0.39 Mt SO_2, and 0.18 Mt Cl were released into the atmosphere over April 9-22, 2021, with SO_2 emissions closely matching satellite-derived values.

3.8 Supplementary Material C3

SIMS Calibration

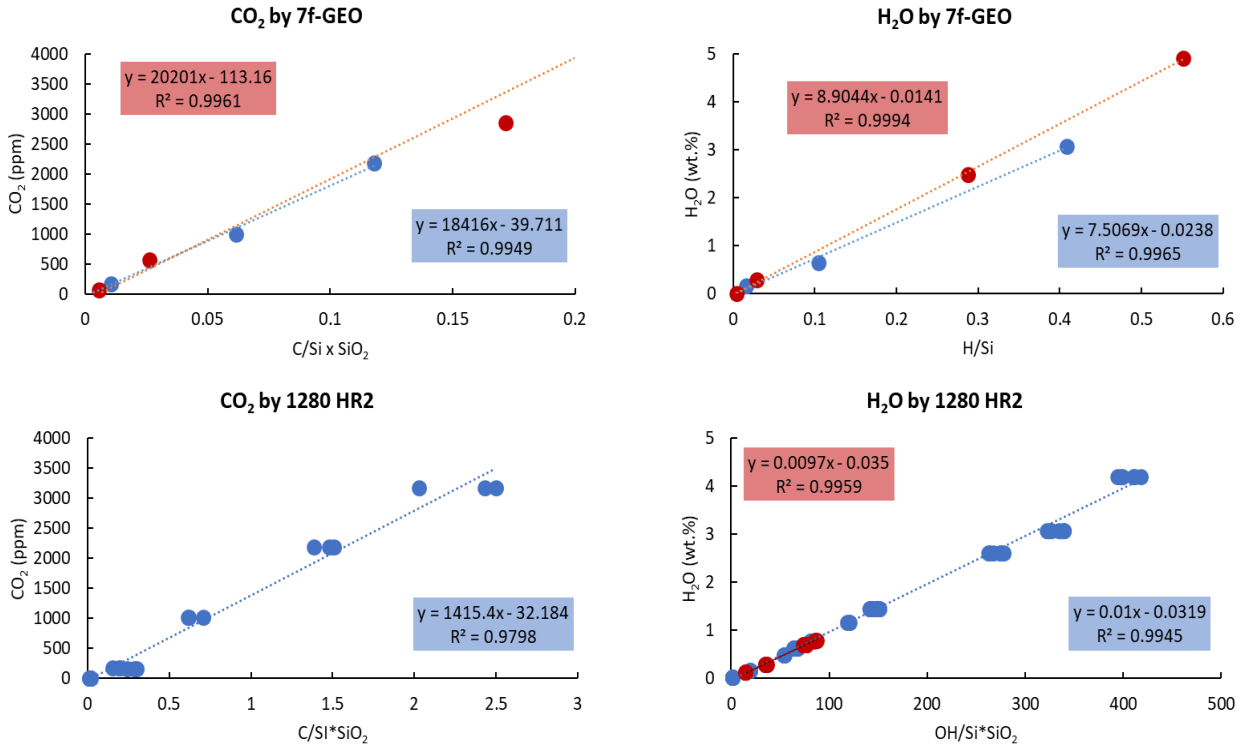

Supplementary Figure 3.S1 – Comparison of calibration curves used to calculate CO_2 and H_2O via different SIMS instruments. CO_2 and H_2O were analysed via Cameca IMS 7f-GEO using the curves of CO_2 vs C/Si * SiO_2 and H_2O vs H/Si based on basaltic and rhyolitic standards and via Cameca IMS 1280 HR2 using the curves of CO_2 vs C/Si*SiO_2 and H_2O vs OH/Si*SiO_2 for basaltic and, rhyolitic standards.

EPMA Standards

Major & Volatile Elements	Standard	Diffraction Crystal	Counting Time (s)	Beam Current (nA)
Si	Wollastonite	TAP	10	4
Ti	TiMnO3	LPET	10	4
Al	Orthoclase	LTAP	20	4
Fe	Fayalite	LLIF	20	4
Mn	TiMnO3	LLIF	10	4
Mg	Forsterite	TAP	10	4
Ca	Wollastonite	LPET	10	4
Na	Albite	LTAP	10	4
K	Orthoclase	LPET	10	4
P	Apatite	PET	30	4
S	VG2	LPET	20 x 5[1]	40
Cl	scap	LPET	20 x 5[1]	40
F	CaF2	TAP, LTAP	20 x 5[1]	40

Supplementary Table 3.S1 - Analytical conditions for the application of EPMA on melt inclusion glasses.

[1] – Volatile elements were analysed with a counting time of 20 seconds for 5 cycles in the same spot, amounting to 100s for each spot.

Major Elements	Standard	Diffraction Crystal	Counting Time (s)	Beam Current (nA)
Si[1]	San Carlos	TAP	10	15
	Wollastonite			
Ti	TiMnO3	PET	10	15
Al	Orthoclase	LTAP	10	15
Fe	Fayalite	LLIF	10	15
Mn	TiMnO3	LLIF	10	15
Mg	Forsterite	TAP	10	15
Ca	Wollastonite	LPET	10	15
Na	Albite	LTAP	10	15
K	Orthoclase	LPET	10	15
Cr	Cr2O3	PET	10	15

Supplementary Table 3.S2 - Analytical conditions for the application of EPMA on crystals hosting melt inclusions

[1] – San Carlos olivine was used to calibrate for Si when measuring olivine crystals, and wollastonite when measuring plagioclase and pyroxene crystals.

Whole Rock Compositions

	Whole Rock Samples					
	Dome	**Unit 1**	**Unit 2**	**Unit 3**	**Unit 5**	**Unit 5 Dense**
		LS21-99a	**LS-2189**	**LS21-87**	**LS21-96**	
SiO_2	54.27	54.05	53.96	53.96	52.81	54.21
TiO_2	0.99	0.91	0.91	0.93	0.94	0.92
Al_2O_3	17.72	18.49	18.71	18.86	18.23	18.19
Fe_2O_3	9.30	9.11	8.94	9.38	9.21	8.83
MnO	0.21	0.17	0.17	0.18	0.17	0.18
MgO	4.06	4.26	3.97	4.38	3.96	3.93
CaO	8.40	8.91	8.94	9.15	8.70	8.50
Na_2O	3.50	3.42	3.46	3.36	3.34	3.44
K_2O	0.55	0.49	0.50	0.51	0.52	0.54
P_2O_5	0.13	0.11	0.11	0.12	0.13	0.13
Ba	0.01	0.01	0.01	0.01	0.01	0.01
Sr	0.02	0.02	0.02	0.02	0.02	0.02
H_2O	0.03	-0.29	0.07	-0.28	0.27	0.00
Total	99.20	99.70	99.80	100.60	97.80	98.90

Supplementary Table 3.S3 – Whole rock compositions in wt.% of dome and scoria samples analysed by ICP-OES. Fe_2O_3 is total iron and H_2O is loss on ignition.

Host compositions

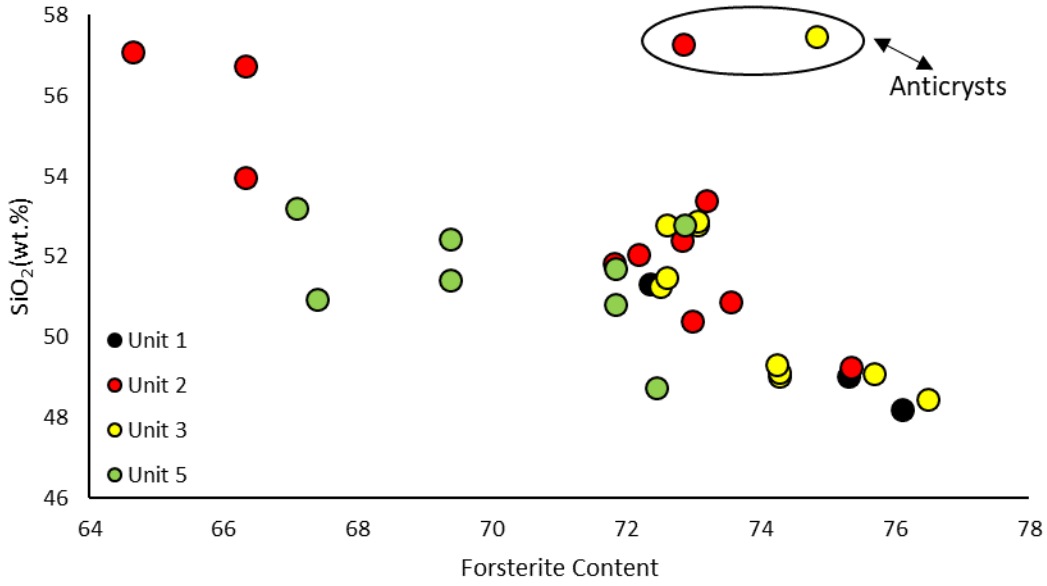

Supplementary Figure 3.S2 - SiO_2 contents of olivine hosted melt inclusions as a function of host olivine compositions. The correlation indicates phenocrysts, while two olivines demonstrate anticryst behavior.

Melt Inclusion Reconstruction

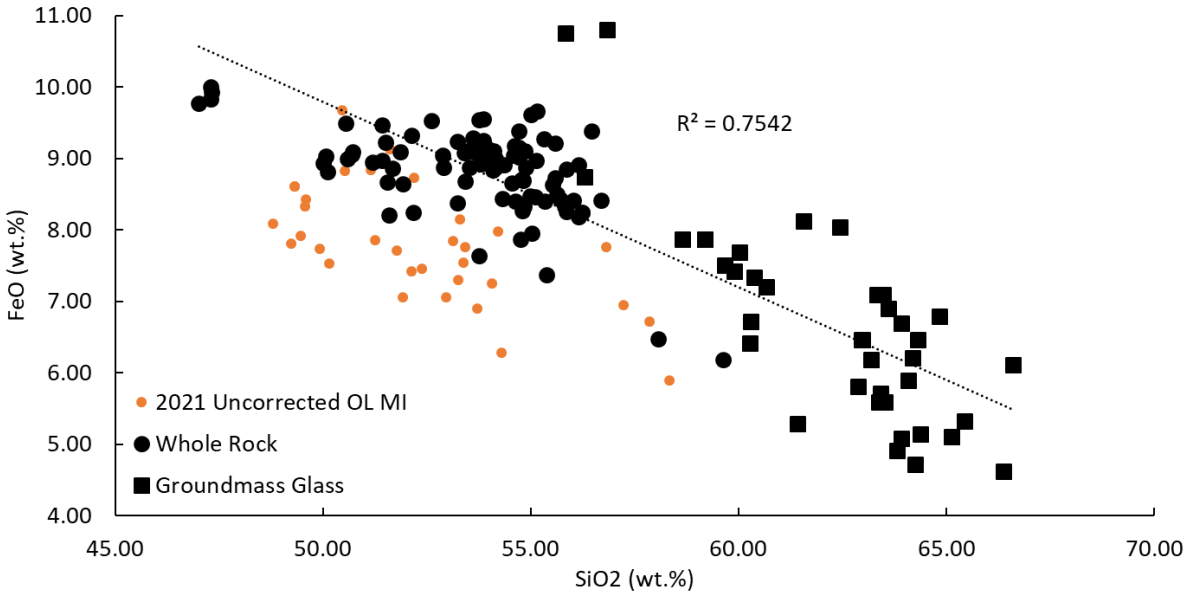

Supplementary Figure 3.S3 – Liquid line of descent of FeO vs SiO_2 and uncorrected olivine hosted melt inclusions showing up to 2 wt.% Fe loss in inclusions.

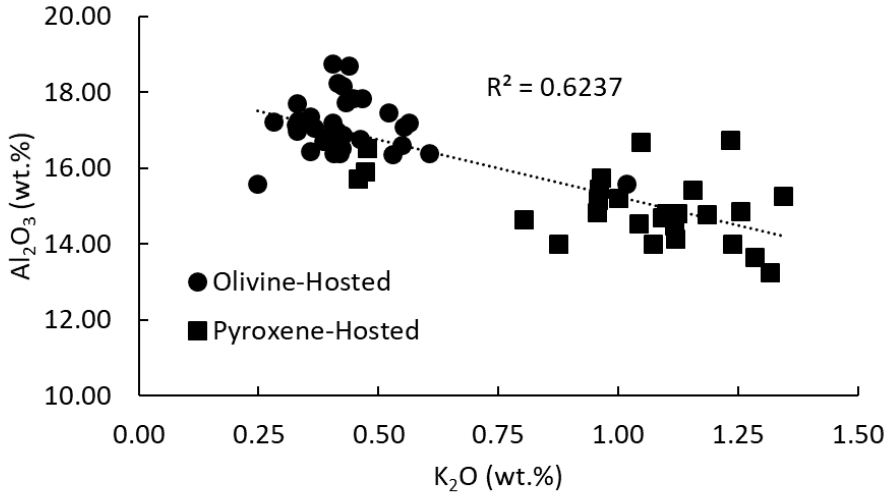

Supplementary Figure 3.S4 – Liquid line of descent of olivine- and pyroxene-hosted inclusions showing a negative correlation of Al_2O_3 with K_2O used to predict plagioclase-hosted inclusion Al_2O_3 values for reconstruction.

Melt Inclusion Bubbles

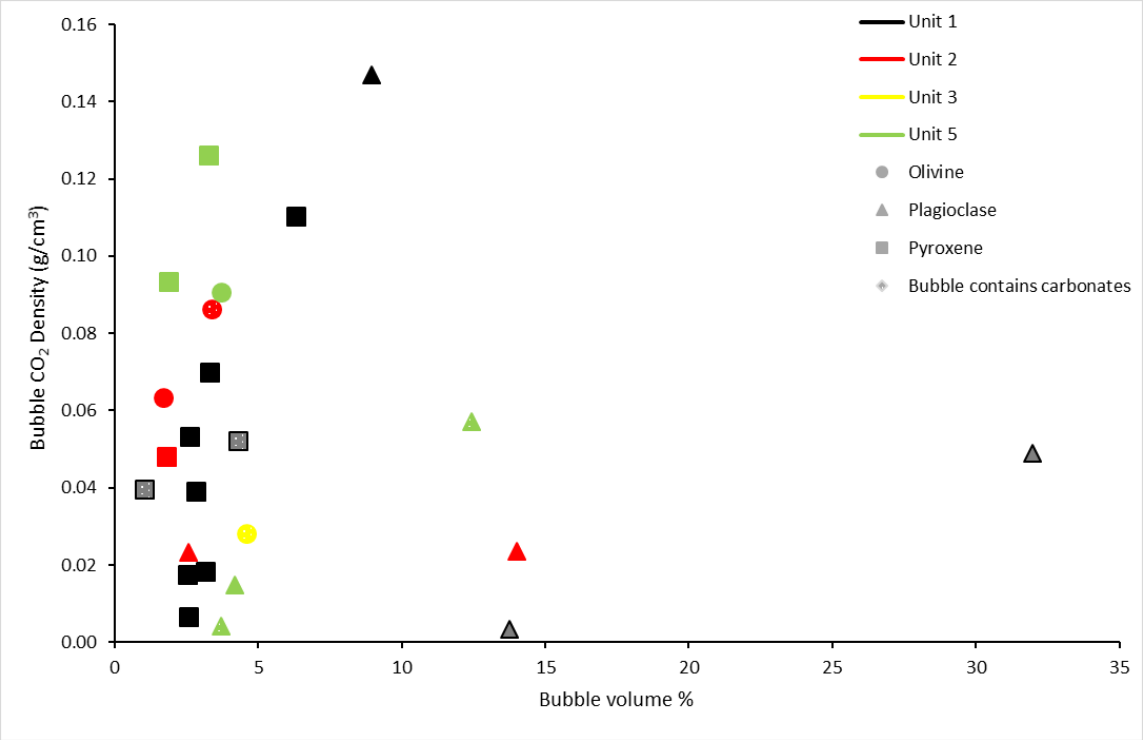

Supplementary Figure 3.S5 – Bubble CO_2 density as a function of bubble volume. Bubbles with CO_2 vapour + carbonates have similar CO_2 densities as bubble with only CO_2 vapour.

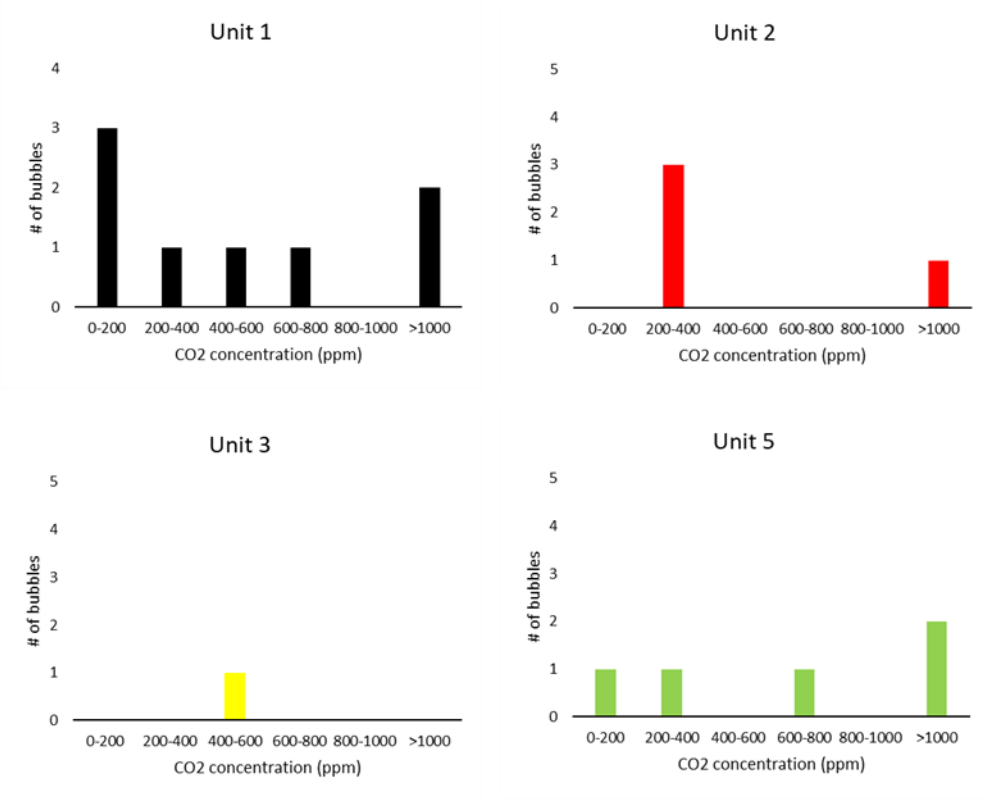

Supplementary Figure 3.S6 – CO_2 concentration of bubbles in melt inclusions from La Soufrière.

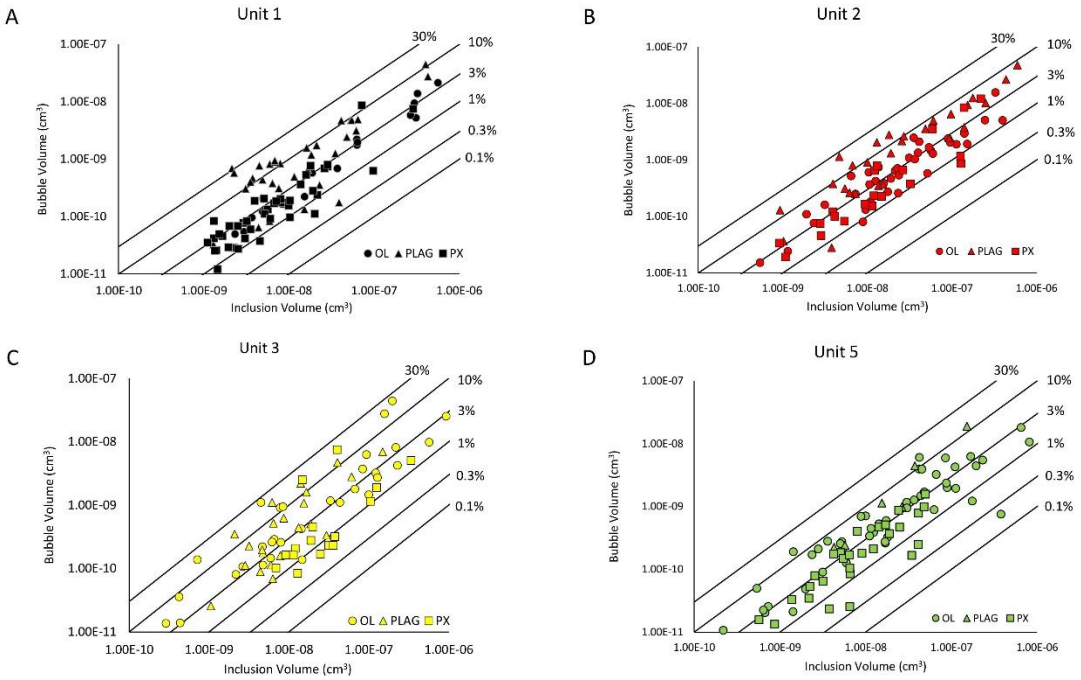

Supplementary Figure 3.S7 – Bubble volume vs inclusion volume for bubbles analysed by Raman spectroscopy. Isovolumetric lines indicate volume percentages occupied by each bubble in their respective melt inclusions. [A] Unit 1. [B] Unit 2. [C] Unit 3. [D] Unit 5.

Melt Inclusion Bubble CO_2 Reconstruction

Melt inclusion bubble CO_2 reconstruction

Sample ID	Bubble Volume (cm^3)	Total Inclusion Volume (cm^3)	Bubble Volume Fraction	Corrected Fermi Diad (cm^{-1})	Error (cm^{-1})	CO_2 density (g cm^{-3})	Error (g cm^{-3})	Glass density (g m^{-3})	CO_2 from bubble (ppm)	CO_2 in glass (ppm)	Total CO_2 (ppm)
Olivine Hosted											
LSS_U2_OL_010_MI1	1.90E-09	1.13E-07	0.02	102.83	0.03	0.06	0.02	2.37	360	n.d.	n.d.
LSS_U2_OL_025_MI2	1.35E-09	3.98E-08	0.03	102.89	0.04	0.09	0.02	2.37	1007	n.d.	n.d.
LSS_U3_OL_001_MI2	9.72E-10	2.12E-08	0.05	102.73	0.02	0.03	0.01	2.37	572	n.d.	n.d.
LSS_U5_OL_034	5.28E-10	1.43E-08	0.04	102.90	0.01	0.09	0.01	2.37	1471	n.d.	n.d.
Plagioclase Hosted											
LSS_U2_PLAG_020_MI1	3.50E-10	1.36E-08	0.03	102.71	0.03	0.02	0.01	2.37	205	n.d.	n.d.
LSS_U5_PLAG_002_MI1	9.87E-10	2.66E-08	0.04	102.66	0.02	0.004	0.01	2.37	68	n.d.	n.d.
LSS_U5_PLAG_002_MI4	2.41E-10	5.74E-09	0.04	102.69	0.02	0.01	0.01	2.37	275	n.d.	n.d.
Pyroxene Hosted											
LSS_U1_PX_001_MI1	6.43E-10	6.24E-08	0.01	102.76	0.02	0.04	0.01	2.37	174	n.d.	n.d.
LSS_U1_PX_006_MI2	5.29E-10	1.59E-08	0.03	102.84	0.03	0.07	0.01	2.37	1014	n.d.	n.d.
LSS_U1_PX_007_MI3	7.68E-10	1.80E-08	0.04	102.79	0.04	0.05	0.02	2.37	986	n.d.	n.d.
LSS_U1_PX_015	4.16E-11	1.32E-09	0.03	102.70	0.03	0.02	0.02	2.37	253	n.d.	n.d.
LSS_U1_PX_024_MI1	8.26E-11	3.20E-09	0.03	102.67	0.02	0.01	0.01	2.37	72	n.d.	n.d.
LSS_U1_PX_024_MI2	6.84E-10	2.62E-08	0.03	102.80	0.02	0.05	0.01	2.37	602	n.d.	n.d.
LSS_U1_PX_025_MI1	2.01E-10	7.94E-09	0.03	102.70	0.03	0.02	0.02	2.37	193	n.d.	n.d.
LSS_U1_PX_025_MI3	8.03E-10	2.83E-08	0.03	102.76	0.02	0.04	0.01	2.37	482	n.d.	n.d.
LSS_U2_PX_023_MI1	1.39E-09	7.78E-08	0.02	102.78	0.03	0.05	0.02	2.37	292	n.d.	n.d.
LSS_U5_PX_001_MI3	4.71E-10	1.43E-08	0.03	103.00	0.01	0.13	0.01	2.37	1807	n.d.	n.d.
LSS_U5_PX_001_MI5	4.68E-10	2.49E-08	0.02	102.91	0.03	0.09	0.02	2.37	753	n.d.	n.d.

n.d. - not determined
Glass density was calculated for one generic inclusion

Supplementary Table 3.S4 - Calculation of CO_2 in bubbles at La Soufrière from the 2020/2021 eruption.

Melt Inclusion Compositions

Sample ID	Major Elements (wt%.)								
	SiO_2	TiO_2	Al_2O_3	FeO	MgO	CaO	Na_2O	K_2O	Total
Olivine-Hosted Melt Inclusions									
LSS_U1_OL_003	49.04	0.97	16.99	9.44	3.52	9.43	2.69	0.33	92.40
LSS_U1_OL_008	51.32	1.11	17.75	9.19	2.72	8.88	3.41	0.43	94.81
LSS_U1_OL_010	48.20	0.95	17.14	9.64	3.80	9.45	2.51	0.33	92.02
LSS_U2_OL_001	50.39	1.19	17.35	9.45	2.80	9.27	3.05	0.36	93.87
LSS_U2_OL_003	50.87	1.18	18.76	9.27	3.13	9.08	3.18	0.40	95.88
LSS_U2_OL_006	53.39	0.83	16.77	8.59	3.08	8.42	2.98	0.46	94.53
LSS_U2_OL_015	49.24	1.29	17.23	9.49	3.82	9.79	2.55	0.28	93.68
LSS_U2_OL_017	52.42	0.85	16.38	8.60	3.26	8.25	2.28	0.42	92.47
LSS_U2_OL_021	57.27	0.67	15.59	7.45	2.72	7.38	3.38	0.25	94.70
LSS_U2_OL_022	51.82	1.11	16.72	9.31	2.57	8.45	3.12	0.40	93.49
LSS_U2_OL_028	52.06	0.92	16.60	8.67	3.06	7.93	3.46	0.55	93.27
LSS_U2_OL_029_MI1	56.73	1.04	16.40	7.87	1.76	5.80	4.64	0.60	94.85
LSS_U2_OL_029_MI2	53.97	1.40	17.10	8.68	1.99	7.13	4.36	0.55	95.18
LSS_U2_OL_030	57.09	1.06	16.38	8.06	1.67	6.55	4.21	0.53	95.55
LSS_U3_OL_002_MI1	52.80	0.95	16.40	8.64	3.05	8.31	2.98	0.41	93.54
LSS_U3_OL_002_MI2	52.90	0.83	16.88	8.66	2.97	8.22	3.17	0.42	94.06
LSS_U3_OL_003	48.45	0.95	17.25	9.60	4.08	9.20	2.47	0.33	92.33
LSS_U3_OL_004	49.09	1.03	17.70	9.69	3.65	9.60	2.72	0.33	93.80
LSS_U3_OL_010	51.25	0.97	17.21	9.27	2.65	8.40	3.17	0.40	93.32
LSS_U3_OL_011_MI2	52.78	1.08	18.17	9.03	2.65	8.59	3.43	0.42	96.16
LSS_U3_OL_011_MI3	51.48	1.15	17.85	9.13	2.81	8.78	3.46	0.45	95.11
LSS_U3_OL_013_MI1	49.08	1.13	16.76	9.59	3.20	8.93	2.85	0.39	91.93
LSS_U3_OL_018_MI1	49.33	1.07	17.05	9.50	3.11	9.10	2.91	0.37	92.43
LSS_U3_OL_023	57.46	1.42	15.60	7.87	2.49	5.28	4.52	1.02	95.66
LSS_U5_OL_002	50.82	1.03	18.24	9.42	2.75	8.95	3.24	0.41	94.86
LSS_U5_OL_003	52.80	1.40	17.20	8.81	2.77	8.49	4.03	0.56	96.06
LSS_U5_OL_004	50.95	0.62	18.71	9.61	1.90	9.37	3.31	0.44	94.91
LSS_U5_OL_023	53.19	1.12	17.48	8.93	2.30	7.97	3.53	0.52	95.04
LSS_U5_OL_032	48.75	1.16	17.84	9.66	3.07	9.43	3.24	0.47	93.62
LSS_U5_OL_037_MI7	51.43	1.16	16.53	9.25	2.54	7.92	3.11	0.42	92.36
LSS_U5_OL_037_MI8	52.44	0.98	16.44	8.91	2.42	7.46	3.08	0.36	92.09

LSS_U5_OL_040	51.70	1.11	16.98	8.95	2.76	8.66	3.39	0.41	93.97
Plagioclase-Hosted Melt Inclusions									
LSS_U1_PLAG_002	52.37	0.93	17.02	8.11	3.62	7.75	3.22	0.42	93.44
LSS_U1_PLAG_003	53.65	0.88	16.93	7.70	3.46	7.68	3.43	0.47	94.21
LSS_U1_PLAG_006	54.84	1.01	16.09	8.28	2.96	6.32	2.64	0.72	92.86
LSS_U1_PLAG_007	60.77	0.74	15.08	6.03	1.41	4.41	4.10	1.23	94.16
LSS_U1_PLAG_008	63.40	0.79	14.93	4.39	1.11	3.70	4.39	1.40	94.30
LSS_U1_PLAG_018	62.52	0.76	15.07	5.74	1.46	4.34	4.60	1.19	96.11
LSS_U1_PLAG_019	50.91	0.83	17.03	7.84	4.73	8.53	2.95	0.42	93.24
LSS_U1_PLAG_024_MI1	53.86	0.66	16.88	7.69	3.86	7.58	2.95	0.50	93.98
LSS_U1_PLAG_024_MI3	53.54	0.72	16.77	8.18	4.03	7.60	2.46	0.50	93.80
LSS_U2_PLAG_009	56.67	0.90	16.63	7.43	2.92	6.84	3.93	0.54	95.86
LSS_U2_PLAG_014	53.07	0.94	17.11	7.93	3.43	7.81	3.43	0.41	94.14
LSS_U2_PLAG_016	53.89	1.03	16.43	8.26	3.38	6.86	3.67	0.61	94.12
LSS_U2_PLAG_028	55.05	0.76	17.01	7.37	3.28	7.23	3.50	0.45	94.64
LSS_U3_PLAG_005	61.37	0.92	15.43	6.20	1.76	4.56	1.56	1.17	92.95
LSS_U3_PLAG_008	59.76	0.99	14.83	6.47	1.66	4.63	3.81	1.27	93.42
LSS_U3_PLAG_009	52.12	0.84	16.75	7.97	3.84	7.49	3.21	0.54	92.76
LSS_U3_PLAG_010	52.65	0.91	17.04	8.81	3.90	7.74	3.45	0.44	94.93
LSS_U3_PLAG_020	53.26	0.88	16.86	8.54	3.41	6.95	3.45	0.50	93.84
LSS_U3_PLAG_021	52.91	0.98	16.86	8.23	3.80	7.67	3.24	0.47	94.17
Orthopyroxene-Hosted Melt Inclusions									
LSS_U1_OPX_007	65.13	0.56	14.13	6.25	1.95	3.30	4.37	1.12	96.81
LSS_U1_OPX_009	58.12	1.10	14.54	7.01	2.48	4.92	4.28	1.04	93.50
LSS_U1_OPX_013	60.03	0.84	14.49	7.17	2.38	4.28	4.49	1.12	94.81
LSS_U1_OPX_028	60.15	0.90	14.79	6.74	2.39	4.33	4.58	1.18	95.05
LSS_U3_OPX_005_MI1	59.33	1.22	15.46	6.77	2.25	5.16	4.37	0.96	95.52
LSS_U3_OPX_005_MI2	60.02	1.05	15.21	6.65	1.97	5.13	4.46	1.00	95.49
LSS_U5_OPX_004	61.62	1.13	14.82	6.56	1.91	4.68	4.46	1.12	96.30
LSS_U5_OPX_1A	58.17	1.21	15.15	7.08	2.91	5.28	4.55	0.96	95.32
LSS_U5_OPX_8A	60.75	1.07	14.69	7.60	2.39	4.72	4.53	1.09	96.84
Clinopyroxene-Hosted Melt Inclusions									
LSS_U1_CPX_001	58.86	0.87	14.00	6.44	2.91	6.08	4.32	1.07	94.57
LSS_U1_CPX_018	60.37	0.90	13.99	6.05	2.54	5.58	4.09	0.88	94.40

LSS_U1_CPX_023_MI1	54.93	0.63	16.75	6.60	3.33	6.85	4.04	1.23	94.37
LSS_U1_CPX_023_MI2	54.30	0.91	15.26	6.87	3.36	7.70	3.54	1.34	93.27
LSS_U2_CPX_002	58.11	1.19	14.02	6.61	3.33	6.16	4.03	1.24	94.67
LSS_U2_CPX_006	59.11	1.09	14.81	6.07	1.68	4.45	4.22	1.10	92.53
LSS_U2_CPX_007_MI1	57.55	0.89	15.73	6.87	2.64	5.94	3.78	0.46	93.85
LSS_U2_CPX_007_MI3	61.38	0.77	13.25	5.83	2.95	5.68	3.83	1.32	95.01
LSS_U2_CPX_017	60.12	1.14	14.86	5.93	1.69	4.24	4.31	1.25	93.54
LSS_U2_CPX_018	55.48	0.90	16.53	7.26	3.34	7.10	2.79	0.48	93.88
LSS_U3_CPX_002	56.42	0.97	15.91	7.00	2.71	6.02	3.64	0.47	93.14
LSS_U3_CPX_007	58.07	1.06	14.65	6.84	2.95	5.64	3.18	0.80	93.18
LSS_U3_CPX_008	58.70	0.97	14.82	6.73	2.18	4.84	4.10	0.96	93.30
LSS_U3_CPX_009	59.64	0.97	15.74	6.56	2.20	4.55	4.83	0.96	95.48
LSS_U3_CPX_010	59.75	1.01	15.42	5.90	2.05	4.91	4.61	1.15	94.80
LSS_U5_CPX_002	55.99	0.99	16.69	6.98	2.60	6.05	3.98	1.05	94.33
LSS_U5_CPX_2B	60.87	0.87	13.67	6.53	2.86	5.49	3.93	1.28	95.50

b.d.l. - below detection limit

Supplementary Table 3.S5 – Major element compositions of La Soufrière 2020/2021 melt inclusions.

Sample ID	Volatile Elements										PEC%	KD
	H_2O (wt.%)	H_2O error	CO_2 (ppm)	CO_2 error	S (ppm)	S error	Cl (ppm)	Cl error	F (ppm)	F error		
Olivine-Hosted Melt Inclusions												
LSS_U1_OL_003	3.94	0.20	129	26	576	75	1264	63	339	115	5.97	0.32
LSS_U1_OL_008	3.97	0.20	37	19	361	54	1537	154	267	120	1.18	0.31
LSS_U1_OL_010	5.10	0.26	661	132	562	56	1156	35	346	384	3.54	0.33
LSS_U2_OL_001	4.92	0.25	b.d.l.	-	467	121	1452	73	396	419	0.78	0.32
LSS_U2_OL_003	3.62	0.18	-	-	411	25	1560	109	205	280	6.03	0.31
LSS_U2_OL_006	5.49	0.27	-	-	291	105	1577	63	216	469	3.66	0.36
LSS_U2_OL_015	-	-	-	-	511	66	1318	119	453	516	6.79	0.33
LSS_U2_OL_017	4.92	0.25	b.d.l.	-	304	73	1638	115	268	317	5.14	0.38
LSS_U2_OL_021	-	-	-	-	-	-	-	-	-	-	4.97	0.36
LSS_U2_OL_022	-	-	-	-	310	102	1487	89	352	222	-1.62	0.35
LSS_U2_OL_028	-	-	-	-	344	96	2051	164	b.d.l..	-	5.90	0.36
LSS_U2_OL_029_MI1	-	-	-	-	163	70	1885	132	692	228	2.55	0.35
LSS_U2_OL_029_MI2	-	-	-	-	256	51	2012	181	769	323	1.29	0.35
LSS_U2_OL_030	4.80	0.24	b.d.l.	-	174	61	1593	143	704	394	-2.03	0.35
LSS_U3_OL_002_MI1	-	-	-	-	325	58	1607	129	239	342	3.57	0.36
LSS_U3_OL_002_MI2	-	-	-	-	297	95	1604	160	b.d.l.	-	3.66	0.36
LSS_U3_OL_003	4.88	0.24	2506	501	620	130	1274	127	b.d.l.	-	5.21	0.34
LSS_U3_OL_004	5.32	0.27	60	32	592	83	1213	61	200	64	2.92	0.33
LSS_U3_OL_010	-	-	-	-	319	89	1538	123	316	205	-1.30	0.33
LSS_U3_OL_011_MI2	3.46	0.17	b.d.l.	-	306	83	1647	99	266	221	0.83	0.31
LSS_U3_OL_011_MI3	3.40	0.17	b.d.l.	-	356	53	1560	62	384	222	2.50	0.31
LSS_U3_OL_013_MI1	5.12	0.26	-	-	545	104	1439	43	b.d.l..	-	0.93	0.33
LSS_U3_OL_018_MI1	5.13	0.26	b.d.l.	-	494	64	1310	79	338	497	0.72	0.32
LSS_U3_OL_023	-	-	-	-	165	23	3375	203	592	225	0.79	0.34
LSS_U5_OL_002	4.15	0.41	b.d.l.	-	293	21	1510	106	237	291	0.86	0.32
LSS_U5_OL_003	3.49	0.35	-	-	294	29	2028	122	539	297	4.56	0.30
LSS_U5_OL_004	4.02	0.40	b.d.l.	-	310	68	1576	173	403	387	-3.92	0.31
LSS_U5_OL_023	-	-	-	-	197	83	1758	35	475	361	-0.28	0.35
LSS_U5_OL_032	-	-	-	-	836	602	1696	187	260	320	5.11	0.33
LSS_U5_OL_037_MI7	-	-	-	-	395	47	1707	120	332	246	-0.73	0.37
LSS_U5_OL_037_MI8	-	-	-	-	396	52	1558	62	285	160	-1.98	0.37

LSS_U5_OL_040	-	-	-	-	323	61	1806	163	b.d.l..	219	3.91	0.32
Plagioclase-Hosted Melt Inclusions												
LSS_U1_PLAG_002	3.69	0.18	49	26	242	53	2102	126	716	50	20.63	-
LSS_U1_PLAG_003	3.65	0.18	b.d.l.	-	195	27	1364	136	819	336	18.70	-
LSS_U1_PLAG_006	5.33	0.27	-	-	236	92	3414	102	880	458	15.77	-
LSS_U1_PLAG_007	-		-	-	92	43	2134	107	372	379	-	-
LSS_U1_PLAG_008	-		-	-	116	50	1623	97	390	105	-	-
LSS_U1_PLAG_018	4.34	0.22	-	-	128	11	2112	63	677	467	-	-
LSS_U1_PLAG_019	-		-	-	-	-	-	-	-	-	19.67	-
LSS_U1_PLAG_024_MI1	4.03	0.20	328	66	188	45	2464	74	731	409	23.53	-
LSS_U1_PLAG_024_MI3	4.16	0.21	-		204	35	2550	128	701	456	20.63	-
LSS_U2_PLAG_009	3.08	0.15	48	25	170	70	1873	506	624	443	9.88	-
LSS_U2_PLAG_014	3.73	0.19	b.d.l.	-	249	42	1300	169	623	255	17.72	-
LSS_U2_PLAG_016	-		-	-	212	25	2515	226	603	235	9.88	-
LSS_U2_PLAG_028	3.12	0.16	-	-	138	62	1204	84	610	189	14.79	-
LSS_U3_PLAG_005	-		-	-	116	31	2251	90	545	251	-	-
LSS_U3_PLAG_008	-		-	-	-	-	-	-	-	-	-	-
LSS_U3_PLAG_009	-		-	-	190	59	1534	77	746	410	22.56	-
LSS_U3_PLAG_010	-		-	-	168	67	1842	55	650	267	18.70	-
LSS_U3_PLAG_020	4.04	0.20	3567	713	285	48	2806	196	450	175	15.77	-
LSS_U3_PLAG_021			-	-	273	79	1400	84	517	393	16.75	-
Orthopyroxene-Hosted Melt Inclusions												
LSS_U1_OPX_007	-		-	-	b.d.l.	-	990	40	714	48	4.62	0.29
LSS_U1_OPX_009	-		-	-	152	53	2236	134	519	197	5.20	0.29
LSS_U1_OPX_013	-		-	-	164	51	2492	174	528	444	5.55	0.29
LSS_U1_OPX_028	-		-	-	306	67	2601	104	451	275	6.45	0.29
LSS_U3_OPX_005_MI1	-		-	-	122	73	2103	126	560	196	-	0.25
LSS_U3_OPX_005_MI2	-		-	-	132	59	2130	85	457	320	-	0.23
LSS_U5_OPX_004	-		-	-	90	22	2292	115	486	311	-	0.24
LSS_U5_OPX_1A	3.34	0.33	162	16	173	42	2204	154	701	442	3.70	0.29
LSS_U5_OPX_8A	3.66	0.37	135	14	157	46	2199	66	552	464	3.10	0.29
Clinopyroxene-Hosted Melt Inclusions												
LSS_U1_CPX_001	-	-	-	-	175	63	2501	100	543	261	13.00	0.28
LSS_U1_CPX_018	4.19	0.21	-	-	126	88	1878	131	414	103	7.30	0.28

LSS_U1_CPX_023_MI1	-	-	-	-	150	60	3796	304	595	363	11.80	0.28
LSS_U1_CPX_023_MI2	-	-	-	-	107	64	5083	203	554	227	10.80	0.28
LSS_U2_CPX_002	-	-	-	-	154	48	3116	93	476	124	12.00	0.28
LSS_U2_CPX_006	4.75	0.24	b.d.l.	-	100	42	2287	91	602	211	-	0.21
LSS_U2_CPX_007_MI1	5.27	0.26	b.d.l.	-	213	64	1724	86	489	337	-	0.23
LSS_U2_CPX_007_MI3	4.84	0.24	434	87	59	31	981	108	438	302	8.60	0.28
LSS_U2_CPX_017	-	-	-	-	83	43	2414	145	470	348	-	0.21
LSS_U2_CPX_018	4.62	0.23	b.d.l.	-	260	60	1775	35	408	196	10.80	0.28
LSS_U3_CPX_002	5.85	0.29	b.d.l.	-	293	53	1607	177	286	614	-	0.23
LSS_U3_CPX_007	3.94	0.20	71	38	185	57	2102	126	633	260	8.65	0.28
LSS_U3_CPX_008	-	-	-	-	135	58	2113	169	472	250	-	0.22
LSS_U3_CPX_009	-	-	-	-	139	49	2274	91	610	256	-	0.24
LSS_U3_CPX_010	4.63	0.23	139	28	139	56	2144	150	527	342	-	0.21
LSS_U5_CPX_002	-	-	-	-	139	33	2853	143	592	379	-	0.21
LSS_U5_CPX_2B	3.57	0.18	136	14	89	102	2523	101	503	317	8.20	0.28

b.d.l. - below detection limit

Supplementary Table 3.S6 – Volatile element compositions of La Soufrière 2020/2021 melt inclusions. PEC and K_D are also given for each melt inclusion.

4 Investigating diffuse CO_2 degassing at Soufrière Hills Volcano, Montserrat and La Soufrière volcano, St Vincent

4.1 Abstract

Soufrière Hills Volcano (SHV), Montserrat and La Soufrière volcano, St Vincent are characterised by relatively high passive CO_2 emissions through the plume of up to 5500 and 7000 tonnes/day respectively. The process of diffuse degassing, while important since it can produce CO_2 emissions which rival that of passive degassing, is poorly studied in the Lesser Antilles. We provide preliminary CO_2 surveys in areas of surface manifestation of the hydrothermal systems (hot springs) at the aforementioned volcanoes using the accumulation chamber method, and produce logarithmic probability plots to distinguish between sources of CO_2, as well as ^{13}C isotopic compositions to identify the source. We find that the diffuse contribution to the SHV significantly decreased from average 4000 to 340 g m^{-2} day^{-1} from 2008 to 2021/2022. While CO_2 fluxes indicate a mixed hydrothermal-biogenic source, the reduction in hydrothermal contribution is reflected in the morphology of the hot spring and in the ^{13}C isotopic signature (-12.14 to -18.13) which has significantly decreased from 1995 to 2021/2022. At La Soufrière, the spatial extent of soil CO_2 surveys was strongly restricted by access to the summit of La Soufrière and is thus limited to the hot springs. At the hot springs, soil CO_2 fluxes are average 76 kg day^{-1} and are also of mixed hydrothermal-biogenic source, although ^{13}C compositions (-9.94 to -12.76) are lower than that of the MORB and of crater fumaroles. At both volcanoes, there are high CO_2 fluxes (>40 g m^{-2} day^{-1}) indicating hydrothermal input. However, this is not reflected in the ^{13}C isotopes and may be due to environmental factors. In order to combat these effects, long time series are needed in order to correct for their influence on soil CO_2, but may be difficult due to the nature of the studied areas (being springs). At present, diffuse CO_2 degassing is not a great contributor to the total CO_2 output.

4.2 Introduction

Carbon is cycled through the outer and inner Earth by plate tectonics and volcanism, with the inner Earth being a reservoir for 90% of all carbon (Burton et al., 2013; Mason et al., 2017). CO_2 is steadily fed to geothermal systems, and as a result, large amounts of CO_2 are released during repose periods, as well during eruptive activity (Hernández et al., 2001a; Hernández et al., 2001b; Burton et al., 2013; Aiuppa et al., 2019; Fischer and Aiuppa, 2020). This CO_2 release can occur from different areas on the volcanic edifice, and includes passive degassing from plumes and fumaroles, and diffuse degassing through soil on the volcano flanks. Diffuse degassing may not occur over the entire volcanic system, but rather in discrete areas that are controlled by factors such as geological formations, tectonic structures, and morphological features (e.g. Chiodini et al., 1998; 2001; 2008). Diffuse degassing of CO_2 can be substantial in comparison to the quantity of CO_2 that is released from discrete fumaroles (e.g. Inguaggiato et al., 2012), can be released on the same scale as that degassed through plumes (e.g. Tarumae volcano; Hernandez et al., 2001), or can account for 100% of the total CO_2 degassing at localities including Iwojima volcano, Japan, where there is no visible plume (e.g. Notsu et al., 2005).

Characterizing the concentration or flux of CO_2 being diffused through the soil in volcanic systems can have manifold uses, including for (i) identification of active structural features, as faults and fractures act as highways for gas release for use in geothermal exploration for example (Hernández et al., 2001; Carapezza et al., 2009); (ii) providing a monitoring tool for active volcanoes, which may help identify future eruptions (Pérez et al., 2022) and aid with risk assessments; (iii) quantifying total CO_2 budgets, thus revealing overall degassing systematics of specific volcanic systems (Chiodini et al., 2008; Viveiros et al., 2010; Boudoire et al., 2017) and (iv) providing a more robust quantification of volcanic CO_2 in relation to the global carbon cycle (Chiodini et al., 1998; Inguaggiato et al., 2012; Aiuppa et al., 2019; Fischer and Aiuppa, 2020).

In zones of diffuse soil degassing, the soil CO_2 flux often has two sources, which are **organic/biogenic sources** that involve microbial decomposition of soil organic matter and root respiration, and **volcanic-hydrothermal sources** that derive from magmatic CO_2 emissions. These two sources can be variably mixed, depending upon time and position (e.g. Hernández et al., 2001; Camarda et al., 2007; Chiodini et al., 2008; Bloomberg et al., 2014). Since carbon is introduced to subduction zones from different sources and via a range of processes, carbon isotopic composition can be used to fingerprint the carbon source and shed light on the processes involved. Based on isotopic signatures, the sources are (i) organic carbon,

which ranges from-20 to -40‰, (ii) the mantle, where the carbon isotopic signature ranges -4 to -8‰, and (iii) inorganic sources such as limestone or other carbonates, normally at ~0‰ (Plank and Manning, 2019).

Diffuse CO_2 degassing is poorly studied in the Lesser Antilles arc, and to date, has only been explored at La Soufrière de Guadeloupe (Allard et al., 2014; Klein et al., 2024). At this volcano, diffuse CO_2 flux from the summit area has seen an increase from 300 kg day^{-1} to 4200 kg day^{-1} over a seventeen-year period between the first measurements in 2006 where diffuse CO_2 degassing accounted for 2-10% of the total CO_2 flux at Guadeloupe (Allard et al., 2014), and subsequent measurements in 2023, translating to ~50% of the total CO_2 flux when compared to emissions from summit fumaroles (Klein et al., 2024), demonstrating the significance of this process in the arc.

Passive degassing (plume degassing in the absence of eruptions) has been a persistent feature at both Soufrière Hills Volcano, Montserrat and La Soufrière volcano, St Vincent, where SO_2 fluxes have been 374 ± 140 tonnes/day from February 2010 to December 2014 (Christopher et al.,2015) and ~200 tonnes/day from (April to November 2021; Joseph et al., 2022) respectively. CO_2 fluxes calculated using CO_2/SO_2 ratios from MultiGAS measurements have been ~300-5500 tonnes/day in 2008 and 2010 at Soufrière Hills Volcano (Edmonds et al., 2014), and are calculated as ~7000 tonnes/day during April and May 2021 at La Soufrière using an average CO_2/S of 34.8 (Christopher et al., in review).

However, the CO_2 fluxes that are associated with diffuse degassing are yet to be comprehensively explored at either volcano. In this study, the aim is to calculate the total flux of CO_2 being diffused through the soil at specific areas of diffuse degassing, and to determine its origin. Results could shed light on the total CO_2 budget of these volcanoes, provide insights into the status of their magmatic/hydrothermal systems, and assist quantification of arc-wide fluxes of magmatic carbon.

4.3 Geological Setting and Volcanic Context

The Lesser Antilles Arc is the product of westward subduction of the Atlantic Plate beneath the Caribbean Plate (Macdonald, 2000; Evain et al., 2011) at rate of ~2 cm/year (DeMets et al., 2000), forming an ~850 km double island chain joining in the centre, where the eastern islands are no longer actively volcanic and are covered by coral and limestone, and the western chain currently comprises of 21 active or potentially active volcanoes spread among 11 islands (Lindsay et al., 2005).

4.3.1 Soufrière Hills Volcano, Montserrat

Montserrat exists in the northern group of islands of the arc (Macdonald et al., 2000), and is comprised of four volcanic centres. Of the four, three are extinct, with the currently active Soufrière Hills Volcano (Figure 4.1) producing andesite in dome-building and explosive events (Robertson et al., 2000; Cassidy et al., 2018), with the last phase of surface activity occurring between 2009-2010.

The Soufrière Hills Volcano has been active for at least 170 ka, with the preceding event occurring ~300-400 years before the series of eruptions which began in 1995-2010 (Young et al., 1998). The volcanic centre features five lava domes, with the present dome rising to 1083 m as of the last eruption and dome collapse ending in 2010 (Stinton et al., 2014a), and also features a prominent collapse scar formed in February 2010 (Stinton et al., 2014b).

At Soufrière Hills Volcano, and prior to the onset of the 1995 eruptions, there were several instances of surface manifestations of the hydrothermal system (Figure 4.1), including (i) four soufrières (high temperature – 98 °C – fumarole fields) on and around the volcano summit (ii) the Hot Pond (48-92 °C; Chiodini et al., 1996a; Pedroni et al., 1999; Younger et al., 2010; Poux and Brophy, 2012; Wright et al., 1976; Bath et al., 1977) located ~5km west of the volcano, and (iii) hot springs (90 °C; Chiodini, 1996a) located near the hot pond. At present, these surface manifestations no longer exist, with the Soufrières being buried or destroyed by eruptions in 1995, and the disappearance of the once bubbling, steaming Hot Pond by 2010.

Zones of structural weaknesses exist over the southern section of the island, where a network of faults (and inferred faults) strike NW-SE from coast to coast (Figure 4.1). Of particular interest is the Hot Pond that is situated approximately 0.6 km south of the nearest fault, where high temperatures, low pH (5.4-6.0; Chiodini et al., 1996a; Jones et al., 2010; Poux and Brophy, 2012), and the isotopic composition of CO_2

were indicative of its interaction (however limited) with the hydrothermal system, as other volatile signatures suggest restricted interaction of magmatic water (Jones et al., 2010).

4.3.2 La Soufrière volcano, St Vincent

St Vincent is located in the southern group of islands in the arc (Macdonald et al., 2000), and is made up of four main volcanic centres, sequentially emplaced from south to north. The northernmost volcano, La Soufrière (Figure 4.1), is currently the only active centre on the island, built from Pliocene to Recent basalt and basaltic andesite products produced in both effusive and explosive eruptions (Aspinall et al., 1973). La Soufrière Volcano extends ~1200 m above sea level (Aspinall et al., 1973), where the main features are four craters which have been the sites of eruptions for the past 4000 years. The largest and most northerly crater is the Somma Ridge, a horseshoe shaped semi-caldera 2.5 km in diameter formed from a basaltic volcano which erupted between 0.36 – 0.69 Ma (Lindsay et al., 2005; Cole et al., 2019). The majority of historic eruptions (post-1700s) have originated in the younger "main" crater which is ~1.6 km in diameter and 300–600 m deep (Lindsay et al., 2005), where features are commonly a dome and/or crater lake. A smaller crater ~450 m wide and 60 m deep was formed on the NE rim of the main crater during the 1812 eruption (Aspinall et al., 1973; Lindsay et al., 2005) and has not been the site of further eruptions to date. The fourth and most recent crater was formed during the explosions of the 2020-2021 eruption, and is located in the western section of the main crater (Figure 4.1).

Throughout historical eruptions, including the 2020/2021 eruption, surface manifestations of the hydrothermal system at La Soufrière consists of (i) fumaroles of temperatures 70–98 °C (Dames and Moore, 1998; van Soest et al., 1998; Robertson et al., 2023) emanating from the crater which actively degasses volatiles including H_2O, CO_2, SO_2 and H_2S into the atmosphere, and is punctuated by areas of acid alteration and sulphur crystals, and (ii) warm springs (37–45 °C; Dames and Moore, 1998; Pedroni et al., 1999; Robertson et al., 2023) in the Wallibou River (Figure 4.1).

A series of faults are known to be present at La Soufrière, but do not intersect the main crater (Figure 4.1). Instead, short faults (~1 km in length) are present on the northern coast, in the vicinity of the warm springs in the Wallibou River, and an 8.5 km fault extends from the north coast, through the rim of the Somma, and terminates at the boundary of the La Soufrière – Morne Garu Volcanic Centres.

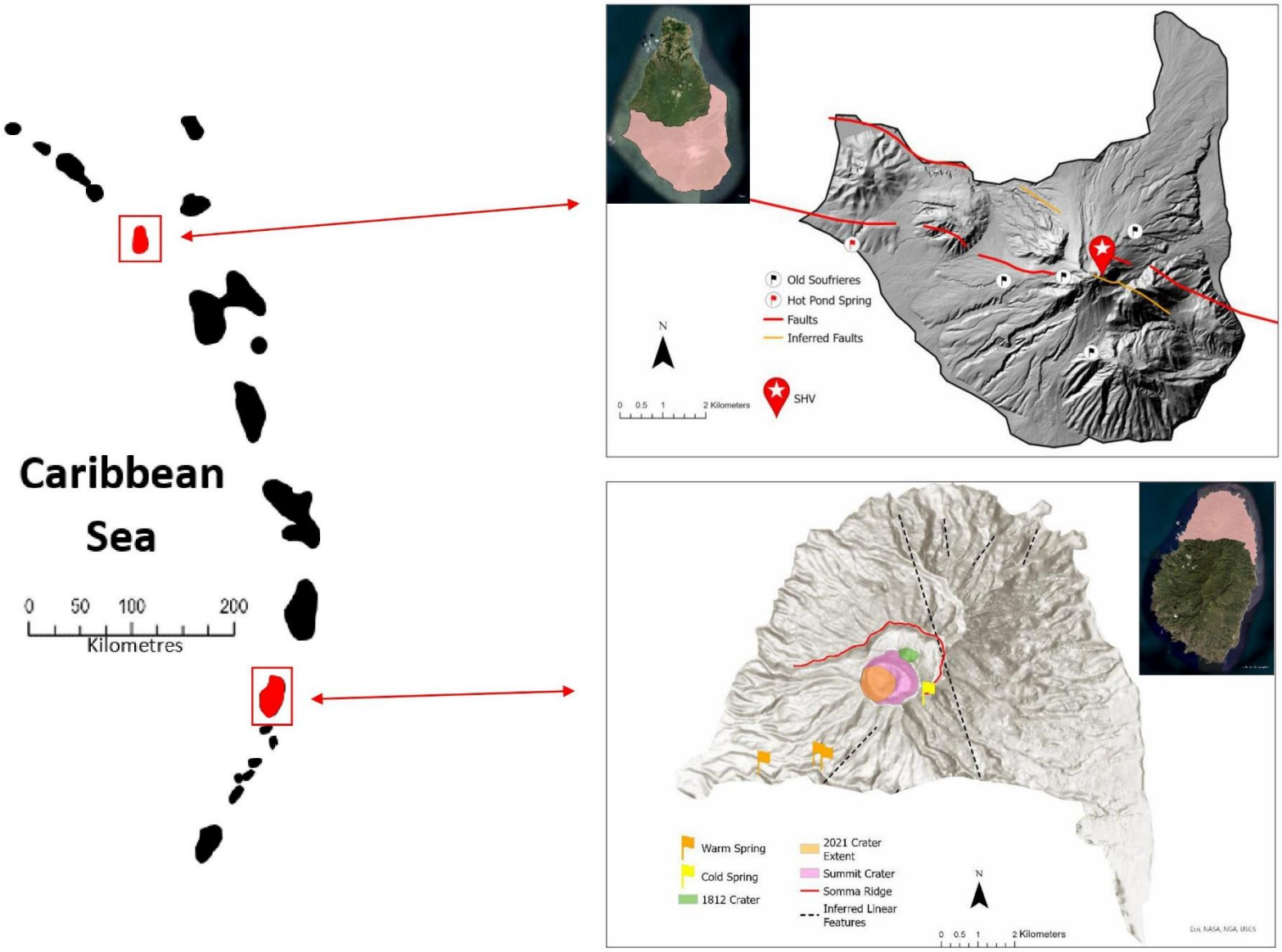
Caribbean
Sea
0 50 100 200
Kilometres
Old Soufrieres
Hot Pond Spring
Faults
Inferred Faults
N
0 0.5 1 2 Kilometers
SHV
Warm Spring
Cold Spring
1812 Crater
2021 Crater Extent
Summit Crater
Somma Ridge
Inferred Linear Features
N
0 0.5 1 2 Kilometers

Figure 4.1 – Overview of surveyed locations within the Lesser Antilles Arc. [B] The islands of the Lesser Antilles arc with the studied islands in red. [B] Overview of the Soufrière Hills Volcanic complex showing main faults and areas of known surface manifestations of the hydrothermal system. [C] Overview of La Soufrière volcano showing main linear features and known surface manifestations of the hydrothermal system.

4.4 Methodology

4.4.1 Soil CO_2 Flux Measurements

Soil CO_2 surveys were carried out at Soufrière Hills Volcano, Montserrat in August 2021 and September/October 2022 along areas with structural linear features in the form of faults, and in areas of previous hydrothermal activity (Figure 4.1B). At La Soufrière volcano, St Vincent, soil CO_2 surveys were carried out around the volcanic edifice in March 2021, with measurements curtailed by changes in activity that heralded the transition to explosive activity in April 2021, and also at the Wallibou River hot springs. Post-eruptions, measurements were only possible at the warm springs in the Wallibou River in October 2024 (Figure 4.1C), with other sites inaccessible due to vegetation growth and cover by a tephra blanket.

398 CO_2 flux measurements at Soufrière Hills Volcano, and 111 at La Soufrière were conducted using a PP Systems EGM-4 Environmental Gas Monitor with accompanying SRC-1 Soil Respiration Chamber, which has a volume of 1171ml, area of 78 m^2, and a CO_2 measurement range of 0-30,000 ppm, with an accuracy of 1% of the reading (Figure 4.2; PP Systems, 2002).

Prior to the beginning of the measurement, the accumulation chamber was fitted into the soil to prevent contamination of atmospheric gas. At the start of the measurement, soil gas is allowed to accumulate in the chamber, which is then transferred into an infra-red CO_2 gas analyser, and back into the chamber. CO_2 flux is then calculated by the instrument by plotting the rate of change of CO_2 in the accumulation chamber using a quadratic fit over 120 seconds. (e.g. Chiodini et al., 1998; Welles et al., 2001; Notsu et al., 2005; Carapezza et al., 2009; Viveiros et al., 2010)

Soil temperature was measured using a thermocouple attached to the EGM-4 in the September/October 2022 occupation at Soufrière Hills Volcano and the October 2024 occupation at La Soufrière.

La Soufrière volcano was initially chosen as the site to conduct an extensive soil CO_2 survey, given the open crater at the summit. The aim was to conduct a soil CO_2 survey during the effusive phase of the eruption in March 2021 and after the eruption ended, in order to compile a syn- and post-eruptive dataset and to compare the diffuse degassing with time. At the beginning of this study, the crater consisted of relatively flat ground, with a 120 m high × 800 m wide (Stinton et al., 2023), older lava dome, a newly growing dome in the middle and a small area of passive degassing. However, effusive activity, resulting in the newly growing dome first appeared in December 2020, and access into the crater was restricted for the following three months, meaning that the survey could not be carried out. Activity at La Soufrière then transitioned from effusive dome building to violent explosive eruptions in April 2021. A survey was therefore planned for October 2024, however, the explosive eruption in 2021 resurfaced the summit crater, destroying both domes, and creating a new, near vertical sided crater. This crater is located at the site of the old, now destroyed dome where fumaroles occurred at its base. Current fumarolic activity is contained to the 2021 crater. The inability to access this new degassing crater, together with challenges in accessing the summit by foot, with no other access avenues, meant that the aim of the study had to be shifted.

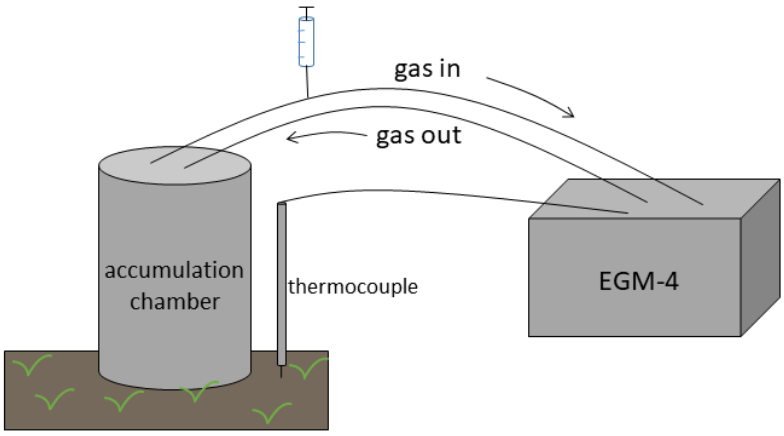

Figure 4.2 – Schematic of the setup for soil CO_2 flux measurements and collection of gas for C isotope analysis.

4.4.2 ^{13}C Isotope Analysis

Gas samples at locations with high CO_2 fluxes were collected for CO_2 isotopic composition ($\delta^{13}C$ CO_2) immediately following soil CO_2 flux measurements. The 'gas in' line from the accumulation chamber to the IRGA was equipped with a T-connector value and a 12 ml syringe, allowing gas to flow directly from the accumulation chamber to the syringe in order to prevent contamination. Gas samples were then transferred from the syringe to 12 ml evacuated glass vials capped with a pierceable butyl rubber septum.

The isotopic composition of CO_2 in samples from both Soufrière Hills Volcano and La Soufrière was measured using an IsoPrime100 Isotope Ratio Mass Spectrometer (IRMS) at Lancaster University.

2 ml of gas was removed from each 12 ml vial and injected into an Elementar iso FLOW GHG where cryotrapping and cryofocussing concentrates the amount of CO_2. The ratios of the heavy (^{13}C) and light (^{12}C) carbon isotopes were then analysed via the IRMS. ^{13}C isotopes are relative to the international standard VPDB and are presented in parts per thousand (‰). Standards used are both international (LSVEC, NBS18 and CO1) and in-house (LEC-CC) and can be found in Supplementary Material 1. The reproducibility (2σ) for Soufrière Hills Volcano samples was 0.01‰ and 0.002‰ for La Soufrière samples, based on repeat analysis of the international and in-house standards.

4.5 Previous Work

4.5.1 Soufrière Hills Volcano, Montserrat – 2008

A soil CO_2 survey of 152 datapoints undertaken in 2008 (Figure 4.5; Figure 4.6; Edmonds, unpublished data) reveals three populations in the dataset.

Population C, consisting of 83% of the dataset ranges from 4-96 g m^{-2} day^{-1}, with a mean of 34 g m^{-2} day^{-1} (Figure 4.3), measured in all investigated areas. Based on the CO_2 fluxes measured outside of Soufrière Hills Volcano in 2021/2022, and published values on CO_2 fluxes in non-volcanic vegetated areas (Norman et al., 1992; Liang et al., 2010; Viveiros et al., 2010), this population benefits from a hydrothermal influence, as CO_2 fluxes exceed 50 g m^{-2} day^{-1}.

Population B accounts for 16% of the dataset, and ranges from 105-733 g m^{-2} day^{-1}, with an average of 277 g m^{-2} day^{-1}. These values are suggestive of hydrothermal CO_2 degassing, and are found in the Hot Pond area.

Population A consists of two data points which are vastly greater than those found in Populations B and C at 3516 and 7083 g m^{-2} day^{-1}. This high CO_2 flux is attributed to intense CO_2 degassing from one area in the Hot Pond (Figure 4.5A, Figure 4.5B).

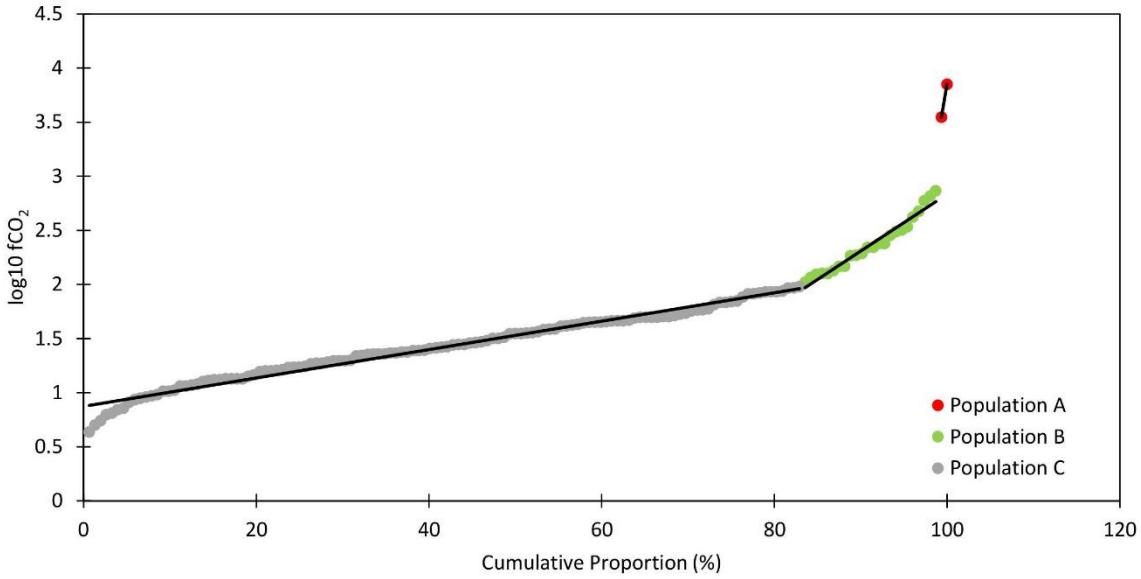

Population	# of points	Proportion (%)	Average soil CO_2 flux ($g\ m^{-2}\ day^{-1}$)	Max CO_2 Flux ($g\ m^{-2}\ day^{-1}$)	Min CO_2 Flux ($g\ m^{-2}\ day^{-1}$)
A	2	1	5299	7083	3516
B	24	16	277	733	105
C	126	83	34	96	4

Figure 4.3 - Logarithmic probability plot of soil CO_2 flux measured at Soufrière Hills Volcano, Montserrat in 2008 by Edmonds, unpublished data. There are three populations within this dataset. Population C (grey) consists of a mixture of biogenic and hydrothermal input, Population B (green) is served by hydrothermal CO_2 degassing of low intensity and Population A (red) is subjected to significant CO_2 degassing from hydrothermal sources. CO_2 fluxes in 2008 were higher than those measured in 2021/2022.

4.6 Results

4.6.1 Soil CO_2 flux

4.6.1.1 Soufrière Hills Volcano, Montserrat – 2021/2022

The soil CO_2 surveys in 2021/2022 reproduced the sites covered in 2008, with additional sites. Over the investigated areas, CO_2 flux ranges from 0 to 273 g m^{-2} day^{-1}. Logarithmic probability plots (Figure 4.4) of log CO_2 flux vs cumulative proportions constructed using the Graphical Statistical Analysis (GSA) method (Sinclair 1974) allow identification of different populations within a dataset, based on inflection points in the curve (Populations A-D). GSA therefore shows a polymodal distribution of the data, with inflections at 21, 87 and 97 cumulative percentiles, defining four distinct populations within the dataset.

Population D, with the lowest CO_2 fluxes, accounts for 21% of the Soufrière Hills Volcano dataset, with a mean of 2 g m^{-2} day^{-1} (Figure 4.4). Values range 0-6 g m^{-2} day^{-1}. CO_2 flux readings from this population are generally measured in the dry riverbed of the Belham Valley (Figure 4.5C) where vegetation is sparse or is completely lacking.

Population C constitutes the largest population of the dataset at 66%, accounting for 263 soil CO_2 flux measurements (Figure 4.4). Here, values range from 6-45 g m^{-2} day^{-1}, with a mean of 21 g m^{-2} day^{-1}, and generally occurs in hot, dry, vegetated areas. Additionally, eight measurements were undertaken outside of the Soufrière Hills boundary/edifice where volcanism is extinct (Supplementary Figure 4.S1), yields values of 1-47 g m^{-2} day^{-1} (mean = 19 g m^{-2} day^{-1}). These values are typical for CO_2 fluxes from biogenic sources, and compare well with a range of vegetation types in different environments that produce CO_2 fluxes of 0-50 g m^{-2} day^{-1} (e.g. Norman et al., 1992; Liang et al., 2010; Viveiros et al., 2010).

Population B accounts for 10% of the dataset, ranging from 47-92 g m^{-2} day^{-1}, measured in areas of vegetation, or in muddy areas of the Hot Pond (Figure 4.1B; Figure 4.5C, Figure 4.5D). This population is situated on the upper bounds of CO_2 fluxes produced by biogenic only sources, and thus, there is a possibility of hydrothermal contributions to this population.

A total range of 115-273 g m^{-2} day^{-1} was measured in Population A, the least populated group (3% of the dataset) with an average of 147 g m^{-2} day^{-1}. Areas contributing to Population A are confined to the muddy soils of the Hot Pond, or in wet, bushy parts of Cork Hill in the area of the Richmond Hill and Belham Valley

faults (Figure 4.5D; Supplementary Figure 4.S1; Supplementary Material; Feulliet et al., 2010; Baird et al., 2015).

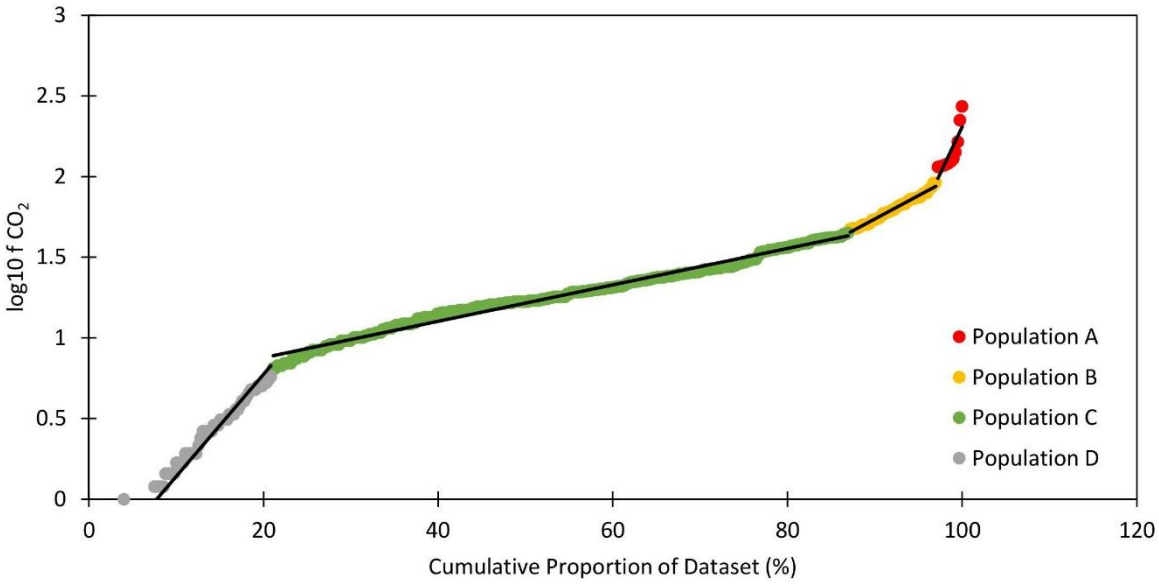

Population	# of points	Proportion (%)	Average soil CO_2 flux (g m^{-2} day^{-1})	Max CO_2 Flux (g m^{-2} day^{-1})	Min CO_2 Flux (g m^{-2} day^{-1})
A	12	3	147	273	115
B	40	10	64	92	47
C	263	66	21	45	6
D	83	21	2	6	0

Figure 4.4 – Logarithmic probability plot of soil CO_2 flux of the Soufrière Hills Volcano edifice. Four populations are present in the dataset, likely representing different sources of CO_2. Populations D (grey) and C (green) do not benefit from a hydrothermal input, but instead from varying degrees of biological input. Population B (yellow) and Population A benefits from hydrothermal input.

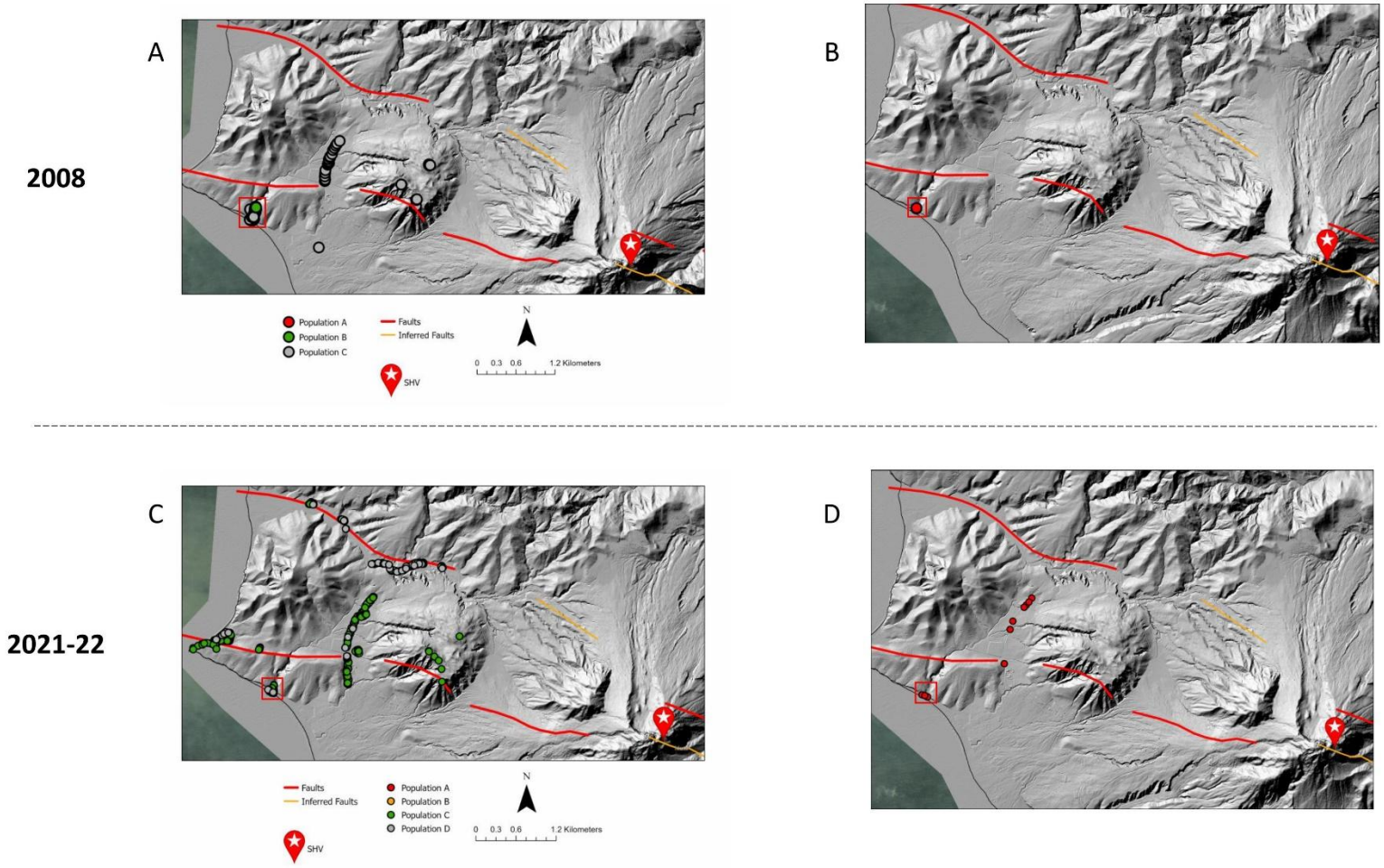

Figure 4.5 – Soil CO_2 survey in areas of interest during 2008 vs 2021. [A] Measurements in 2008 were undertaken primarily at the Hot Pond and along a stretch of road in Cork Hill, located perpendicular to two faults. [B] Locations of the 2008 survey where high CO_2 belonging to Population A were found. [C] Measurements in 2021-2022 were reproduced in similar location to that of 2008 to enable comparisons. Additional measurements were also undertaken along fault lines. [D] Locations of the 2021-2022 surveys where high CO_2 belonging to Population A were found. Red outlined squares show the location of the Hot Pond.

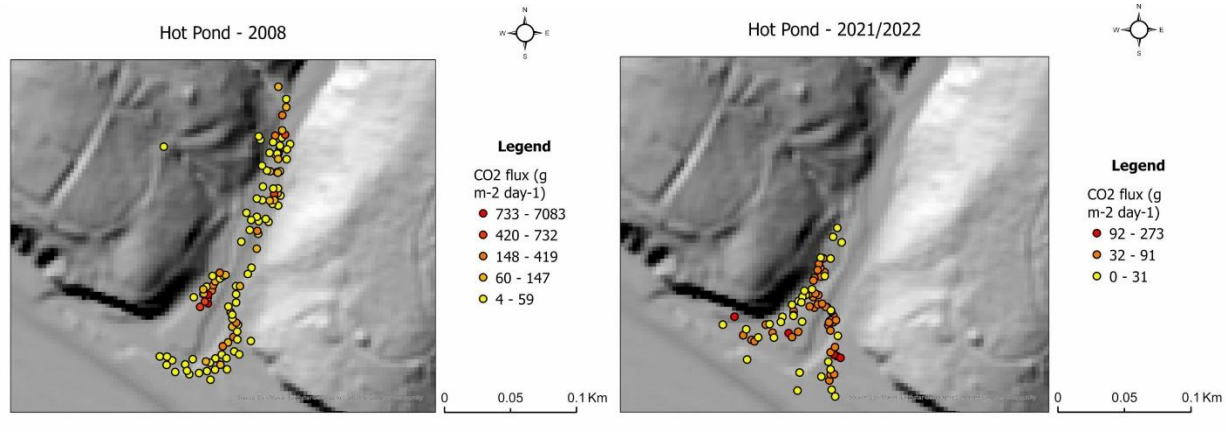

Figure 4.6 – Soil CO_2 surveys undertaken at the Hot Pond in 2008 vs 2021/2022. [A] CO_2 fluxes in 2008 ranges 4-7083 g m^{-2} day^{-1}. [B] CO_2 fluxes measured in 2021/2022 ranged 0-273 g m^{-2} day^{-1}

4.6.1.2 La Soufrière volcano, St Vincent

Graphical Statistical Analysis identifies three populations (Figure 4.7) within the La Soufrière dataset as a result of differing sources of CO_2 being diffused through the soil. While total soil CO_2 fluxes range 0-433 g m^{-2} day^{-1}, the majority of the dataset is characterised by low CO_2 fluxes. The proportions of each population, the average, minimum and maximum CO_2 fluxes are listed in Figure 4.6.

Population C accounts for 11% of the dataset, and contain the lowest values of soil CO_2 fluxes ranging from 0 – 3 g m^{-2} day^{-1}, with a mean of 3 g m^{-2} day^{-1}. Population C typically occurs in dry soils or dry river beds where the input of CO_2 from biological sources is minimal. Soil temperatures are below 30 °C (Figure 4.8).

In Population B which account for 59% of the dataset, CO_2 fluxes range from 4 – 40 g m^{-2} day^{-1}. This population benefits from a biogenic input of CO_2 flux, and the fluxes are similar to soil CO_2 fluxes measured in grassy areas outside of the La Soufrière edifice which ranged from 25 – 36 g m^{-2} day^{-1}, further cementing the biogenic source with lack of hydrothermal input.

The CO_2 fluxes of Population A range from 51-433 g m^{-2} day^{-1} with a mean of 143 g m^{-2} day^{-1}. These high fluxes which are 20% of the dataset are ascribed to input from the volcanic/hydrothermal system, and occur in soils with slightly elevated temperatures of 33 - 39°C around the warm springs of the Wallibou River, with one measurement of 75 g m^{-2} day^{-1} taken in the summit crater (Figure 4.9).

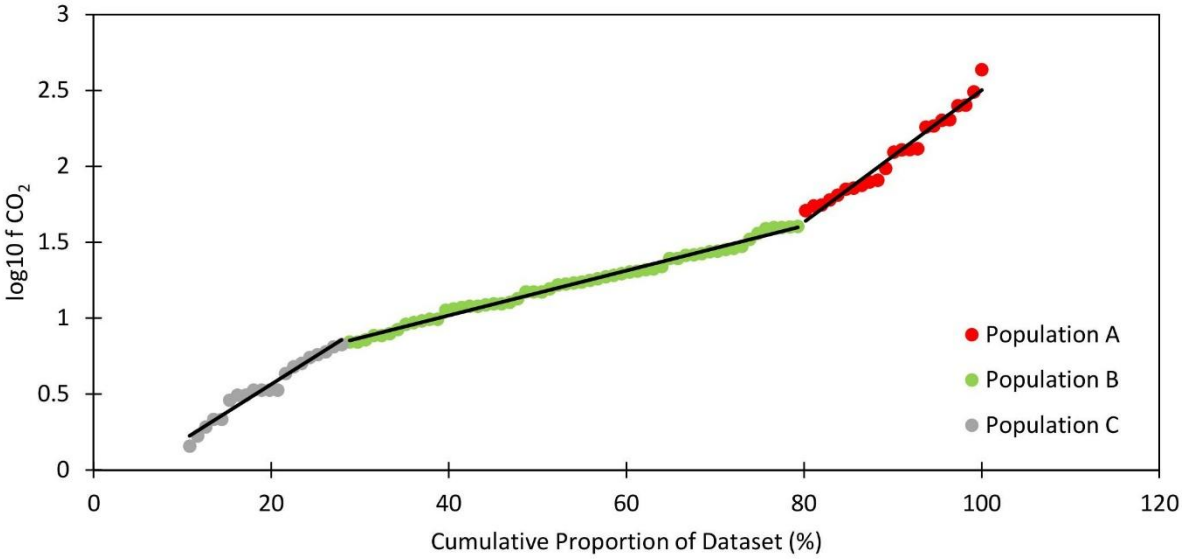

Population	# of points	Proportion (%)	Average soil CO_2 flux (g m^{-2} day^{-1})	Max CO_2 Flux (g m^{-2} day^{-1})	Min CO_2 Flux (g m^{-2} day^{-1})
A	22	20	143	433	51
B	65	59	17	40	4
C	12	11	3	3	0

Figure 4.7 – Logarithmic probability plot of soil CO_2 flux around La Soufrière volcano, St Vincent showing three populations within the dataset and the breakdown of CO_2 flux populations at La Soufrière. Population C (grey) and Population B (green) benefits from varying amounts of biogenic CO_2, while Population A (red) benefits from a hydrothermal input of CO_2.

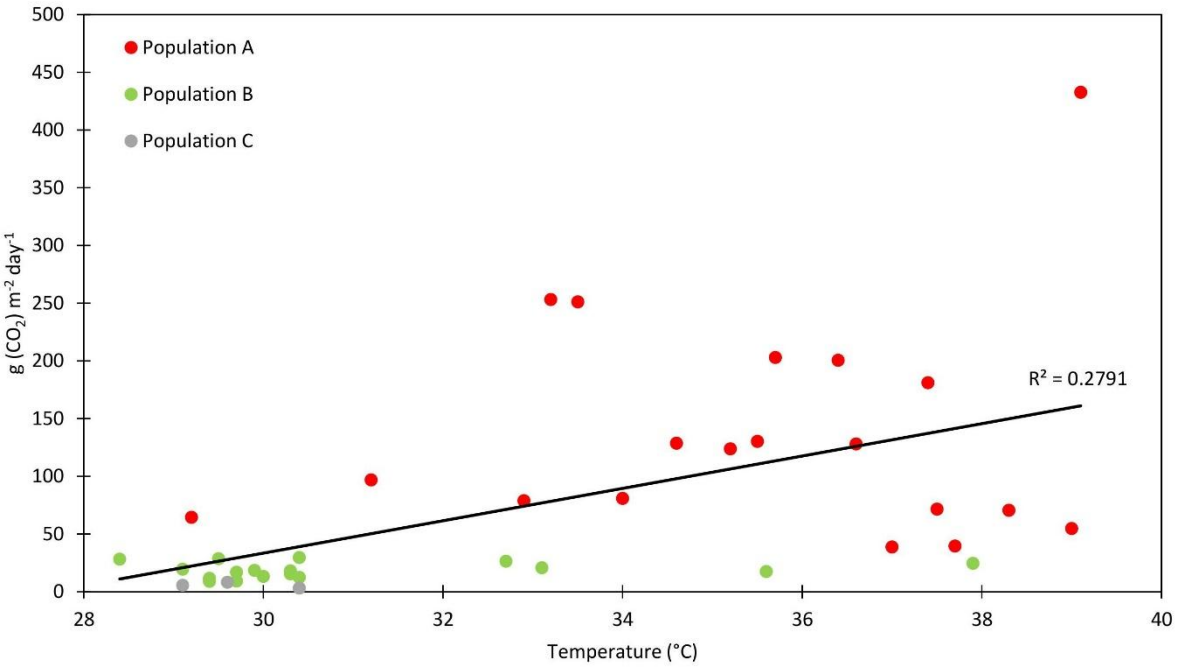

Figure 4.8 – CO_2 flux vs soil temperature at La Soufrière volcano, St Vincent. CO_2 flux can generally be seen as increasing with soil temperature, but due to the nature of the environment – a warm spring - a conclusive assessment cannot be made.

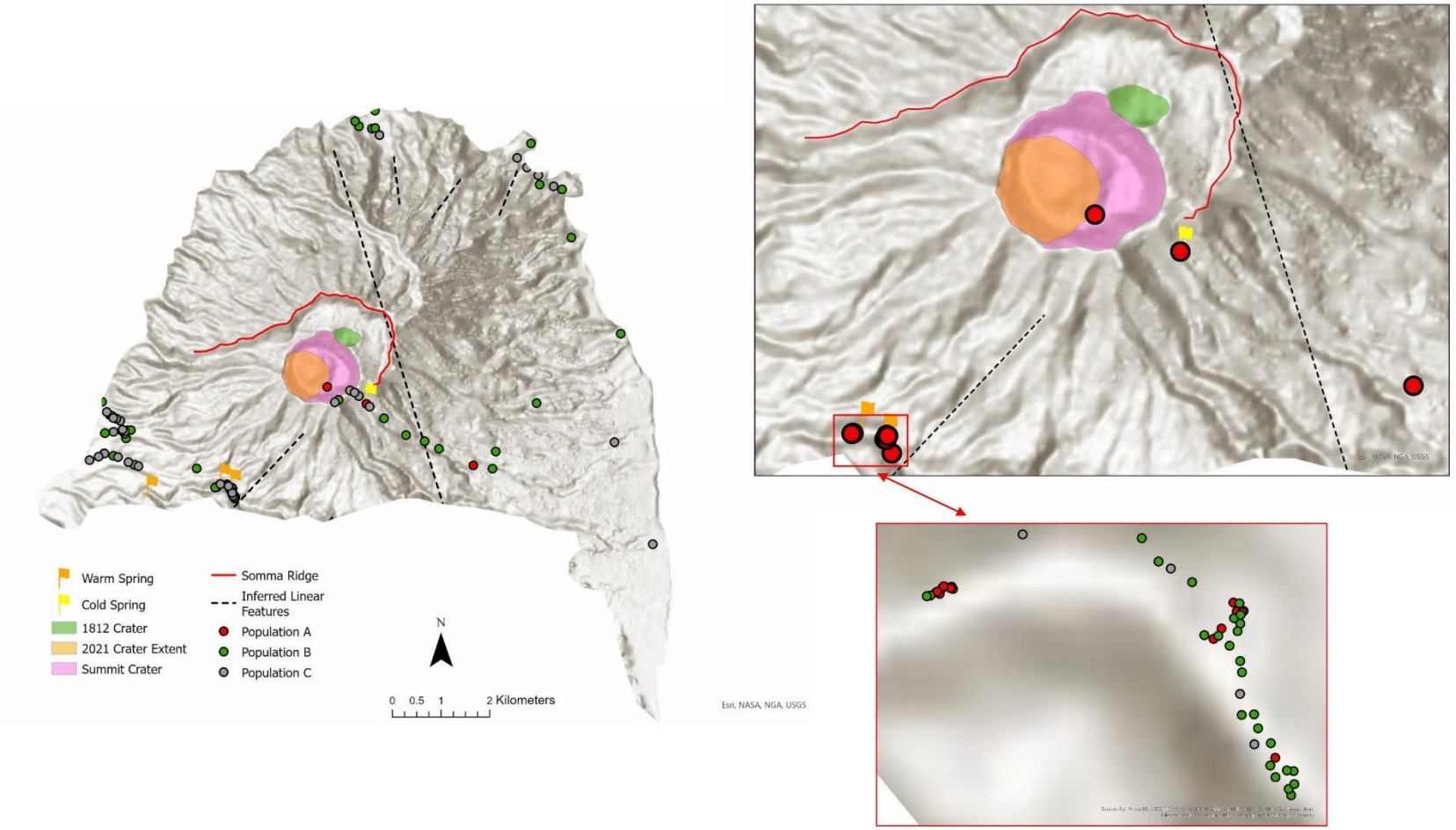

Figure 4.9 – The La Soufrière edifice and associated soil CO_2 measurements. The vast majority of the highest CO_2 fluxes belonging to Population A were found in the warm spring area of the Wallibou River. A single measurement taken in the crater, and one measurement in the vicinity of the cold spring also belongs to Population A.

4.6.2 $\delta^{13}C$ CO_2 Isotopic Chemistry

4.6.2.1 Soufrière Hills Volcano, Montserrat

The isotopic composition of carbon from CO_2 measured across the study area was -12.14‰ to -19.26‰ (Figure 4.10; Table 4.1). In the previously identified area of the Hot Pond, values range -12.14‰ to -18.13‰. The isoptopic composition of vegetation taken outside of the volcanic edifice amounts to -18.63. $\delta^{13}C$ CO_2 measured in the study is far lighter than the -2.4‰ to -3.8‰ measured in samples from the Soufrières in February 1995 and the -0.04‰ to -0.45‰ measured in samples from the Hot Pond in November 1995. There is no significant difference in the isotope ratio of the high vs the low flux locations (populations A vs B vs C vs D) which is unexpected.

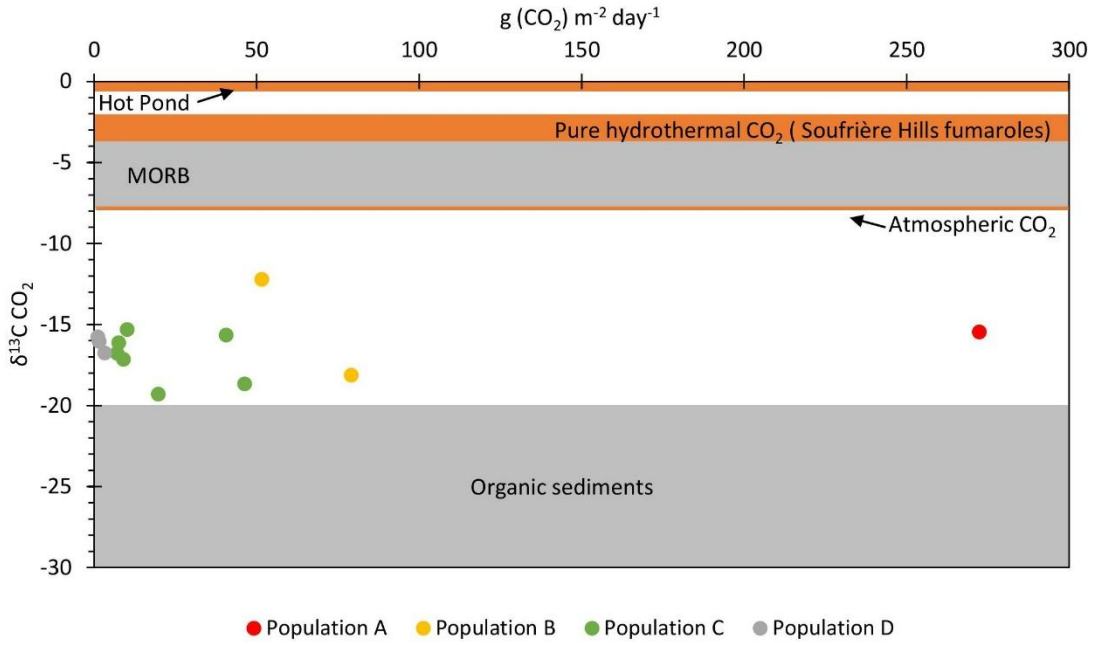

Figure 4.10 – $\delta^{13}C$ Composition of soil CO_2 from the Soufrière Hills edifice vs soil CO_2 flux. MORB is the $\delta^{13}C$ composition of mid-ocean ridge basalts, and pure hydrothermal CO_2 and Hot Pond refers to the isotopic composition of Soufrière Hills Volcano fumaroles and the Hot Pond as measured by van Soest et al., (1998) and Pedroni et al., (1999).

4.6.2.2 La Soufrière volcano, St Vincent

The carbon isotopic signature at twelve sites in the warm springs of the Wallibou river ranges from -9.94‰ to -12.76‰ (Figure 4.11; Table 4.1). These values are lower than those measured in the Wallibou (-4.4‰ to -5.7‰) and from the summit crater fumaroles (-6.04‰ to -6.60‰; Van Soest et al., 1998; Pedroni et al., 1999) in 1995. Again there is no relationship between isotope ratio and flux (population A vs B) which is unexpected. It is expected that higher CO_2 flux fed from hydrothermal sources have ^{13}C isotopic signatures reflecting that.

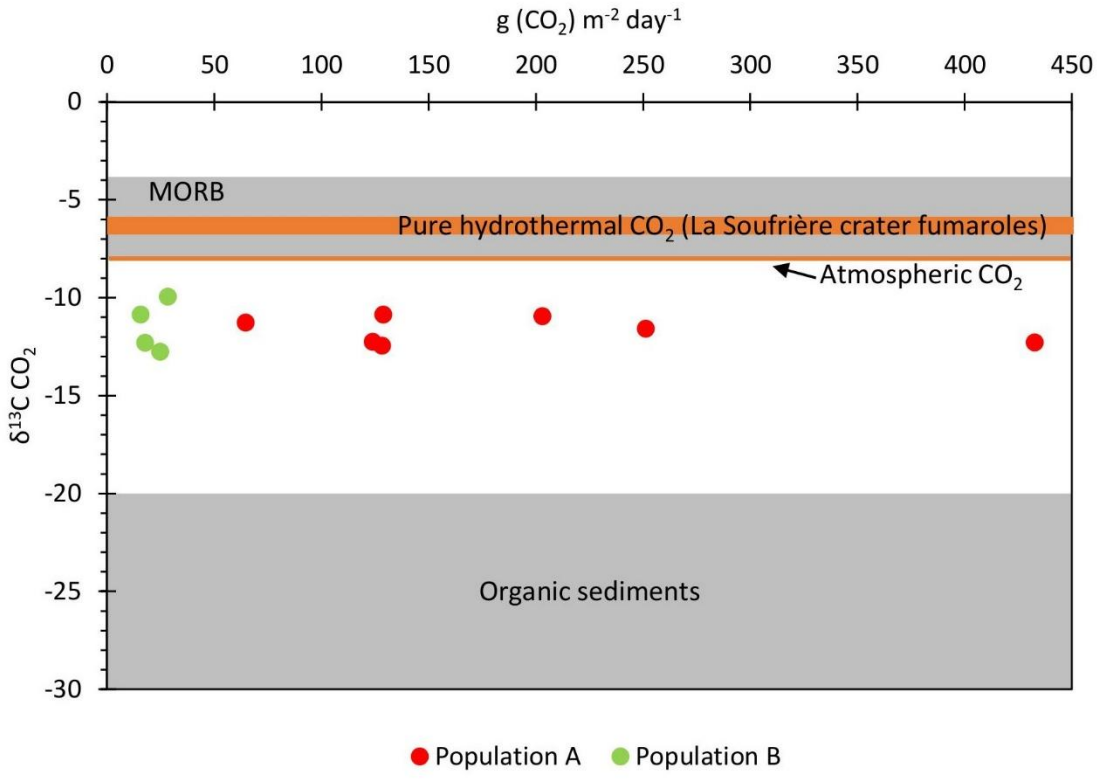

Figure 4.11 – $\delta^{13}C$ composition of soil CO_2 from the Wallibou warm springs vs soil CO_2 flux. MORB is the $\delta^{13}C$ composition of mid-ocean ridge basalts, and pure hydrothermal CO_2 refers to the isotopic composition of La Soufrière volcano fumaroles as measured by van Soest et al., (1998) and Pedroni et al., (1999).

CO_2 isotopic composition			
Soufrière Hills Volcano		**La Soufrière**	
Sample ID	**$\delta^{13}C$ (‰)**	**Sample ID**	**$\delta^{13}C$ (‰)**
HP058	-12.14 ± -0.12	SVG020	-9.94 ± -0.02
HP058	-12.16 ± -0.12	SVG038	-10.86 ± -0.02
CH056	-15.25 ± -0.15	SVG006	-10.86 ± -0.02
CH082	-15.29 ± -0.15	SVG031	-10.94 ± -0.02
CH030	-15.42 ± -0.15	SVG011	-11.27 ± -0.02
HP054	-15.60 ± -0.16	SVG001	-11.58 ± -0.02
BV066	-15.72 ± -0.16	SVG024	-12.25 ± -0.02
BV027	-16.00 ± -0.16	SVG027	-12.28± -0.02
CH065	-16.08 ± -0.16	SVG023	-12.31 ± -0.02
BV071	-16.65 ± -0.17	SVG021	-12.45 ± -0.02
BV054	-16.71 ± -0.17	SVG042	-12.45 ± -0.02
CH003	-16.73 ± -0.17	SVG026	-12.76 ± -0.02
CH019	-17.03 ± -0.17		
CH019	-17.10 ± -0.17		
HP009	-17.56 ± -0.18		
HP001	-18.03 ± -0.18		
HP001	-18.13 ± -0.18		
GPS274	-18.50 ± -0.19		
N001	-18.63 ± -0.19		
GPS274	-18.72 ± -0.19		
CH088	-19.26 ± -0.19		

Table 4.1 – Isotopic composition of gas samples collected at Soufrière Hills Volcano, Montserrat and La Soufrière volcano, St Vincent. At Soufrière Hills Volcano, $\delta^{13}C$ ranges from -12.14 to -19.26, with $\delta^{13}C$ measured outside of the volcanic edifice at -18.63. At La Soufrière volcano, $\delta^{13}C$ ranges from -9.94 to -12.76. $\delta^{13}C$ from all sites indicate non-magmatic sources of CO_2.

4.7 Discussion

4.7.1 Diffuse degassing and total CO_2 budget

The process of diffuse degassing is an important aspect of the total volatile output at volcanoes, as a significant portion of CO_2 can be lost through the soil, leading to an underestimation of the total CO_2 budget at a specific volcano if this flux were ignored (Notsu et al., 2005; Figure 4.12). Sequential Gaussian simulation (sGs) is often used as a method of defining the shape and extent of the surveyed degassing area by simulating the spatial variability of soil CO_2 flux (e.g. Cardellini et al., 2003; Chiodini et al., 2008). However, due to the small size of the investigated areas, the total degassing of CO_2 is estimated by multiplying the extent of the surveyed area by the average high CO_2 flux.

At Soufrière Hills Volcano, the investigated area of the Hot Pond in 2008 was ~6000 m^2, estimated as the area of a polygon around the surveyed area using ArcGIS Pro. Using the average high CO_2 fluxes from Populations A and B (663 g m^{-2} day^{-1}), the total CO_2 degassing at the Hot Pond amounts to 4000 kg d^{-1}. Applying this method to the 2021/2022 survey, it is calculated that total CO_2 degassing amounts to 340 g m^{-2} day^{-1}, a reduction of more than 90% of CO_2 output from 2008 to 2021/2022.

A total CO_2 budget for 2008 can be estimated by summing plume CO_2 flux calculated using SO_2 flux measurements from UV spectrometer and CO_2/SO_2 ratios collected in July 2008 via Multi-component Gas Analyser System – MultiGAS (Edmonds et al., 2014), and that estimated for the diffusively degassing site at Hot Pond. An average of 1.5×10^6 kg/day being emitted at the summit through the plume, and an average of 4000 kg d^{-1} shows that diffuse CO_2 degassing does not play a significant role at Soufrière Hills Volcano, Montserrat, with only a 0.1% contribution to the total output (99.9% contribution from plume degassing). This distribution of CO_2 flux is similar to that of White Island, New Zealand, where diffuse CO_2 contributes ~9×10^3 kg day^{-1} in comparison to plume degassing which contributes 2.6×10^6 kg day^{-1} or 99.7% of total CO_2 output. This is however contrary to neighbouring volcano La Soufrière de Guadeloupe where ~50% of diffuse degassing contributes to total CO_2 output (Klein et al., 2024), and wider arc volcanoes such as Iwojima, Miyakejima and Usu in Japan and Cerro Negro in Nicaragua where diffuse degassing contributes ~100% of total CO_2 output (Figure 4.12; Hernandez et al., 2001a; Hernandez et al., 2001b; Salazar et al., 2001; Notsu et al., 2005).

For La Soufrière, St Vincent, diffuse degassing in the warm springs of the Wallibou river is partitioned into two fault-controlled areas separated by approximately 300 m (straight line distance). The area investigated in the upper section covered ~300 m^2 estimated as above, and saw an average CO_2 flux of 187 g m^{-2} day^{-1}, thereby producing a total of 56 kg day^{-1} over the area. In the lower section, an area ~130 m^2 saw an average of 127 g m^{-2} day^{-1}, for a total of 16 kg day^{-1} of CO_2. Therefore, it is estimated that roughly 76 kg day^{-1} of CO_2 is degassed from the warm springs of the Wallibou. Total CO_2 degassing (plume + diffuse) for La Soufrière volcano is estimated by summing that of the warm springs to that that of the plume (2×10^5 kg day^{-1} from May-November 2021; Joseph et al., 2022). Similarly to Montserrat, CO_2 from diffuse soil degassing does not contribute significantly to the total CO_2 budget of the volcano, and almost 100% of total CO_2 degassing comes from the plume. In other arc volcanoes such as Satsuma-Iwojima, Japan and Vulcano, Italy where CO_2 flux is low ($1\text{-}2\times10^5$ kg day^{-1}), diffuse degassing makes up 17-20% of total CO_2 output (Baubron et al., 1990; Shimoike et al., 2002).

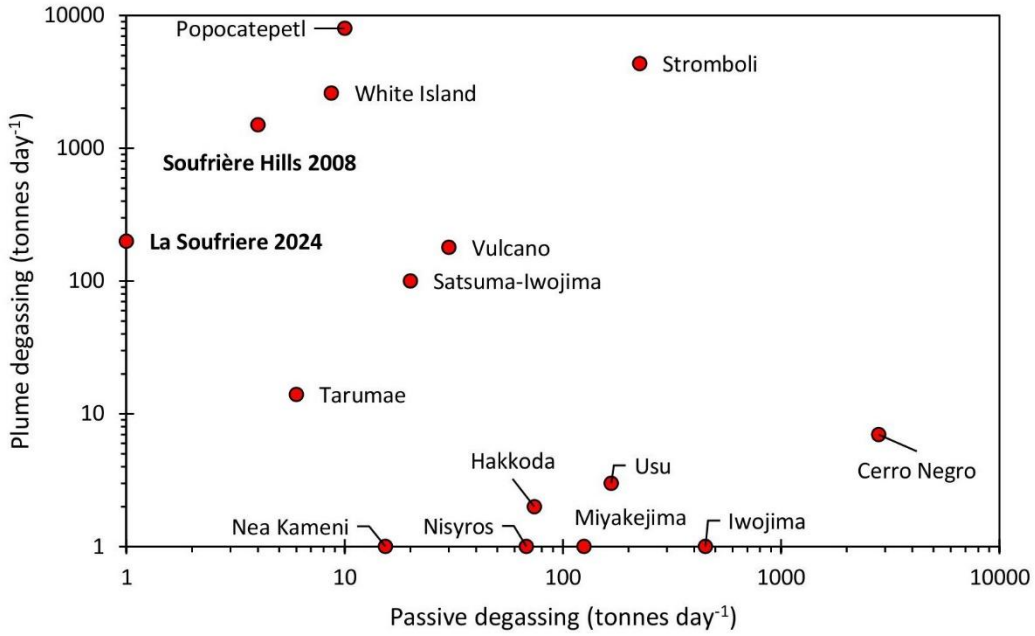

Figure 4.12 – Compilation and comparison of CO_2 degassing via diffuse and passive routes from arc settings around the world from. My Soufrière Hills and La Soufrière data is added to a data compilation from Notsu et al., (2005).

4.7.2 Source of CO_2

CO_2 released at arc volcanoes is typically sourced from either the mantle, sedimentary organic carbon, or from carbonates (Mason et al., 2017). In 1995, the isotopic composition of CO_2 from the now-destroyed soufrières of Soufrière Hills Volcano, Montserrat was ~1.5‰ heavier than values of the mid-ocean ridge basalt (MORB) at -2.4 to -3.8 (van Soest et al., 1998), and the Hot Pond, located near the fault system, yielded $\delta^{13}C$ of +0.45 to -0.04‰ (Pedroni et al., 1999), much heavier than the mid-ocean ridge basalt (MORB) range and also heavier than that of the fumaroles. Both locations benefited from the input of carbonate-derived carbon, although this input from carbonate was much more pronounced at the Hot Pond. Isotopes measured in this study are much lighter, extending down to -19.26‰.

At La Soufrière volcano, St Vincent, the ^{13}C isotopic composition of summit fumaroles and hydrothermal springs fell well within range of the MORB at -2.21‰ to -6.6‰ during 1995 (van Soest et al., 1998; Pedroni et al., 1999); on the other hand, isotopic compositions are also much lighter, down to -12.14‰ in 2021/2024.

While areas surveyed at both volcanoes measured CO_2 fluxes too high to be purely of biogenic origin, the isotopic compositions do not correspond to values associated with a purely hydrothermal source. Contamination of the vial with atmospherics gas is ruled out, as the isotopic composition of air is ~-8‰ (NOAA Global Monitoring Laboratory), and several theories are explored to explain this mismatch.

1) Fractionation of the gas in the vials during storage – Gas collected for ^{13}C analysis in pierced septum capped vials were stored for analysis for 35 days prior to analysis. Investigation of ^{13}C analysis with time shows a decrease in both precision (from 0.01 to 0.10‰) and accuracy (0.07‰) after nine days of storage (Tu et al., 2001). However, if there is leakage of atmosphere into the vials, this should trend the samples toward ~-8‰.

2) Reduction of the input from the hydrothermal source –

    a. Soufrière Hills Volcano, Montserrat – Prior to, and during 2008, the area of the Hot Pond showed physical signs of input from the hydrothermal system beneath the island, in the form of a steaming bubbling pond of water, along with geochemical signals based on ^{13}C isotopes and low pH. Over time, the Hot Pond has decreased in temperature (from 90°C

to ~40°C from 1977 to 2008; Jones et al., 2010), the once steaming, bubbling pond is no more, vegetation has regrown since 2008, illustrated by the coverage of the survey undertaken in 2008 vs that of 2021/2022 (Figure 4.6), and ^{13}C isotopes are now lighter. It is also noted that the eruption state of the volcano has changed since 2008, as there has been a cessation of surface activity in the form of lava extrusion and explosions since 2010. Based on both physical and chemical signs, it is likely that input from the hydrothermal system has ceased in these specific locations, although the mechanism by which this occurred is unclear, and is outside the scope of this study. However, the Soufrière Hills Volcano has been in a state of unrest since 2010, with a small increase in the level of unrest since 2018. Unrest signals include (i) an increase in the rate of volcano-tectonic earthquakes from 0.4 to 1.2 per day from 2018-2021, (ii) inflation of the volcano as measured by the GPS network indicating ongoing input into the deep magmatic system, (iii) SO_2 fluxes far greater than 50 tonnes/day which indicate a potential for future eruptions, and (iv) high temperature fumarole temperatures up to 580 °C (Ryan et al., 2024).

b. La Soufrière volcano, St Vincent – Available documentation in the form of ^{13}C isotopic chemistry and elevated temperatures support a model of hydrothermal input into the Wallibou river, likely due to structural weaknesses in the form of faulting (Figure 4.1; Figure 4.9). While temperatures measured in the warm spring of the Wallibou are still elevated (as of October 2023), ^{13}C of gases collected are lighter than those measured in 1995, and down ~5‰ from mantle range.

3) Environmental factors – soil CO_2 flux is dependent on a number of factors, including environmental and meteorological factors such as rainfall, soil temperature, air temperature, soil water content, barometric pressure, as well as diurnal and seasonal changes (Hinkle, 1994; Chiodini et al., 1998; Viveiros et al., 2008; Boudoire et al., 2017). The biggest influences of soil CO_2 flux are soil temperature, air temperature and barometric pressure, except in areas of precipitation (e.g. Hinkle et al., 1994; Viveiros et al., 2008; Viveiros et al., 2009; Boudoire et al., 2017). This is especially true for barometric pressure and rainfall in areas where the CO_2 concentrations are low (Viveiros et al., 2009). While most survey days occurred in dry, stable conditions, the highest CO_2 fluxes at both La Soufrière volcano, and Soufrière Hills Volcano

occurred in areas with a high soil water content (e.g. Wallibou River, Hot Pond) or where rainfall saturated soils in high density vegetated areas (e.g. a few locations in Cork Hill, Montserrat). Wet conditions affects CO_2 flux by increasing the concentration of CO_2 in the soil, due to the creation of an impermeable barrier in the upper layer of the soil, trapping CO_2 as it rises (Hinkle, 1994), and also by reducing porosity, therefore reducing the amount of CO_2 that can occupy pore spaces (Viveiros et al., 2009). Another consequence of the high water content of soils being investigated stems from the fact that evapouration of water vapour has the ability to displace air in the accumulation chamber during measurement, diluting the CO_2 concentration. At La Soufrière, soil CO_2 flux can generally be seen as increasing with soil temperature (Figure 4.8), however, since the highest CO_2 fluxes are situated in the warm springs of the Wallibou River, and since there is a large spread to the data (R^2 = 0.2791), assessing the correlation between higher CO_2 fluxes with higher soil temperatures is inconclusive. It is therefore possible that high CO_2 fluxes which cannot be explained by biological sources alone are the result of environmental factors.

4) Input of organic carbon – the isotopic chemistry of CO_2 from organic sources ranges from -20‰ to -40‰, whereas CO_2 sourced from the mantle has ^{13}C of -4‰ to -8‰. Overall, total ^{13}C measured at the investigated sites at both volcanoes range -9.94‰ to -19.26‰, and in known hydrothermal areas from -9.94‰ to -12.76‰ at La Soufrière and -12.14‰ to -18.13‰ at Soufrière Hills. Measured ^{13}C therefore falls outside of the range for both sources of CO_2, but also falls between the isotopic signatures of mantle and organic CO_2, indicating that the source of carbon in these areas is a mixture of magmatic CO_2 contaminated by biologic sediments.

5) Precipitation of carbonates in the subsurface – as CO_2 degasses from the magma storage region, it can react with Ca and Mg ions to precipitate carbonates within the crust, leading to C isotope fractionation, where the direction of C isotope fractionation is temperature dependent (Barry et al., 2014). At Soufriere Hills Volcano, geothermal temperatures are estimated to be 180-200°C (Poux and Brophy, 2012), and therefore the low C isotope values in samples can be explained by low temperature (<192°C) carbonate precipitation. Estimated geothermal temperatures at La Soufriere however cover a wider range, from 150-240°C (Dames and Moore, 1998), making the link between carbonate precipitation and mid-ranged C isotopic signature in samples difficult.

With the physical and chemical evidence taken into consideration, the relatively high CO_2 fluxes, although decreased from 2008 to 2021/2022, together with the mid-range ^{13}C values in documented hydrothermally active areas suggests a decrease in input to the Hot Pond from the hydrothermal system at Soufrière Hills Volcano, with mixing of both magmatic and biologically sources gases.

At La Soufrière volcano, St Vincent, there is still independent evidence of hydrothermal input into the river, however, the current ^{13}C isotopic chemistry demonstrates additional input from organic sediments.

4.8 Conclusions and Future Work

The first estimates of the contribution of diffuse soil CO_2 flux to the total CO_2 output at two Lesser Antilles volcanoes has been provided together with new ^{13}C isotopic compositions of the diffused gases.

At Soufrière Hills Volcano, Montserrat, there has been a decrease in the contribution of diffuse CO_2 flux from the Hot Pond from maximum values of 7100 to 270 g m^{-2} day^{-1} along with a marked decrease in ^{13}C composition from ~0‰ down to -12‰ to -18‰ from over the last fourteen years, indicating reduced hydrothermally sourced input into the area. Overall, the Hot Pond has seen a reduction of more than 90% of CO_2 output from 2008 to 2021/2022.

At La Soufrière volcano, St Vincent, diffuse degassing on the flanks of the volcano are restricted to small areas in the Wallibou River at a maximum of 433 g m^{-2} day^{-1}. While high CO_2 fluxes indicate a hydrothermal source, there is some mismatch with ^{13}C composition.

While the contribution of CO_2 to the total CO_2 budget is currently negligible, additional soil CO_2 surveys would be beneficial as the flux can change over years (e.g. at decreased at Soufrière Hills Volcano, but increased at La Soufrière de Guadeloupe; Klein et al., 2024) and can serve as precursory activity to eruptions. There is also scope to: (i) establish diffuse degassing baselines for the future, (ii) combine diffuse degassing with geophysical surveys to understand the structures and deeper fluid flow, (iii) produce soil CO_2 flux maps for risk prevention in islands such as St Lucia where populations surround the hydrothermal areas and (iv) compare soil CO_2 degassing together with passive degassing at other Lesser Antillean volcanoes, for a combined CO_2 budget of the arc.

4.9 Supplementary Material C4

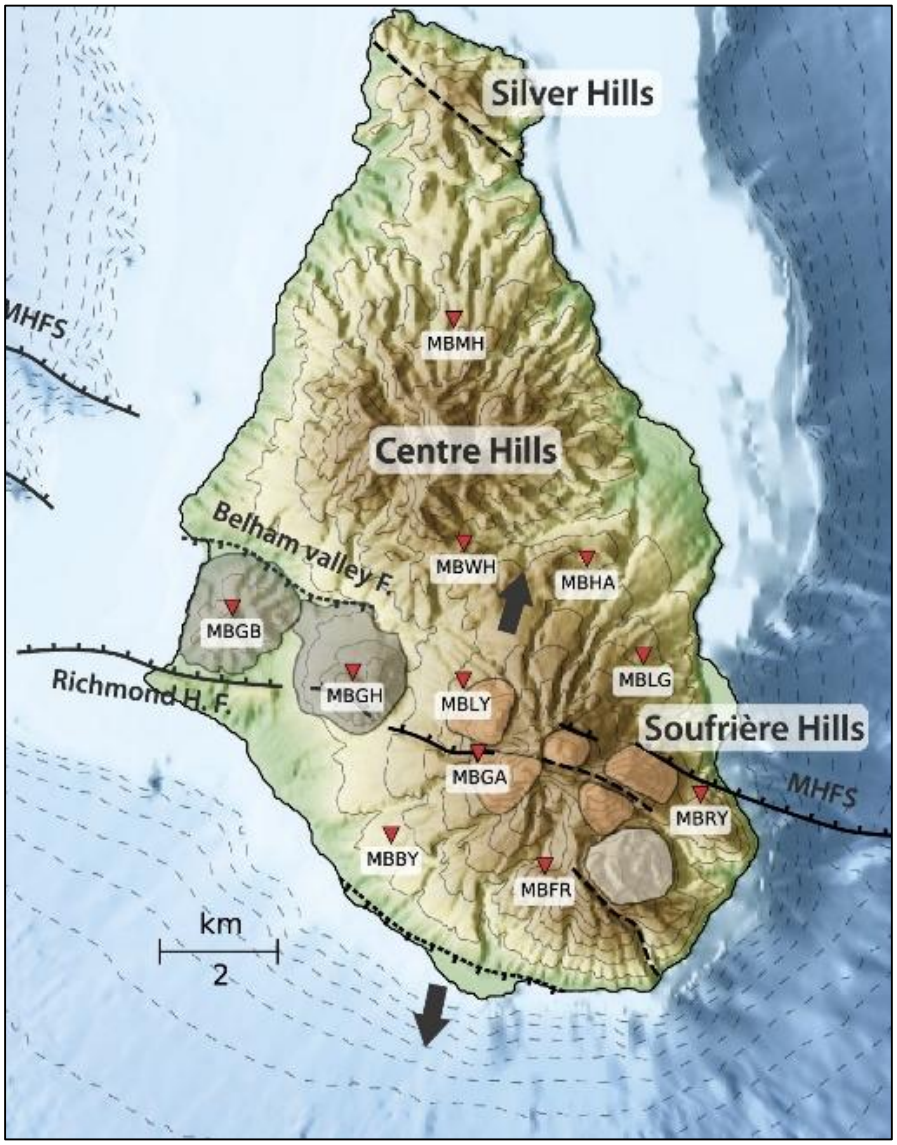

Supplementary Figure 4.S1 – Map of Montserrat showing main faults around Soufrière Hills Volcano and seismic stations (red triangles). Active faults are shown as solid black lines, less active or inferred faults are dashed black lines. Modified from Feulliet et al., (2010).

5 Discussion

Throughout this thesis, two subaerial volcanic systems have been studied, both of which hold great importance in the Lesser Antilles arc, having been two of three sub-aerial volcanoes with eruptions over the last 100 years. At Soufrière Hills Volcano, Montserrat, four phases of eruptions spanning 15 years have been investigated, and at La Soufrière volcano, St Vincent, the explosive phase of the most recent 2020/2021 eruption. Overall, this thesis has provided (i) new insights into the plumbing system of Soufrière Hills Volcano and La Soufrière based on dissolved volatiles in melt inclusions, (ii) quantification of the pre-eruptive volatile budgets of both magmatic systems for a range of volatiles in the melt (H_2O, CO_2, S, Cl, F), and for S in the gas phase at La Soufrière, (iii) the contribution of volatile release including CO_2, SO_2, HCl and HF to the atmosphere, and (iv) the contribution of diffuse CO_2 degassing towards the total CO_2 budget at both volcanoes.

At Soufrière Hills Volcano, Montserrat the first measurements of total magmatic CO_2 in melt inclusions, which include both vapour bubble and glass components, show that the magmatic plumbing system is vertically extensive through the upper to mid crust at a depth range of 5.7 ± 0.8 to 17 ± 2.5 km. This range of depths remained constant over a period of 15 years, spanning the first to the fifth phases of eruptive activity. Although the major and volatile elements evolved throughout time, whole rock compositions remained steady. The magmatic temperature was also calculated, with no systematic trend over the eruptive period. It is also shown that over the studied time period, the Soufrière Hills magma contained a minimum 4.5 Mt of CO_2, calculated using the petrological method. Using this data in conjunction with published values of CO_2 degassing from the plume, the amount of CO_2 released from the magma to the atmosphere was calculated for two eruptive phases, yielding values of 0.24 (Phase 4) to 0.29 Mt (Phase 5). While the amount of CO_2 degassed through the plume at Soufrière Hills is quantified, it is acknowledged that a significant portion of CO_2 can be lost through the soil. The contribution of CO_2 degassing from the soil was investigated in 2008 and 2022/2023, and while an average of 4 tonnes/day was emitted through the soil in 2008, this value has significantly decreased by 90% to only 0.7 tonnes/day, signifying that there is a reduction of hydrothermal input into the investigated diffuse degassing area. This realisation was also corroborated by the chemistry of the gases being emitted, noted by a decrease in the ^{13}C isotopic composition from -0.04 to -0.45‰ (mantle sourced) in 1995 to -12.14 to -18.13‰ (mixed to biogenic sourced). This change in the configuration of the hydrothermal system underlines the importance of both passive and diffuse CO_2 flux monitoring at Soufrière Hills Volcano and it opens discussion on important

questions such as whether the reduction of CO_2 flux is only seen in diffuse degassing areas, or also in the plume. Another important question is – if the pathway to the diffuse degassing areas are somehow blocked, does the system compensate for this by emitting larger quantities of CO_2 through the plume? Since we have suggested that CO_2 flushing is a process occurring at Soufrière Hills Volcano, an increase in CO_2 flushing through the system caused by a blocked outlet has the ability to drive intense explosive eruptions, and CO_2 monitoring therefore has significant impacts on risk assessment at Soufrière Hills Volcano.

Study of melt inclusions and their mineral hosts at La Soufrière volcano, St Vincent reinforce the model of two main zones of magma storage within the crust. H_2O-CO_2 solubility relationships show melt inclusions in equilibrium at ~6 km depth. However, testing of chemical equilibrium demonstrates that crystallisation of olivine, plagioclase, orthopyroxene and clinopyroxene did not occur in the same storage regions. We show that olivine and high An plagioclase crystallised in a hot reservoir likely of basaltic-andesite composition (54 wt.% SiO_2). On the other hand, the pyroxene and low An plagioclase likely crystallised in a cooler reservoir of andesitic composition (~62 wt.% SiO_2). In addition, clinopyroxene-only barometry places this storage region in the upper crust beneath La Soufrière at 1.1-8.0 km depth. Therefore, the hotter, basaltic-andesite magma most likely exists at depths below 8 km. Since H_2O-CO_2 constraints place the bulk of our melt inclusion dataset at ~6 km, we propose that decrepitation occurred during migration of magma from the deeper storage region into the shallow zone prior to eruption. The degassing path of S is modelled and shows that at La Soufrière, degassing occurs at ~9 km depths – in contrast with shallower depths (~5.4 km) of degassing at other arc volcanoes such as Etna. In fact, once it has ascended to a depth of 5 km, the La Soufrière magma has lost ~60% of its S. Further modelling of the molar ratios of CO_2/S_T (S_T = total sulphur, SO_2 + H_2S gases) in the melt inclusion dataset was carried out in order to compare to CO_2/ST ratios measured in the plume, as a proxy for magma degassing. Several scenarios were modelled, representing the three depth groups shown by the melt inclusions (~5, 9 and 22 km). Our modelling shows that at atmospheric pressure, CO_2/ST ratios in the plume are ~1-4, indicating that higher ratios are indicative of deeper degassing. Using the lowest measured CO_2/ST ratio in the plume, our modelling suggests degassing at ~6 km depth, corroborating our clinopyroxene-only barometric results, and serving as an independent method of depth estimation. Since three methods of magma depth estimation are in agreement, we shifted our focus on calculating the pre-eruptive budget of La Soufrière, as well as calculating volatile release to the atmosphere using the petrologic method. Here, it was found that 2.99,

0.06 and 0.18 Mt of H_2O, SO_2 and Cl respectively were released from the melt. However, the excess sulphur issue at arc volcanoes highlights that S also exists in a gas phase within the magmatic system. Taking the amount of S partitioned into the gas phase, we can update SO_2 release from the 2021 explosive eruption to 0.39 Mt, which compares well with satellite-derived SO_2 measurements. Additionally, diffuse CO_2 degassing is investigated at La Soufrière, however, this process is very localized, was impossible to characterise thoroughly due to access constraints, and appears not to significantly contribute to the overall carbon flux.

Overall, the results from the two studied systems – Soufrière Hills Volcano, Montserrat and La Soufrière volcano, St Vincent – demonstrate that while different in terms of location within the arc, magmatic evolution, volatile content, compositions of erupted material, temperature and final depths of storage within the crust, both volcanoes have the ability to produce transitional eruptions consisting of large, violent explosions interspersed with or following lava dome effusion. Both demonstrate the presence of vertically extensive transcrustal magma storage regions, although their systematics differ in detail.

The melt inclusion data presented here fills a large gap in terms of available data from Soufrière Hills Volcano where total CO_2 is now measured across 15 years of eruptions, and at La Soufrière where the full suite of volatiles are now available for the 2020/2021 eruption.

6 Conclusions

Analysis of melt inclusion bubbles at Soufriere Hills Volcano, Montserrat and La Soufriere volcano, St Vincent illustrate the importance in quantifying total melt inclusion CO_2.

At Soufriere Hills Volcano, melt inclusion bubbles contain up to 99% (median of 90%) of CO_2. When used together with H_2O in solubility models, saturation pressures relate to depths of ~6-17 km, a marked increase from ~6 km when only the glass portion of the melt inclusion is considered, demonstrating a vertically extensive transcrustal magmatic storage region below the volcano, in line with geophysical methods. Based on the total melt inclusion CO_2, the pre-eruptive budget of Soufriere Hills Volcano indicates that ~1500-1750 tonnes/day of CO_2 can be degassed from magma at this volcano, which aids in monitoring, as CO_2 fluxes >1750 tonnes/day may indicate other processes (such as flushing) which can trigger eruptions. Additionally, measurements of diffuse CO_2 degassing at this volcano indicate a decrease in CO_2 being degassed through the soil in 2008 vs 2021, along with an increase in C isotopic chemistry, coinciding with the cessation of surface activity in 2010.

The first measurements of total CO_2 at La Soufriere indicate decrepitation of melt inclusions and resulting CO_2 loss, based on the presence of carbonates in volatile free bubbles. Therefore, saturation pressures and inferred depths based on mixed CO_2-H_2O solubility models are largely underestimated and are unreliable. Using additional information such as mineral-melt equilibria, geothermometry and clinopyroxene-only barometry, a polybaric transcrustal magmatic system is identified for La Soufriere. Using the petrological method, it is estimated that a total of 3.7 Mt of SO_2, H_2O, CO_2 and HCl was emitted during the explosive phase of the 2020/2021 eruption. A survey of soil CO_2 reveals limited diffuse degassing at La Soufriere, where almost 100% of the degassing is through the plume.

References

Aiuppa, A., Bitetto, M., Donne, D.D., Paolo, F., Tamburello, G., Coppola, D., Della Schiava, M., Innocenti, L., Lacanna, G., Laiolo, M., Massimetti, F., Pistolesi, M., Silengo, M.C. and Ripepe, M. (2021). Volcanic CO $_2$ tracks the incubation period of basaltic paroxysms. *Science Advances*, 7(38). doi:https://doi.org/10.1126/sciadv.abh0191.

Aiuppa, A., Bitetto, M., Francofonte, V., Velasquez, G., Parra, C.B., Giudice, G., Liuzzo, M., Moretti, R., Moussallam, Y., Peters, N., Tamburello, G., Valderrama, Oscar.A. and Curtis, A. (2017). A CO_2 -gas precursor to the March 2015 Villarrica volcano eruption. *Geochemistry, Geophysics, Geosystems*, 18(6), pp.2120–2132. doi:https://doi.org/10.1002/2017gc006892.

Aiuppa, A., Fischer, T.P., Plank, T. and Bani, P. (2019). CO_2 flux emissions from the Earth's most actively degassing volcanoes, 2005–2015. *Scientific Reports*, 9(1). doi:https://doi.org/10.1038/s41598-019-41901-y.

Allard, P. (2010). A CO_2-rich gas trigger of explosive paroxysms at Stromboli basaltic volcano, Italy. *Journal of Volcanology and Geothermal Research*, 189(3-4), pp.363–374. doi:https://doi.org/10.1016/j.jvolgeores.2009.11.018.

Allard, P., Aiuppa, A., Beauducel, F., Gaudin, D., Di Napoli, R., Calabrese, S., Parello, F., Crispi, O., Hammouya, G. and Tamburello, G. (2014). Steam and gas emission rate from La Soufrière volcano, Guadeloupe (Lesser Antilles): Implications for the magmatic supply during degassing unrest. *Chemical Geology*, 384, pp.76–93. doi:https://doi.org/10.1016/j.chemgeo.2014.06.019.

Allison, C.M., Roggensack, K. and Clarke, A.B. (2021). Highly explosive basaltic eruptions driven by CO 2 exsolution. *Nature Communications*, 12(1), p.217. doi:https://doi.org/10.1038/s41467-020-20354-2.

Allison, C.M., Roggensack, K. and Clarke, A.B. (2022). MafiCH: a general model for H_2O–CO_2 solubility in mafic magmas. *Contributions to Mineralogy and Petrology*, 177(3). doi:https://doi.org/10.1007/s00410-022-01903-y.

Alshembari, R., Hickey, J., Pascal, K. and Syers, R. (2024). Declining magma supply to a poroelastic magma mush explains long-term deformation at Soufrière Hills Volcano. *Earth and planetary science letters*, 631, pp.118624–118624. doi:https://doi.org/10.1016/j.epsl.2024.118624.

Anderson, A.T. and Brown, G.G. (1993). CO_2 contents and formation pressures of some Kilauean melt inclusions. *American Mineralogist*, 78(7-8), pp.794–803.

Ardnt, N.T. (1997). Partitioning of nickel between olivine and ultrabasic komatiite liquids. *Carnegie Institution of Washington Yearbook*, 76, pp.553–557.

Ariskin, A.A. and Barmina, G.S. (1996). An empirical model for the calculation of spinel-melt equilibria in mafic igneous systems at atmospheric pressure: 2. Fe-Ti oxides. *Contributions to Mineralogy and Petrology*, 134(2-3), pp.251–263. doi:https://doi.org/10.1007/s004100050482.

Aspinall, W.P., Miller, A.D., Lynch, L.L., Latchman, J.L., Stewart, R.C., White, R.A. and Power, J.A. (1998). Soufrière Hills Eruption, Montserrat, 1995-1997: Volcanic earthquake locations and fault plane solutions. *Geophysical Research Letters*, 25(18), pp.3397–3400. doi:https://doi.org/10.1029/98gl00858.

Aspinall, W.P., Sigurdsson, H. and Shepherd, J.B. (1973). Eruption of Soufrière Volcano on St. Vincent Island, 1971-1972. *Science*, 181(4095), pp.117–124. doi:https://doi.org/10.1126/science.181.4095.117.

Aster, E.M., Wallace, P.J., Moore, L.R., Watkins, J., Gazel, E. and Bodnar, R.J. (2016). Reconstructing CO_2 concentrations in basaltic melt inclusions using Raman analysis of vapour bubbles. *Journal of Volcanology and Geothermal Research*, 323, pp.148–162. doi:https://doi.org/10.1016/j.jvolgeores.2016.04.028.

Aubaud, C., Hauri, E.H. and Hirschmann, M.M. (2004). Hydrogen partition coefficients between nominally anhydrous minerals and basaltic melts. *Geophysical Research Letters*, 31(20). doi:https://doi.org/10.1029/2004gl021341.

Audetat, A. and Lowenstern, J.B. (2014). Melt Inclusions. In: H.D. Holland and K.K. Turekian, eds., *Treatise on Geochemistry, Second Edition, vol 13*. Oxford: Elsevier, pp.143–173.

Baird, A.F., Kendall, J.-M., Sparks, S.J. and Baptie, B. (2015). Transtensional deformation of Montserrat revealed by shear wave splitting. *Earth and Planetary Science Letters*, 425, pp.179–186. doi:https://doi.org/10.1016/j.epsl.2015.06.006.

Baker, P.E. (1984). Geochemical evolution of St Kitts and Montserrat, Lesser Antilles. *Journal of the Geological Society*, 141(3), pp.401–411. doi:https://doi.org/10.1144/gsjgs.141.3.0401.

Balcone-Boissard, H., Boudon, G., Blundy, J.D., Martel, C., Brooker, R.A., Deloule, E., Solaro, C. and Matjuschkin, V. (2018). Deep pre-eruptive storage of silicic magmas feeding Plinian and dome-forming eruptions of central and northern Dominica (Lesser Antilles) inferred from volatile contents of melt

inclusions. *Contributions to Mineralogy and Petrology*, 173(12). doi:https://doi.org/10.1007/s00410-018-1528-4.

Balcone-Boissard, H., Boudon, G., d'Augustin, T., Erdmann, S., Deloule, E. and Vicente, J. (2023). Architecture of the Lesser Antilles Arc Illustrated by Melt Inclusions. *Journal of Petrology*, 64(6). doi:https://doi.org/10.1093/petrology/egad020.

Barclay, J., Rutherford, M.J., Carroll, M., Murphy, M.D., Devine, J.D., Gardner, J.E. and Sparks, J. (1998). Experimental phase equilibria constraints on pre-eruptive storage conditions of the Soufrière Hills magma. *Geophysical Research Letters*, 25(18), pp.3437–3440. doi:https://doi.org/10.1029/98gl00856.

Barth, A. and Plank, T. (2021). The Ins and Outs of Water in Olivine-Hosted Melt Inclusions: Hygrometer vs. Speedometer. *Frontiers in Earth Science*, 9. doi:https://doi.org/10.3389/feart.2021.614004.

Beattie, P. (1993). Olivine-melt and orthopyroxene-melt equilibria. *Contributions to Mineralogy and Petrology*, 115(1), pp.103–111. doi:https://doi.org/10.1007/bf00712982.

Berlo, K., Stix, J., Roggensack, K. and Ghaleb, B. (2011). A tale of two magmas, Fuego, Guatemala. *Bulletin of Volcanology*, 74(2), pp.377–390. doi:https://doi.org/10.1007/s00445-011-0530-8.

Best, M.G. (2003). *Igneous and Metamorphic Petrology*. 2nd ed.

Bezard, R., Turner, S., Davidson, J., Schmitt, A.K. and Lindsay, J. (2017). Origin and Evolution of Silicic Magmas in Oceanic Arcs; an in situ Study from St Lucia, Lesser Antilles. *Journal of Petrology*, 58(7), pp.1279–1318. doi:https://doi.org/10.1093/petrology/egx053.

Bickle, M.J. (1996). Metamorphic decarbonation, silicate weathering and the long-term carbon cycle. *Terra Nova*, 8(3), pp.270–276. doi:https://doi.org/10.1111/j.1365-3121.1996.tb00756.x.

Blake, S. (2003). Correlations between eruption magnitude, SO_2 yield, and surface cooling. *Geological Society, London, Special Publications*, 213, pp.371–380. doi:https://doi.org/10.1144/gsl.sp.2003.213.01.22.

Blank, J.G. and Brooker, R.A. (1994). Chapter 5. EXPERIMENTAL STUDIES OF CARBON DIOXIDE IN SILICATE MELTS: SOLUBILITY, SPECIATION, AND STABLE CARBON ISOTOPE BEHAVIOR. In: J.R. Holloway, ed., *Volatiles in Magmas*. De Gruyter, pp.157–186. doi:https://doi.org/10.1515/9781501509674-011.

Bloomberg, S., Werner, C., Rissmann, C.F., Mazot, A., Horton, T.W., Gravley, D.M., Kennedy, B.W. and Oze, C. (2014). Soil CO_2emissions as a proxy for heat and mass flow assessment, Taupō Volcanic Zone, New Zealand. *Geochemistry Geophysics Geosystems*, 15(12), pp.4885–4904. doi:https://doi.org/10.1002/2014gc005327.

Blundy, J. and Cashman, K. (2008). Petrologic Reconstruction of Magmatic System Variables and Processes. *Reviews in Mineralogy and Geochemistry*, 69(1), pp.179–239. doi:https://doi.org/10.2138/rmg.2008.69.6.

Blundy, J., Cashman, K.V., Rust, A. and Witham, F. (2010). A case for CO_2-rich arc magmas. *Earth and Planetary Science Letters*, 290(3-4), pp.289–301. doi:https://doi.org/10.1016/j.epsl.2009.12.013.

Bodnar, R. and Student, J.J. (2006). CHAPTER 1: MELT INCLUSIONS IN PLUTONIC ROCKS: PETROGRAPHY AND MICROTHERMOMETRY. In: *Melt Inclusions in Plutonic Rocks*. Mineralogical Association of Canada. https://doi.org/10.3749/9780921294757.ch01.

Bolikhovskaya, S.V., Vasil'eva, M.O. and Koptev-Dvornikov, E.V. (1995). Modelling of low-Ca pyroxene crystallisation in basic systems (New versions of geothermometers). *Geokhimia*, 12, pp.1710–1727.

Borisov, A.A. and Shapkin, A.I. (1990). A new empirical equation rating Fe3+/Fe2+ in magmas to their composition, oxygen fugacity, and temperature. *Geochemistry International*, 27, pp.111–116.

Boudoire, G., Di Muro, A., Liuzzo, M., Ferrazzini, V., Peltier, A., Gurrieri, S., Michon, L., Giudice, G., Kowalski, P. and Boissier, P. (2017). New perspectives on volcano monitoring in a tropical environment: Continuous measurements of soil CO_2 flux at Piton de la Fournaise (La Réunion Island, France). *Geophysical Research Letters*, 44(16), pp.8244–8253. doi:https://doi.org/10.1002/2017gl074237.

Boudoire, G., Pasdeloup, G., Schiavi, F., Cluzel, N., Rafflin, V., Grassa, F., Giuffrida, G., Liuzzo, M., Harris, A., Laporte, D. and Rizzo, A.L. (2023). Magma storage and degassing beneath the youngest volcanoes of the Massif Central (France): Lessons for the monitoring of a dormant volcanic province. *Chemical Geology*, 634, pp.121603–121603. doi:https://doi.org/10.1016/j.chemgeo.2023.121603.

Bouvier, A-S., Deloule, E. and Métrich, N. (2010). Fluid Inputs to Magma Sources of St. Vincent and Grenada (Lesser Antilles): New Insights from Trace Elements in Olivine-hosted Melt Inclusions. *Journal of Petrology*, 51(8), pp.1597–1615. doi:https://doi.org/10.1093/petrology/egq031.

Bouvier, A-S., Métrich, N. and Deloule, E. (2008). Slab-Derived Fluids in the Magma Sources of St. Vincent (Lesser Antilles Arc): Volatile and Light Element Imprints. *Journal of Petrology*, 49(8), pp.1427–1448. doi:https://doi.org/10.1093/petrology/egn031.

Bouvier, A-S., Métrich, N. and Deloule, E. (2010). Light elements, volatiles, and stable isotopes in basaltic melt inclusions from Grenada, Lesser Antilles: Inferences for magma genesis. *Geochemistry Geophysics Geosystems*, 11(9). doi:https://doi.org/10.1029/2010gc003051.

Bouysse, P. (1988). Opening of the Grenada back-arc Basin and evolution of the Caribbean plate during the Mesozoic and early Paleogene. *Tectonophysics*, 149(1-2), pp.121–143. doi:https://doi.org/10.1016/0040-1951(88)90122-9.

Bouysse, P. and Westercamp, D. (1990). Subduction of Atlantic aseismic ridges and Late Cenozoic evolution of the Lesser Antilles island arc. *Tectonophysics*, 175(4), pp.349–380. doi:https://doi.org/10.1016/0040-1951(90)90180-g.

Bouysse, P., Westercamp, D. and Andreieff, P. (1990). *The Lesser Antilles island arc*. Proceedings of the Ocean Drilling Program. Scientific Results, pp.29–44.

Briden, J.C., Rex, D.C., Faller, A.M. and Tomblin, J.F. (1979). K-Ar geochronology and palaeomagnetism of volcanic rocks in the Lesser Antilles island arc. *Philosophical Transactions of the Royal Society of London. Series A, Mathematical and Physical Sciences*, 291(1383), pp.485–528. doi:https://doi.org/10.1098/rsta.1979.0040.

Brown, G.M., Holland, J.G., Sigurdsson, H., Tomblin, J.F. and Arculus, R.J. (1977). Geochemistry of the Lesser Antilles volcanic island arc. *Geochimica et Cosmochimica Acta*, 41(6), pp.785–801. doi:https://doi.org/10.1016/0016-7037(77)90049-7.

Bucholz, C.E., Gaetani, G.A., Behn, M.D. and Shimizu, N. (2013). Post-entrapment modification of volatiles and oxygen fugacity in olivine-hosted melt inclusions. *Earth and Planetary Science Letters*, 374, pp.145–155. doi:https://doi.org/10.1016/j.epsl.2013.05.033.

Buckley, V.J.E., Sparks, R.S.J. and Wood, B.J. (2006). Hornblende dehydration reactions during magma ascent at Soufrière Hills Volcano, Montserrat. *Contributions to Mineralogy and Petrology*, 151(2), pp.121–140. doi:https://doi.org/10.1007/s00410-005-0060-5.

Burton, M., Allard, P., MuréF. and La Spina, A. (2007). Magmatic Gas Composition Reveals the Source Depth of Slug-Driven Strombolian Explosive Activity. *Science*, 317(5835), pp.227–230. doi:https://doi.org/10.1126/science.1141900.

Burton, M., Hayer, C., Miller, C. and Christenson, B. (2021). Insights into the 9 December 2019 eruption of Whakaari/White Island from analysis of TROPOMI SO_2 imagery. *Science Advances*, 7(25), p.eabg1218. doi:https://doi.org/10.1126/sciadv.abg1218.

Burton, M.R., Sawyer, G.M. and Granieri, D. (2013). Deep Carbon Emissions from Volcanoes. *Reviews in Mineralogy and Geochemistry*, 75(1), pp.323–354. doi:https://doi.org/10.2138/rmg.2013.75.11.

Camarda, M., De Gregorio, S., Favara, R. and Gurrieri, S. (2007). Evaluation of carbon isotope fractionation of soil CO_2 under an advective–diffusive regimen: A tool for computing the isotopic composition of unfractionated deep source. *Geochimica et Cosmochimica Acta*, 71(12), pp.3016–3027. doi:https://doi.org/10.1016/j.gca.2007.04.002.

Camejo-Harry, M., Blundy, J., Forsyth, J., Hudson, T., Kendall, J.-M., Christopher, T., Contreras-Arratia, R., Latchman, J.L. and Henry, L. (2025). Petrological Evidence for Magma Mobilisation Years Before the 2020/21 Eruption of La Soufrière Volcano, St. Vincent. *ESS Open Archive*. doi:https://doi.org/10.22541/essoar.173724514.42850941/v1.

Camejo-Harry, M., Melekhova, E., Blundy, J. and Robertson, R. (2019). Evolution in magma storage conditions beneath Kick-'em-Jenny and Kick-'em-Jack submarine volcanoes, Lesser Antilles arc. *Journal of Volcanology and Geothermal Research*, 373, pp.1–22. doi:https://doi.org/10.1016/j.jvolgeores.2019.01.023.

Camejo-Harry, M., Pascal, K., Euillades, P., Grandin, R., Hamling, I., Euillades, L., Contreras-Arratia, R., Ryan, G.A., Latchman, J.L., Lynch, L. and Jo, M. (2023). Monitoring volcano deformation at La Soufrière, St Vincent during the 2020–21 eruption with insights into its magma plumbing system architecture. *Geological Society, London, Special Publications*, 539(1), pp.41–62. doi:https://doi.org/10.1144/sp539-2022-270.

Cann, J. (1982). Rayleigh fractionation with continuous removal of liquid. *Earth and Planetary Science Letters*, 60(1), pp.114–116. doi:https://doi.org/10.1016/0012-821x(82)90026-7.

Cannatelli, C., Doherty, A.L., Esposito, R., Lima, A. and De Vivo, B. (2016). Understanding a volcano through a droplet: A melt inclusion approach. *Journal of Geochemical Exploration*, 171, pp.4–19. doi:https://doi.org/10.1016/j.gexplo.2015.10.003.

Carapezza, M.L. and Granieri, D. (2004). CO_2 soil flux at Vulcano (Italy): comparison between active and passive methods. *Applied Geochemistry*, 19(1), pp.73–88. doi:https://doi.org/10.1016/s0883-2927(03)00111-2.

Carapezza, M.L., Ricci, T., Ranaldi, M. and Tarchini, L. (2009). Active degassing structures of Stromboli and variations in diffuse CO_2 output related to the volcanic activity. *Journal of Volcanology and Geothermal Research*, 182(3-4), pp.231–245. doi:https://doi.org/10.1016/j.jvolgeores.2008.08.006.

Caricchi, L., Sheldrake, T.E. and Blundy, J. (2018). Modulation of magmatic processes by CO_2 flushing. *Earth and Planetary Science Letters*, 491, pp.160–171. doi:https://doi.org/10.1016/j.epsl.2018.03.042.

Carn, S.A. and Prata, F.J. (2010). Satellite-based constraints on explosive SO_2release from Soufrière Hills Volcano, Montserrat. *Geophysical Research Letters*, 37(19). doi:https://doi.org/10.1029/2010gl044971.

Carroll, M.R. and Webster, J.D. (1994). Solubilities of sulfur, noble gases, nitrogen, chlorine and fluorine in magmas. In: M.R. Carroll and J.R. Holloway, eds., *Volatile in Magmas*. Mineralogical Society of America Reviews in Mineralogy, pp.231–279. doi: 10.1515/9781501509674-013.

Cashman, K. and Mangan, M. (1994). Chapter 11b. PHYSICAL ASPECTS OF MAGMATIC DEGASSING II. Constraints on vesiculation processes from textural studies of eruptive products. In: M.R. Carroll and J.R. Holloway, eds., *Volatiles in Magmas*. de Gruyter, pp.447–478.

Cashman, K.V. (2004). Volatile controls on magma ascent and eruption. *The State of the Planet: Frontiers and Challenges in Geophysics. Geophysical Monograph 150, IUGG Volume 19*, pp.109–124. doi:https://doi.org/10.1029/150gm10.

Cashman, K.V. and Edmonds, M. (2019). Mafic glass compositions: a record of magma storage conditions, mixing and ascent. *Philosophical Transactions of the Royal Society A: Mathematical, Physical and Engineering Sciences*, 377. doi:https://doi.org/10.1098/rsta.2018.0004.

Cashman, K.V. and Scheu, B. (2015). Chapter 25. Magmatic Fragmentation. *The Encyclopedia of Volcanoes*, pp.459–471. doi:https://doi.org/10.1016/b978-0-12-385938-9.00025-0.

Cashman, K.V., Sparks, R.S.J. and Blundy, J.D. (2017). Vertically extensive and unstable magmatic systems: A unified view of igneous processes. *Science*, 355(6331), p.eaag3055. doi:https://doi.org/10.1126/science.aag3055.

Cassidy, M., Edmonds, M., Watt, S.F.L., Palmer, M.R. and Gernon, T.M. (2015a). Origin of Basalts by Hybridization in Andesite-dominated Arcs. *Journal of Petrology*, 56(2), pp.325–346. doi:https://doi.org/10.1093/petrology/egv002.

Cassidy, M., Manga, M., Cashman, K. and Bachmann, O. (2018). Controls on explosive-effusive volcanic eruption styles. *Nature Communications*, 9(1), p.2839. doi:https://doi.org/10.1038/s41467-018-05293-3.

Cassidy, M., Watt, S., Talling, P.J., Palmer, M.R., Edmonds, M., Jutzeler, M., Wall-Palmer, D., Manga, M., Coussens, M., Gernon, T.M., Taylor, R.N., Michalik, A., Inglis, E., Breitkreuz, C., Le Friant, A., Ishizuka, O., Boudon, G., McCanta, M.C., Adachi, T. and Hornbach, M.J. (2015b). Rapid onset of mafic magmatism facilitated by volcanic edifice collapse. *Geophysical Research Letters*, 42(12), pp.4778–4785. doi:https://doi.org/10.1002/2015gl064519.

Chaussard, E. and Amelung, F. (2014). Regional controls on magma ascent and storage in volcanic arcs. *Geochemistry, Geophysics, Geosystems*, 15(4), pp.1407–1418. doi:https://doi.org/10.1002/2013gc005216.

Chen, Y., Provost, A., Schiano, P. and Cluzel, N. (2012). Magma ascent rate and initial water concentration inferred from diffusive water loss from olivine-hosted melt inclusions. *Contributions to Mineralogy and Petrology*, 165, pp.525–541.

Chiodini, G., Caliro, S., Cardellini, C., Avino, R., Granieri, D. and Schmidt, A. (2008). Carbon isotopic composition of soil CO_2 efflux, a powerful method to discriminate different sources feeding soil CO_2 degassing in volcanic-hydrothermal areas. *Earth and Planetary Science Letters*, 274(3-4), pp.372–379. doi:https://doi.org/10.1016/j.epsl.2008.07.051.

Chiodini, G., Cardellini, C., Amato, A., Boschi, E., Caliro, S., Frondini, F. and Ventura, G. (2004). Carbon dioxide Earth degassing and seismogenesis in central and southern Italy. *Geophysical Research Letters*, 31(7). doi:https://doi.org/10.1029/2004gl019480.

Chiodini, G., Cioni, R., Frullani, A., Guidi, M., Marini, L., Prati, F. and Raco, B. (1996). Fluid geochemistry of Montserrat Island, West Indies. *Bulletin of Volcanology*, 58(5), pp.380–392. doi:https://doi.org/10.1007/s004450050146.

Chiodini, G., Cioni, R., Guidi, M., Raco, B. and Marini, L. (1998). Soil CO_2 flux measurements in volcanic and geothermal areas. *Applied Geochemistry*, 13(5), pp.543–552. doi:https://doi.org/10.1016/s0883-2927(97)00076-0.

Chiodini, G., Frondini, F., Cardellini, C., Granieri, D., Marini, L. and Ventura, G. (2001). CO_2 degassing and energy release at Solfatara volcano, Campi Flegrei, Italy. *Journal of Geophysical Research: Solid Earth*, 106(B8), pp.16213–16221. doi:https://doi.org/10.1029/2001jb000246.

Chiodini, G., Frondini, F. and Raco, B. (1996). Diffuse emission of CO 2 from the Fossa crater, Vulcano Island (Italy). *Bulletin of Volcanology*, 58(1), pp.41–50. doi:https://doi.org/10.1007/s004450050124.

Christeson, G.L., Mann, P., Escalona, A. and Aitken, T.J. (2008). Crustal structure of the Caribbean-northeastern South America arc-continent collision zone. *Journal of Geophysical Research: Solid Earth*, 113(B8). doi:https://doi.org/10.1029/2007jb005373.

Christopher, T., Edmonds, M., Humphreys, M.C.S. and Herd, R.A. (2010). Volcanic gas emissions from Soufrière Hills Volcano, Montserrat 1995-2009, with implications for mafic magma supply and degassing. *Geophysical Research Letters*, 37(19). doi:https://doi.org/10.1029/2009gl041325.

Christopher, T., Edmonds, M., Taisne, B., Odbert, H., Costa, A., Hards, V. and Wadge, G. (2014a). Periodic sulphur dioxide degassing from the Soufrière Hills Volcano related to deep magma supply. *Geological Society, London, Special Publications*, 410(1), pp.123–141. doi:https://doi.org/10.1144/sp410.11.

Christopher, T.E., Blundy, J., Cashman, K., Cole, P., Edmonds, M., Smith, P.J., Sparks, R.S.J. and Stinton, A. (2015). Crustal-scale degassing due to magma system destabilization and magma-gas decoupling at Soufrière Hills Volcano, Montserrat. *Geochemistry, Geophysics, Geosystems*, 16(9), pp.2797–2811. doi:https://doi.org/10.1002/2015gc005791.

Christopher, T.E., Humphreys, M.C.S., Barclay, J., Genareau, K., De Angelis, S.M.H., Plail, M. and Donovan, A. (2014b). Chapter 17 Petrological and geochemical variation during the Soufrière Hills eruption, 1995 to 2010. *Geological Society, London, Memoirs*, 39(1), pp.317–342. doi:https://doi.org/10.1144/m39.17.

Clark, S.A., Sobiesiak, M., Zelt, C.A., Magnani, M.B., Miller, M.S., Bezada, M.J. and Levander, A. (2008). Identification and tectonic implications of a tear in the South American plate at the southern end of the Lesser Antilles. *Geochemistry, Geophysics, Geosystems*, 9(11). doi:https://doi.org/10.1029/2008gc002084.

Clift, P.D. (2017). A revised budget for Cenozoic sedimentary carbon subduction. *Reviews of Geophysics*, 55(1), pp.97–125. doi:https://doi.org/10.1002/2016rg000531.

Clog, M., Aubaud, C., Cartigny, P. and Dosso, L. (2013). The hydrogen isotopic composition and water content of southern Pacific MORB: A reassessment of the D/H ratio of the depleted mantle reservoir. *Earth and Planetary Science Letters*, 381, pp.156–165. doi:https://doi.org/10.1016/j.epsl.2013.08.043.

Coca, J., Ohde, T., Redondo, A., García-Weil, L., Santana-Casiano, M., González-Dávila, M., Arístegui, J., Nuez, E.F. and Ramos, A.G. (2014). Remote sensing of the El Hierro submarine volcanic eruption plume. *International Journal of Remote Sensing*, 35(17), pp.6573–6598. doi:https://doi.org/10.1080/01431161.2014.960613.

Cofano, A., Cigna, F., Santamaria Amato, L., Siciliani de Cumis, M. and Tapete, D. (2021). Exploiting Sentinel-5P TROPOMI and Ground Sensor Data for the Detection of Volcanic SO_2 Plumes and Activity in 2018–2021 at Stromboli, Italy. *Sensors*, 21(21), p.6991. doi:https://doi.org/10.3390/s21216991.

Cole, P., Smith, P.J., Stinton, A., Odbert, H., Bernstein, M., Komorowski, J. and Stewart, R.C. (2014). Chapter 5 Vulcanian explosions at Soufrière Hills Volcano, Montserrat between 2008 and 2010. *Geological Society, London, Memoirs*, 39(1), pp.93–111. doi:https://doi.org/10.1144/m39.5.

Cole, P.D., Barclay, J., Robertson, A., Mitchell, S., Davies, B.V., Constantinescu, R., Sparks, J., Aspinall, W. and Stinton, A. (2023). Explosive sequence of La Soufrière, St Vincent, April 2021: insights into drivers and consequences via eruptive products. *Special publication - Geological Society of London/Geological Society, London, special publications*, 539(1), pp.81–106. doi:https://doi.org/10.1144/sp539-2022-292.

Cole, P.D., Robertson, R.E.A., Fedele, L. and Scarpati, C. (2019). Explosive activity of the last 1000 years at La Soufrière, St Vincent, Lesser Antilles. *Journal of Volcanology and Geothermal Research*, 371, pp.86–100. doi:https://doi.org/10.1016/j.jvolgeores.2019.01.002.

Cooper, G.F., Macpherson, C.G., Blundy, J.D., Maunder, B., Allen, R.W., Goes, S., Collier, J.S., Bie, L., Harmon, N., Hicks, S.P., Iveson, A.A., Prytulak, J., Rietbrock, A., Rychert, C.A., Davidson, J.P., Cooper, G.F., Macpherson, C.G., Blundy, J.D., Maunder, B. and Allen, R.W. (2020). Variable water input controls evolution of the Lesser Antilles volcanic arc. *Nature*, 582(7813), pp.525–529. doi:https://doi.org/10.1038/s41586-020-2407-5.

Costa, A., Caricchi, L. and Bagdassarov, N. (2009). A model for the rheology of particle-bearing suspensions and partially molten rocks. *Geochemistry, Geophysics, Geosystems*, 10(3). doi:https://doi.org/10.1029/2008gc002138.

Créon, L., Levresse, G., Remusat, L., Bureau, H. and Carrasco-Núñez, G. (2018). New method for initial composition determination of crystallized silicate melt inclusions. *Chemical Geology*, 483, pp.162–173. doi:https://doi.org/10.1016/j.chemgeo.2018.02.038.

d'Augustin, T., Balcone-Boissard, H., Boudon, G., Martel, C., Deloule, E. and Bürckel, P. (2020). Evidence for an Active, Transcrustal Magma System in the Last 60 ka and Eruptive Degassing Budget (H_2O, CO_2, S, F, Cl, Br): The Case of Dominica. *Geochemistry, geophysics, geosystems*, 21(9). doi:https://doi.org/10.1029/2020gc009050.

Danyushevsky, L.V. (2001). The effect of small amounts of H_2O on crystallisation of mid-ocean ridge and backarc basin magmas. *Journal of Volcanology and Geothermal Research*, 110(3-4), pp.265–280. doi:https://doi.org/10.1016/s0377-0273(01)00213-x.

Danyushevsky, L.V., Della-Pasqua, F.N. and Sokolov, S. (2000). Re-equilibration of melt inclusions trapped by magnesian olivine phenocrysts from subduction-related magmas: petrological implications. *Contributions to Mineralogy and Petrology*, 138(1), pp.68–83. doi:https://doi.org/10.1007/pl00007664.

Danyushevsky, L.V., Leslie, R.A.J., Crawford, A.J. and Durance, P. (2004). Melt Inclusions in Primitive Olivine Phenocrysts: the Role of Localized Reaction Processes in the Origin of Anomalous Compositions. *Journal of Petrology*, 45(12), pp.2531–2553. doi:https://doi.org/10.1093/petrology/egh080.

Danyushevsky, L.V., Perfit, M.R., Eggins, S. and Falloon, T.J. (2003). Crustal origin for coupled 'ultra-depleted' and 'plagioclase' signatures in MORB olivine-hosted melt inclusions: evidence from the Siqueiros Transform Fault, East Pacific Rise. *Contributions to Mineralogy and Petrology*, 144(5), pp.619–637. doi:https://doi.org/10.1007/s00410-002-0420-3.

Danyushevsky, L.V. and Plechov, P. (2011). Petrolog3: Integrated software for modeling crystallisation processes. *Geochemistry, Geophysics, Geosystems*, 12(7). doi:https://doi.org/10.1029/2011gc003516.

Dasgupta, R. and Hirschmann, M.M. (2010). The deep carbon cycle and melting in Earth's interior. *Earth and Planetary Science Letters*, 298(1-2), pp.1–13. doi:https://doi.org/10.1016/j.epsl.2010.06.039.

De Vivo, B., Lima, A. and Webster, J.D. (2005). Volatiles in Magmatic-Volcanic Systems. *Elements*, 1(1), pp.19–24. doi:https://doi.org/10.2113/gselements.1.1.19.

DeMets, C. (2001). A new estimate for present-day Cocos-Caribbean Plate motion: Implications for slip along the Central American Volcanic Arc. *Geophysical Research Letters*, 28(21), pp.4043–4046. doi:https://doi.org/10.1029/2001gl013518.

DeMets, C., Jansma, P.E., Mattioli, G.S., Dixon, T.H., Farina, F., Bilham, R., Calais, E. and Mann, P. (2000). GPS geodetic constraints on Caribbean-North America Plate Motion. *Geophysical Research Letters*, 27(3), pp.437–440. doi:https://doi.org/10.1029/1999gl005436.

Devine, J.D., Murphy, M.D., Rutherford, M.J., Barclay, J., Sparks, J., Carroll, M.R., Young, S.R. and Gardner, J.E. (1998). Petrologic evidence for pre-eruptive pressure-temperature conditions, and recent reheating, of andesitic magma erupting at the Soufrière Hills Volcano, Montserrat, W.I. *Geophysical Research Letters*, 25(19), pp.3669–3672. doi:https://doi.org/10.1029/98gl01330.

Devine, J.D., Rutherford, M.J., Norton, G.E. and Young, S.R. (2003). Magma Storage Region Processes Inferred from Geochemistry of Fe-Ti Oxides in Andesitic Magma, Soufrière Hills Volcano, Montserrat, W.I. *Journal of Petrology*, 44(8), pp.1375–1400. doi:https://doi.org/10.1093/petrology/44.8.1375.

Devine, J.D. and Sigurdsson, H. (1983). The liquid composition and crystallisation history of the 1979 Soufrière magma, St. Vincent, W.I. *Journal of Volcanology and Geothermal Research*, 16(1-2), pp.1–31. doi:https://doi.org/10.1016/0377-0273(83)90082-3.

Devine, J.D., Sigurdsson, H., Davis, A.N. and Self, S. (1984). Estimates of sulfur and chlorine yield to the atmosphere from volcanic eruptions and potential climatic effects. *Journal of Geophysical Research: Solid Earth*, 89(B7), pp.6309–6325. doi:https://doi.org/10.1029/jb089ib07p06309.

Ding, S., Plank, T., Wallace, P.J. and Rasmussen, D.J. (2023). Sulfur_X: A Model of Sulfur Degassing During Magma Ascent. *Geochemistry Geophysics Geosystems*, 24(4). doi:https://doi.org/10.1029/2022gc010552.

Dixon, J.E. (1997). Degassing of alkalic basalts. *American Mineralogist*, 82(3-4), pp.368–378. doi:https://doi.org/10.2138/am-1997-3-415.

Dohmen, R., Ter heege, J.H., Becker, H.-W. and Chakraborty, S. (2016). Fe-Mg interdiffusion in orthopyroxene. *American Mineralogist*, 101(10), pp.2210–2221. doi:https://doi.org/10.2138/am-2016-5815.

Druitt, T.H., Young, S.R., Baptie, B., Bonadonna, C., Calder, E.S., Clarke, A.B., Cole, P.D., Harford, C.L., Herd, R.A., Luckett, R., Ryan, G. and Voight, B. (2002). Episodes of cyclic Vulcanian explosive activity with fountain collapse at Soufrière Hills Volcano, Montserrat. *Geological Society, London, Memoirs*, 21(1), pp.281–306. doi:https://doi.org/10.1144/gsl.mem.2002.021.01.13.

Dualeh, E.W., Ebmeier, S.K., Wright, T.J., Poland, M.P., Grandin, R., Stinton, A.J., Camejo-Harry, M., Esse, B. and Burton, M. (2023). Rapid pre-explosion increase in dome extrusion rate at La Soufrière, St. Vincent quantified from synthetic aperture radar backscatter. *Earth and Planetary Science Letters*, 603. doi:https://doi.org/10.1016/j.epsl.2022.117980.

Duan, X. (2014). A general model for predicting the solubility behavior of H_2O–CO_2 fluids in silicate melts over a wide range of pressure, temperature and compositions. *Geochimica et Cosmochimica Acta*, 125, pp.582–609. doi:https://doi.org/10.1016/j.gca.2013.10.018.

Dueñas, C., Fernández, M.C., Carretero, J., Liger, E. and Pérez, M. (1995). Emissions of CO_2 from some soils. *Chemosphere*, 30(10), pp.1875–1889. doi:https://doi.org/10.1016/0045-6535(95)00069-k.

Edmonds, M. and Herd, R.A. (2007). A volcanic degassing event at the explosive-effusive transition. *Geophysical Research Letters*, 34(21). doi:https://doi.org/10.1029/2007gl031379.

Edmonds, M., Herd, R.A., Galle, B. and Oppenheimer, C.M. (2003). Automated, high time-resolution measurements of SO_2 flux at Soufrière Hills Volcano, Montserrat. *Bulletin of Volcanology*, 65(8), pp.578–586. doi:https://doi.org/10.1007/s00445-003-0286-x.

Edmonds, M., Humphreys, M.C., Hauri, E.H., Herd, R.A., Wadge, G., Rawson, H., Ledden, R., Plail, M., Barclay, J., Aiuppa, A., Christopher, T.E., Giudice, G. and Guida, R. (2014). Chapter 16 Pre-eruptive vapour and its role in controlling eruption style and longevity at Soufrière Hills Volcano. *Geological Society London Memoirs*, 39(1), pp.291–315. doi:https://doi.org/10.1144/m39.16.

Edmonds, M., Kohn, S.C., Hauri, E.H., Humphreys, M.C.S. and Cassidy, M. (2016). Extensive, water-rich magma reservoir beneath southern Montserrat. *Lithos*, 252-253, pp.216–233. doi:https://doi.org/10.1016/j.lithos.2016.02.026.

Edmonds, M., Pyle, D. and Oppenheimer, C. (2001). A model for degassing at the Soufrière Hills Volcano, Montserrat, West Indies, based on geochemical data. *Earth and Planetary Science Letters*, 186(2), pp.159–173. doi:https://doi.org/10.1016/s0012-821x(01)00242-4.

Edmonds, M., Pyle, D. and Oppenheimer, C. (2002). HCl emissions at Soufrière Hills Volcano, Montserrat, West Indies, during a second phase of dome building: November 1999 to October 2000. *Bulletin of Volcanology*, 64(1), pp.21–30. doi:https://doi.org/10.1007/s00445-001-0175-0.

Edmonds, M. and Wallace, P.J. (2017). Volatiles and Exsolved Vapour in Volcanic Systems. *Elements*, 13(1), pp.29–34. doi:https://doi.org/10.2113/gselements.13.1.29.

Edmonds, M. and Woods, A.W. (2018). Exsolved volatiles in magma reservoirs. *Journal of Volcanology and Geothermal Research*, 368, pp.13–30. doi:https://doi.org/10.1016/j.jvolgeores.2018.10.018.

Elsworth, D., Mattioli, G., Taron, J., Voight, B. and Herd, R. (2008). Implications of Magma Transfer Between Multiple Reservoirs on Eruption Cycling. *Science*, 322(5899), pp.246–248. doi:https://doi.org/10.1126/science.1161297.

Esposito, R., Lamadrid, H.M., Redi, D., Steele-MacInnis, M., Bodnar, R.J., Manning, C.E., De Vivo, B., Cannatelli, C. and Lima, A. (2016). Detection of liquid H_2O in vapour bubbles in reheated melt inclusions: Implications for magmatic fluid composition and volatile budgets of magmas?. *The American Mineralogist*, 101(7), pp.1691–1695. doi:https://doi.org/10.2138/am-2016-5689.

Esse, B., Burton, M., Hayer, C., Contreras-Arratia, R., Christopher, T., Joseph, E.P., Varnam, M. and Johnson, C. (2023). SO_2 emissions during the 2021 eruption of La Soufrière, St Vincent, revealed with back-trajectory analysis of TROPOMI imagery. *Geological Society London Special Publications*, 539(1), pp.231–244. doi:https://doi.org/10.1144/sp539-2022-77.

Evain, M., Galve, A., Charvis, P., Laigle, M., Kopp, H., Bécel, A., Weinzierl, W., Hirn, A., Flueh, E.R. and Gallart, J. (2011). Structure of the Lesser Antilles subduction forearc and backstop from 3D seismic refraction tomography. *Tectonophysics*, 603, pp.55–67. doi:https://doi.org/10.1016/j.tecto.2011.09.021.

Fall, A., Tattitch, B. and Bodnar, R.J. (2011). Combined microthermometric and Raman spectroscopic technique to determine the salinity of H_2O–CO_2–NaCl fluid inclusions based on clathrate melting. *Geochimica et Cosmochimica Acta*, 75(4), pp.951–964. doi:https://doi.org/10.1016/j.gca.2010.11.021.

Fauria, K.E. and Manga, M. (2018). Pyroclast cooling and saturation in water. *Journal of Volcanology and Geothermal Research*, 362, pp.17–31. doi:https://doi.org/10.1016/j.jvolgeores.2018.07.002.

Fedele, L., Cole, P.D., Scarpati, C. and Robertson, R.E.A. (2021). Petrological insights on the last 1000 years of explosive activity at La Soufrière volcano, St. Vincent (Lesser Antilles). *Lithos*, 392-393, p.106150. doi:https://doi.org/10.1016/j.lithos.2021.106150.

Feignon, J.G., Cluzel, N., Schiavi, F., Moune, S., Roche, O., Clavero, J., Schiano, P. and Auxerre, M. (2022). High CO_2 content in magmas of the explosive andesitic Enco eruption of Mocho-Choshuenco volcano (Chile). *Bulletin of Volcanology*, 84(4). doi:https://doi.org/10.1007/s00445-022-01550-y.

Feuillet, N., Leclerc, F., Tapponnier, P., Beauducel, F., Boudon, G., Le Friant, A., Deplus, C., Lebrun, J.-F., Nercessian, A., Saurel, J.-M. and Clément, V. (2010). Active faulting induced by slip partitioning in Montserrat and link with volcanic activity: New insights from the 2009 GWADASEIS marine cruise data. *Geophysical Research Letters*, 37(19). doi:https://doi.org/10.1029/2010gl042556.

Fink, L.K. (1972). Bathymetric and geologic studies of the Guadeloupe region, Lesser Antilles Island Arc. *Marine Geology*, 12(4), pp.267–288. doi:https://doi.org/10.1016/0025-3227(72)90003-5.

Fischer, T.P. and Aiuppa, A. (2020). AGU Centennial Grand Challenge: Volcanoes and Deep Carbon Global CO 2 Emissions From Subaerial Volcanism—Recent Progress and Future Challenges. *Geochemistry, Geophysics, Geosystems*, 21(3). doi:https://doi.org/10.1029/2019gc008690.

Foroozan, R., Elsworth, D., Voight, B. and Mattioli, G.S. (2010). Dual reservoir structure at Soufrière Hills Volcano inferred from continuous GPS observations and heterogeneous elastic modeling. *Geophysical research letters*, 37(19). doi:https://doi.org/10.1029/2010gl042511.

Frey, H.M., Manon, M.R., Barclay, J., Davies, B.V., Walters, S.A., Cole, P.D., Christopher, T.E. and Joseph, E.P. (2023). Petrology of the explosive deposits from the April 2021 eruption of La Soufrière volcano, St Vincent: a time-series analysis of microlites. *Geological Society, London, Special Publications*, 539(1), pp.201–230. doi:https://doi.org/10.1144/sp539-2022-291.

Frezzotti, M.L., Tecce, F. and Casagli, A. (2012). Raman spectroscopy for fluid inclusion analysis. *Journal of Geochemical Exploration*, 112, pp.1–20. doi:https://doi.org/10.1016/j.gexplo.2011.09.009.

Gaetani, G.A., O'Leary, J.A., Shimizu, N., Bucholz, C.E. and Newville, M. (2012). Rapid reequilibration of H_2O and oxygen fugacity in olivine-hosted melt inclusions. *Geology*, 40(10), pp.915–918. doi:https://doi.org/10.1130/g32992.1.

Gardner, J.E., Hilton, M. and Carroll, M.R. (2000). Bubble growth in highly viscous silicate melts during continuous decompression from high pressure. *Geochimica et Cosmochimica Acta*, 64(8), pp.1473–1483. doi:https://doi.org/10.1016/s0016-7037(99)00436-6.

Gardner, J.E., Wadsworth, F.B., Carley, T.L., Llewellin, E.W., Kusumaatmaja, H. and Sahagian, D. (2023). Bubble Formation in Magma. *Annual Review of Earth and Planetary Sciences*, 51(1). doi:https://doi.org/10.1146/annurev-earth-031621-080308.

Gardner, J.V., Hilton, M.J. and Carroll, M.C. (1999). Experimental constraints on degassing of magma: isothermal bubble growth during continuous decompression from high pressure. *Earth and Planetary Science Letters*, 168(1-2), pp.201–218. doi:https://doi.org/10.1016/s0012-821x(99)00051-5.

Gerlach, T.M. (1980). Evaluation of volcanic gas analyses from Kilauea volcano. *Journal of Volcanology and Geothermal Research*, 7(3-4), pp.295–317. doi:https://doi.org/10.1016/0377-0273(80)90034-7.

Gerlach, T.M. and Graeber, E.J. (1985). Volatile budget of Kilauea volcano. *Nature*, 313(6000), pp.273–277. doi:https://doi.org/10.1038/313273a0.

Gerlach, T.M., Westrich, H.R., Casadevall, T.J. and Finnegan, D.L. (1994). Vapour saturation and accumulation in magmas of the 1989–1990 eruption of Redoubt Volcano, Alaska. *Journal of Volcanology and Geothermal Research*, 62(1-4), pp.317–337. doi:https://doi.org/10.1016/0377-0273(94)90039-6.

Gerya, T.V., Fossati, D., Cantieni, C. and Seward, D. (2009). Dynamic effects of aseismic ridge subduction: numerical modelling. *European Journal of Mineralogy*, 21(3), pp.649–661. doi:https://doi.org/10.1127/0935-1221/2009/0021-1931.

Ghiorso, M.S. and Gualda, G.A.R. (2015). An H_2O–CO_2 mixed fluid saturation model compatible with rhyolite-MELTS. *Contributions to Mineralogy and Petrology*, 169(6). doi:https://doi.org/10.1007/s00410-015-1141-8.

Gillis, K.M. and Coogan, L.A. (2011). Secular variation in carbon uptake into the ocean crust. *Earth and Planetary Science Letters*, 302(3-4), pp.385–392. doi:https://doi.org/10.1016/j.epsl.2010.12.030.

Giordano, D. and Dingwell, D.B. (2003). Non-Arrhenian multicomponent melt viscosity: a model. *Earth and Planetary Science Letters*, 208(3-4), pp.337–349. doi:https://doi.org/10.1016/s0012-821x(03)00042-6.

Giordano, D., Russell, J.K. and Dingwell, D.B. (2008). Viscosity of magmatic liquids: A model. *Earth and Planetary Science Letters*, 271(1-4), pp.123–134. doi:https://doi.org/10.1016/j.epsl.2008.03.038.

Gottsmann, J., Flynn, M. and Hickey, J. (2020). The Transcrustal Magma Reservoir Beneath Soufrière Hills Volcano, Montserrat: Insights From 3-D Geodetic Inversions. *Geophysical Research Letters*, 47(20). doi:https://doi.org/10.1029/2020gl089239.

Gottsmann, J., Harris, A.J.L. and Dingwell, D.B. (2004). Thermal history of Hawaiian pāhoehoe lava crusts at the glass transition: implications for flow rheology and emplacement. *Earth and Planetary Science Letters*, 228(3-4), pp.343–353. doi:https://doi.org/10.1016/j.epsl.2004.09.038.

Graham, A.M. and Thirlwall, M.F. (1981). Petrology of the 1979 eruption of Soufrière volcano, St. Vincent, Lesser Antilles. *Contributions to Mineralogy and Petrology*, 76(3), pp.336–342. doi:https://doi.org/10.1007/bf00375460.

Gualda, G.A.R., Ghiorso, M.S., Lemons, R.V. and Carley, T.L. (2012). Rhyolite-MELTS: a Modified Calibration of MELTS Optimized for Silica-rich, Fluid-bearing Magmatic Systems. *Journal of Petrology*, 53(5), pp.875–890. doi:https://doi.org/10.1093/petrology/egr080.

Gudmundsson, A. (2007). Infrastructure and evolution of ocean-ridge discontinuities in Iceland. *Journal of Geodynamics*, 43(1), pp.6–29. doi:https://doi.org/10.1016/j.jog.2006.09.002.

GURENKO, A.A., TRUMBULL, R.B., THOMAS, R. and LINDSAY, J.M. (2005). A Melt Inclusion Record of Volatiles, Trace Elements and Li–B Isotope Variations in a Single Magma System from the Plat Pays Volcanic Complex, Dominica, Lesser Antilles. *Journal of Petrology*, 46(12), pp.2495–2526. doi:https://doi.org/10.1093/petrology/egi063.

Häkli, T.A. and Wright, T.L. (1967). The fractionation of nickel between olivine and augite as a geothermometer. *Geochimica et Cosmochimica Acta*, 31(5), pp.877–884. doi:https://doi.org/10.1016/s0016-7037(67)80036-x.

Hallis, L.J., Huss, G.R., Nagashima, K., Taylor, G.J., Halldórsson, S.A., Hilton, D.R., Mottl, M.J. and Meech, K.J. (2015). Evidence for primordial water in Earth's deep mantle. *Science*, 350(6262), pp.795–797. doi:https://doi.org/10.1126/science.aac4834.

Hamada, M., Laporte, D., Cluzel, N., Koga, K.T. and Kawamoto, T. (2010). Simulating bubble number density of rhyolitic pumices from Plinian eruptions: constraints from fast decompression experiments. *Bulletin of Volcanology*, 72(6), pp.735–746. doi:https://doi.org/10.1007/s00445-010-0353-z.

Hamada, M., Ushioda, M., Fujii, T. and Takahashi, E. (2013). Hydrogen concentration in plagioclase as a hygrometer of arc basaltic melts: Approaches from melt inclusion analyses and hydrous melting experiments. *Earth and Planetary Science Letters*, 365, pp.253–262. doi:https://doi.org/10.1016/j.epsl.2013.01.026.

Hanyu, T., Yamamoto, J., Kimoto, K., Shimizu, K. and Ushikubo, T. (2020). Determination of total CO_2 in melt inclusions with shrinkage bubbles. *Chemical Geology*, 557, pp.119855–119855. doi:https://doi.org/10.1016/j.chemgeo.2020.119855.

Harford, C.L., Sparks, R.S.J. and Fallick, A.E. (2003). Degassing at the Soufrière Hills Volcano, Montserrat, Recorded in Matrix Glass Compositions. *Journal of Petrology*, 44(8), pp.1503–1523. doi:https://doi.org/10.1093/petrology/44.8.1503.

Hartley, M.E., Bali, E., Maclennan, J., Neave, D.A. and Halldórsson, S.A. (2018). Melt inclusion constraints on petrogenesis of the 2014–2015 Holuhraun eruption, Iceland. *Contributions to Mineralogy and Petrology*, 173(2). doi:https://doi.org/10.1007/s00410-017-1435-0.

Hartley, M.E., Maclennan, J., Edmonds, M. and Thordarson, T. (2014). Reconstructing the deep CO_2 degassing behaviour of large basaltic fissure eruptions. *Earth and Planetary Science Letters*, 393, pp.120–131. doi:https://doi.org/10.1016/j.epsl.2014.02.031.

Hauri, E. (2002). SIMS analysis of volatiles in silicate glasses, 2: isotopes and abundances in Hawaiian melt inclusions. *Chemical Geology*, 183(1-4), pp.115–141. doi:https://doi.org/10.1016/s0009-2541(01)00374-6.

Heath, E., Macdonald, R., Belkin, H., Hawkesworth, C. and Sigurdsson, H. (1998). Magmagenesis at Soufrière Volcano, St Vincent, Lesser Antilles Arc. *Journal of Petrology*, 39(10), pp.1721–1764. doi:https://doi.org/10.1093/petroj/39.10.1721.

Helo, C., Longpré, M.-A., Shimizu, N., Clague, D.A. and Stix, J. (2011). Explosive eruptions at mid-ocean ridges driven by CO_2-rich magmas. *Nature Geoscience*, 4(4), pp.260–263. doi:https://doi.org/10.1038/ngeo1104.

Hernandez, P.A., Notsu, K., Salazar, J.M., Mori, T., Natale, G., Okada, H., Virgili, G., Shimoike, Y., Sato, M. and PérezN.M. (2001). Carbon Dioxide Degassing by Advective Flow from Usu Volcano, Japan. *Science*, 292(5514), pp.83–86. doi:https://doi.org/10.1126/science.1058450.

Hernández, P.A., Salazar, J., Shimoike, Y., Mori, T., Notsu, K. and Pérez, N.M. (2001). Diffuse emission of CO_2 from Miyakejima volcano, Japan. *Chemical Geology*, 177(1-2), pp.175–185. doi:https://doi.org/10.1016/s0009-2541(00)00390-9.

Hinkle, M.E. (1994). Environmental conditions affecting concentrations of He, CO_2, O2 and N2 in soil gases. *Applied Geochemistry*, 9(1), pp.53–63. doi:https://doi.org/10.1016/0883-2927(94)90052-3.

Holloway, J.R. and Blank, J.G. (1994). Chapter 6. APPLICATION OF EXPERIMENTAL RESULTS TO C-O-H SPECIES IN NATURAL MELTS. In: M.R. Carroll and J.R. Holloway, eds., *Volatiles in Magmas*. De Gruyter, pp.187–230. https://doi.org/10.1515/9781501509674-012.

Hooft, E.E. and Detrick, R.S. (1993). The role of density in the accumulation of basaltic melts at mid-ocean ridges. *Geophysical Research Letters*, 20(6), pp.423–426. doi:https://doi.org/10.1029/93gl00295.

Howe, T.A., Christopher, T.E., Moune, S., Tuffen, H. and Schiavi, F. (2025). Melt inclusion bubbles provide new insights into crystallisation depths and CO_2 systematics at Soufrière Hills Volcano, Montserrat. *Frontiers in Earth Science*, 12. doi:https://doi.org/10.3389/feart.2024.1509409.

Huber, C., Townsend, M., Degruyter, W. and Bachmann, O. (2019). Optimal depth of subvolcanic magma chamber growth controlled by volatiles and crust rheology. *Nature Geoscience*, 12(9), pp.762–768. doi:https://doi.org/10.1038/s41561-019-0415-6.

Humphreys, M.C.S., Edmonds, M., Christopher, T. and Hards, V. (2009). Chlorine variations in the magma of Soufrière Hills Volcano, Montserrat: Insights from Cl in hornblende and melt inclusions. *Geochimica et Cosmochimica Acta*, 73(19), pp.5693–5708. doi:https://doi.org/10.1016/j.gca.2009.06.014.

Humphreys, M.C.S., Edmonds, M., Christopher, T. and Hards, V. (2010). Magma hybridisation and diffusive exchange recorded in heterogeneous glasses from Soufrière Hills Volcano, Montserrat. *Geophysical Research Letters*, 37(19). doi:https://doi.org/10.1029/2009gl041926.

Humphreys, M.C.S., Edmonds, M. and Klöcking, M.S. (2016). The validity of plagioclase-melt geothermometry for degassing-driven magma crystallisation. *The American Mineralogist*, 101(4), pp.769–779. doi:https://doi.org/10.2138/am-2016-5314.

Iacono-Marziano, G., Morizet, Y., Le Trong, E. and Gaillard, F. (2012). New experimental data and semi-empirical parameterization of H_2O–CO_2 solubility in mafic melts. *Geochimica et Cosmochimica Acta*, 97, pp.1–23. doi:https://doi.org/10.1016/j.gca.2012.08.035.

Iacovino, K., Matthews, S., Wieser, P.E., Moore, G. and Bégué, F. (2021). VESIcal Part I: An Open-Source Thermodynamic Model Engine for Mixed Volatile (H_2O-CO_2) Solubility in Silicate Melts. *Earth and Space Science*, 8(11). doi:https://doi.org/10.1029/2020ea001584.

Iacovino, K. and Till, C.B. (2019). DensityX: A program for calculating the densities of hydrous magmatic liquids from 427-1,627 °C and up to 30 kbar. *Volcanica*, 2(1), pp.1–10. doi:https://doi.org/10.30909/vol.02.01.0110.

Jarrard, R.D. (1986). Relations among subduction parameters. *Reviews of Geophysics*, 24(2), p.217. doi:https://doi.org/10.1029/rg024i002p00217.

Jicha, B.R. and Mahlburg Kay, S. (2018). Quantifying arc migration and the role of forearc subduction erosion in the central Aleutians. *Journal of Volcanology and Geothermal Research*, 360, pp.84–99. doi:https://doi.org/10.1016/j.jvolgeores.2018.06.016.

Johnson, E. and Rossman, G. (2013). The diffusion behavior of hydrogen in plagioclase feldspar at 800-1000 C: Implications for re-equilibration of hydroxyl in volcanic phenocrysts. *American Mineralogist*, 98(10), pp.1779–1787.

Johnson, M.C., Anderson, A.T. and Rutherford, M.J. (1994). Pre-eruptive Volatiles in Magma. In: M.R. Carroll and J.R. Holloway, eds., *Volatile in Magmas*. De Gruyter, pp.281–330.

Johnston, F.K.B., Turchyn, A.V. and Edmonds, M. (2011). Decarbonation efficiency in subduction zones: Implications for warm Cretaceous climates. *Earth and Planetary Science Letters*, 303(1-2), pp.143–152. doi:https://doi.org/10.1016/j.epsl.2010.12.049.

Jones, M.T., Hembury, D.J., Palmer, M.R., Tonge, B., Darling, W.G. and Loughlin, S.C. (2010). The weathering and element fluxes from active volcanoes to the oceans: a Montserrat case study. *Bulletin of Volcanology*, 73(3), pp.207–222. doi:https://doi.org/10.1007/s00445-010-0397-0.

Jorgenson, C., Higgins, O.J., Petrelli, M., Bégué, F. and Caricchi, L. (2022). A Machine Learning-Based Approach to Clinopyroxene Thermobarometry: Model Optimization and Distribution for Use in Earth Sciences. *Journal of Geophysical Research: Solid Earth*, 127(4). doi:https://doi.org/10.1029/2021jb022904.

Joseph, E.P., Camejo-Harry, M., Christopher, T., Contreras-Arratia, R., Edwards, S., Graham, O., Johnson, M., Juman, A., Latchman, J.L., Lynch, L., Miller, V.L., Papadopoulos, I., Pascal, K., Robertson, R., Ryan, G.A.,

Stinton, A., Grandin, R., Hamling, I., Jo, M.-J. . and Barclay, J. (2022a). Responding to eruptive transitions during the 2020–2021 eruption of La Soufrière volcano, St. Vincent. *Nature Communications*, 13(1), p.4129. doi:https://doi.org/10.1038/s41467-022-31901-4.

Joseph, E.P., Camejo-Harry, M., Christopher, T., Contreras-Arratia, R., Edwards, S., Graham, O., Johnson, M., Juman, A., Latchman, J.L., Lynch, L., Miller, V.L., Papadopoulos, I., Pascal, K., Robertson, R., Ryan, G.A., Stinton, A., Grandin, R., Hamling, I., Jo, M.J. and Barclay, J. (2022b). Responding to eruptive transitions during the 2020–2021 eruption of La Soufrière volcano, St. Vincent. *Nature Communications*, 13(1), p.4129. doi:https://doi.org/10.1038/s41467-022-31901-4.

Kawakami, Y., Yamamoto, J. and Kagi, H. (2003). Micro-Raman Densimeter for CO_2 Inclusions in Mantle-Derived Minerals. *Applied Spectroscopy*, 57(11), pp.1333–1339.

Kay, S.M., Godoy, E. and Kurtz, A. (2005). Episodic arc migration, crustal thickening, subduction erosion, and magmatism in the south-central Andes. *Geological Society of America Bulletin*, 117(1), p.67. doi:https://doi.org/10.1130/b25431.1.

Kelemen, P.B. and Manning, C.E. (2015). Reevaluating carbon fluxes in subduction zones, what goes down, mostly comes up. *Proceedings of the National Academy of Sciences*, 112(30), pp.E3997–E4006. doi:https://doi.org/10.1073/pnas.1507889112.

Kent, A.J.R. (2008). Melt Inclusions in Basaltic and Related Volcanic Rocks. *Reviews in Mineralogy and Geochemistry*, 69(1), pp.273–331. doi:https://doi.org/10.2138/rmg.2008.69.8.

Klein, A., Jessop, D.E., Donnadieu, F., Pierre, J. and Moretti, R. (2024). Dome permeability and fluid circulation at La Soufrière de Guadeloupe implied from soil CO$$_2$$ degassing, thermal flux and self-potential. *Bulletin of Volcanology*, 86(4). doi:https://doi.org/10.1007/s00445-024-01713-z.

Knoepp, J.D. and Vose, J.M. (2002). *Quantitative comparison of in situ soil* CO_2 *flux measurement methods*. Asheville, NC: U.S. Department of Agriculture, Forest Service, Southern Research Station.

Kokelaar, B.P. (2002). Setting, chronology and consequences of the eruption of Soufrière Hills Volcano, Montserrat (1995-1999). *Geological Society, London, Memoirs*, 21(1), pp.1–43. doi:https://doi.org/10.1144/gsl.mem.2002.021.01.02.

Kopp, H., Weinzierl, W., Bécel, A., Charvis, P., Evain, M., Flueh, E.R., Gailler, A., Galve, A., Hirn, A., Kandilarov, A., Klaeschen, D., Laigle, M., Papenberg, C., Planert, L. and Roux, E. (2011). Deep structure of

the central Lesser Antilles Island Arc: Relevance for the formation of continental crust. *Earth and Planetary Science Letters*, 304(1-2), pp.121–134. doi:https://doi.org/10.1016/j.epsl.2011.01.024.

Kudo, A.M. and Weill, D.F. (1970). An igneous plagioclase thermometer. *Contributions to Mineralogy and Petrology*, 25(1), pp.52–65. doi:https://doi.org/10.1007/bf00383062.

Kyser, T.K. and O'Neil, J.R. (1984). Hydrogen isotope systematics of submarine basalts. *Geochimica et Cosmochimica Acta*, 48(10), pp.2123–2133. doi:https://doi.org/10.1016/0016-7037(84)90392-2.

Lamadrid, H.M., Moore, L.A., Moncada, D., Rimstidt, J.D., Burruss, R.C. and Bodnar, R.J. (2017). Reassessment of the Raman CO 2 densimeter. *Chemical Geology*, 450, pp.210–222. doi:https://doi.org/10.1016/j.chemgeo.2016.12.034.

Latchman, J.L. and Aspinall, W. (2023). La Soufrière volcano, St Vincent, eruption 2020–21: assessing unrest and eruptive states from limited volcano-seismic data. *Geological Society, London, Special Publications*, 539(1). doi:https://doi.org/10.1144/sp539-2022-223.

Laurencin, M., Marcaillou, B., Graindorge, D., Klingelhoefer, F., Lallemand, S., Laigle, M. and Lebrun, J. -F. (2017). The polyphased tectonic evolution of the Anegada Passage in the northern Lesser Antilles subduction zone. *Tectonics*, 36(5), pp.945–961. doi:https://doi.org/10.1002/2017tc004511.

Le Bas, M.J., Maitre, R.W.L., Streckeisen, A. and Zanettin, B. (1986). A Chemical Classification of Volcanic Rocks Based on the Total Alkali-Silica Diagram. *Journal of Petrology*, 27(3), pp.745–750. doi:https://doi.org/10.1093/petrology/27.3.745.

Le Friant, A., Boudon, G., Arnulf, A. and Robertson, R.E.A. (2009). Debris avalanche deposits offshore St. Vincent (West Indies): Impact of flank-collapse events on the morphological evolution of the island. *Journal of Volcanology and Geothermal Research*, 179(1-2), pp.1–10. doi:https://doi.org/10.1016/j.jvolgeores.2008.09.022.

Le Gall, N. and Pichavant, M. (2016). Homogeneous bubble nucleation in H 2 O- and H 2 O-CO 2 -bearing basaltic melts: Results of high temperature decompression experiments. *Journal of Volcanology and Geothermal Research*, 327, pp.604–621. doi:https://doi.org/10.1016/j.jvolgeores.2016.10.004.

Liang, N., Hirano, T., Zheng, Z.-M., Tang, J. and Fujinuma, Y. (2010). Soil CO_2 efflux of a larch forest in northern Japan. *Biogeosciences*, 7(11), pp.3447–3457. doi:https://doi.org/10.5194/bg-7-3447-2010.

Lindsay, J.M., Robertson, R.E.A., Shepherd, J.B. and Ali, S. eds., (2005). *Volcanic Hazard Atlas of the Lesser Antilles*. Trinidad and Tobago, WI: Seismic Research Unit, The University of the West Indies.

Liu, Y., Zhang, Y. and Behrens, H. (2005). Solubility of H_2O in rhyolitic melts at low pressures and a new empirical model for mixed H_2O–CO_2 solubility in rhyolitic melts. *Journal of Volcanology and Geothermal Research*, 143(1-3), pp.219–235. doi:https://doi.org/10.1016/j.jvolgeores.2004.09.019.

Liuzzo, M., Gurrieri, S., Giudice, G. and Giuffrida, G. (2013). Ten years of soil CO_2continuous monitoring on Mt. Etna: Exploring the relationship between processes of soil degassing and volcanic activity. *Geochemistry, Geophysics, Geosystems*, 14(8), pp.2886–2899. doi:https://doi.org/10.1002/ggge.20196.

Lloyd, A.S., Plank, T., Ruprecht, P., Hauri, E.H. and Rose, W. (2012). Volatile loss from melt inclusions in pyroclasts of differing sizes. *Contributions to Mineralogy and Petrology*, 165(1), pp.129–153. doi:https://doi.org/10.1007/s00410-012-0800-2.

Lowenstern, J. (1995). Applications of silicate melt inclusions to the study of magmatic volatiles. In: J.F.H. Thompson, ed., *Magmas, Fluids and Ore Deposits*. Mineralogical Association of Canada Short Course Volume, pp.71–99.

Lowenstern, J. (2001). Carbon dioxide in magmas and implications for hydrothermal systems. *Mineralium Deposita*, 36(6), pp.490–502. doi:https://doi.org/10.1007/s001260100185.

Macdonald, R., Hawkesworth, C.J. and Heath, E. (2000). The Lesser Antilles volcanic chain: a study in arc magmatism. *Earth-Science Reviews*, 49(1-4), pp.1–76. doi:https://doi.org/10.1016/s0012-8252(99)00069-0.

Maclennan, J. (2017). Bubble formation and decrepitation control theCO_2content of olivine-hosted melt inclusions. *Geochemistry, Geophysics, Geosystems*, 18(2), pp.597–616. doi:https://doi.org/10.1002/2016gc006633.

Manley, C.R. (1996). Morphology and maturation of melt inclusions in quartz phenocrysts from the Badlands rhyolite lava flow, southwestern Idaho. *American Mineralogist*, 81(1-2), pp.158–168. doi:https://doi.org/10.2138/am-1996-1-220.

Mann, C.P., Wallace, P.J. and Stix, J. (2013). Phenocryst-hosted melt inclusions record stalling of magma during ascent in the conduit and upper magma reservoir prior to vulcanian explosions, Soufrière Hills

volcano, Montserrat, West Indies. *Bulletin of Volcanology*, 75(2). doi:https://doi.org/10.1007/s00445-013-0687-4.

Marianelli, P., Sbrana, A., Métrich, N. and Cecchetti, A. (2005). The deep feeding system of Vesuvius involved in recent violent strombolian eruptions. *Geophysical Research Letters*, 32(2). doi:https://doi.org/10.1029/2004gl021667.

Mason, E., Edmonds, M. and Turchyn, A.V. (2017). Remobilization of crustal carbon may dominate volcanic arc emissions. *Science*, 357(6348), pp.290–294. doi:https://doi.org/10.1126/science.aan5049.

Mason, W.G., Moresi, L., Betts, P.G. and Miller, M.S. (2010). Three-dimensional numerical models of the influence of a buoyant oceanic plateau on subduction zones. *Tectonophysics*, 483(1-2), pp.71–79. doi:https://doi.org/10.1016/j.tecto.2009.08.021.

Mattioli, G.S., Dixon, T.H., Farina, F., Howell, E.S., Jansma, P.E. and Smith, A.L. (1998). GPS measurement of surface deformation around Soufrière Hills Volcano, Montserrat from October 1995 to July 1996. *Geophysical Research Letters*, 25(18), pp.3417–3420. doi:https://doi.org/10.1029/98gl00931.

Mattioli, G.S., Herd, R.A., Strutt, M.H., Ryan, G., Widiwijayanti, C. and Voight, B. (2010). Long term surface deformation of Soufrière Hills Volcano, Montserrat from GPS geodesy: Inferences from simple elastic inverse models. *Geophysical Research Letters*, 37(19). doi:https://doi.org/10.1029/2009gl042268.

Mazzarini, F., Musumeci, G., Montanari, D. and Corti, G. (2010). Relations between deformation and upper crustal magma emplacement in laboratory physical models. *Tectonophysics*, 484(1-4), pp.139–146. doi:https://doi.org/10.1016/j.tecto.2009.09.013.

McCann, W.R. and Sykes, L.R. (1984). Subduction of aseismic ridges beneath the Caribbean Plate: Implications for the tectonics and seismic potential of the northeastern Caribbean. *Journal of Geophysical Research: Solid Earth*, 89(B6), pp.4493–4519. doi:https://doi.org/10.1029/jb089ib06p04493.

McGee, L., Reagan, M., Handley, H., Turner, S., Sparks, R.S., Berlo, K., Barclay, J. and Turner, M. (2019). Volatile behaviour in the 1995-2010 eruption of the Soufrière Hills Volcano, Montserrat recorded by U-series disequilibria in mafic enclaves and andesite host. *Earth and Planetary Science Letters*, 524, p.115730. doi:https://doi.org/10.1016/j.epsl.2019.115730.

Melekhova, E., Blundy, J., Martin, R., Arculus, R. and Pichavant, M. (2017). Petrological and experimental evidence for differentiation of water-rich magmas beneath St. Kitts, Lesser Antilles. *Contributions to mineralogy and petrology*, 172(11-12). doi:https://doi.org/10.1007/s00410-017-1416-3.

Melekhova, E., Blundy, J., Robertson, R. and Humphreys, M.C.S. (2015). Experimental Evidence for Polybaric Differentiation of Primitive Arc Basalt beneath St. Vincent, Lesser Antilles. *Journal of Petrology*, 56(1), pp.161–192. doi:https://doi.org/10.1093/petrology/egu074.

Melekhova, E., Schlaphorst, D., Blundy, J., Kendall, J.-M., Connolly, C., McCarthy, A. and Arculus, R. (2019). Lateral variation in crustal structure along the Lesser Antilles arc from petrology of crustal xenoliths and seismic receiver functions. *Earth and Planetary Science Letters*, 516, pp.12–24. doi:https://doi.org/10.1016/j.epsl.2019.03.030.

Melnik, O. and Sparks, R.S.J. (2002). Dynamics of magma ascent and lava extrusion at Soufrière Hills Volcano, Montserrat. *Geological Society, London, Memoirs*, 21(1), pp.153–171. doi:https://doi.org/10.1144/gsl.mem.2002.021.01.07.

Metcalfe, A., Moune, S., Komorowski, J-C., Robertson, R., Christopher, T.E., Joseph, E.P. and Moretti, R. (2023a). Diverse magma storage and major and volatile magma composition: What are the implications on the eruptive style across a volcanic arc? An example of the Lesser Antilles Arc. *Earth-science reviews*, 241, pp.104440–104440. doi:https://doi.org/10.1016/j.earscirev.2023.104440.

Metcalfe, A., Moune, S., Komorowski, J.-C. and Moretti, R. (2022). Bottom-up vs top-down drivers of eruption style: Petro-geochemical constraints from the holocene explosive activity at La Soufrière de Guadeloupe. *Journal of Volcanology and Geothermal Research*, 424. doi:https://doi.org/10.1016/j.jvolgeores.2022.107488.

Metcalfe, A., Moune, S., Moretti, R., Komorowski, J. and Aubry, T.J. (2023b). Volatile emissions from past eruptions at La Soufrière de Guadeloupe (Lesser Antilles): insights into degassing processes and atmospheric impacts. *Frontiers in Earth Science*, 11. doi:https://doi.org/10.3389/feart.2023.1143325.

Metrich, N. and Wallace, P.J. (2008). Volatile Abundances in Basaltic Magmas and Their Degassing Paths Tracked by Melt Inclusions. *Reviews in Mineralogy and Geochemistry*, 69(1), pp.363–402. doi:https://doi.org/10.2138/rmg.2008.69.10.

Moldover, M.R. (1974). Visual observation of the critical temperature and density: CO_2 and C_2H_4. *Journal of chemical physics online/˜The œJournal of chemical physics/Journal of chemical physics*, 61(5), pp.1766–1778. doi:https://doi.org/10.1063/1.1682173.

Moore, G. (2008). Interpreting H_2O and CO_2 contents in melt inclusions: constraints from solubility experiments and modeling. In: K.D. Putirka and J.F. Tepley, eds., *Minerals, Inclusions and Volcanic processes*. Reviews in Mineralogy and Geochemistry, pp.333–361.

Moore, L., Gazel, E., Tuohy, R.M., Hodder, S., Esposito, R., Steele-MacInnis, M., Hauri, E.H., Wallace, P.K., Plank, T. and Bodnar, R.J. (2015). Bubbles matter: An assessment of the contribution of vapour bubbles to melt inclusion volatile budgets. *American Mineralogist*, 100(4), pp.806–823. doi:https://doi.org/10.2138/am-2015-5036.

Moore, L.R. and Bodnar, R.J. (2019). A pedagogical approach to estimating the CO_2 budget of magmas. *Journal of the Geological Society*, 176(2), pp.398–407. doi:https://doi.org/10.1144/jgs2018-094.

Moretti, R., Métrich, N., Arienzo, I., Di Renzo, V., Aiuppa, A. and Allard, P. (2018). Degassing vs. eruptive styles at Mt. Etna volcano (Sicily, Italy). Part I: Volatile stocking, gas fluxing, and the shift from low-energy to highly explosive basaltic eruptions. *Chemical Geology*, 482, pp.1–17. doi:https://doi.org/10.1016/j.chemgeo.2017.09.017.

Moune, S., Sigmarsson, O., Thordarson, T. and Gauthier, Pierre-J. (2007). Recent volatile evolution in the magmatic system of Hekla volcano, Iceland. *Earth and Planetary Science Letters*, 255(3-4), pp.373–389. doi:https://doi.org/10.1016/j.epsl.2006.12.024.

Müller, T., Dohmen, R., Becker, H.W., ter Heege, J. and Chakraborty, S. (2013). Fe–Mg interdiffusion rates in clinopyroxene: experimental data and implications for Fe–Mg exchange geothermometers. *Contributions to Mineralogy and Petrology*, 166(6), pp.1563–1576. doi:https://doi.org/10.1007/s00410-013-0941-y.

Natland, J. (1984). Occurrences of air-fall volcanic ash derived from the Lesser Antilles arc at Leg 78a drill sites. In: B. Biju-Duval and T. Moore, eds., *Initial Reports of the Deep Sea Drilling Project Vol. 78A*. US Government Printing Office, pp.369–375.

Neave, D.A., Hartley, M.E., Maclennan, J., Edmonds, M. and Thordarson, T. (2017). Volatile and light lithophile elements in high-anorthite plagioclase-hosted melt inclusions from Iceland. *Geochimica et Cosmochimica Acta*, 205, pp.100–118. doi:https://doi.org/10.1016/j.gca.2017.02.009.

Neave, D.A. and Putirka, K.D. (2017). A new clinopyroxene-liquid barometer, and implications for magma storage pressures under Icelandic rift zones. *American Mineralogist*, 102(4), pp.777–794. doi:https://doi.org/10.2138/am-2017-5968.

Neill, I., Kerr, A.C., Hastie, A.R., Stanek, K.-P. and Millar, I.L. (2011). Origin of the Aves Ridge and Dutch–Venezuelan Antilles: interaction of the Cretaceous 'Great Arc' and Caribbean–Colombian Oceanic Plateau?. *Journal of the Geological Society*, 168(2), pp.333–348. doi:https://doi.org/10.1144/0016-76492010-067.

Nerlich, R., Clark, S.R. and Bunge, H.-P. (2014). Reconstructing the link between the Galapagos hotspot and the Caribbean Plateau. *GeoResJ*, 1-2, pp.1–7. doi:https://doi.org/10.1016/j.grj.2014.02.001.

Newcombe, M.E., Plank, T., Barth, A., Asimow, P.D. and Hauri, E. (2020). Water-in-olivine magma ascent chronometry: Every crystal is a clock. *Journal of volcanology and geothermal research*, 398, pp.106872–106872. doi:https://doi.org/10.1016/j.jvolgeores.2020.106872.

Newman, S. and Lowenstern, J.B. (2002). VolatileCalc: a silicate melt–H_2O–CO_2 solution model written in Visual Basic for excel. *Computers & Geosciences*, 28(5), pp.597–604. doi:https://doi.org/10.1016/s0098-3004(01)00081-4.

Ni, H. and Keppler, H. (2013). Carbon in Silicate Melts. *Reviews in Mineralogy and Geochemistry*, 75(1), pp.251–287. doi:https://doi.org/10.2138/rmg.2013.75.9.

Nielsen, R., Crum, J. and Bourgeois, R. (1995). Melt inclusions in high-An plagioclase from the Gorda Ridge: an example of the local diversity of MORB parent magmas. *Contributions to Mineralogy and Petrology*, 122, pp.34–50. doi:https://doi.org/10.1007/s004100050111.

Nielsen, R.L. (2011). The effects of re-homogenization on plagioclase hosted melt inclusions. *Geochemistry, Geophysics, Geosystems*, 12(10), p.n/a-n/a. doi:https://doi.org/10.1029/2011gc003822.

Nimis, P. (1995). A clinopyroxene geobarometer for basaltic systems based on crystal-structure modeling. *Contributions to Mineralogy and Petrology*, 121(2), pp.115–125. doi:https://doi.org/10.1007/s004100050093.

Nimis, P. (1999). Clinopyroxene geobarometry of magmatic rocks. Part 2. Structural geobarometers for basic to acid, tholeiitic and mildly alkaline magmatic systems. *Contributions to Mineralogy and Petrology*, 135(1), pp.62–74. doi:https://doi.org/10.1007/s004100050498.

NOAA (2023). *Global Monitoring Laboratory - Carbon Cycle Greenhouse Gases*. [online] gml.noaa.gov. Available at: https://gml.noaa.gov/ccgg/isotopes/chemistry.html.

Norman, J.M., Garcia, R. and Verma, S.B. (1992). Soil surface CO_2fluxes and the carbon budget of a grassland. *Journal of Geophysical Research*, 97(D17), p.18845. doi:https://doi.org/10.1029/92jd01348.

Notsu, K., Sugiyama, K., Hosoe, M., Uemura, A., Shimoike, Y., Tsunomori, F., Sumino, H., Yamamoto, J., Mori, T. and Hernández, P.A. (2004). Diffuse CO_2 efflux from Iwojima volcano, Izu-Ogasawara arc, Japan. *Journal of Volcanology and Geothermal Research*, 139(3-4), pp.147–161. doi:https://doi.org/10.1016/j.jvolgeores.2004.08.003.

Papale, P., Moretti, R. and Barbato, D. (2006). The compositional dependence of the saturation surface of H_2O+CO_2 fluids in silicate melts. *Chemical Geology*, 229(1-3), pp.78–95. doi:https://doi.org/10.1016/j.chemgeo.2006.01.013.

Parfitt, L. and Wilson, L. (2009). *Fundamentals of Physical Volcanology*. John Wiley & Sons.

Pedroni, A., Hammerschmidt, K. and Friedrichsen, H. (1999). He, Ne, Ar, and C isotope systematics of geothermal emanations in the Lesser Antilles Islands Arc. *Geochimica et Cosmochimica Acta*, 63(3-4), pp.515–532. doi:https://doi.org/10.1016/s0016-7037(99)00018-6.

Pérez, N.M., Padilla, G.D., Padrón, E., Hernández, P.A., Melián, G.V., Barrancos, J., Dionis, S., Nolasco, D., Rodríguez, F., Calvo, D. and Hernández, Í. (2012). Precursory diffuse $CO_2$and H2S emission signatures of the 2011-2012 El Hierro submarine eruption, Canary Islands. *Geophysical Research Letters*, 39(16). doi:https://doi.org/10.1029/2012gl052410.

Petrelli, M., Caricchi, L. and Perugini, D. (2020). Machine Learning Thermo-Barometry: Application to Clinopyroxene-Bearing Magmas. *Journal of Geophysical Research: Solid Earth*, 125(9). doi:https://doi.org/10.1029/2020jb020130.

Phillips, K. (2022). *Insights into Conduit Dynamics and Eruptive Behaviour During the April 2021 La Soufrière, St. Vincent Explosive Eruption*. MSc Thesis.

Pichavant, M., Mysen, B.O. and Macdonald, R. (2002). Source and H_2O content of high-MgO magmas in island arc settings: an experimental study of a primitive calc-alkaline basalt from St. Vincent, lesser antilles arc. *Geochimica et Cosmochimica Acta*, 66(12), pp.2193–2209. doi:https://doi.org/10.1016/s0016-7037(01)00891-2.

Pichavant, M., Poussineau, S., Lesne, P., Solaro, C. and Bourdier, J.-L. (2018). Experimental Parametrization of Magma Mixing: Application to the ad 1530 Eruption of La Soufrière, Guadeloupe (Lesser Antilles). *Journal of Petrology*, 59(2), pp.257–282. doi:https://doi.org/10.1093/petrology/egy030.

Pindell, J.L., Cande, S.C., Pitman, W.C., Rowley, D.B., Dewey, J.F., Labrecque, J. and Haxby, W. (1988). A plate-kinematic framework for models of Caribbean evolution. *Tectonophysics*, 155(1-4), pp.121–138. doi:https://doi.org/10.1016/0040-1951(88)90262-4.

Pindell, J.L. and Kennan, L. (2009). Tectonic evolution of the Gulf of Mexico, Caribbean and northern South America in the mantle reference frame: an update. *Geological Society, London, Special Publications*, 328(1), pp.1–55. doi:https://doi.org/10.1144/sp328.1.

Plank, T., Kelley, K.A., Zimmer, M.M., Hauri, E.H. and Wallace, P.J. (2013). Why do mafic arc magmas contain ~4wt% water on average? *Earth and Planetary Science Letters*, 364, pp.168–179. doi:https://doi.org/10.1016/j.epsl.2012.11.044.

Plank, T. and Manning, C.E. (2019). Subducting carbon. *Nature*, 574(7778), pp.343–352. doi:https://doi.org/10.1038/s41586-019-1643-z.

Poux, B. and Brophy, P. (2012). Geothermal Exploration on the Island of Montserrat, Caribbean. *GRC Transactions*, 36, pp.737–744.

Powell, C.F. (1938). The Royal Society expedition to Montserrat, B.W.I. Final report. *Philosophical transactions of the Royal Society of London*, 237(771), pp.1–34. doi:https://doi.org/10.1098/rsta.1938.0002.

Putirka, K., Johnson, M., Kinzler, R., Longhi, J. and Walker, D. (1996). Thermobarometry of mafic igneous rocks based on clinopyroxene-liquid equilibria, 0-30 kbar. *Contributions to Mineralogy and Petrology*, 123(1), pp.92–108. doi:https://doi.org/10.1007/s004100050145.

Putirka, K., Ryerson, F.J. and Mikaelian, H. (2003). New igneous thermobarometers for mafic and evolved lava compositions, based on clinopyroxene + liquid equilibria. *American Mineralogist*, 88, pp.1542–1554.

Putirka, K.D. (2008). Thermometers and Barometers for Volcanic Systems. *Reviews in Mineralogy and Geochemistry*, 69(1), pp.61–120. doi:https://doi.org/10.2138/rmg.2008.69.3.

Qin, Z., Lu, F. and Anderson, A. (1992). Diffusive reequilibration of melt and fluid inclusions. *American Mineralogist*, 77(5-6), pp.565–576.

Queißer, M., Burton, M.G., Theys, N., Pardini, F., Salerno, G., Caltabiano, T., Varnam, M., Esse, B. and Kazahaya, R. (2019). TROPOMI enables high resolution SO_2 flux observations from Mt. Etna, Italy, and beyond. *Scientific Reports*, 9(1). doi:https://doi.org/10.1038/s41598-018-37807-w.

Rasmussen, D.J., Kyle, P.R., Wallace, P.J., Sims, K.W.W., Gaetani, G.A. and Phillips, E.H. (2017). Understanding Degassing and Transport of CO_2-rich Alkalic Magmas at Ross Island, Antarctica using Olivine-Hosted Melt Inclusions. *Journal of Petrology*, 58(5). doi:https://doi.org/10.1093/petrology/egx036.

Rasmussen, D.J., Plank, T.A., Roman, D.C. and Zimmer, M.M. (2022). Magmatic water content controls the pre-eruptive depth of arc magmas. *Science*, 375(6585), pp.1169–1172. doi:https://doi.org/10.1126/science.abm5174.

Rasmussen, D.J., Plank, T.A., Wallace, P.J., Newcombe, M.E. and Lowenstern, J.B. (2020). Vapour-bubble growth in olivine-hosted melt inclusions. *American Mineralogist*, 105(12), pp.1898–1919. doi:https://doi.org/10.2138/am-2020-7377.

Robertson, A., Barclay, J., Joseph, E.P. and Sparks, J. (2023). An overview of the eruption of La Soufrière Volcano, St. Vincent 2020 to 2021. *Geological Society, London, Special Publications*, 539(1). doi:https://doi.org/10.1144/sp539-2023-95.

Robock, A. (2000). Volcanic eruptions and climate. *Reviews of Geophysics*, 38(2), pp.191–219. doi:https://doi.org/10.1029/1998rg000054.

Roedder, E. (1979). Origin and significance of magmatic inclusions. *Bulletin de Minéralogie*, 102(5), pp.487–510. doi:https://doi.org/10.3406/bulmi.1979.7299.

Rose, W.I., Heiken, G., Wohletz, K.H., Eppler, D., Barr, S., Miller, T.L., Chuan, R.L. and Symonds, R.T. (1988). Direct Rate Measurements of Eruption Plumes at Augustine Volcano: A Problem of Scaling and Uncontrolled Variables. *Journal of Geophysical Research: Solid Earth*, 93(B5), pp.4485–4499. doi:https://doi.org/10.1029/jb093ib05p04485.

Rose-Koga, E.F., Bouvier, A.-S., Gaetani, G.A., Wallace, P.J., Allison, C.M., Andrys, J.A., Angeles de la Torre, A., Barth, A., Bodnar, R.J., Bracco Gartner, A.J.J., Butters, D., Castillejo, A., Chilson-Parks, B., Choudhary, B.R., Cluzel, N., Cole, M., Cottrell, E., Daly, A., Danyushevsky, L.V. and DeVitre, C.L. (2021). Silicate melt inclusions in the new millennium: A review of recommended practices for preparation, analysis, and data

presentation. *Chemical Geology*, 570, pp.120145–120145. doi:https://doi.org/10.1016/j.chemgeo.2021.120145.

Rosenthal, A., Hauri, E.H. and Hirschmann, M.M. (2015). Experimental determination of C, F, and H partitioning between mantle minerals and carbonated basalt, CO 2 /Ba and CO 2 /Nb systematics of partial melting, and the CO 2 contents of basaltic source regions. *Earth and Planetary Science Letters*, 412, pp.77–87. doi:https://doi.org/10.1016/j.epsl.2014.11.044.

Rust, A.C., Cashman, K.V. and Wallace, P.J. (2004). Magma degassing buffered by vapour flow through brecciated conduit margins. *Geology*, 32(4), p.349. doi:https://doi.org/10.1130/g20388.2.

Rust, A.C., Manga, M. and Cashman, K.V. (2003). Determining flow type, shear rate and shear stress in magmas from bubble shapes and orientations. *Journal of Volcanology and Geothermal Research*, 122(1-2), pp.111–132. doi:https://doi.org/10.1016/s0377-0273(02)00487-0.

Rutherford, M.J. and Devine, J.D. (2003). Magmatic Conditions and Magma Ascent as Indicated by Hornblende Phase Equilibria and Reactions in the 1995-2002 Soufrière Hills Magma. *Journal of Petrology*, 44(8), pp.1433–1453. doi:https://doi.org/10.1093/petrology/44.8.1433.

Ryan, G., Stinton, A., Bass, V., Christopher, T., Fergus, M., Rowan, A., Marrero, J., Pascal, K., Stewart, R., Syers, R. and Williams, P. (2024). *MVO Scientific Report for Volcanic Activity between 1 October 2023 and 31 March 2024 . Open File Report OFR 24-01*. Flemmings, Montserrat: Montserrat Volcano Observatory.

Ryan, G.A., Loughlin, S.C., James, M.R., Jones, L.D., Calder, E.S., Christopher, T., Strutt, M.H. and Wadge, G. (2010). Growth of the lava dome and extrusion rates at Soufrière Hills Volcano, Montserrat, West Indies: 2005-2008. *Geophysical Research Letters*, 37(19). doi:https://doi.org/10.1029/2009gl041477.

Ryan, M.J. and Sammis, C.G. (1981). The glass transition in basalt. *Journal of Geophysical Research: Solid Earth*, 86(B10), pp.9519–9535. doi:https://doi.org/10.1029/jb086ib10p09519.

Sano, Y. and Marty, B. (1995). Origin of carbon in fumarolic gas from island arcs. *Chemical Geology*, 119(1-4), pp.265–274. doi:https://doi.org/10.1016/0009-2541(94)00097-r.

Sano, Y. and Williams, S.N. (1996). Fluxes of mantle and subducted carbon along convergent plate boundaries. *Geophysical Research Letters*, 23(20), pp.2749–2752. doi:https://doi.org/10.1029/96gl02260.

Scaillet, B., Luhr, J.F. and Carroll, M.R. (2003). Petrological and Volcanological Constraints on Volcanic Sulfur Emissions to the Atmosphere. In: A. Robock and C. Oppenheimer, eds., *Volcanism and the Earth's Atmosphere, Volume 139*. American Geophysical Union, pp.11–40. doi: 10.1029/139GM02.

Schiavi, F., Bolfan-Casanova, N., Buso, R., Laumonier, M., Laporte, D., Medjoubi, K., Venugopal, S., Gómez-Ulla, A., Cluzel, N. and Hardiagon, M. (2020). Quantifying magmatic volatiles by Raman microtomography of glass inclusion-hosted bubbles. *Geochemical perspectives letters*, 16, pp.17–24. doi:https://doi.org/10.7185/geochemlet.2038.

Schipper, C.I., White, J.D.L., Houghton, B.F., Shimizu, N. and Stewart, R.B. (2010). Explosive submarine eruptions driven by volatile-coupled degassing at Lō`ihi Seamount, Hawai`i. *Earth and Planetary Science Letters*, 295(3-4), pp.497–510. doi:https://doi.org/10.1016/j.epsl.2010.04.031.

Scholz, K., Townsend, M., Huber, C., Troch, J., Bachmann, O. and Coonin, A.N. (2023). Investigating the Impact of an Exsolved H_2O-CO_2 Phase on Magma Chamber Growth and Longevity: A Thermomechanical Model. *Geochemistry Geophysics Geosystems*, 24(12). doi:https://doi.org/10.1029/2023gc011151.

Sharma, K., Blake, S., Self, S. and Krueger, A.J. (2004). SO_2emissions from basaltic eruptions, and the excess sulfur issue. *Geophysical Research Letters*, 31(13). doi:https://doi.org/10.1029/2004gl019688.

Shea, T. (2017). Bubble nucleation in magmas: A dominantly heterogeneous process? *Journal of Volcanology and Geothermal Research*, 343, pp.155–170. doi:https://doi.org/10.1016/j.jvolgeores.2017.06.025.

Shepherd, J.B., Aspinall, W.P., Rowley, K.C., Pereira, J., Sigurdsson, H., Fiske, R.S. and Tomblin, J.F. (1979). The eruption of Soufrière volcano, St Vincent April–June 1979. *Nature*, 282(5734), pp.24–28. doi:https://doi.org/10.1038/282024a0.

Shepherd, J.B. and Sigurdsson, H. (1982). Mechanism of the 1979 explosive eruption of Soufrière volcano, St. Vincent. *Journal of Volcanology and Geothermal Research*, 13(1-2), pp.119–130. doi:https://doi.org/10.1016/0377-0273(82)90023-3.

Shepherd, J.B., Tomblin, J.F. and Woo, D.A. (1971). Volcano-seismic crisis in Montserrat, West Indies, 1966–67. *Bulletin Volcanologique*, 35(1), pp.143–162. doi:https://doi.org/10.1007/bf02596813.

Shipboard Scientific Party (1984). Oceanic reference site east of the barbados ridge complex. In: B. Biju-Duval and T. Moore, eds., *Initial Reports of the Deep Sea Drilling Project Vol. 78A*. US Government Printing Office, pp.227–289.

Sigurdsson, H. and Carey, S. (n.d.). Marine Tephrochronology and Quaternary Explosive Volcanism in the Lesser Antilles Arc. In: S. Self and R.S.J. Sparks, eds., *Tephra Studies. NATO Advanced Study Institutes Series*. Dordrecht: Springer, pp.255–280.

Sigurdsson, H., Carey, S., Palais, J.M. and Devine, J. (1990). Pre-eruption compositional gradients and mixing of andesite and dacite magma erupted from Nevado del Ruiz Volcano, Colombia in 1985. *Journal of Volcanology and Geothermal Research*, 41(1-4), pp.127–151. doi:https://doi.org/10.1016/0377-0273(90)90086-u.

Sinclair, A.J. (1974). Selection of threshold values in geochemical data using probability graphs. *Journal of Geochemical Exploration*, 3(2), pp.129–149. doi:https://doi.org/10.1016/0375-6742(74)90030-2.

Smith, A.L., Roobol, M.J. and Gunn, B.M. (1980). The Lesser Antilles — A discussion of the Island arc magmatism. *Bulletin Volcanologique*, 43(2), pp.287–302. doi:https://doi.org/10.1007/bf02598033.

Smith, P. (2013). Volcano-Tectonic Seismicity of Soufrière Hills Volcano, Montserrat. *Encyclopedia of Earthquake Engineering*, pp.1–14. doi:https://doi.org/10.1007/978-3-642-36197-5_93-1.

Spandler, C., O'Neill, H. and Kamenetsky, V.S. (2007). Survival times of anomalous melt inclusions from element diffusion in olivine and chromite. *Nature*, 447(7142), pp.303–306. doi:https://doi.org/10.1038/nature05759.

Sparks, J., Aspinall, W.P., Barclay, J., Renfrew, I.A., Contreras-Arratia, R. and Stewart, R. (2023). Analysis of magma flux and eruption intensity during the 2021 explosive activity at the Soufrière of St Vincent, West Indies. *Geological Society, London, Special Publications*, 539(1), pp.63–79. doi:https://doi.org/10.1144/sp539-2022-286.

Sparks, J., Barclay, J., Jaupart, C., Mader, H.M. and Phillips, J.C. (1994). Chapter 11a. PHYSICAL ASPECTS OF MAGMA DEGASSING I. Experimental and theoretical constraints on vesiculation. *De Gruyter eBooks*, pp.413–446. doi:https://doi.org/10.1515/9781501509674-017.

Sparks, R.S.J. (1978). The dynamics of bubble formation and growth in magmas: A review and analysis. *Journal of Volcanology and Geothermal Research*, 3(1-2), pp.1–37. doi:https://doi.org/10.1016/0377-0273(78)90002-1.

Sparks, R.S.J., Annen, C., Blundy, J.D., Cashman, K.V., Rust, A.C. and Jackson, M.D. (2019). Formation and dynamics of magma reservoirs. *Philosophical Transactions of the Royal Society A: Mathematical, Physical and Engineering Sciences*, 377(2139). doi:https://doi.org/10.1098/rsta.2018.0019.

Sparks, R.S.J. and Cashman, K.V. (2017). Dynamic Magma Systems: Implications for Forecasting Volcanic Activity. *Elements*, 13(1), pp.35–40. doi:https://doi.org/10.2113/gselements.13.1.35.

Sparks, R.S.J. and Young, S.R. (2002). The eruption of Soufrière Hills Volcano, Montserrat (1995-1999): overview of scientific results. *Geological Society, London, Memoirs*, 21(1), pp.45–69. doi:https://doi.org/10.1144/gsl.mem.2002.021.01.03.

Speed, R.C. (1985). Cenozoic collision of the Lesser Antilles Arc and continental South America and the origin of the El Pilar Fault. *Tectonics*, 4(1), pp.41–69. doi:https://doi.org/10.1029/tc004i001p00041.

Spilliaert, N., Allard, P., Métrich, N. and Sobolev, A.V. (2006a). Melt inclusion record of the conditions of ascent, degassing, and extrusion of volatile-rich alkali basalt during the powerful 2002 flank eruption of Mount Etna (Italy). *Journal of Geophysical Research*, 111(B4). doi:https://doi.org/10.1029/2005jb003934.

Spilliaert, N., Metrich, N. and Allard, P. (2006b). S–Cl–F degassing pattern of water-rich alkali basalt: Modelling and relationship with eruption styles on Mount Etna volcano. *Earth and Planetary Science Letters*, 248(3-4), pp.772–786. doi:https://doi.org/10.1016/j.epsl.2006.06.031.

Steele-Macinnis, M., Esposito, R. and Bodnar, R.J. (2011). Thermodynamic Model for the Effect of Post-entrapment Crystallisation on the H_2O-CO_2 Systematics of Vapour-saturated, Silicate Melt Inclusions. *Journal of Petrology*, 52(12), pp.2461–2482. doi:https://doi.org/10.1093/petrology/egr052.

Stinton, A., Cole, P.L., Odbert, H.M., Christopher, T., Avard, G. and Bernstein, M.P. (2014a). Chapter 6 Dome growth and valley fill during Phase 5 (8 October 2009–11 February 2010) at the Soufrière Hills Volcano, Montserrat. *Geological Society, London, Memoirs*, 39(1), pp.113–131. doi:https://doi.org/10.1144/m39.6.

Stinton, A.J. (2023). Growth and evolution of the lava dome and coulée during the 2020–21 eruption of La Soufrière, St Vincent. *Geological Society, London, Special Publications*, 539(1), pp.25–39. doi:https://doi.org/10.1144/sp539-2022-304.

Stinton, A.J., Cole, P.D., Stewart, R.C., Odbert, H.M. and Smith, P. (2014b). Chapter 7 The 11 February 2010 partial dome collapse at Soufrière Hills Volcano, Montserrat. *Geological Society, London, Memoirs*, 39(1), pp.133–152. doi:https://doi.org/10.1144/M39.7.

Stopler, E. (1982). Water in silicate glasses: An infrared spectroscopic study. *Contributions to Mineralogy and Petrology*, 81(1), pp.1–17. doi:https://doi.org/10.1007/bf00371154.

Stopler, E. (1989). Temperature dependence of the speciation of water in rhyolitic melts and glasses. *American Mineralogist*, 74(11-12), pp.1247–1257.

Sugawara, T. (2000). Empirical relationships between temperature, pressure, and MgO content in olivine and pyroxene saturated liquid. *Journal of Geophysical Research: Solid Earth*, 105(B4), pp.8457–8472. doi:https://doi.org/10.1029/2000jb900010.

Symonds, R.B., Gerlach, T.M. and Reed, M.H. (2001). Magmatic gas scrubbing: implications for volcano monitoring. *Journal of Volcanology and Geothermal Research*, 108(1-4), pp.303–341. doi:https://doi.org/10.1016/s0377-0273(00)00292-4.

Symonds, R.B., Rose, W.I., Bluth, G.J.S. and Gerlach, T.M. (1994). Chapter 1. VOLCANIC-GAS STUDIES: METHODS, RESULTS, AND APPLICATIONS. In: M.R. Carroll and J.R. Holloway, eds., *Volatiles in Magmas*. De Gruyter, pp.1–66. doi:https://doi.org/10.1515/9781501509674-007.

Theys, N., Hedelt, P., De Smedt, I., Lerot, C., Yu, H., Vlietinck, J., Pedergnana, M., Arellano, S., Galle, B., Fernandez, D., Carlito, C.J.M., Barrington, C., Taisne, B., Delgado-Granados, H., Loyola, D. and Van Roozendael, M. (2019). Global monitoring of volcanic SO_2 degassing with unprecedented resolution from TROPOMI onboard Sentinel-5 Precursor. *Scientific Reports*, 9(1). doi:https://doi.org/10.1038/s41598-019-39279-y.

Tollan, P.M.E., Bindeman, I. and Blundy, J.D. (2011). Cumulate xenoliths from St. Vincent, Lesser Antilles Island Arc: a window into upper crustal differentiation of mantle-derived basalts. *Contributions to Mineralogy and Petrology*, 163(2), pp.189–208. doi:https://doi.org/10.1007/s00410-011-0665-9.

Tomblin, J.F. (1975). The Lesser Antilles and Aves Ridge. In: A.E.M. Nairn and F.G. Stehli, eds., *The Gulf of Mexico and the Caribbean*. Boston, MA: Springer. https://doi.org/10.1007/978-1-4684-8535-6_11.

Toplis, M.J. (2005). The thermodynamics of iron and magnesium partitioning between olivine and liquid: criteria for assessing and predicting equilibrium in natural and experimental systems. *Contributions to Mineralogy and Petrology*, 149(1), pp.22–39. doi:https://doi.org/10.1007/s00410-004-0629-4.

Toramaru, A. (1995). Numerical study of nucleation and growth of bubbles in viscous magmas. *Journal of Geophysical Research*, 100(B2), pp.1913–1931. doi:https://doi.org/10.1029/94jb02775.

Tu, F.H., Thornton, D.C., Bandy, A.R., Carmichael, G.R., Tang, Y., Thornhill, K.L., Sachse, G.W. and Blake, D.R. (2004). Long-range transport of sulfur dioxide in the central Pacific. *Journal of Geophysical Research*, 109(D15). doi:https://doi.org/10.1029/2003jd004309.

Tu, K.P., Brooks, P.D. and Dawson, T.E. (2001). Using septum-capped vials with continuous-flow isotope ratio mass spectrometric analysis of atmospheric CO_2 for Keeling plot applications. *Rapid Communications in Mass Spectrometry*, 15(12), pp.952–956. doi:https://doi.org/10.1002/rcm.320.

Tucker, J.M., Hauri, E.H., Pietruszka, A.J., Garcia, M.O., Marske, J.P. and Trusdell, F.A. (2019). A high carbon content of the Hawaiian mantle from olivine-hosted melt inclusions. *Geochimica et Cosmochimica Acta*, 254, pp.156–172. doi:https://doi.org/10.1016/j.gca.2019.04.001.

Tuffen, H., James, M.R., Castro, J.M. and Schipper, C.I. (2013). Exceptional mobility of an advancing rhyolitic obsidian flow at Cordón Caulle volcano in Chile. *Nature Communications*, 4(1). doi:https://doi.org/10.1038/ncomms3709.

van der Meer, D.G., Zeebe, R.E., van Hinsbergen, D.J.J. and Torsvik, T.H. (2014). Plate tectonic controls on atmospheric CO_2 levels since the Triassic. *PNAS*, 111(12), pp.4380–4385. doi:https://doi.org/10.1073/pnas.1315657111.

van Soest, M.C., Hilton, D.R. and Kreulen, R. (1998). Tracing crustal and slab contributions to arc magmatism in the lesser antilles island arc using helium and carbon relationships in geothermal fluids. *Geochimica et Cosmochimica Acta*, 62(19-20), pp.3323–3335. doi:https://doi.org/10.1016/s0016-7037(98)00241-5.

Venugopal, S., Schiavi, F., Moune, S., Bolfan-Casanova, N., Druitt, T. and Williams-Jones, G. (2020). Melt inclusion vapour bubbles: the hidden reservoir for major and volatile elements. *Scientific Reports*, 10(1). doi:https://doi.org/10.1038/s41598-020-65226-3.

Viveiros, F., Cardellini, C., Ferreira, T., Caliro, S., Chiodini, G. and Silva, C. (2010). Soil CO_2emissions at Furnas volcano, São Miguel Island, Azores archipelago: Volcano monitoring perspectives, geomorphologic studies, and land use planning application. *Journal of Geophysical Research*, 115(B12). doi:https://doi.org/10.1029/2010jb007555.

Viveiros, F., Ferreira, M.T., Silva, C. and Rocha, L.A. (2009). Meteorological factors controlling soil gases and indoor CO_2 concentration: A permanent risk in degassing areas. *Science of the Total Environment*, 407(4), pp.1362–1372. doi:https://doi.org/10.1016/j.scitotenv.2008.10.009.

Viveiros, F., Ferreira, T., Cabral Vieira, J., Silva, C. and Gaspar, J.L. (2008). Environmental influences on soil CO_2 degassing at Furnas and Fogo volcanoes (São Miguel Island, Azores archipelago). *Journal of Volcanology and Geothermal Research*, 177(4), pp.883–893. doi:https://doi.org/10.1016/j.jvolgeores.2008.07.005.

Voight, B., Sparks, R.S.J., Miller, A.D., Stewart, R.C., Hoblitt, R.P. and Clarke, A. (1999). Magma Flow Instability and Cyclic Activity at Soufrière Hills Volcano, Montserrat, British West Indies. *Science*, 283(5405), pp.1138–1142. doi:https://doi.org/10.1126/science.283.5405.1138.

Wadge, G. (1984). Comparison of volcanic production rates and subduction rates in the Lesser Antilles and Central America. *Geology*, 12(9), pp.555–558. doi:https://doi.org/10.1130/0091-7613(1984)12%3C555:covpra%3E2.0.co;2.

Wadge, G. and Shepherd, J.B. (1984). Segmentation of the Lesser Antilles subduction zone. *Earth and Planetary Science Letters*, 71(2), pp.297–304. doi:https://doi.org/10.1016/0012-821X(84)90094-3.

Wadge, G., Voight, B., Sparks, R.S.J., Cole, P.D., Loughlin, S.C. and Robertson, R.E.A. (2014). Chapter 1 An overview of the eruption of Soufrière Hills Volcano, Montserrat from 2000 to 2010. *Geological Society, London, Memoirs*, 39(1), pp.1.1-40. doi:https://doi.org/10.1144/m39.1.

Walker, G.P.L. (1989). Gravitational (density) controls on volcanism, magma chambers and intrusions. *Australian Journal of Earth Sciences*, 36(2), pp.149–165. doi:https://doi.org/10.1080/08120098908729479.

Wallace, P., Plank, T., Bodnar, R.J., Gaetani, G.A. and Shea, T. (2021). Olivine-Hosted Melt Inclusions: A Microscopic Perspective on a Complex Magmatic World. *Annual Review of Earth and Planetary Sciences*, 49(1), pp.465–494. doi:https://doi.org/10.1146/annurev-earth-082420-060506.

Wallace, P.J. (2001). Volcanic SO_2 emissions and the abundance and distribution of exsolved gas in magma bodies. *Journal of Volcanology and Geothermal Research*, 108(1-4), pp.85–106. doi:https://doi.org/10.1016/s0377-0273(00)00279-1.

Wallace, P.J. (2003). From mantle to atmosphere: magma degassing, explosive eruptions, and volcanic volatile budgets. *Melt Inclusions in Volcanic Systems - Methods, Applications and Problems*, 5, pp.105–127. doi:https://doi.org/10.1016/s1871-644x(03)80026-8.

Wallace, P.J. (2005). Volatiles in subduction zone magmas: concentrations and fluxes based on melt inclusion and volcanic gas data. *Journal of Volcanology and Geothermal Research*, 140(1-3), pp.217–240. doi:https://doi.org/10.1016/j.jvolgeores.2004.07.023.

Wallace, P.J. and Anderson, A.T. (2000). Volatiles in Magmas. In: H. Sigurdsson, ed., *The Encyclopedia of Volcanoes*. Academic Press, pp.149–170. doi:https://doi.org/10.1016/b978-0-12-385938-9.00007-9.

Wallace, P.J. and Gerlach, T.M. (1994). Magmatic Vapour Source for Sulfur Dioxide Released During Volcanic Eruptions: Evidence from Mount Pinatubo. *Science*, 265(5171), pp.497–499. doi:https://doi.org/10.1126/science.265.5171.497.

Wallace, P.J., Plank, T., Edmonds, M. and Hauri, E.H. (2015). Volatiles in Magmas. In: *The Encyclopedia of Volcanoes. Second Edition*. Academic Press, pp.163–183. doi:https://doi.org/10.1016/b978-0-12-385938-9.00007-9.

Wallace, P.K., Anderson, A.B. and Davis, A.M. (1999). Gradients in H_2O, CO_2, and exsolved gas in a large-volume silicic magma system: Interpreting the record preserved in melt inclusions from the Bishop Tuff. *Journal of Geophysical Research*, 104(B9). doi:https://doi.org/10.1029/1999jb900207.

Wallace, P.K., Meffre, S. and Cervantes, P. (2015). Melt inclusion CO_2 contents, pressures of olivine crystallisation, and the problem of shrinkage bubbles. *American Mineralogist*, 100(4), pp.787–794. doi:https://doi.org/10.2138/am-2015-5029.

Wang, X., Hou, T., Wang, M., Zhang, C., Zhang, Z., Pan, R., Marxer, F. and Zhang, H. (2021). A new clinopyroxene thermobarometer for mafic to intermediate magmatic systems. *European Journal of Mineralogy*, 33(5), pp.621–637. doi:https://doi.org/10.5194/ejm-33-621-2021.

Waters, L.E. and Lange, R.A. (2015). An updated calibration of the plagioclase-liquid hygrometer-thermometer applicable to basalts through rhyolites. *American Mineralogist*, 100(10), pp.2172–2184. doi:https://doi.org/10.2138/am-2015-5232.

Weber, G., Blundy, J., Barclay, J., Pyle, D.M., Cole, P., Frey, H., Manon, M., Davies, B.V. and Cashman, K. (2023). Petrology of the 2020–21 effusive to explosive eruption of La Soufrière Volcano, St Vincent: insights into plumbing system architecture and magma assembly mechanism. *Geological Society, London, Special Publications*, 539(1), pp.171–200. doi:https://doi.org/10.1144/sp539-2022-177.

Welles, J.M., Demetriades-Shah, T.H. and McDermitt, D.K. (2001). Considerations for measuring ground CO_2 effluxes with chambers. *Chemical Geology*, 177(1-2), pp.3–13. doi:https://doi.org/10.1016/s0009-2541(00)00388-0.

Westrich, H.R. and Gerlach, T.M. (1992). Magmatic gas source for the stratospheric SO_2 cloud from the June 15,1991, eruption of Mount Pinatubo. *Geology*, 20(10), p.867. doi:https://doi.org/10.1130/0091-7613(1992)020%3C0867:mgsfts%3E2.3.co;2.

Wieser, P., Kent, A.J.R. and Till, C.B. (2023). Barometers Behaving Badly II: a Critical Evaluation of Cpx-Only and Cpx-Liq Thermobarometry in Variably-Hydrous Arc Magmas. *Journal of Petrology*, 64(8). doi:https://doi.org/10.1093/petrology/egad050.

Wieser, P.E., Iacovino, K., Matthews, S., Moore, G. and Allison, C.M. (2022a). VESIcal: 2. A Critical Approach to Volatile Solubility Modeling Using an Open-Source Python3 Engine. *Earth and Space Science*, 9(2). doi:https://doi.org/10.1029/2021ea001932.

Wieser, P.E., Kent, A.J.R., Till, C.B., Donovan, J., Neave, D.A., Blatter, D.L. and Krawczynski, M.J. (2022b). Barometers Behaving Badly I: Assessing the Influence of Analytical and Experimental Uncertainty on Clinopyroxene Thermobarometry Calculations at Crustal Conditions. *Journal of Petrology*, 64(2). doi:https://doi.org/10.1093/petrology/egac126.

Wieser, P.E., Lamadrid, H., Maclennan, J., Edmonds, M., Matthews, S., Iacovino, K., Jenner, F.E., Gansecki, C., Trusdell, F., Lee, R.L. and Ilyinskaya, E. (2021). Reconstructing Magma Storage Depths for the 2018

Kīlauean Eruption From Melt Inclusion CO 2 Contents: The Importance of Vapour Bubbles. *Geochemistry, Geophysics, Geosystems*, 22(2). doi:https://doi.org/10.1029/2020gc009364.

Witham, F. (2010). Conduit convection, magma mixing, and melt inclusion trends at persistently degassing volcanoes. *Earth and Planetary Science Letters*, 301(1-2), pp.345–352. doi:https://doi.org/10.1016/j.epsl.2010.11.017.

Witham, F., Blundy, J.D., Kohn, S.C., Lesne, P., Dixon, J., Churakov, S.V. and Botcharnikov, R.E. (2012). SolEx: A model for mixed COHSCl-volatile solubilities and exsolved gas compositions in basalt. *Computers & Geosciences*, 45, pp.87–97. doi:https://doi.org/10.1016/j.cageo.2011.09.021.

Wong, K., Mason, E., Brune, S., East, M., Edmonds, M. and Zahirovic, S. (2019). Deep Carbon Cycling Over the Past 200 Million Years: A Review of Fluxes in Different Tectonic Settings. *Frontiers in Earth Science*, 7. doi:https://doi.org/10.3389/feart.2019.00263.

Yang, T.F., Lee, T., Chen, C.-H., Cheng, S.-N., Knittel, U., Punongbayan, R.S. and Rasdas, A.R. (1996). A double island arc between Taiwan and Luzon: consequence of ridge subduction. *Tectonophysics*, 258(1-4), pp.85–101. doi:https://doi.org/10.1016/0040-1951(95)00180-8.

Yoshimura, S. and Nakamura, M. (2011). Carbon dioxide transport in crustal magmatic systems. *Earth and Planetary Science Letters*, 307(3-4), pp.470–478. doi:https://doi.org/10.1016/j.epsl.2011.05.039.

Young, S.R., Francis, P.W., Barclay, J., Casadevall, T.J., Gardner, C.A., Darroux, B., Davies, M.A., Delmelle, P., Norton, G.E., Maciejewski, H., Oppenheimer, C., Stix, J. and Watson, I.M. (1998a). Monitoring SO_2 emission at the Soufrière Hills Volcano: Implications for changes in eruptive conditions. *Geophysical Research Letters*, 25(19), pp.3681–3684. doi:https://doi.org/10.1029/98gl01406.

Young, S.R., Sparks, R.S.J., Aspinall, W.P., Lynch, L.L., Miller, A.D., Robertson, R.E.A. and Shepherd, J.B. (1998b). Overview of the eruption of Soufrière Hills Volcano, Montserrat, 18 July 1995 to December 1997. *Geophysical Research Letters*, 25(18), pp.3389–3392. doi:https://doi.org/10.1029/98gl01405.

Young, S.R., Voight, B. and Duffell, H.J. (2003). Magma extrusion dynamics revealed by high-frequency gas monitoring at Soufrière Hills volcano, Montserrat. *Geological Society, London, Special Publications*, 213(1), pp.219–230. doi:https://doi.org/10.1144/gsl.sp.2003.213.01.13.

Zellmer, G.F. (2003). Geochemical Evolution of the Soufrière Hills Volcano, Montserrat, Lesser Antilles Volcanic Arc. *Journal of Petrology*, 44(8), pp.1349–1374. doi:https://doi.org/10.1093/petrology/44.8.1349.

Zellmer, G.F., Edmonds, M. and Straub, S.M. (2014). Volatiles in subduction zone magmatism. *Geological Society, London, Special Publications*, 410(1), pp.1–17. doi:https://doi.org/10.1144/SP410.13.

Zhang, H., Yang, Y., Yan, Q., Shi, X., Zhu, Z., Su, W., Qin, C. and Ye, J. (2016). Ca/Al of plagioclase-hosted melt inclusions as an indicator for post-entrapment processes at mid-ocean ridges? *Geologica Acta*, 14(1), pp.1–12.

Zurek, J., Moune, S., Williams-Jones, G., Vigouroux, N. and Gauthier, Pierre-J. (2019). Melt inclusion evidence for long term steady-state volcanism at Las Sierras-Masaya volcano, Nicaragua. *Journal of Volcanology and Geothermal Research*, 378, pp.16–28. doi:https://doi.org/10.1016/j.jvolgeores.2019.04.007.